RESPONSE OF METALLIC PLATES TO SMALL ARMS PROJECTILE IMPACT

Ph.D. THESIS

by

SENTHIL K

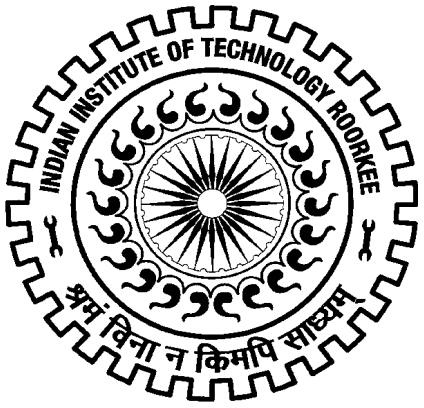

DEPARTMENT OF CIVIL ENGINEERING
INDIAN INSTITUTE OF TECHNOLOGY ROORKEE
ROORKEE - 247 667 (INDIA)
JANUARY, 2015

RESPONSE OF METALLIC PLATES TO SMALL ARMS PROJECTILE IMPACT

A THESIS
Submitted in partial fulfilment of the requirements for the award of the degree of

DOCTOR OF PHILOSOPHY

in
CIVIL ENGINEERING

by

SENTHIL K

DEPARTMENT OF CIVIL ENGINEERING
INDIAN INSTITUTE OF TECHNOLOGY ROORKEE
ROORKEE – 247 667 (INDIA)
JANUARY, 2015

INDIAN INSTITUTE OF TECHNOLOGY ROORKEE
ROORKEE

CANDIDATE'S DECLARATION

I hereby certify that the work which is being presented in this thesis entitled **"RESPONSE OF METALLIC PLATES TO SMALL ARMS PROJECTILE IMPACT",** in partial fulfilment of the requirements for the award of the Degree of Doctor of Philosophy and submitted in the Department of **Civil Engineering** of the Indian Institute of Technology Roorkee, Roorkee is an authentic record of my own work carried out during the period from **December, 2010 to January, 2015** under the supervision of Dr. Mohd. Ashraf Iqbal, Associate Professor, Department of Civil Engineering, Indian Institute of Technology Roorkee.

The matter presented in the thesis has not been submitted by me for the award of any other degree of this or any other institute.

SENTHIL K

This is to certify that the above statement made by the candidate is correct to the best of my knowledge.

(Mohd. Ashraf Iqbal)
Supervisor

Date: , 2015

The Ph.D. Viva-Voce Examination of **SENTHIL K**, Research Scholar, has been held on ……..

Chairman, SRC Signature of External Examiner

This is to certify that the student has made all the corrections in the thesis.

Signature of Supervisor Head of the Department

ABSTRACT

The present study is based on the experimental and finite element investigations of the response of metallic plates subjected to small arms projectile impact. The mild steel, Armox 500T steel and 7075-T651 aluminium alloy plates of various thicknesses were impacted by Armor Piercing Incendiary (API) projectiles at increasing angles of incidence until the occurrence of projectile ricochet. The Armox 500T steel targets of thicknesses 6, 8 and 10 mm were impacted by 7.62 API projectiles and those of thicknesses 5, 10, 15 and 20 mm impacted by 12.7 API projectiles. The 7075-T651 aluminium targets of thicknesses 20, 32, 40 and 50 mm were impacted by 12.7 API projectiles. The 7.62 API projectiles were fired through sniper rifle and 12.7 API projectiles through air defence gun. The incidence velocity of both of these projectiles was close to 820 m/s. The incidence and residual projectile velocities were measured with the help of infrared optical measurement device. The high speed video camera was employed for recording the residual projectile velocity as well as for studying the mechanics of penetration and perforation. The experimental results thus obtained were simulated by carrying out the three-dimensional finite element analysis on ABAQUS/Explicit finite element code. The ballistic performance of mild steel targets of thicknesses 4.7, 6, 10, 12, 16, 20 and 25 mm was also studied against 7.62 API projectiles by performing the finite element simulations and the results thus obtained were validated through the experiments performed by Gupta and Madhu (1992, 1997). The numerical simulations enabled the determination of ballistic limit for all the target materials at normal impact.

The characterization of the target material was carried out under varying stress state, strain rate and temperature. The possible anisotropy of a material was studied by extracting

the flat specimens in three different orientations i.e., 0°, 45° and 90° from the middle of the thickness of the plate. The mild steel and Armox 500T steel plates were found to be isotropic while 7075-T651 aluminium alloy plates have been found to possess high degree of anisotropy.

The tension tests were carried out on smooth cylindrical specimens at a constant strain-rate, 6×10^{-4} s^{-1}. The gauge diameter of the cylindrical specimen was 6.25 and the gauge length 25 mm. The diameter reduction of the specimen was measured up to fracture and the true stress-strain relationship was obtained.

The influence of stress triaxiality was studied by performing quasi-static tests under tension on notched cylindrical specimens with initial notch radius varying from 0.4 to 10 mm. The results thus obtained revealed a decrease in ductility and an increase in strength of the material with increase in stress triaxiality.

The low, medium and high strain rate tension tests were performed on smooth cylindrical specimens of diameter 3 mm and gauge length 10 mm. The strain rate in the range 1×10^{-4} s^{-1} - 1500 s^{-1} was obtained on Universal Testing Machine and Split Hopkinson pressure bar apparatus. In general, the strength of the material has been found to increase and the ductility decreased with increase in strain rate.

The thermal sensitivity of the material was studied by performing quasi-static tension tests at varying temperature on cylindrical specimens of diameter 6.25 mm and gauge length 25 mm. A portable furnace with 220 mm height and 60 mm internal diameter was employed for controlling the temperature of the specimens during testing. The tests were carried out in the temperature range of 27 °C to 900 °C. The flow stress of all the materials has been found

to increase initially with increase in temperature from 100 °C to 300 °C due to blue brittle effect, and subsequently it decreased with further increase in temperature.

The material of 7.62 API and 12.7 API projectiles was also characterized at varying stress triaxility, strain rate and temperature. The material coupons were extracted from the hardened steel core of the bullet.

The material tests thus performed enabled the calibration of the Johnson-Cook (JC) elasto-viscoplastic constitutive model for the target as well as the projectile material. All the parameters of Johnson-Cook flow and fracture model were calibrated through curve fitting method. The calibrated material parameters of the JC model were validated by simulating the high strain rate material tests conducted on Split Hopkinson Pressure Bar (SHPB). The ABAQUS/Explicit finite element code was employed for carrying out the axi-symmetric simulations for the validation of the material model.

The experimental and numerical results with respect to failure mechanism, residual projectile velocity, maximum angle of perforation and critical angle of ricochet have been compared. A close correlation between the experimental findings and the predicted results has been found. In general, the ballistic resistance has been found to increase with increase in angle of obliquity. Moreover, the critical angle of projectile ricochet and maximum angle of perforation was found to decrease with increase in target thickness.

The ballistic limit of 10 mm thick Armox 500T steel has been found to be 100% higher than the equivalent mild steel target against 7.62 API projectile. The ballistic limit of 20 mm thick Armox 500T steel has been found to be 55% higher than the equivalent 7075-T651 aluminium target against 12.7 API projectile.

The ballistic performance of mild steel and Armox 500T steel as a function of target areal density has been compared against 7.62 API projectile. It has been found that 78 kg/m^2 Armox 500T steel offered the ballistic limit equivalent to that of the 196 kg/m^2 mild steel. Therefore, with respect to thickness as well as areal density the ballistic limit of Armox steel is 2.5 time higher than mild steel against 7.62 API threat.

The ballistic performance of Armox 500T and 7075-T651 aluminium materials has also been compared against 12.7 API projectiles as a function of areal density. The 108 kg/m^2 of 7075-T651 aluminium offered the ballistic limit equivalent to that of 157 kg/m^2 of Armox 500T steel. Therefore, if the performance of Armox steel and aluminium is compared with respect to thickness, the aluminium target should be two times thicker than Armox steel target to stop the 12.7 API projectile. However, if the areal density of the two materials is compared, Armox steel would be two times heavier than the equivalent aluminium target to stop the 12.7 API projectile.

The study thus presents a detailed investigation of the material behaviour and ballistic performance of mild steel, Armox 500T steel and 7075-T651 aluminium alloys and leads to some important conclusions pertaining to the mechanics of projectile and target interaction.

ACKNOWLEDGEMENT

I express my deep sense of indebtedness to my esteemed guide **Dr. Mohd. Ashraf Iqbal** for his invaluable guidance, inspiration, keen interest and constant motivation throughout this work.

I would like to take this opportunity to acknowledge the members of my examining committee for their careful examination of the work and invaluable comments, which made a deep impact on my research. I am also thankful to **Prof. D. Kashyap**, Head, Department of Civil Engineering for extending the experimental, computational and other facilities in department.

I would like to acknowledge the contributions of **Prof. P. Bhargava,** Department of Civil Engineering, IIT Roorkee and **Prof. N.K. Gupta,** Department of Applied Mechanics, IIT Delhi for their help to overcome some important issues.

I am highly thankful to the MAA Panel DRDO for providing the financial support for the work presented in the thesis.

I am highly grateful to the Gun Group, TBRL Chandigarh for their invaluable support for ballistic tests and high strain rate material tests. I would like to thank **Ms. Ipsita Biswas** for all the administrative support at TBRL. Special thanks are extended to **Mr. Prince Sharma**, **Dr. B. Debarthi, Dr. Pradeep Chandel, Mr. Vikas Bharadwaj** and **Mr. Vikas Mangla** for their substantial help. I would like to thank **Dr. V. Madhu,** DMRL, Hyderabad for providing constructive and important suggestions in streamlining the experimental programme.

With regard to preparing the testing, I would like to acknowledge the contributions of Technical and Non-Technical staff of Structural Engineering Laboratory for the instrumental support including technical contributions.

I am highly thankful to **Mr. Manjot Singh Cheema** for providing the valuable source for machining of high strength steel specimens. Also, I would like to thank **Dr. N. K. Singh** and **Mr. S. H. Khan** for all sorts of technical help throughout the tenure of my research.

Special thanks to my co-scholars in the this institute, **Mr. A.B. Danie, Mr. J.R. Prince, Mr. G. Tiwari, Mr. N. Prabhu, Mr. G.B. Ramesh, Mr. Vimal, Mr. S. Chidhambaram, Mr. A. Rajput, Mr. Mohd. Zaid and Mr. Venkatesan J.,** for extending all sorts of helps

without any hesitation and making my stay very pleasant and memorable during the entire tenure at IIT Roorkee.

I would like to thank **Prof. K.S. Sathyanarayanan** and **Mr. Kalishwaran** for the spiritual support and insights throughout the tenure of my academic carrier.

Last but certainly not least, my heartfelt thanks goes to my parents for the continuous support to achieve many things in my life. I am also grateful to **Mr. V.M. Tamizarasan** for their valuable support in my life. I would like to express my warmest thanks to **Ms. S. Rupali, Mrs. S. Sujata** and **Mr. Sanjay** who endured all the sufferings silently and looked forward to this day.

I express all of my gratitude to the universe which enabled me to compile this thesis.

Indian Institute of Technology **(SENTHIL K)**
Roorkee, India

CONTENTS

LIST OF FIGURES

LIST OF TABLES

CHAPTER 1

Introduction

1.1 INTRODUCTION

The safety of personnel and equipment is a major requirement behind any successful military operation. The purpose of an amour is not only to shield but also to provide the psychological strength to the recruits for moving fearlessly in the battlefield. Carefully engineered armour may change the course of battle by minimizing the damage and casualties. The material and design of armour in spite of significant excellence and sophistication remains to achieve perfection due to the equivalent and consistent advancement in precision and lethality of the weapons. A majority of ancient armament comprised of clubs, swords, battle axes, spears, bows and arrows. These remained effective up to seventeenth century until the development of muzzle loaded rifle. The development of machine gun in 1884 enabled concurrent firing through single triggering. The addition of Avtomat Kalashnikova in 1945 enhanced the rate of firing up to 600 rounds per minute. The innovation in the small arms technology is still under progress with the development of more advanced and youngest member of the family, Adaptive Combat Rifle, which enabled firing of 800 rounds per minute.

The light weight and high strength materials had always been a primary requirement for weapon and armour industries. There was a rapid increase in the demand of these materials during and after World War II that led to the competitive improvement in their material properties and machinability for achieving best performance for indenter as well as armour. The selection of a suitable armour material is highly crucial for designing military vehicles, battle tanks and protective structures. The ideal ballistic material should possess lowest areal density, high ductility and high strength. The steel and aluminium alloys are considered to be the most suitable materials for armour applications due to their high

absolute strength and hardness combined with high ductility and low price compared to advanced composite materials.

The interaction between the projectile and target is highly influenced by the shape, size, hardness and incidence velocity of the projectile, thickness, density, ductility and microstructure of the target as well as impact conditions such as angle of incidence and vicinity of the target. The material behaviour of the projectile and target has also been found to play a major role on the perforation mechanics. The associated large strains, high strain rate and high temperature complicate the understanding of the perforation phenomenon as well as the description of the material behaviour of interacting bodies.

The present study is based on the experimental and finite element investigation of the response of metallic plates subjected to small arms projectile impact. The mild steel, Armox 500T steel and 7075-T651 aluminium alloy plates of various thicknesses were impacted by Armor Piercing Incendiary (API) projectiles. The angle of obliquity was varied until the occurrence of projectile ricochet. The perforation, failure mechanism and ballistic performance of the target was studied at normal as well as oblique impact. The critical angle of ricochet was also obtained for each target thickness. The material of the target and the projectile was characterized under varying stress state, strain rate and temperature and the flow stress and fracture strain parameters of the Johnson-Cook elasto-viscoplastic material model were calibrated. The calibrated material parameters were validated by numerically simulating the high strain rate tension tests performed on Hopkinson pressure bar apparatus. These material parameters were subsequently employed for predicting the behaviour of the projectile as well as target in order to numerically reproduce the ballistic tests. The numerical simulations enabled the determination of ballistic limit and the critical angle of ricochet. The

finite element simulations were carried out using ABAQUS/Explicit finite element code. The numerical simulations enabled a close examination of the perforation and failure mechansim of the target, critical angle of ricochet and evaluation of the ballistic limit. The number of experimetnal tests was also reduced by carrying out the detailed finite element simulations.

1.2 STEEL ALLOYS AS ARMOUR MATERIAL

A material's suitability for armour application is dependent upon its geometric and material properties along with the areal density. The ideal armour must possess low areal density and high strength associated with high ductility. There are a number of monolithic, laminate and composite materials capable to satisfy this requirement, however, the availability and economy of steel alloys supplemented with superior mechanical properties and machinability distinguish them to be the most suitable armour material even in today's modern era. There are a number of steel alloys readily available with varying strength, hardness and ductility which may satisfy the specific armour requirements. The most suitable armour steel has been identified in the present study, for small arms applications, based up on the following studies available in the literature.

Bhat (1985) discussed some basic principles for identifying the material for effective armour. The material should be able to sustain the strain gradients without cracking up. This is possible only when the ductility which is an important quality for good armour, increases with strain rate. High hardness and impedance of the armour material can induce high stresses on the projectile by virtue of which the projectile can absorb its own kinetic energy by experiencing plastic deformation and fracture.

Borvik et al. (2009b) conducted experimental and numerical studies on Weldox 500E, Weldox 700E, Hardox 400E, Domex Protect 500E and Armox 560T targets by 7.62 mm BR6 and BR7 projectiles. It was found that only Armox 560T and Domex 500 could meet the requirements of EN 1063 bullet of BR6 and BR7 standard. It was also concluded that strength of the target is more important characteristic than ductility against non-deformable small arms projectiles.

Brian Leavy (1996) observed that the Improved Rolled Homogenous Armour (IRHA) steel performed better than standard Rolled Homogenous Armour (RHA) steel against the L/D 5KE (Length to Diameter Ratio 5 Kinetic Energy) penetrators. Despite undergoing more breakouts the high hardness IRHA has been found to be ballistically superior to standard RHA steel.

Buchar et al. (2002) conducted experimental and numerical studies with single and layered (dual) high strength steel targets. The targets of dual hardness exhibited very good resistance against the impact of Armour Piercing (AP) projectile. The ballistic performance increased with an increase in the thickness of higher hardness steel layer. The addition of a ductile interlayer led to further improvement in the given performance.

Demir et al. (2008) studied the ballistic performance of high strength steel AISI4140 with areal densities 55, 70, 85, 100 and 115 kg/m^2 and hardness 38, 50, 53 and 60 HRC against 7.62 AP projectiles. Although the increase in the hardness level improved the ballistic behaviour, the steel specimens having either 50 or 60 HRC were broken in a brittle manner instead of being perforated by the projectile. The best ballistic performance occurred corresponding to the target with hardness level 53 HRC.

Dikshit et al. (1995) performed experiments on 20 and 80 mm thick RHA steel targets of varying hardness level, 295 HV - 520 HV, by 20 mm diameter ogive-nose projectile in a velocity range 300 - 800 m/s. The failure mechanism of the target has been found to be a function of target hardness and projectile incidence velocity. When the hardness was more than 400 HV and incidence velocity above 400 m/s, the target experienced failure through plugging. When the hardness was lesser than 400 HV the target experienced failure through ductile hole enlargement. The 20mm thick target (350 HV) stopped the 20 mm diameter ogive nosed projectile when impacted at 30° to 45° obliquity at incidence velocity up to 800 m/s while at 0° to 15° obliquity it could defeat the projectile only up to 600 m/s incidence velocity [Dikshit et al. (1998)]. The penetration depth decreased with increase in the angle of obliquity and has reduced to minimum at the oblique angle corresponding to critical ricochet.

Gooch et al. (2007) performed experiments on High Hardness Armour (HHA) steel (530HB) and Ultra High Toughness Armour (UHTA) steel (450HB) targets through AP and Fragment Simulating Projectile (FSP). The UHTA plates experienced failure through adiabatic shearing against FSP. It was observed that as the hardness of the steel plates increased, the ballistic limit also increased against AP projectiles. As such the ballistic performance of UHTA and HHA was almost identical however UHTA has been found to possess better weldability and structural properties and had also offered consistent ballistic performance than HHA.

Madhu and Bhat (2011) described various approaches used in the high hardness steel, titanium, ceramic and polymer to improve the survivability of battle tank and Infantry Combat Vehicle (ICV). The high hardness steel being three to four times cheaper than ceramics and composites is continuously being used as the main element in armour vehicles.

It was concluded that the cost of active armour protection would depend on the sophistication of the system as well as buyer.

Prifti et al. (1997) conducted experiments with IRHA (40 and 48 HRC) and RHA (33 HRC) plates against 0.5 caliber APM2 projectiles. The 48 HRC IRHA plate offered better ballistic performance than the 40 HRC against steel core APM2 projectiles. Moreover, the IRHA steel has been found to have superior ballistic resistance than RHA steel against APM2 as well as brittle tungsten carbide penetrators like 20mm API M602.

Showalter et al. (2008) performed experiments on Armox 600T and Armox Advance steel targets of 5, 6 and 7 mm thicknesses impacted by 0.3 and 0.5 caliber APM2 projectiles. It was concluded that both Armox 600T and Armox Advance steel targets have significantly high ballistic performance than standard MIL-DTL-46100E high hardness targets.

Ubeyli et al. (2007) studied the performance of steel alloy with different hardness such as 40, 50 and 60 HRC plates impacted by 7.62 AP projectiles. All the targets except 60 HRC experienced failure against 7.62 AP projectiles. It was observed that hardness levels in steel plates played an important role in the ballistic performance. When the hardness of the steel plates increased, the penetration and propagation ability of the projectile decreased.

Woodward (1978) conducted experiments on steel and titanium alloy targets to predict the critical energies of penetration. The penetration resistance initially increased linearly with increase in hardness as the target deformed through ductile hole enlargement up to 320 HV. With further increase in hardness, the penetration dropped due to adiabatic effects and reached a minimum. However, subsequently the penetration resistance increased with further increase in hardness as a result of projectile shattering.

The results obtained in the above studies illustrated that high strength and high hardness are important parameters for a material to be used for armour application. The high strength is an essential characteristic to avoid indentation and failure of the armour against small arms projectiles. High hardness induces stresses on the projectile causing its breakage and thereby dissipation of kinetic energy in projectile deformation. In the present study therefore the Armox 500T steel has been studied as an armour material as it possesses better strength, hardness and ductility than other steel alloys. However, in order substantiate the advantage of Armox 500T steel with respect to material characteristics and ballistic efficiency, a detailed material and ballistic evaluation has also been carried out for the conventional mild steel. The results thus obtained enabled a direct comparison of the ballistic performance of both materials and facilitated a quantitative assessment of the degree of improvement by replacing mild steel with that of the Armox steel as armour material.

1.3 ALUMINIUM ALLOYS AS ARMOUR MATERIAL

Aluminium alloys are considered as primary material for structural components of aircraft since 1930 due to their light weight and good machinability. The aim of the present study was to explore lightweight aluminium alloy with high strength and high fracture toughness. There are many drivers and parameters involved in the selection of the material for primary application of military, army, navy and air force. These include, but not limited to, low structural weight, safety, cost, availability, reliability, manufacturability and maintainability. The identification of the aluminium alloy for the present study is based upon the detailed survey of the state of art studies presented in the following section.

Borvik et al. (2010) conducted experimental and numerical investigation on 20 mm thick 7075-T651 aluminum plates impacted by 20 mm diameter, 197 grams hardened steel blunt and ogival-nosed projectiles. The thermoelastic–thermoviscoplastic constitutive model and fracture criterion were used to perform numerical simulations using finite element code LS-DYNA. The numerical simulations reasonably captured the failure modes however, some deviations were observed in the predicted ballistic limit velocities.

Forrestal et al. (1992) conducted ballistic experiments on 7075-T651 aluminum targets by 7.1 mm diameter and 25 grams ogival-nosed rods at impact velocities in the range 370 to 1260 m/s. They developed analytical model to predict the forces and penetration depth of long rod projectile. The model predicted the penetration depths in good agreement with the data for the given impact velocities.

Forrestal et al. (2010) conducted an experimental study with 20mm thick monolithic and 40 mm thick double layered 7075 T651 aluminium armour plates by 7.62 APM2 bullet in the velocity range 600 to 1100 m/s. It was found that the brass jacket and lead filler had relatively small effect on the perforation process as well as the residual velocities.

Forrestal et al. (2014) conducted experiments wherein 20 mm thick 6082-T651 aluminum target was impacted by 7.62 APM2 projectile at varying angle of obliquity. The measured residual and ballistic limit velocities for the full bullet as well as steel core led to the conclusion that the perforation process was dominated by the hard steel core of the bullet. The ballistic limit and residual projectile velocities were also predicted by cavity-expansion model and found to be in agreement with those of their actual values.

Goldsmith and Finnegan (1986) performed ballistic experiments at 0° to 50° obliquity on 2024 aluminium targets of 1.78 to 25.4 mm thicknesses by cylindro-conical and blunt

projectiles in a velocity range 20 to 1025 m/s. The influence of target material, thickness, initial projectile velocity and angle of incidence was studied. The nose shape and mass of the projectiles were found to have insignificant and slight effect on the ballistic limit respectively. The non-dimensional velocity drop of the projectile was found to decrease with increase in angle of obliquity up to 20° and thereafter it increased with further increase in obliquity.

Madhu et al. (2005) studied the ballistic performance of 95% and 99.5% alumina ceramic tiles backed by metal plates at normal incidence against 7.62 and 12.7 mm AP projectiles. The higher purity alumina (99.5%) showed better ballistic performance than 95% alumina. Further, the 99.5% alumina exhibited predominantly transcrystalline fracture while 95% alumina showed less defined fracture surface.

Pedersen et al. (2011) conducted experiments on 20 mm thick 7075-T651 aluminum alloy plates by blunt and ogival-nosed projectiles. The aluminum plates experienced more delamination and fragmentation against ogival projectile than blunt projectile. The fractured surface of the material specimens tested under tension and compression were compared with that of the surface of fractured targets. It was concluded that the simple material tests with varying stress triaxiality gave a good indication of the fracture mode, delamination and fragmentation of the target.

Starke and Staley (1996) studied the performance and material characteristics for suitability as airframe components. It was observed that 7075–T6 aluminium is suitable for various aircraft structural components as it has relatively better strength, fracture toughness, fatigue crack propagation, stress corrosion cracking (SCC) and elastic modulus than other many other commercial aluminium alloys, Fig. 1.1.

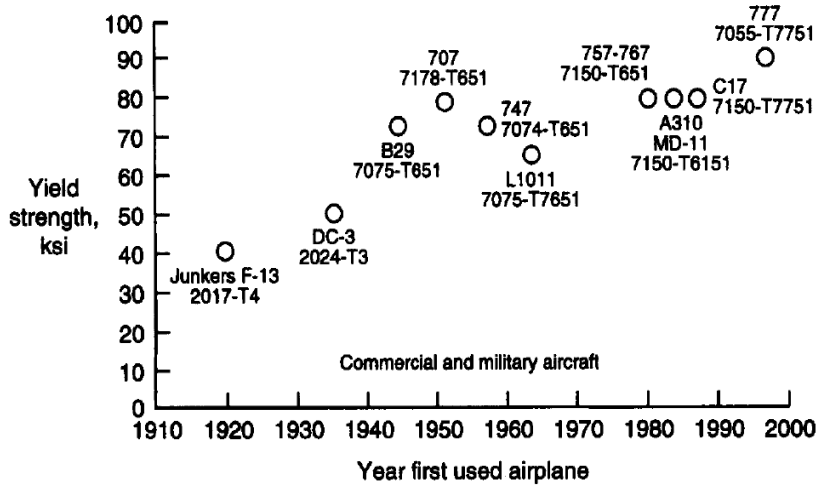

Fig. 1.1 Yield strength of various aluminium alloys and the year of the first application

Tajally and Emadoddin (2011) investigated the mechanical properties, anisotropic behaviour and formability of 7075 aluminum alloy thin sheet at various annealing temperatures. The tensile properties and formability parameters were correlated with the limit drawing ratio (LDR) and Erichsen test. It was found that the sheets annealed at 400 °C possess good ductility, strain hardening and r-value such that the formability of 7075 aluminum alloy can be improved by increasing annealing temperature to 350 °C to 400 °C.

The studies available in the literature led to the conclusion that the mechanical properties of 7075 T651 are most suitable for aerospace applications as it possesses high fracture toughness and high hardness compared to other high strength aluminium alloys. Aluminium 7075 T651 was among the first aluminium alloys used in European military aircrafts.

1.4 SMALL ARMS PROJECTILES

The perforation and indentation mechanism, in addition to the characteristics of the target, is largely dependent upon the structural and mechanical properties of the impacting

projectile. A suitable strength, hardness, size and configuration of the projectile are collectively responsible for resultant failure of the target. Thus, it is pertinent to understand the individual contribution of each of these characteristics in order to evaluate the overall performance of the projectile.

The interaction between the projectile and target initiate complex mechanical and thermal processes leading to significant physical changes in both of these interacting bodies such as plastic deformation, splitting, fragmentation of the projectile and local and global deformation, spalling, scabbing, tunneling and petalling in the target. There are two basic principles of degradation of armor-piercing projectiles upon striking the target;

- Stripping of jacket
- Breakage of penetrator

These failure mechanisms have the major influence on the subsequent damage and penetration capability, AGARD (2001). In general, the projectiles can be classified into exploding and non-exploding projectiles

An exploding projectile contains charge which explodes during penetration and results in fragment penetration and development of blast over pressure on the target.

The non-exploding projectiles include small arms projectiles, AAA (Anti-aircraft Artillery) projectiles and missile warhead fragments. Non exploding projectiles of caliber greater than 14.5 mm are generally classified as AAA (Anti-Aircraft Artillery) or cannon projectiles. The small arms projectiles comprise of a solid metal core typically surrounded by thin metal jacket, see Fig. 1.2. The following is an important category of small arms projectiles and the corresponding gun employed to facilitate their launching;

- 14.5 mm API (KPV/Slostin heavy Machine Gun)
- 14.5 mm API Tungston Carbide core (KPV/Slostin heavy Machine Gun)
- 12.7 mm API (Anti-Aircraft Machine Gun)
- 7.62 mm API (Rifle)
- 7.62 mm Light Ball (Rifle)
- 7.62 mm Heavy Ball (Rifle/Machine Gun)
- 7.62 mm Tracer (Rifle/Machine Gun)

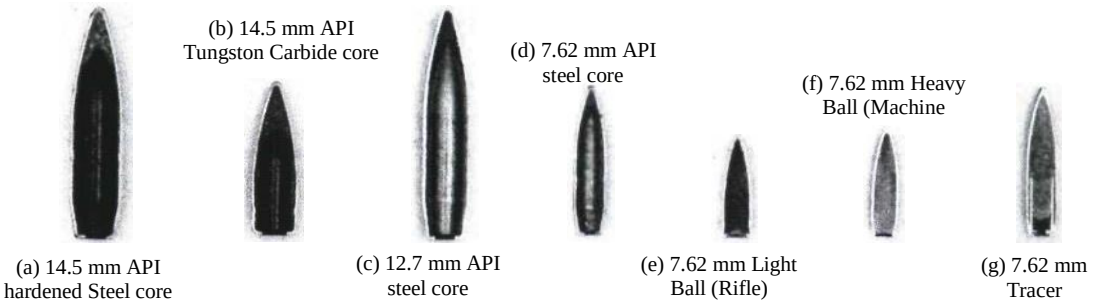

Fig. 1.2 Small arms projectiles

The 7.62 mm Tracer projectile comprises solid lead core of diameter 7.62 mm that is fired against personnel, light armour, unarmed targets and concrete shelters. The 7.62 mm Ball projectiles have relatively soft core of diameter 7.62 mm intended to be used against humans. The Armor Piercing projectiles have hardened steel core of diameter indicated by the number against their name (e.g.; 7.62, 12.7, 14.5). These projectiles are designed to penetrate hard targets like armor vehicle, battle tank, explosive container and aircraft. The Incendiary projectiles contain thermally active filler that ignites during impact and hence causes ignition of on-board flammables. Therefore, many projectiles combine some of the above capabilities, like, 7.62 API and 12.7 API are basically armor piercing-incendiary projectiles and the 23 mm API-T is armor piercing-incendiary-tracer.

The 7.62 API projectile is considered a common threat to humans while the 12.7 API projectile is a threat to armoured vehicles and aircrafts. Both of these projectiles are thermally active and capable to pierce the high strength steel and aluminum targets. Thus keeping in view their high threshold, widespread application and availability, both of these projectiles have been identified to be studied in the present investigation.

1.5 CONSTITUTIVE MODELS

In order to numerically simulate the perforation mechanics and the material behaviour of the interacting bodies, the phenomenological constitutive models are employed which reproduce the complex stress-strain relations in a simplified manner based on principle of mechanics. A number of constitutive models are available for predicting the plastic deformation and fracture behaviour of metals under high rate of loading. A competent model should be capable of incorporating various phenomena occurring simultaneously during the flow and fracture process under varying strain rate. The practical issues such as number of material parameters, their availability, calibration procedure and compatibility of the model with available commercial finite element codes are fairly important considerations. A complex model with large number of material parameters may be quite accurate in predicting the in-depth local material behaviour however its calibration would be highly complicated and time consuming and therefore a simpler model capable of capturing the overall structural response and employing fewer material parameters is considered more practical.

Teng and Wierzbicki (2006) employed six distinct fracture models to predict the damage in Weldox 460 E steel and 2024-T351 aluminium plates against blunt and conical projectiles. The predicted failure mechanism and residual projectile velocities were compared

with their actual values and the limitations of each model were discussed. The Wilkins failure model predicted unrealistic spallation of material due to vanishing ductility effects. The maximum shear stress criterion could not predict the shear plugging under a range of incidence velocities. The resultant critical shear stress caused either premature or incomplete failure of the target. The modified Cockcroft-Latham model employed only one parameter to characterize the material, however, the single parameter could not represent the damage due to varying stress triaxiality. Similarly, the conventional critical strain and the simplified Bao-Wierzbicki (BW) fracture models failed to give satisfactory results for a wide range of problems. On the other hand, the Johnson-Cook (JC) failure model predicted the realistic fracture behaviour and residual velocities. It was concluded, however, that the capability of the JC model to predict the shear dominant failure has not been established yet.

Banerjee (2005) studied the limitations of the available constitutive models by simulating the behaviour of OFHC copper under varying strain rate and temperature. The one dimensional tension and compression tests as well as the Taylor impact tests were simulated using JC, Steinberg-Cocharan-Guinan-Lund (SCGL), Zerilli-Armstrong (ZA), Mechanical Threshold (MTS) and Preston-Tonks-Wallace (PTW) models. The JC model overestimated the initial yield for the quasi-static test performed at room temperature. The rate of hardening was underestimated for the test performed at room temperature and 8000 s^{-1} strain rate while the strain rate dependence of the yield stress was under estimated at high temperature, 1173 K. The SCGL model underestimated the softening associated with increasing temperature, however, the yielding at 8000 s^{-1} strain rate was predicted reasonably accurately. At 4000 s^{-1} strain rate the performance of the model was worse at high temperature. The ZA model accurately predicted the quasi-static yield stress at room temperature however underestimated

the same at 8000 s^{-1} strain rate. The yield stress at 4000 s^{-1} strain rate was reasonably predicted however the decrease in yield stress with increasing temperature was overestimated. The MTS model predicted higher yield stress under quasi-static test performed at high temperature (1173 K), whereas, the higher strain rate tests performed at high temperature were in agreement with the experimental results. The PTW model explicitly accounted for the rapid increase in yield stress at strain rate above 1000 s^{-1} and performed better under the tests carried out in compression than in tension. For Taylor impact tests however, the JC model predicted the mushroomed diameter and the final length most accurately. All the other models though correctly predicted the final length however under predicted the mushroomed diameter.

The Taylor impact tests were also carried out by Emrah et al. (2011) on stainless steel 304 L and the results obtained were reproduced using Zerilli-Armstrong and Johnson-Cook models. Both the flow stress models predicted the peripheral bulging accurately however, the Zerilli-Armstrong model underestimated the final deformed length.

Borvik et al. (1999, 2001) slightly modified the equivalent flow stress and fracture strain expressions of the JC model and calibrated the material parameters for Weldox 460 E steel through uniaxial tension tests performed at varying strain rate and temperature. The model was then employed to simulate the perforation of 6 and 12 mm thick Weldox 460 E steel plates by blunt, conical and hemispherical projectiles in a series of studies Borvik et al. (1999, 2001, 2002a, 2002b, 2004, 2009b) and results thus obtained were validated through experiments. The numerical model qualitatively captured the overall physical behaviour of the target and accurately predicted the failure modes, energy absorption, maximum target deformation and residual projectiles velocities. The ballistic limit velocity for each projectile

was predicted within 8% accuracy. In the case of conical projectile, however, there was a problem of distortion of the elements and error termination. To avoid this, erosion of the elements was carried out at an early stage by reducing the fracture strain parameters. The adaptive meshing technique was also employed in order to reduce the critical element distortion against conical projectile. The simulations employing adaptive meshing with original fracture parameters were successfully completed and these reproduced good correlation with experiments. The ballistic limit velocity and the residual velocities of the blunt and hemispherical projectiles were also reproduced with and without adaptive meshing and both of these approaches led to same outcome.

Clausen et al. (2004) studied the flow and fracture characteristics of AA5083-H116 aluminium alloy as a function of stress-triaxiality, strain rate and temperature. The material exhibited negative strain rate sensitivity at strain rate, $10^{-4} – 1\ s^{-1}$, and significant reduction in flow stress at temperatures, 400 - 500 °C. The material characterization enabled the calibration of the parameters for modified JC model, Borvik et al. (2001). The model was then employed for predicting the perforation of 15-30 mm thick AA5083-H116 aluminium plates by 20 mm diameter conical projectiles using 2D axisymmetric elements and adaptive rezoning, Borvik et al. (2009a). The simulations predicted the ballistic limit with a maximum deviation of 5% from the experimental results.

Dey et al. (2006) studied the influence of fracture criterion in numerical simulations of the perforation of three different steel alloys. The five parameter Johnson–Cook fracture criterion calibrated through relatively simple tensile tests has been found to provide good results quantitatively as well as qualitatively. However, from the point of view of design

consideration, the one parameter Cockroft-Latham fracture criterion has also been employed and found to reproduce equally good results as the Johnson-Cook criterion.

Hopperstad et al. (2003a, b) conducted quasi-static and dynamic tension tests on smooth and notched cylindrical specimens of Weldox 460 E steel. The experimental results were reproduced through finite element simulations employing the Johnson-Cook flow and fracture model. The experimental and numerical results were found to have good correlation with respect to the stress-strain relationship of the material.

Sjoberg et al. (2013) calibrated the JC and ZA constitutive models for alloy 718 and simulated the impact tests performed on a specially designed setup. The simulations with JC model had closer agreement with the experiments compared to the ZA model for the tests conducted at room temperature.

The studies reviewed above led to the conclusion that the Johnson-Cook flow and fracture model accurately captures the global structural behaviour in predicting the perforation phenomenon in metals and possesses simplistic formulation and relatively easier calibration approach. Thus in the present study the flow and fracture behaviour of the projectile as well as target material has been incorporated employing the JC model.

1.6 MATERIAL CHARACTERIZATION

The accuracy of the finite element simulation is also dependent upon establishing the influence of various complex phenomena occurring during perforation process. The large strains, high strain rate and high temperature occurring simultaneously during the perforation process complicate the material behaviour as well as its characterization.

Lee et al. (2000) studied the dynamic impact properties of 7075 aluminum alloy using a split Hopkinson bar. The cylindrical specimens of 10 mm height and equivalent diameter were compressed dynamically at temperatures ranging from 25 to 300 °C and at strain rates ranging from 1 x 10^3 to 5 x 10^3 s^{-1}. The influence of strain rate and temperature, fracture mechanism and the occurrence of shear localization was studied. It was found that the compressive stress-strain response depends upon the applied strain rate and temperature.

Magd and Abouridouane (2006) studied the material behavior of aluminium 7075, Magnesium AZ80, and Titanium Ti–6Al–4V alloys at varying strain rate, 0.001 - 5000 s^{-1}, and temperature, 20 °C - 450 °C, under compression as well as tension. The influence of strain hardening, strain rate and temperature was studied on the fracture stress and deformation and the results led to the conclusion that flow stress and limits of deformation are controlled by strain rate and temperature. The numerical simulations of the smooth and notched tension tests enabled the validation of the material model. The simulations of differently notched specimens also enabled the determination of the failure criterion for AZ80 and Ti-6Al-4V alloys.

Nilsson (2003) studied the behaviour of Armox 500T and Armox 600T steel at varying strain rate and temperature. The material parameters of Johnson-Cook, Zerilli-Armstrong, Johnson-Cook-Weerasooriya and Huang-Liang model were calibrated by curve fitting the experimental data. It was concluded that fitting experimental data to different strength models or using different fitting approaches to extract the parameters will give significantly different results when applying the extracted model to calculate the yield strength at high strain and high strain rates. It was also concluded that the main difference between the different models was the ability to capture the thermal softening.

Sharma et al. (2013) studied the strain rate sensitivity of 5052-H34 aluminium alloy under tension and compression. The tension tests were carried out on smooth cylindrical specimens of gauge length 50 and diameter 12.5 mm while the compression tests on cylindrical tablets of 10 mm diameter and equivalent height. The negative strain rate sensitivity was observed in the material at strain rate 10^{-4} to 1 s^{-1}, however, with further increase in strain rate, 1 - 10^{3} s^{-1}, the nature of strain rate sensitivity changed to positive.

1.7 BALLISTIC INTERACTION OF PROJECTILE AND TARGET

As discussed earlier, the interaction between the projectile and target is influenced by the strength, hardness and configuration of the projectile as well as, density, ductility and microstructure of the target. In addition to these however, physical characteristics such as shape and size of projectile, thickness, configuration, span and boundary conditions of the targets as well other impact conditions such as angle of incidence and vicinity of the target are some of the important factors which influence the performance of both projectile as well as target during impact.

Balos et al. (2010) studied the impact response of 50CrV4 and Hardox 450 perforated steel targets impacted by 12.7 APM8 projectiles. It was observed that the 50CrV4 perforated plate failed without any plastic deformation. On the other hand, significant plastic deformation was observed in the impact zone of Hardox 450 steel. It was concluded that the steel with a very high hardness and low ductility is not suitable to be used as perforated target.

Borvik et al. (2002a, b) carried out experimental and numerical investigation for studying the impact performance of 12 mm thick Weldox 460E steel targets against 20 mm

diameter blunt, hemispherical and conical nosed projectiles of equivalent mass, 197 grams. The blunt projectiles were found efficient penetrators than hemispherical and conical projectiles at low incidence velocities. At higher incidence velocities however, the conical projectiles were found most efficient to perforate the targets. The predicted failure modes and residual velocities were found to have good agreement with the experimental results.

Borvik et al. (2011) conducted experimental and numerical investigation on 6084-T4 aluminium plates impacted by 7.62 AP projectiles of soft lead and hard steel core at 0°, 15°, 30°, 45° and 60° obliquity. It was observed that due to low strength, the soft lead bullet failed immediately after the impact and hence the velocity drop of the soft bullet decreased continuously with increase in obliquity. However, the velocity drop of the hard core bullet was almost constant up to 30° while at 60° obliquity it increased substantially.

Borvik et al. (2015) studied the impact response of granular materials i.e., wet sand, dry sand, gravel, crushed stone and crushed rock against 7.62 mm soft lead and hard steel core and 12.7 mm soft steel and tungsten carbide core. The penetration depth was found to be strongly influenced by the deviation of the bullet from its original trajectory. A good agreement between the experimental results and the numerical results was found with respect to penetration depth.

Chocron et al. (2001) conducted a combined analytical, numerical and experimental investigation to examine the conditions to fracture the core of 7.62 API projectiles. The analytical model was based on Timoshenko beam theory idealizing the projectile as semi-infinite cylinder. A 3D numerical model of the core was developed for studying the transient effects, influence of constitutive model and target properties on the magnitude of projectile

bending strains. The results of the experiments and the calculated maximum strains suggested that the computed axial strains must exceed 2% to achieve projectile fracture.

Corbett et al. (1996) reviewed the recent research on the penetration and perforation of plates and cylindrical shells by free-flying projectiles at low incidence velocities. It was concluded that most of the research at present is concerned on normal and oblique impact of homogeneous, non-homogeneous, metallic and non-metallic targets of monolithic and layered configuration by non-deformable and deformable projectiles. The analytical developments on important characteristics of the penetration and perforation process were also reviewed. It was concluded that for some impact situations fairly simple analytical models are capable of predicting target response reasonably accurately, but for others, particularly when both local and global mechanisms contribute significantly to overall target response, more complicated models are required.

Corran et al. (1983) conducted experiments on mild steel, stainless steel and aluminium targets against blunt projectiles. The effect of projectile mass, nose shape and hardness has been studied on the target response. It was concluded that an increase in the projectile nose radius changed the failure mode of the target.

Dey et al. (2004) conducted experiments and numerical simulations for studying the impact response of 12 mm thick Weldox 460E, Weldox 700E and Weldox 900E steel plates against blunt, conical and ogival-nosed projectiles. It was found that the ballistic limit velocity decreased with increase in target strength for blunt projectiles, however, it increased for conical and ogival projectiles. Moreover, the shattering of the projectile nose tip occurred during penetration of conical-nosed projectile in Weldox 700E and Weldox 900E steel

targets. The numerical code was found capable to describe the physical mechanisms during the perforation events with good accuracy.

Dey et al. (2007) studied the performance of 12 mm thick monolithic and layered targets of Weldox 700E steel by blunt and ogival-nosed projectiles through experiments and finite element simulations. Against blunt nosed projectile, the ballistic performance of 12 mm thick monolithic target was found to be inferior to that of the double layered in contact target of equivalent thickness. When the layers were spaced by 24 mm, their performance was between monolithic and layered in contact target. However, when the same configuration was impacted by ogival-nosed projectile, monolithic target offered highest ballistic performance followed by layered and spaced target respectively. It was concluded that the change in deformation and failure mode is responsible for the superior or inferior performance of a given configuration of the target.

Gupta and Madhu (1992, 1997) carried out studies on normal and oblique impact behaviour of ogive nosed armour-piercing projectiles on a single and multi-layered metallic plates. Simple mathematical relations based on the experimental results were proposed for predicting the residual velocity, velocity drop, ballistic limit, and the angle of critical ricochet. It was found that the residual velocity for relatively thick targets in two layers was comparable to that of the monolithic target of equal thickness. For comparatively thin targets however, the layered combination gave higher residual velocity. Again the residual velocity for spaced (layered) targets was higher when the plates were in contact.

Gupta et al. (2007, 2008) studied the influence of projectile nose shape, impact velocity and target thickness on the ballistic resistance of single and layered aluminum targets by blunt, ogive and hemispherical nosed projectiles at normal incidence. For 0.5,

0.71, 1.0 and 1.5 mm thick aluminum targets, the ogive nosed projectile was found to be the most efficient penetrator. For 2.0, 2.5 and 3.0 mm thick targets however, blunt nosed projectiles required lesser resistance against perforation. In case of layered in-contact targets however, the ogive nosed projectile was found to be the most efficient penetrator. Hemispherical nosed projectile remained least efficient to perforate both single as well as layered targets.

Hong et al. (2008) performed numerical simulations to study the vehicle impact on roadside guardrail. Numerical results indicated that the guardrail successfully contains the 2 ton vehicle impact at a speed of 100 km/h with 25° incidence angles and 8 ton truck impact at a speed of 80 km/h with 15° incidence angle.

Hosseini and Abbas (2006) presented detailed analysis of experimental data of the strike of spherical projectile on thin metallic targets in order to predict the hole-diameter in the target. A non-dimensional model for the prediction of hole diameter was presented which incorporates the geometric and material properties of the target and projectile as well the angle of incidence. The proposed model performed well for each material independently as well as for all the data. The model has also been found to work well for the whole range of incidence velocities for predicting the hole diameter.

Iqbal et al. (2010a, b) studied the ballistic resistance of 12 mm thick Weldox 460 E steel against conical nosed and 1 mm thick 1100 H12 aluminum targets against ogival nosed projectiles at varying angle of incidence. The internal nose angle of conical projectile and caliber radius head (CRH) of ogive nosed projectile was also varied, Senthil et al. (2013b). The ballistic limit of the steel target remained almost constant up to 30° obliquity and thereafter it increased by 10% at 45° and 81% at 60° obliquity. On the other hand, the

ballistic limit of aluminum target increased by 5.7%, 12.4% and 25.3% at 15°, 30° and 45° obliquity, respectively as compared to normal impact. Moreover, the ballistic limit of steel target increased almost linearly with the decrease in the projectile nose angle while the ballistic limit of aluminum target increased as the CRH increased from 0 to 0.5 and with further increase in CRH to 1.0, 1.5, 2.0 and 2.5 its values were found to decrease significantly.

Iqbal et al. (2012) performed numerical simulations on 1100-H12 aluminum targets of varying span and configurations impacted by blunt and ogive nosed projectiles. The span diameter of 1 mm thick targets was varied for 50 to 500 mm and configuration as monolithic, double layered in contact and double layered spaced with varying spacing. The ballistic limit was found to increase with increase in target span diameter for both the projectiles, however, the increase in ballistic limit was found to be higher for blunt nosed projectile than for ogive nosed projectile for all the spans except in the case of 50 mm span for which the ballistic limit was higher for ogive nosed projectile. The highest ballistic limit was observed for monolithic target followed by layered in-contact and spaced targets. The variation of spacing between layers did not have significant influence on the ballistic limit in the case of ogive projectile but some effect was seen in the case of blunt projectile.

Iqbal et al. (2013) conducted experiment and numerical investigations on 1100-H14 aluminum targets by double-nosed projectiles. The different types of projectiles according to front and second nose shape studied were blunt-blunt, conico-blunt and blunt-conico nose. The ballistic limit of the target was found to be highest against blunt-blunt followed by conico-blunt and blunt-conico projectile.

Jena et al. (2010a) conducted ballistic experiments on 7017 aluminium and high strength armour steel by 7.62 AP projectiles at normal incidence. The armour steel was also heat treated at 200 and 650 °C temperature and the results thus obtained among all the steels as well as aluminum alloy were compared. The armour steel tempered at 200 °C has been found to offer maximum ballistic resistance. Further, experiments were carried out by heat treating the steel at 200, 300, 400, 500 and 600 °C, Jena et al. (2010b). The mechanical properties such as tensile strength, ductility, Charpy impact strength, hardness and microstructure were found to have influenced by the tempering temperature. It was concluded that these properties collectively are responsible the change in ballistic behaviuor. An optimum combination of strength, hardness and toughness is essential for good ballistic performance.

Kolla et al. (2011) conducted experiments on Fe–C–Si–Mn–Co–Cr–V steel target against 7.62 API projectiles. The yield strength and fracture toughness of the steel target is 1900 MPa and 50 MPa $m^{½}$ achieved by the heat treatment of 200 – 600 °C temperature. It was concluded that the steel shows 25% reductions in weight than rolled homogeneous armour (RHA) steel.

Krishnamurthy et al. (2001, 2003) studied the impact response of composite shell using Fourier series and finite element method. The impactor velocity was varied as 10, 20 and 30 m/s. The effect of impactor mass, velocity and shell curvature was studied on the ballistic performance and the results led to the conclusion that the increase in the extent of damage is directly proportion to the contact force and the impactor velocity.

Mannan et al. (2008) conducted experimental and analytical studies on aluminium beams of thicknesses 0.81 - 6.55 mm by impacting through blunt nose projectile at incidence

velocities 11 - 114 m/s. Three modes of failure occurred, first a fracture at the point of strike, second a fracture at one or both supports and third a fracture at the point of strike with bulging and turn around supports after fracture. The deflection of the beams has been found to reduce with increase in thickness. The maximum deflection for un-fractured beams was predicted by the analytical model and was found in good agreement with the experiments.

Mishra et al. (2012, 2013) studied the ballistic response of armour steel plates against 7.62 AP projectiles after tempering them at 200 °C to 600 °C temperature. It was observed that the depth of penetration was lesser for the plate tempered at 200 °C than at 600 °C. It was concluded that the hardness decreased with increase in tempering temperature resulting in corresponding increase in depth of penetration.

Nadeem et al. (2014) conducted experiments on RC shielded steel plates impacted by ogivel and bi-conical nose projectile with same mass and varying velocity. The damage level in terms of deformation, fracture and perforation were studied. The ballistic limit velocity of ogivel projectile for RC shield was found lower than bi-conical projectile. The ogivel-nose projectile was found more damaging to the steel plate than bi-conical nose projectile.

Piekutowski et al. (1996) conducted experiments on 6061-T6511 aluminum targets by long rod ogival nosed steel projectiles in the velocity range 0.5 to 3.0 km/s in order to study the influence of projectile strength on the ballistic performance. The projectiles were made by vacuum arc remelted (VAR) 4340 steel (HRC 38) and AerMet 100 steel (HRC 53). The behaviour of the target was found to be same against both the projectiles at a given incidence velocity in the velocity regime studied. The penetration path was straight by AerMet projectiles while the path of VAR projectiles was found to be curved at all the velocities. It

was therefore concluded that the performance of AerMet projectile is better than VAR projectile.

Su et al. [2008] performed numerical simulations to study the aluminium foam protected masonry walls against blast loads. The material models for masonry, aluminum foam and interface were coded into LS-DYNA. It was found that the thickness and density of aluminum foam had great influence on mitigation of blast effects on masonry walls. Also, Wu et al. (2011) studied the performance of aluminum foam protected RC slabs against blast loads. It was found that the foam layers used to protect RC slabs were effective in mitigating blast effect on RC slabs.

Teng et al. (2008) performed the finite element simulations on Domex Protect 500 and Weldox 460E steel against four types of conical projectile impacted at low velocity. It was concluded that at low incidence velocity the double layered steel plate with upper layer of high ductility and low strength material and lower layer of low ductility and high strength material offered best performance compared to monolithic plates. At high incidence velocity however, the performance was found to be dependent on target strength and projectile shape.

Velmurugan and Gupta (2003) conducted experimental and analytical studies on metallic, composite shells and tubes under quasi-static compressive loading. The progressive failure and energy absorption capacities were studied under axial compression. The analytical expressions were derived to find the mean collapse load and the fold length based on the formation of plastic hinges and the results thus obtained were compared with the experiments. It was observed that presence of foam increased the energy absorbing capacity and delayed the formation of the vertical crack in conical shells of larger cone angles. Both the round and the rectangular tubes had similar variation of peak and minimum load with

respect to mean collapse load. The analytical results were in good agreement with the experimental results for all the cases.

Velmurugan et al. (2010) and Rahul et al. (2012) conducted experiments on Kevlar/Epoxy composite laminates impacted by parabellum projectile. Each laminate of a particular thickness was prepared for four different orientations (0/90, 0/90/30/-60, 0/90/45/-45 and 30/-60/60/-30). It was observed that the 0/90 lay-up sequence offered maximum resistance against impact. For all lay-up sequences, energy absorption capacity increased with increase in thicknesses. The damaged area on the rear side also increased with increasing thickness. The results obtained from analytical study were found to be in good agreement with the experimental results.

1.8 GAPS IDENTIFIED

The literature survey concludes that the subject of ballistic resistance of metallic and non-metallic targets has been studied thoroughly in the last few decades. Researchers have used experimental, numerical and analytical approaches for studying the ballistic performance of metallic as well as composite targets against conventional and real ammunition projectiles, however, the following gaps have been identified in the subject of projectile and target interaction after carrying out a detailed literature survey;

- The ballistic resistance of high strength steel and aluminium targets against real ammunition such as 7.62 API and 12.7 API projectiles are very limited.
- The ballistic resistance of Armox 500T steel could not be found in the available literature despite the fact that it possesses high strength, high hardness and high ductility which have been identified as the ideal properties for armour.

- The studies pertaining to 7075-T651 aluminium are limited to normal impact.
- Many researchers have addressed the problem of oblique impact through experiments most of which are at low angles of incidence. There are very few studies wherein the behavior of target at high obliquity has been addressed. Moreover, the numerical simulation of oblique impact phenomenon is rarely available in the open literature.
- Limited studies are reported on thick metallic targets.

1.9 OBJECTIVE AND SCOPE OF THE PRESENT STUDY

- The present study is based on the experimental and finite element investigation of the response of Armox 500T steel and 7075-T651 aluminium alloy targets subjected to small arms projectile impact.
- The Armox 500T steel plates of thickness 6, 8 and 10 mm and corresponding areal density 47, 63 and 78 kg/m^2 respectively were impacted by 7.62 API projectiles.
- The Armox 500T steel plates of thickness 5, 10, 15 and 20 mm and corresponding areal density 40, 79, 118 and 157 kg/m^2 respectively were impacted by 12.7 API projectiles.
- The 7075-T651 aluminium plates of thickness 20, 32, 40 and 50 mm and corresponding areal density 54, 87, 108 and 135 kg/m^2 respectively were impacted by 12.7 API projectiles.
- The ballistic resistance of mild steel targets of thickness 4.7, 6, 10, 12, 16, 20 and 25 mm has also been studied by performing the finite element simulations and the results thus obtained, were validated with the experiments performed by Gupta and Madhu (1992, 1997).

- The angle of incidence was varied until the occurrence of projectile ricochet.
- The perforation, failure mechanism and ballistic performance of the target was studied at each angle of incidence.
- The target as well as projectile material was characterized under varying stress state, strain rate and temperature.
- The material parameters of the Johnson-Cook elasto-viscoplastic model were calibrated.
- The calibrated material parameters were validated by numerically simulating the high strain rate tension tests performed on Split Hopkinson Pressure Bar apparatus.
- The material parameters are subsequently employed for predicting the behavior of the projectile as well as target in order to numerically reproduce the ballistic tests.
- The ballistic performance of mild steel, Armox 500T and 7075-T651 aluminum plates have been compared with respect to thickness and areal density against a given projectiles.
- The performance of the 7.62 API and 12.7 API projectiles have also been compared for a given target and given obliquity.

1.10 ORGANIZATION OF THESIS

The thesis has been organized in eight chapters

In the present chapter; a general introduction of the problem has been given, discussing the development of the weapons and their complexity as well as the importance of different issues related to the present study. A detailed literature review is also presented in this chapter which has been divided in six broad categories viz., studies on steel, aluminium,

projectiles, constitutive modelling, material characterization and interaction of projectile and target. The research gaps have been identified and scope of the present study has been described.

Chapter 2 describes the detailed characterization of mild steel, Armox 500T steel, 7075-T651 aluminium alloy and API Projctiles. The material has been studied under varying stress-triaxiality, strain rate and temperature. The calibration of the material parameters for the Johnson-Cook elasto-viscoplastic model has also been discussed.

Chapter 3 describes the finite element modelling of mild steel, Armox 500T and 7075-T651 aluminium targets as well as the 7.62 and 12.7 API projectiles. The mesh convergence study was carried out by refining the element size of the target until the convergence of the residual velocity of projectile was achieved. The calibrated material parameters were validated by numerically simulating the high strain rate tension tests performed on Split Hopkinson Pressure bar.

Chapter 4 describes the ballistic studies conducted on Armox 500T steel targets of various thicknesses impacted by 7.62 API and 12.7 API projectiles. The angle of incidence was varied until the occurrence of projectile ricochet. The finite element simulations were carried out using the ABAQUS/Explicit finite element code. The numerical results of failure mechanism, residual projectile velocities and critical angle of ricochet were also presented in this chapter.

Chapter 5 describes the ballistic studies carried out on 7075-T651 aluminium targets of various thicknesses impacted by 12.7 API projectiles. The angle of incidence was varied until the occurrence of projectile ricochet. The finite element simulations were carried out using the ABAQUS/Explicit finite element code. The results thus obtained through finite element

simulations were compared with those of the experiments with respect to failure mechanism, residual projectile velocity and critical angle of ricochet.

Chapter 6 describes the ballistic evaluation of mild steel targets of various thickness impacted by 7.62 API projectiles. The numerical simulation results thus obtained validated with the available experiments.

Chapter 7 summarizes the entire work of this thesis in a concise form and describes the comparative studies on the mild steel, Armox 500T and 7075-T651 aluminium. The capacity of each material to stop the projectile as well as the efficiency of 7.62 API and 12.7 API projectiles has been compared and discussed.

Chapter 8; This chapter presents the conclusions and scope of the future work.

The thesis finally presents the bibliography and list of publications.

CHAPTER 2

Material Characterization and Calibration

2.1 GENERAL

The perforation mechanics, in addition to physical characteristics, is significantly influenced by the material behaviour of the projectile and target. The simultaneous occurrence of large strains, high strain rate and high temperature associated with the phenomenon, however, makes the description of the material behaviour as well as its characterization quite complex.

A detailed material characterization is discussed in this chapter to describe the behaviour of projectile and target under different phenomena occurring during perforation process. The materials identified in the present study have been characterized under varying stress state, strain rate and temperature. The possible anisotropy of Mild steel, Armox 500T steel, 7075-T651 aluminum plates has been studied by performing the uniaxial tension tests under quasi-static loading on the specimens extracted from 12 – 20 mm thick plates of respective materials from 0°, 45° and 90° orientations. The ductility of the material and stress states were studied by performing the uniaxial tension tests on notched cylindrical specimens under quasi-static loading. The notch radius of the specimen was varied from 0.4 to 10 mm. The strain rate sensitivity of the material was studied by carrying out the tension tests on cylindrical specimens at strain rate 1×10^{-4} – 1500 s^{-1}. The thermal sensitivity of the material has been studied by performing tension tests on cylindrical specimens in the temperature range 27 – 950 °C. The material tests thus performed enabled the calibration of the Johnson-Cook (1983, 1985) elasto-viscoplastic model. All the parameters of Johnson-Cook flow and fracture model were calibrated through curve fitting method. The anisotropy observed in 7075-T651 aluminum plates has been addressed by obtaining the stress-strain relations at

different material orientation. The calibrated Johnson-Cook (1983, 1985) model was finally employed for carrying out the numerical simulations of the ballistic tests.

2.2 CONSTITUTIVE MODELLING

The quality of material model is a key factor affecting the accuracy of results of a finite element simulation. Two types of material models are generally used in numerical simulations. One of these represents plastic flow and the other fracture of the material. The metal plasticity models in ABAQUS employ the Mises stress potential for simulating isotropic behavior while the Hill stress potential is employed for simulating anisotropic behavior of material. Both of these potentials depend only on the deviatoric stress, therefore, the plastic part of the response is incompressible.

2.2.1 Modelling of Flow Behaviour

The constitutive model based on the viscoplasticity and continuum damage mechanics described in the present study was proposed by Johnson and Cook (1983, 1985). The ABAQUS code has an inbuilt option of the material model proposed by Johnson and Cook (1983, 1985). It includes linear thermo-elasticity, the von Mises yield criterion, the associated flow rule, isotropic strain hardening, strain rate hardening, softening due to adiabatic heating and a failure criterion. The static yield stress of the model is defined as;

$$\sigma^0 = \left[A + B(\bar{\varepsilon}^{pl})^n\right]\left[1 - \hat{T}^m\right] \quad (1)$$

where $\bar{\varepsilon}^{pl}$ is equivalent plastic strain, A, B, n and m are material parameters measured at or below the transition temperature, T_0. The non-dimensional temperature $\hat{T}$ is defined as;

$$\hat{T} = \begin{cases} 0 & \text{for} \quad T < T_0 \\ (T - T_0)/(T_{melt} - T_0) & \text{for} \quad T_0 \le T \le T_{melt} \\ 1 & \text{for} \quad T > T_{melt} \end{cases} \tag{2}$$

where T is the current temperature, T_{melt} is the melting point temperature and T_0 is the transition temperature defined as the one at or below which there is no temperature dependence on the expression of the yield stress. When $T > T_{melt}$, the material melts down and behaves like fluid and hence does not offer shear resistance i.e., $\sigma^0 = 0$.

The Johnson-Cook strain rate dependence assumes;

$$\bar{\sigma} = \sigma^0(\bar{\varepsilon}^{pl}, \hat{T})\ R(\dot{\bar{\varepsilon}}^{pl}) \tag{3}$$

and;

$$\dot{\bar{\varepsilon}}^{pl} = \dot{\varepsilon}_0\ exp\left\lfloor \frac{1}{C}\ (R-1) \right\rfloor \qquad \text{for} \quad \bar{\sigma} \ge \sigma^0 \tag{4}$$

where $\bar{\sigma}$ is the yield stress at non zero strain rate, $\dot{\bar{\varepsilon}}^{pl}$ is equivalent plastic strain rate, $\dot{\varepsilon}_0$ and C are the material parameters measured at or below the transition temperature T_0, $\sigma^0(\bar{\varepsilon}^{pl}, \hat{T})$ is the static yield stress and $R(\dot{\bar{\varepsilon}}^{pl})$ is the ratio of the yield stress at non zero strain rate to the static yield stress.

The equivalent von Mises yield stress is therefore expressed as;

$$\bar{\sigma} = \left[A + B(\bar{\varepsilon}^{pl})^n\right]\left[1 + C\ln\left(\frac{\dot{\bar{\varepsilon}}^{pl}}{\dot{\varepsilon}_0}\right)\right]\left[1 - \hat{T}^m\right] \tag{5}$$

2.2.2 Modelling of Fracture Behaviour

Johnson and Cook (1985) extended the failure criterion proposed by Hancock and Mackenzie (1976) by incorporating the effect of strain path, strain rate and temperature in the fracture strain expression, in addition to stress triaxiality. The fracture criterion is based on

the damage evolution wherein the damage of the material has been assumed to occur when the damage parameter, ω, exceeds unity;

$$\omega = \sum \left(\frac{\Delta \bar{\varepsilon}^{\mathrm{pl}}}{\bar{\varepsilon}_f^{pl}} \right) \tag{6}$$

where $\Delta \bar{\varepsilon}^{\mathrm{pl}}$ is an increment of the equivalent plastic strain, $\bar{\varepsilon}_f^{pl}$ is the strain at failure, and the summation is performed over all the increments throughout the analysis. The strain at failure $\bar{\varepsilon}_f^{pl}$ is assumed to be dependent on a non-dimensional plastic strain rate, $\frac{\dot{\bar{\varepsilon}}^{\mathrm{pl}}}{\dot{\varepsilon}_0}$; a dimensionless pressure-deviatoric stress ratio, $\frac{\sigma_{\mathrm{m}}}{\bar{\sigma}}$ (where σ_{m} is the mean stress and $\bar{\sigma}$ is the equivalent von Mises stress) and the non-dimensional temperature, $\widehat{\mathrm{T}}$, defined earlier in the Johnson-Cook hardening model. The dependencies are assumed to be separable and are of the form;

$$\bar{\varepsilon}_f^{pl} \left(\frac{\sigma_m}{\bar{\sigma}}, \dot{\bar{\varepsilon}}^{\mathrm{pl}}, \widehat{\mathrm{T}} \right) = \left[\mathrm{D}_1 + \mathrm{D}_2 \exp\left(\mathrm{D}_3 \frac{\sigma_{\mathrm{m}}}{\bar{\sigma}} \right) \right] \left[1 + \mathrm{D}_4 \ln\left(\frac{\dot{\bar{\varepsilon}}^{\mathrm{pl}}}{\dot{\varepsilon}_0} \right) \right] \left[1 + \mathrm{D}_5 \widehat{\mathrm{T}} \right] \tag{7}$$

where $\mathrm{D}_1 - \mathrm{D}_5$ are material parameters determined from different mechanical test, $\dot{\bar{\varepsilon}}^{\mathrm{pl}}$ is equivalent plastic strain rate and $\dot{\varepsilon}_0$ is a reference strain rate.

When the damage occurs, the stress-strain relationship no longer accurately represents the material behaviour. The use of stress-strain relationship beyond ultimate stress introduces a strong mesh dependency based on strain localization i.e., the energy dissipation decreases with the decrease in element size. Hillerborg's et al. (1976) fracture energy criterion has been employed to reduce mesh dependency by creating a stress-displacement response after damage is initiated. It is defined as the energy required to open a unit crack area,$\mathrm{G_f}$;

$$G_f = \frac{\sigma_{y0} \times \bar{u}_f^{pl}}{2} \quad (8)$$

where σ_{y0} is ultimate stress and $\bar{u}_f^{pl}$ is the equivalent plastic displacement at failure. With this approach, the softening response after damage initiation characterized by a stress-displacement response instead of stress-strain response. In the present study therefore the fracture energy approach has been employed as damage evolution criterion in conjunction with Johnson-cook damage initialization criteria. The damage evolution criterion assumes that the damage characterized by the progressive degradation of material stiffness leading to its failure. It also takes into account the combined effect of different damage mechanisms acting simultaneously on the same material.

2.2.3 Hill's Yield Criterion

Most of the engineering metallic materials are made in the form of extruded and rolled plates. Before 1990, the von Mises yield criterion based on the elastic-plastic FE models was generally employed for the engineering applications. After 1990 however, it has been observed that some of the engineering materials possess anisotropy. After the pioneering work by Hill (1948), a tremendous effort has been made to improve the modeling of anisotropy in constitutive and fracture models [Agarwal et al. (2006), Aretz et al. (2007), Arminjon and Bacroix (1991), Arminjon (1994), Barlat and Chung (1993), Barlat et al. (2003), Bron and Besson (2004), Chakraborty and Gopalakrishnan (2005), choi et al. (2004), Fourmeau et al. (2011), Hill (1987, 1990), Kant (1982), Karafillis and Boyce (1993), Kim et al. (2007), Leacock (2006), Mallikarjuna and Kant (1992), Monchiet (2008), Sandeep (2008), Soare and Barlat (2010), Sridhar (2006), Van Houtte and Van Bael (2004), Yang et al. (2008a, b) and Zinkham (1968)]. The von Mises criterion has been replaced by the

anisotropic Hill criterion, Hill (1948, 1950) for plastically incompressible materials in many of the FE codes. Hill's stress function is a simple extension of the Mises criterion to allow anisotropic behavior. The Hill's stress function in terms of rectangular Cartesian stress components can be represented in the following manner;

$$f(\sigma) = \sqrt{F(\sigma_{22} - \sigma_{33})^2 + G(\sigma_{33} - \sigma_{11})^2 + H(\sigma_{11} - \sigma_{22})^2 + 2L{\sigma_{23}}^2 + 2M{\sigma_{31}}^2 + 2N{\sigma_{12}}^2} \quad (9)$$

where *F*, *G*, *H*, *L*, *M* and *N* are the constants which are determined by testing the material in different orientations, σ_{11} , σ_{22} and σ_{33} are tensile stress components, and σ_{23} , σ_{31} and σ_{12} are shear stress components.

2.3 FLOW AND FRACTURE BEHAVIOUR OF MILD STEEL

Experimental investigation on the characterization of mild steel has been carried out under varying stress triaxiality, strain rate and temperature. The effect of stress triaxiality was studied by performing tension tests on notched cylindrical specimens. The radius of the notch has been varied as 0.2, 0.4, 0.6, 0.8, 1, 2, 3, 4, 5 and 10 mm. The smooth cylindrical specimens were tested under tension at varying strain rate and temperature. The strain rate in the range 6 x 10^{-4} s^{-1} - 1500 s^{-1} was obtained from a universal testing machine and Hopkinson pressure bar apparatus. The tests at elevated temperature were carried out using a portable furnace which enabled the variation of temperature from 27 to 750°C.

2.3.1 Preliminary Tests

The mild steel in the form of plates of 12 mm thickness was procured with chemical composition almost similar to what has been employed for ballistic evaluation by Gupta and Madhu (1992, 1997), see Table 2.1. The Vicker's hardness of the mild steel used for the

ballistic experimentation by Gupta and Madhu (1992, 1997) as well as material characterization of the present study has been found to be almost identical, Table 2.2. It may therefore be concluded that the mild steel tested in the present study was almost similar to what has been used in the experiments carried out by Gupta and Madhu (1992, 1997).

Table 2.1 Chemical composition of mild steel

Chemical elements	Gupta & Madhu (1992)	Present study
C	0.150	0.188
Si	-	0.1855
Mn	0.970	0.8375
S	0.025	0.0342
Cr	-	0.0213
Ni	-	0.0217
Al	-	0.0762

Table 2.2 Hardness of mild steel

Thickness (mm)	Gupta & Madhu (1997)	Present study
10.0	140-145	-
12.0		142
16.0		-
20.0		-
25.0		-

Fig. 2.1 Undeformed and deformed smooth flat specimens

The possible anisotropy of the target material has been studied by extracting the flat specimens from three different directions 0°, 45° and 90° and performing the uniaxial tension

tests under quasi-static loading. The thickness of the flat specimen was 10 mm, width 12 mm and gauge length 25 mm, see Fig. 2.1.

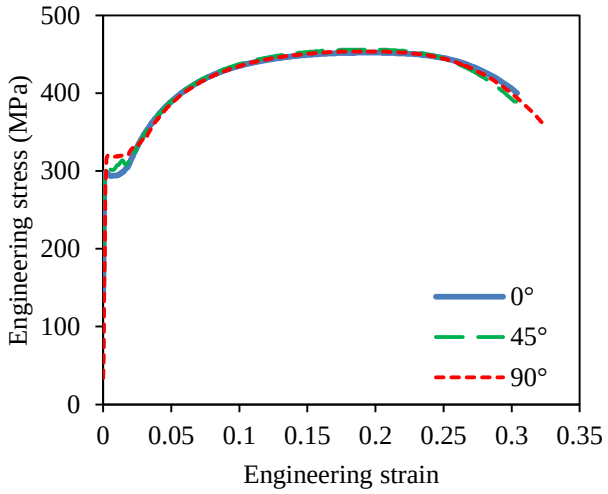

Fig. 2.2 Stress-strain relationship under quasi-static loading

The engineering stress-strain relationship of the specimens did not indicate any sign of anisotropy except the fact that the specimen corresponding to 90° orientation has indicated slightly higher yield stress as well as final elongation, see Fig. 2.2. Thus, the material in principle was isotropic and hence the material coupons for the complete characterization were extracted from the centre of 12 mm thick plate corresponding to 0° direction. Each test was repeated three times to ensure the accuracy and the repeatability and therefore the results reported in this study are the average of the three tests. The true stress-strain relationship has been obtained by performing the tension tests on smooth cylindrical specimens of diameter 6.25 and gauge length 25 mm, Fig. 2.3, at a strain rate of 6×10^{-4} s^{-1}.

Fig. 2.3 Undeformed and deformed smooth cylindrical specimens

The true stress was measured as the force per unit actual cross-sectional area, $F/A_{current}$. The actual cross-sectional area of the specimen was measured during the tension tests using a digital vernier caliper. The true strain was obtained as; $ln\ (A_{initial}/A_{current})$. The stress in the specimen is particularly uniaxial before the onset of necking. However, after the necking starts, the stress state becomes three-dimensional. In ductile material, due to the formation of neck at large strains a component of hydrostatic tension increases the net tensile stress than the equivalent stress. Therefore, according to Bridgeman (1952) and Le Roy et al. (1981) the obtained stress in the smooth specimen should be corrected. The measured and Bridgeman corrected true stress-strain relationship along with the engineering stress-strain relationship is shown in Fig. 2.4 for comparison.

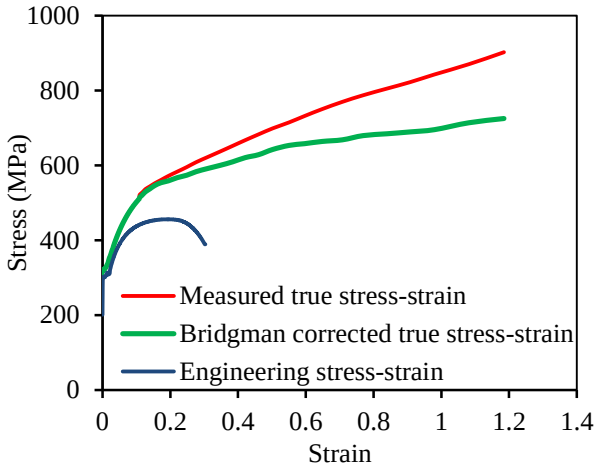

Fig. 2.4 Engineering and true stress-strain relationship of the material

2.3.2 Effect of Stress Triaxiality

The initial stress triaxiality in the cylindrical specimens was introduced by an artificial notch, see Fig. 2.5, in which a smooth cylindrical specimen develops at ultimate load. The stress triaxiality is a measure of material ductility, represented in terms of maximum stress triaxiality ratio, σ^*_{max}, defined as;

$$\sigma^*_{max} = \frac{1}{3} + ln\left(1 + \frac{a}{2R}\right) \quad (10)$$

where "*R*" is curvature radius of notch and "*a*" is the radius of the specimen in the notched region. The stress triaxiality ratio in the present study has been varied as 2.5, 1.92, 1.61, 1.41, 1.27, 0.91, 0.75, 0.66, 0.60 and 0.47 by varying the curvature radius of the notched specimen as 0.2, 0.4, 0.6, 0.8, 1, 2, 3, 4, 5 and 10, see Fig. 2.5.

Fig. 2.5 Undeformed and deformed notched cylindrical specimens

The diameter of the notched specimens was considered identical to that of the smooth cylindrical specimen of diameter 6.25 mm and these were subjected to quasi-static tension test at strain rate of 6 x 10^{-4} s^{-1}. The average stress-strain relationship for varying stress triaxility ratios is shown in Fig. 2.6(a). The results of three trials performed for notch radius 2, 3 and 4 mm are shown in Figs. 2.6(b) to (d) respectively to indicate the scatter in the results. A remarkable decrease in the material ductility has been found with increase in the stress triaxiality i.e., decrease in notch radius. The strength of the material increased while the total strain decreased with the increase in stress triaxiality.

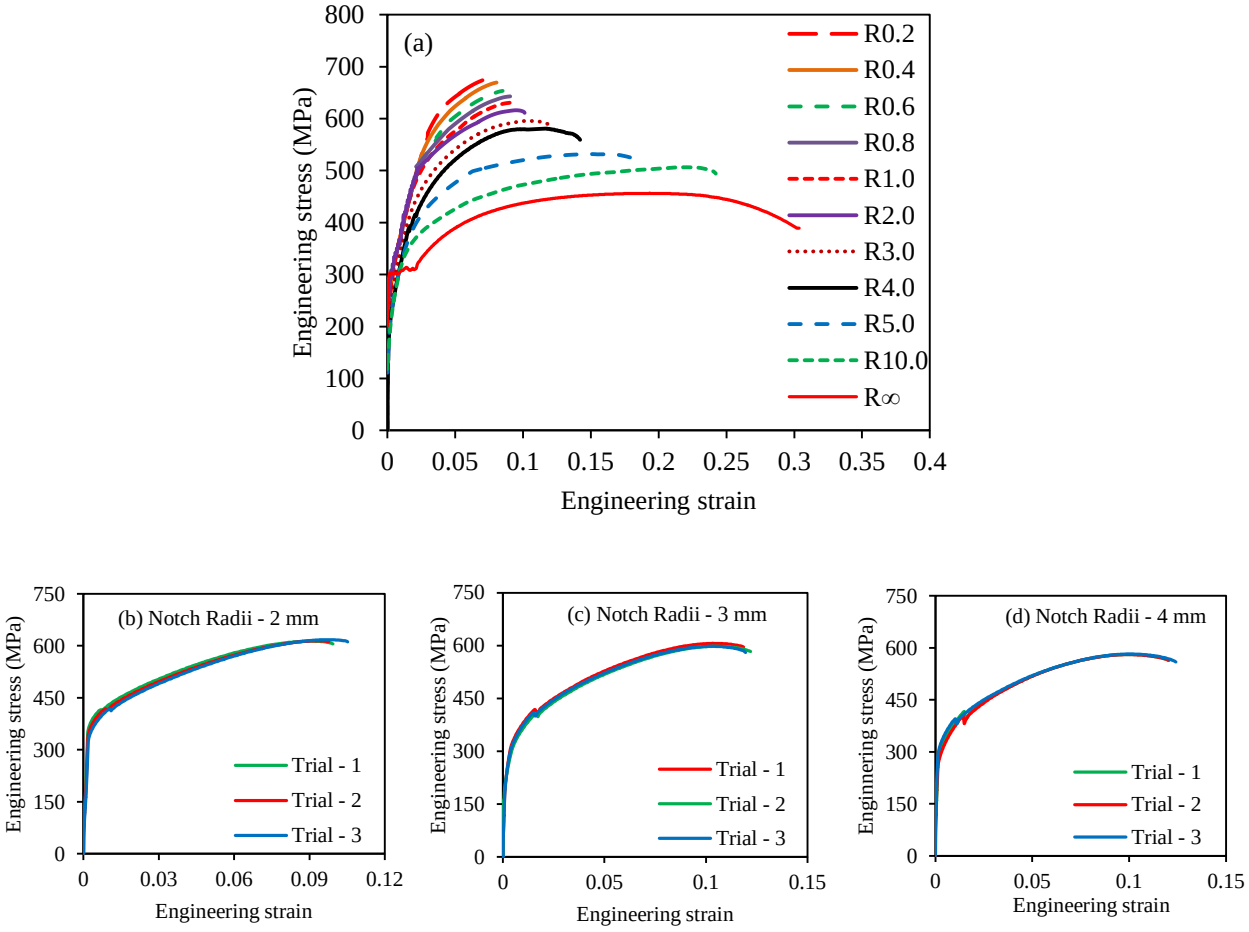

Fig. 2.6 Stress-strain relationship as a function of stress triaxiality; (a) Average stress-strain relationship for various notch radii (b) 2 mm (c) 3 mm (d) 4 mm

2.3.3 Effect of Strain Rate

The material tests under different strain rates have been performed both under tension and compression. The low and intermediate strain rate (6×10^{-4} s^{-1} - 6×10^{-2} s^{-1}) tests have been conducted on Tinius Olsen H75KS Universal Testing Machine of maximum capacity 75 kN. The smooth cylindrical specimens of diameter 6.25 mm and gauge length 25 mm were subjected to uniaxial tension, Fig. 2.3(a). The high strain rate tests have been performed on the Split Hopkinson Pressure Bar apparatus at strain rates in the range 500 s^{-1} – 1500 s^{-1}. The tension tests were performed on the cylindrical specimens of diameter 3 mm and gauge length 10 mm, see Fig. 2.7(a). The compression tests have been performed on the specimens prepared in the form of tablets of diameter 10 mm and length 10 mm, see Fig. 2.8(a).

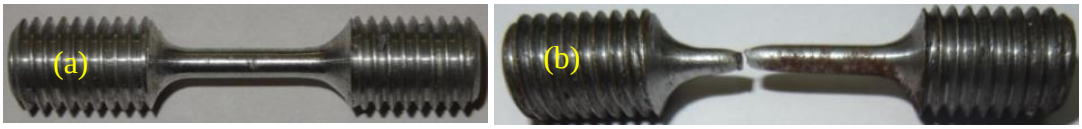

Fig. 2.7 Tension test specimen of (a) undeformed and (b) deformed profile

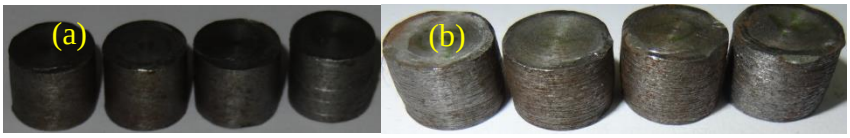

Fig. 2.8 Compression test specimen of (a) undeformed and (b) deformed profile

The measured engineering stress-strain curves obtained through the tension tests performed at varying strain rate are shown in Fig. 2.9(a). A nominal increase in the strength has been found when the strain rate increased from 6×10^{-4} s^{-1} to 6×10^{-2} s^{-1}. The hardening behaviour of the material has been found to be identical under this regime. At high strain rate however, the strength of material has been found to increase abruptly while the ductility has

decreased. The average yield strength has been found to be 325, 365, 387 and 400 MPa at strain rate 6 x 10^{-4} s^{-1}, 6 x 10^{-3} s^{-1}, 2 x 10^{-2} s^{-1} and 6 x 10^{-2} s^{-1} respectively, see Fig. 2.9(b).

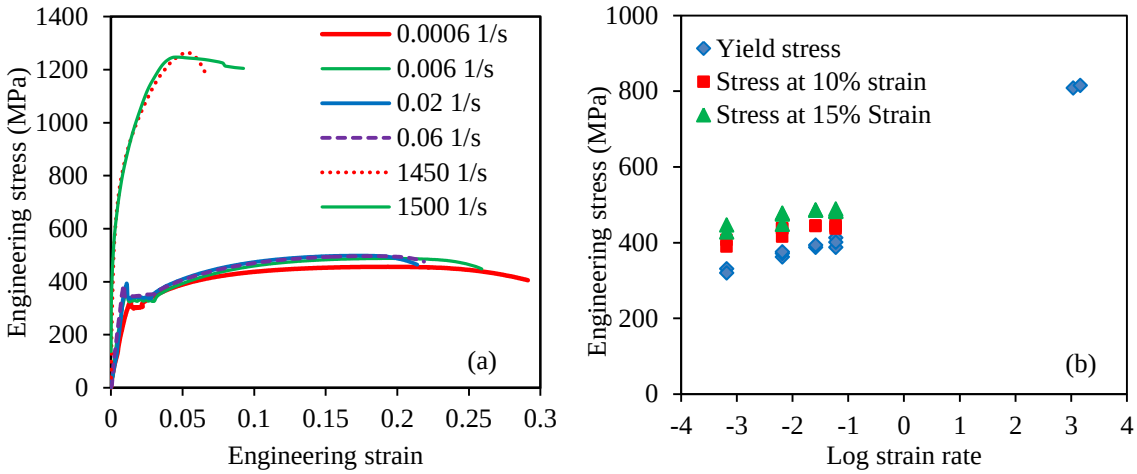

Fig. 2.9 Behaviour of material under varying strain rate subjected to tension (a) Average stress strain relationship at varying strain rate (b) Stress variation with varying strain rate

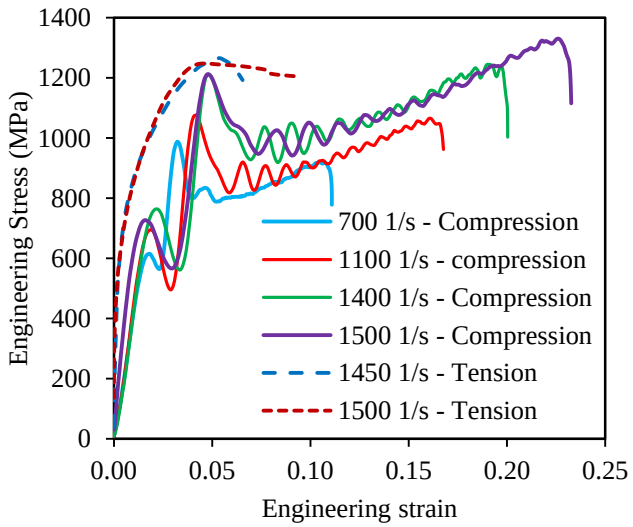

Fig. 2.10 Stress-strain relationship under high strain rate; a comparison between the tension and compression behaviour

However, the yield strength has increased to 850 MPa at a strain rate of 1450 s^{-1}. The proof stress at 5% and 10% strain has also been found to have a sharp increment at a strain rate of 1450 s^{-1}. In order to verify this behaviour, the material tests at high strain rate had

been performed under compression and the stress-strain relationship thus obtained has been plotted in Fig. 2.10. At the strain rate of 1500 s^{-1}, the pattern of stress-strain relationship under tension and compression has been found to have close agreement.

It may be concluded here that the material has positive strain rate sensitivity. The yield strength of the material under compression has been found to be 614, 693, 723 and 726 MPa at 700 s^{-1}, 1100 s^{-1}, 1400 s^{-1} and 1500 s^{-1} strain rates respectively. Singh et al. (2013) also studied the strain rate sensitivity of mild steel under tension as well as compression and reported the dynamic yield stress under tension to be 891 MPa, at a strain rate 750 s^{-1}, and static yield stress, 363 MPa, at strain rate 1 x 10^{-3} s^{-1}. On the other hand, the dynamic yield stress under compression has been reported to be 822 MPa, at strain rate 1300 s^{-1}, while the static yield stress as 541 MPa, at strain rate, 1 x 10^{-3} s^{-1}.

2.3.4 Effect of Temperature

The temperature sensitivity of the material has been studied by performing the tension tests under quasi-static loading, 6 x 10^{-4} s^{-1}. The cylindrical specimens of diameter 6.25 mm and gauge length 25 mm were tested on a 500 kN universal testing machine. A portable furnace shown in Fig. 2.11 was employed for heating the specimen to the required temperature. The temperature of the furnace was controlled by a micro-temperature controller. The furnace had a hollow cylindrical shape, open from top and bottom for inserting the specimen. The specimen was held through the top and bottom jaws of the universal testing machine and it was passed through the furnace, which was kept on a steel platform. The openings of the furnace at the top and bottom were closed by glass wool in order to control the temperature dissipation. The specimen was heated to the desired temperature at a rate of 0.167 °C/sec. The testing temperature was maintained for half an

hour in order to get the specimen heated uniformly before the application of mechanical load. The inside temperature of the furnace has been recorded using the K-Type thermocouples held near the centre of specimen. The elongation of the specimen was measured by two LVDTs (Linear Variable Displacement Transducers). The temperature has been varied from 27 °C to 750 °C.

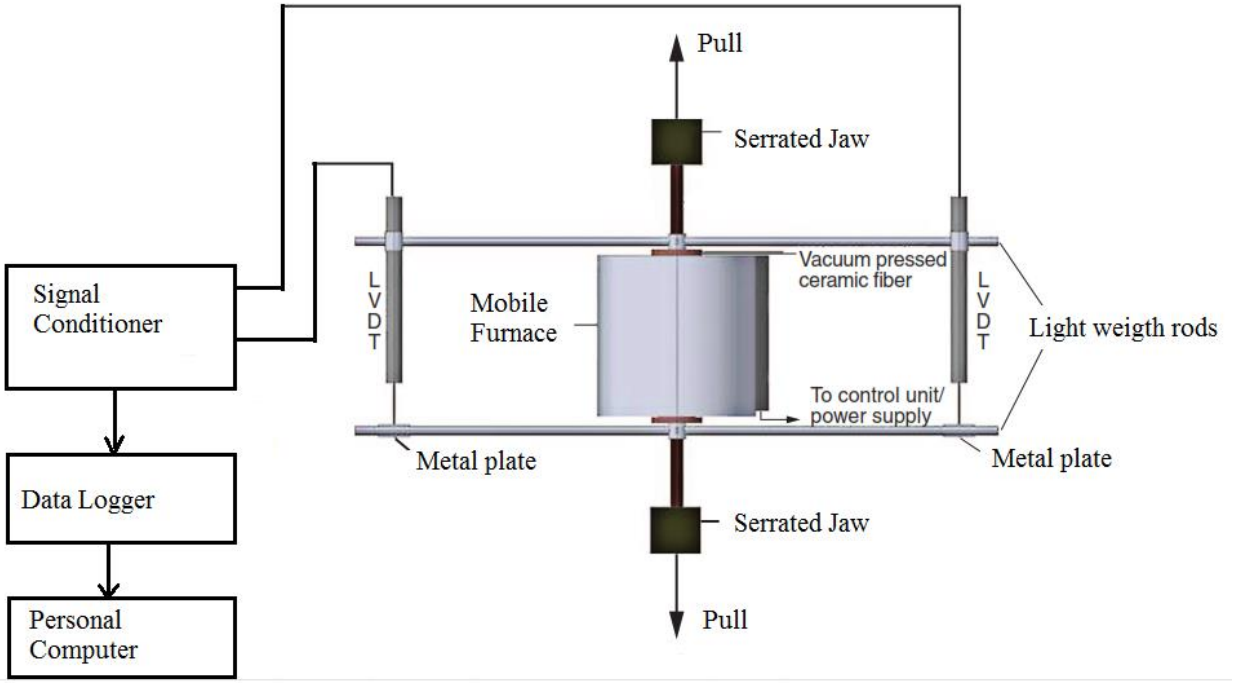

Fig. 2.11 Schematic of the high temperature testing setup

The engineering stress-strain relationship at varying temperature is highlighted in Fig. 2.12(a). The flow stress has been found to increase initially with increase in temperature up to 300 °C and then found to decrease with further increase in temperature. The proof stress of material at 0.2% permanent strain has been found to be 295, 356, 408, 336, 307, 248, 138 and 96 MPa at 27, 100, 200, 300, 400, 500, 600 and 750 °C temperature respectively, see Fig. 2.12(b).

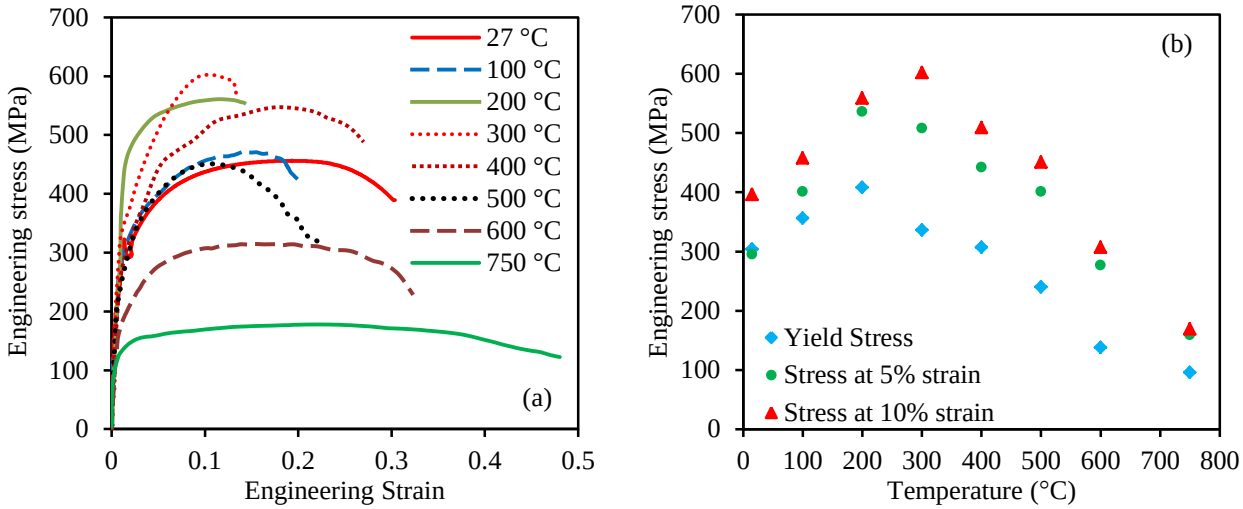

Fig. 2.12 Material (a) stress-strain relationship (b) variation of stress at varying temperature

The material showed maximum strength between the temperature 200 to 300 °C and minimum at 750 °C. The increase in the strength with increase in temperature is known as blue brittle effect and the temperature range witnessing the increased material strength is called blue brittle region. This phenomenon is a material characteristic of low carbon steels which occurs due to the interaction of nitrogen atoms with dislocations in a temperature range of 100 - 300 °C. Borvik et al. (2001) studied the thermal sensitivity of Weldox 460E steel and observed the blue brittle effect in the material between 200 °C to 300 °C temperature. Beyond the blue brittle region, the flow stress has sharply decreased and the elongation of the specimen increased. The fracture of material up to 300 °C did not have any temperature influence. The same is also distinguished from the colour of tested specimens see Fig. 2.13. Further increase in temperature resulted in the softening of material and reduction in the fractured diameter. The diameter of the untested specimen was 6.25 mm. However, the diameter of the fractured specimen was 4.28, 4.22, 4.7, 4.89, 4.4, 4.04, 3.31, 2.13 mm at 27, 100, 200, 300, 400, 500, 600 and 750 °C temperature respectively. Thus, the fractured diameter initially increased until the temperature reached 300 °C, and thereafter it

decreased with further increase in temperature. However, the elongation of the specimen remained unaffected up to 600 °C, and at 750 °C, it increased exactly 50%, see Fig. 2.13.

Fig. 2.13 Deformed specimens at varying temperature

Figs. 2.14(a)-(d) illustrate the growth of voids under varying temperature at a magnification of 500x. The plastic strain and hydrostatic stresses enabled the voids to grow and subsequently coalesce with increase in temperature. The growth of voids is responsible for reduced strength and coalescing of voids is responsible for the increased ductility.

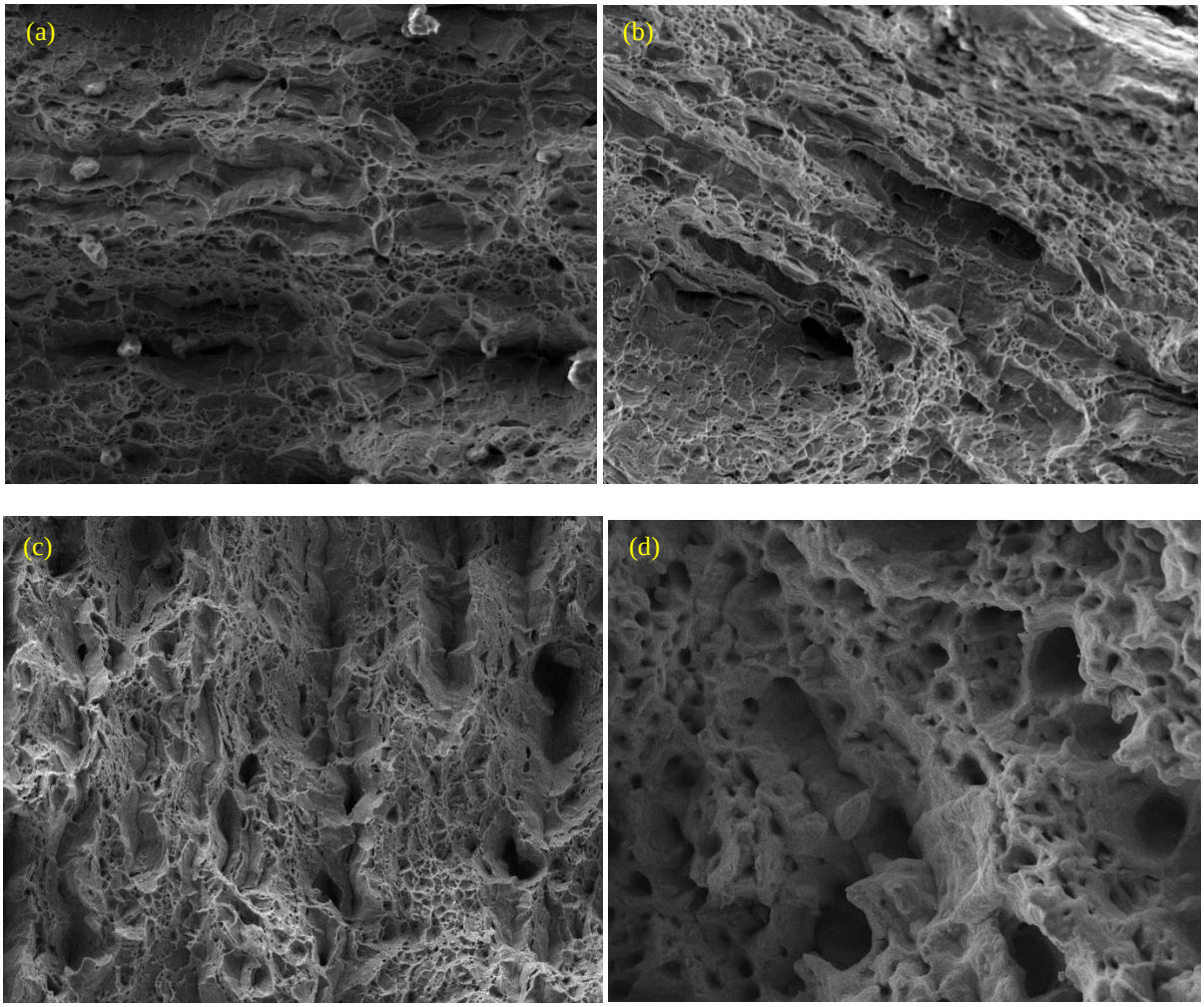

Fig. 2.14 Fractograph of the fractured surface of specimens (500 times magnified) at (a) 100 °C (b) 200 °C (c) 500 °C and (d) 750 °C temperature

2.4 CALIBRATION OF MILD STEEL

The calibration of the material parameters of the Johnson-Cook constitutive model has been carried out by using the curve fitting through least square method. The elastic constants E and υ were obtained by testing the flat specimens at low strain rate, 6×10^{-4} s^{-1}. The yield strength, A, used in the first bracket of the JC flow stress [Eqn. 5] has been obtained from the engineering stress-strain curves pertaining to the specimen oriented in 0° direction. It should be noted that the strength of the material has been found to be 304, 298

and 315 MPa corresponding to specimens oriented in 0°, 45° and 90° direction respectively. Knowing the static yield stress *A*, the hardening parameters *B* and *n* employed in the first bracket of the JC flow stress were obtained by fitting the expression, $B(\bar{\varepsilon}^{pl})^{n}$, with the experimentally measured true stress-strain curve, see Fig. 2.15(a). The software Origin Pro version 8.5.1 was used for fitting the curve and obtaining the parameters *B* and *n*.

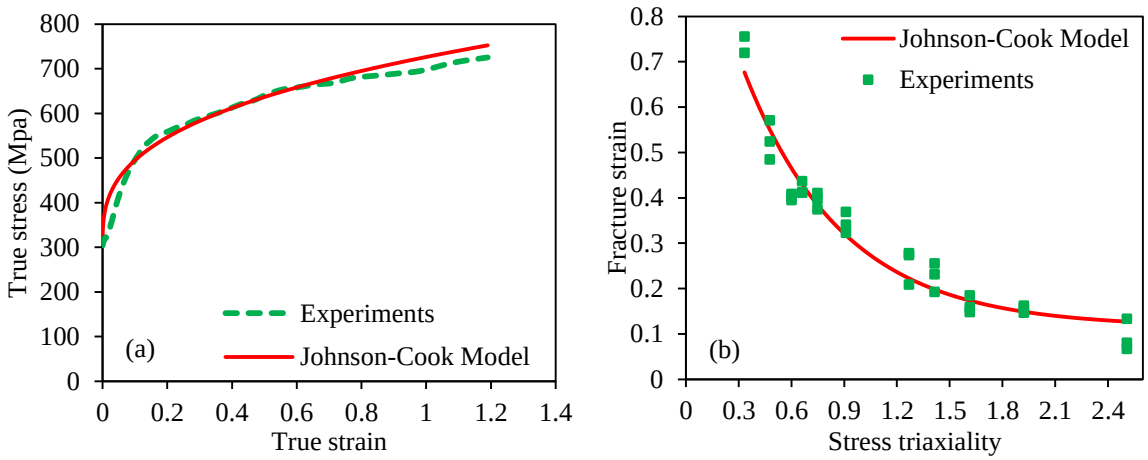

Fig. 2.15 Calibration of the Johnson-Cook model using (a) true stress-strain relation (b) fracture strain as a function of stress triaxiality

The stress-triaxiality parameters, D_1, D_2 and D_3 used in the equivalent failure strain expression of the JC model [Eqn. 7] have been obtained by fitting the expression, $\left[D_1 + D_2 \exp\left(D_3 \frac{\sigma_m}{\bar{\sigma}}\right)\right]$, with the observed true failure strain under varying stress triaxiality i.e., the fracture strain corresponding to the specimens of varying notch radii, see Fig. 2.15(b). The true fracture strain of the material was obtained with the help of original (d_0) and fractured diameter (d_f) of the specimens using the expression; $2\,ln(\frac{d_0}{d_f})$. An exponential curve has been fitted with experimentally obtained data points using Origin Pro.

The strain rate sensitivity parameter *C* employed in the second bracket of the JC flow stress has been obtained by fitting the expression, $\left[1 + C\ln\left(\frac{\dot{\bar{\varepsilon}}^{pl}}{\dot{\varepsilon}_0}\right)\right]$, with the observed yield strength under varying strain rate, see Fig. 2.16(a). A linear curve has been fitted with the experimental data points as per the requirement of the model.

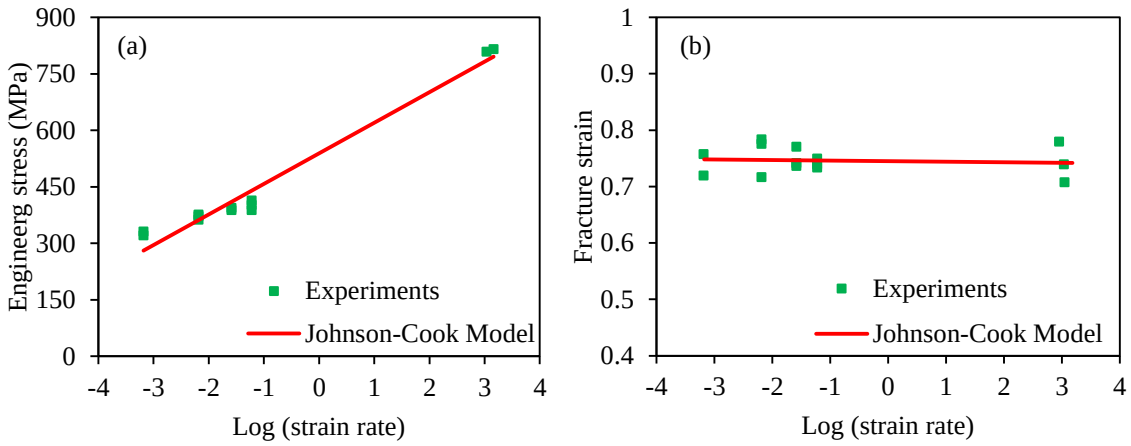

Fig. 2.16 Calibration of the Johnson-Cook model (a) engineering stress as a function of strain rate (b) fracture strain as a function of strain rate

The strain rate dependent damage parameter D_4 has been obtained by fitting the expression, $\left[1 + D_4 ln\left(\frac{\dot{\bar{\varepsilon}}^{pl}}{\dot{\varepsilon}_0}\right)\right]$, with the observed true fracture strain corresponding to varying strain rate, see Fig. 2.16(b). A linear trend line has been fitted with the experimental data points.

The thermal sensitivity parameter *m* employed in the third bracket of the JC flow stress has been obtained by fitting the expression, $\left[1 - \hat{T}^{m}\right]$, with the observed yield strength under varying temperature, see Fig. 2.17(a). A nonlinear curve has been fitted as per the requirement of the model. A prerequisite stress, 536 MPa, corresponding to the 200 °C temperature was considered in order to get the best fit. According to the experimental results,

the strength of the material initially increased up to 300 °C temperature and subsequently decreased with further increase in temperature. However the Johnson and Cook (1985) flow stress expression suggests a continuous decrease in strength with increase in temperature. Hence, the fitted curve could not follow the initial increase in strength and predicted a consistent decrease in stress with increase in temperature.

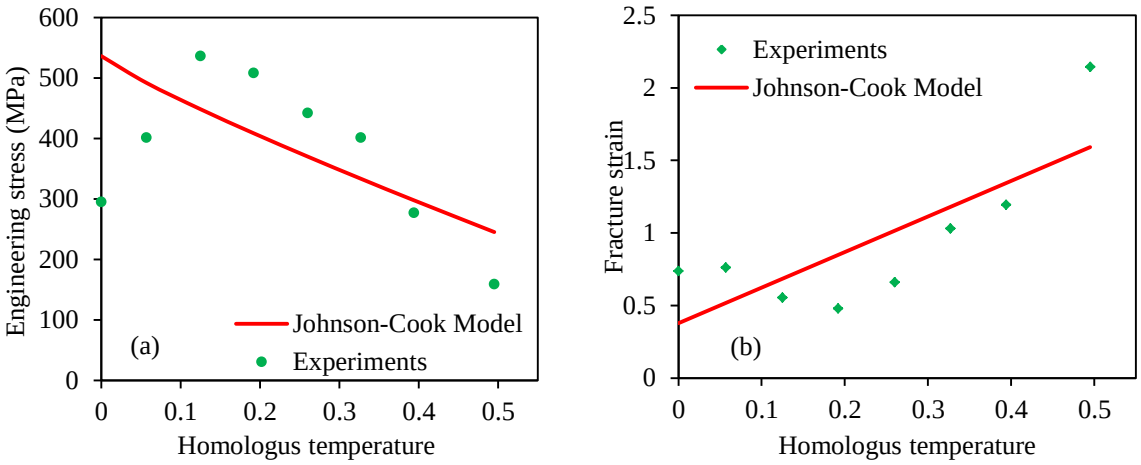

Fig. 2.17 Calibration of the Johnson-Cook model using (a) engineering stress and (b) fracture strain as a function of temperature

The temperature dependent fracture strain parameter D_5 has been obtained by fitting the corresponding expression, $\left[1 + D_5\hat{T}\right]$, with the observed failure strain at varying temperature, see Fig. 2.17(b). In this case also a linear curve has been fitted with the experimentally obtained true fracture strain at varying temperatures. The experiments however, indicated a nonlinear trend due to blue brittle effect i.e., the fracture strain initially decreased up to 300 °C temperature and then increased with further increase in temperature. The JC model however, suggests a linear trend for predicting the thermal influence on the material damage. The fitted curve therefore could not follow the initial decreasing trend of the fracture strain. The calibrated material parameters of JC model for Mild steel are presented in Table 2.3.

Table 2.3 Material parameters of mild steel

Description	Notation	Numerical Value
Modulus of elasticity	E (N/m^2)	203 x 10^9
Poisson's ratio	ν	0.33
Density	ρ (Kg/ m^3)	7850
Yield stress constant	A (N/ m^2)	304.330 x 10^6
Strain hardening constant	B (N/ m^2)	422.007 x 10^6
	n	0.345
Viscous effect	C	0.0156
Thermal softening constant	m	0.87
Reference strain rate	$\dot{\varepsilon}_0$	0.0001 s^{-1}
Melting temperature	θ_{melt} (K)	1800
Transition temperature	$\theta_{transition}$ (K)	293
Fracture strain constant	D_1	0.1152
	D_2	1.0116
	D_3	-1.7684
	D_4	-0.05279
	D_5	0.5262

2.5 FLOW AND FRACTURE BEHAVIOUR OF ARMOX 500T STEEL

The material characterization of Armox 500T steel has been carried out under varying stress triaxiality, strain rate and temperature. The effect of stress triaxiality was studied by performing tension tests on notched cylindrical specimens. The radius of the notch has been varied as 0.4, 0.8, 2, 3 and 4 mm. The smooth cylindrical specimens were tested under tension at varying strain rate and temperature. The strain rate in the range 6 x 10^{-4} - 1000 s^{-1} was obtained from universal testing machine and the Hopkinson pressure bar apparatus. The tests at elevated temperature were carried out using a portable furnace which enabled the variation of temperature from 100°C to 900°C. All the parameters of Johnson-Cook flow and fracture model were calibrated through curve fitting method.

2.5.1 Preliminary Tests

The Armox 500T steel was procured in the form of plates of various thicknesses and the coupons for material tests were extracted out from the middle of the thickness of 20 mm plate. The hardness of such a square shape specimen, of 10 mm x 10 mm, was studied in both in plane as well as out of plane surface. The in plane and out of plane surface hardness of the Armox 500T steel specimen was ±10%, while the average hardness was 501 BHN, see Table 2.4.

Table 2.4 Hardness of Armox 500T steel

In-plane	Out-plane	Average
554	447	501

The chemical composition of the Armox 500T steel was also studied by Energy-Dispersive X-ray (EDX) Spectroscopy and the percentage of the ingredients is compared with what has been provided by the manufacturer, see Table 2.5.

Table 2.5 Chemical composition of Armox 500T steel

Chemical composition	EDX Spectroscopy	As per the certificate of SSAB
C	0.3484	0.28
Si	0.2732	0.26
Mn	0.7672	0.91
P	0.0208	0.008
S	0.0066	0.001
Cr	0.5042	0.5
Ni	0.7498	0.94
Mo	-	0.349
Al	0.0243	0.053
Cu	0.1429	-

The specimens were prepared with geometries as per ASTM 370-12 standard. The possible anisotropy of the plate material has been studied by extracting the cylindrical specimens from three different directions 0°, 45° and 90° and performing the uniaxial tension tests under quasi-static loading. The gauge diameter and gauge length of the smooth cylindrical specimen was 6.25 and 25 mm respectively. The quasi-static tensile tests were carried out on smooth cylindrical specimens at room temperature at a constant strain rate of 1.6×10^{-4} s^{-1}. These specimens were tested on Tinius Olsen H75KS and Milano Controls UTM (Universal Testing Machine) machine. The diameter reduction of the smooth cylindrical specimen was measured up to fracture with the help of a digital vernier caliper to obtain the true stress-strain relation. The true stress–strain relationship thus obtained through the specimens extracted from different orientation is plotted in Fig. 2.18(a) and the corresponding J-C model fit is shown in Fig. 2.18(b).

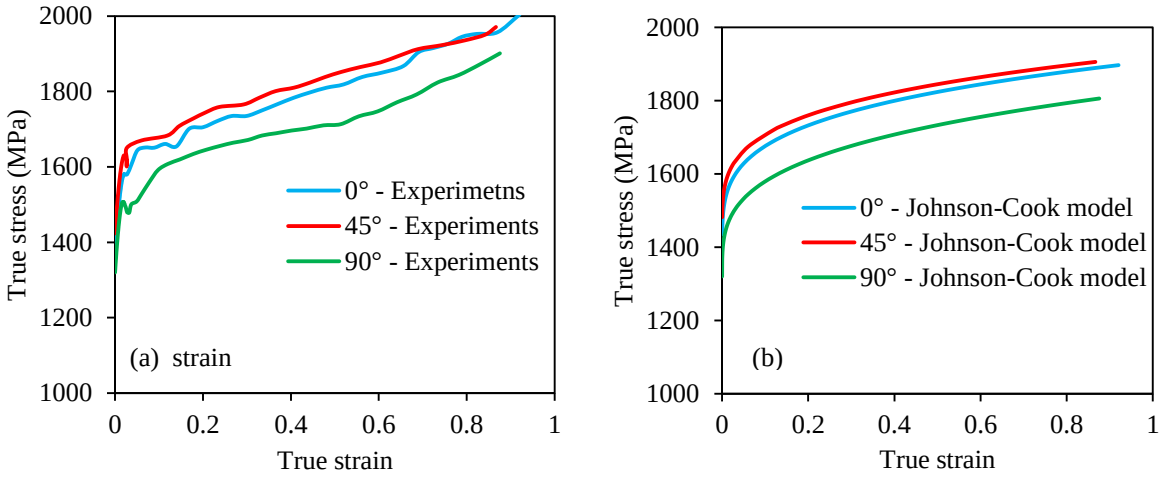

Fig. 2.18 True stress-strain relationship of (a) experiments (b) experiments with JC model

The influence of possible anisotropy of the material on the JC parameters has also been studied and the results thus obtained with respect to yield stress, strain hardening

parameter and strain hardening exponent are shown in Table 2.6. The results led to the conclusion that the effect of anisotropy is insignificant.

Table 2.6 Material parameters - different direction of plates

Orientation	A	B	n
0°	1372.488	535.022	0.2467
45°	1423.264	499.414	0.2455
90°	1319.869	504.696	0.2892

2.5.2 Effect of Stress Triaxilality

The initial stress triaxiality in the cylindrical specimens was introduced by an artificial notch produced in a smooth cylindrical specimen. The stress triaxiality is a measure of material ductility, represented in terms of maximum stress triaxiality ratio, σ^*_{max}, see Eqn. 10. The stress triaxiality ratio in the specimen has been varied as 1.95, 1.43, 0.927, 0.765 and 0.67 by varying the curvature radius of the notched specimen as 0.4, 0.8, 2.0, 3.0 and 4.0 mm. These specimens were tested on Servo-Hydraulic machine at a constant strain-rate of 1.6 x 10^{-4} s^{-1}. The stress-strain curves obtained at different values of stress triaxility are shown in Fig. 2.19.

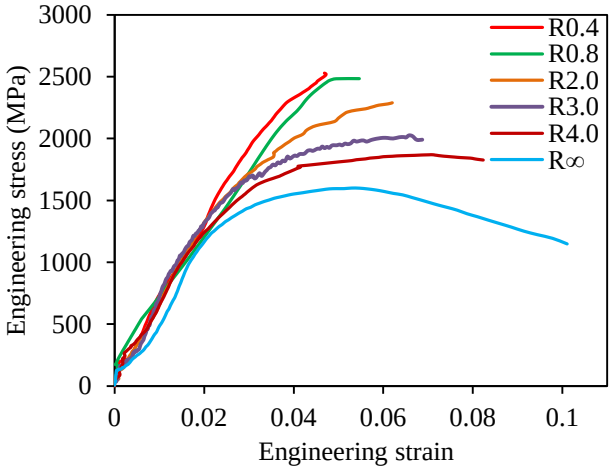

Fig. 2.19 Variation of stress and strain as a function of notch

The fracture strain has been found to decrease with an increase in the stress triaxiality. It may therefore be concluded that the ductility of the material is decreased with increase in stress triaxiality. The fractured specimens of varying notch radius are shown in Fig. 2.20.

Fig. 2.20 Deformed specimens of different notch radius

2.5.3 Effect of Strain Rate

The low and intermediate strain rate tests under tension have been carried out on smooth cylindrical specimens of diameter 6.25 mm and gauge length 25 mm. These tests were performed on Tinius Olsen H75KS Universal Testing Machine, at strain rate in the range 1.6×10^{-4} to 3.3×10^{-2} s^{-1}. The tension tests at high strain rate were performed on smooth cylindrical specimens of diameter 3 mm and gauge length 10 mm on Split Hopkinson Pressure Bar apparatus at strain rate 500 – 1000 s^{-1}. The ductility of the material at low strain rate has been found to be significantly higher than what has been observed at high strain rate. The fractured specimens at high strain rate are shown in Fig. 2.21.

Fig. 2.21 Deformed specimen at high strain rate

The engineering stress-strain curves obtained through the tension tests performed at low, intermediate and high strain rate are shown in Fig. 2.22. The tests carried out at strain rate 1.6 x 10^{-4} to 3.3 x 10^{-2} s^{-1} showed insignificant influence on the material behaviour with respect to stress strain relationship as well as the fracture behaviour of the specimen. The hardening behaviour of the material has also been found to be identical under this regime. At high strain rate however the strength of material has been found to increase abruptly while the ductility has decreased. The sudden increase in strength at high strain rate has also been observed in mild steel, see Fig. 2.9.

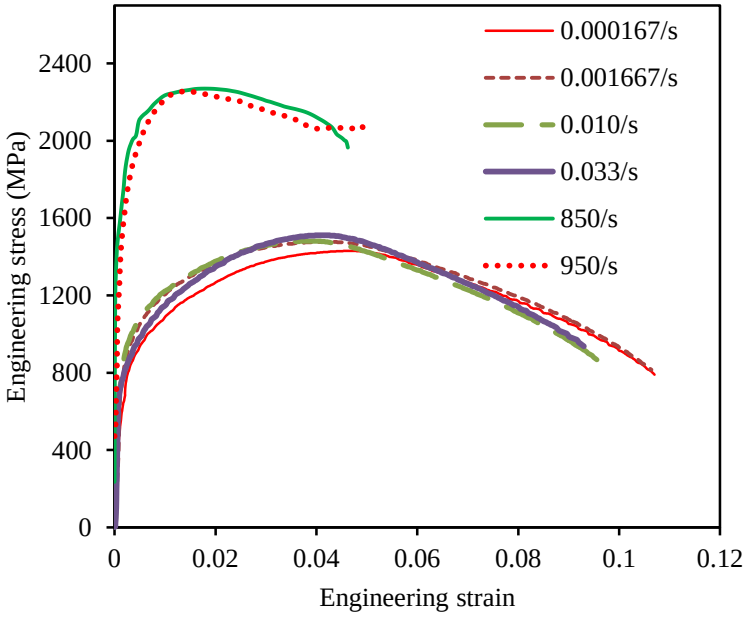

Fig. 2.22 Stress strain curves of the material at varying strain

2.5.4 Effect of Temperature

The tension tests at varying temperature were carried out on smooth cylindrical specimens of gauge diameter 6.25 and gauge length 25 mm. These tests were performed at 100, 200, 300, 400, 500, 600, 750 and 900 °C on servo-hydraulic UTM at a strain rate of 1.6 x 10^{-4} s^{-1}. A portable furnace of internal diameter 60 and height 220 mm was used to vary the temperature of the specimen, Fig. 2.11. The furnace was firmly held between the steel platens of the UTM with the help of steel fixture and the specimen was placed inside the furnace. The temperature of the furnace was controlled by the high temperature furnace microcontroller. Two thermocouples were used to measure temperature inside the furnace. The rate of temperature was kept 10 °C per minute. The temperature was kept constant for about 30 minutes before the test in order to ensure proper heating of the specimen. The longitudinal strain of the specimen was measured with the help of two LVDTs.

The flow stress of the material was found to be significantly affected by the temperature. Initially the flow stress increased slightly when the temperature increased up to 200°C. This phenomenon is known as the blue brittle region where the strength of steel is increased and the ductility is decreased on heating, see Fig. 2.23. At 300 °C temperature, however, the ultimate stress of the material was seen to reduce while the fracture strain increased. At 600°C temperature the ultimate stress reduced abruptly. At 900°C temperature the material lost all of its strength and the specimen underwent significant elongation before breakage. The high temperature tests thus carried out led to the conclusion that the yield stress of the material decreased almost linearly with increase in temperature and the strength has been found maximum at a temperature of about 200°C.

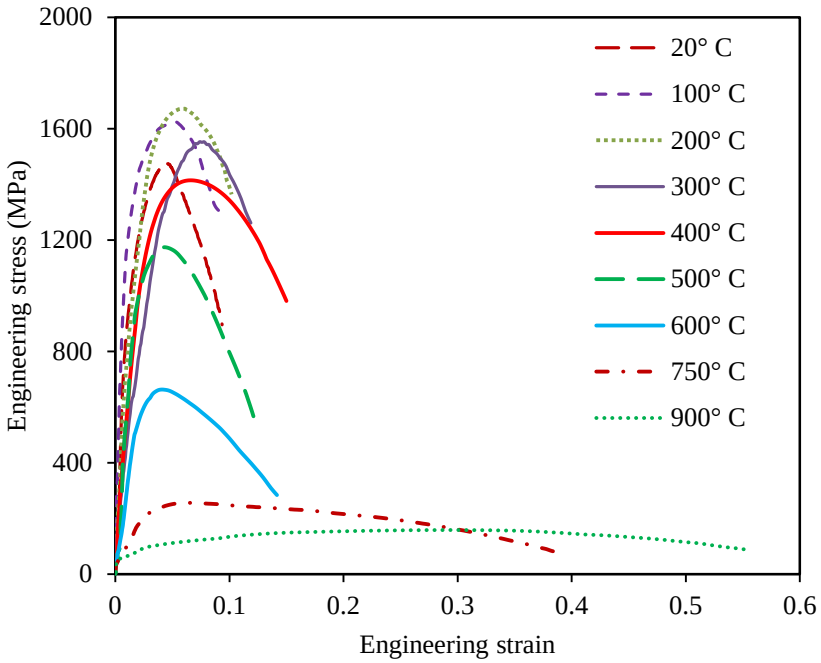

Fig. 2.23 Stress-strain relationship at varying temperature

Fig. 2.24 Smooth cylindrical deformed specimens at varying temperature

The tested specimens at varying temperature are shown in Fig. 2.24. The plastic strain and hydrostatic stresses enabled the voids to grow and subsequently coalesce with increase in temperature. The growth of void is responsible for reduced strength and coalescing of voids for the increased ductility, see Fig. 2.25.

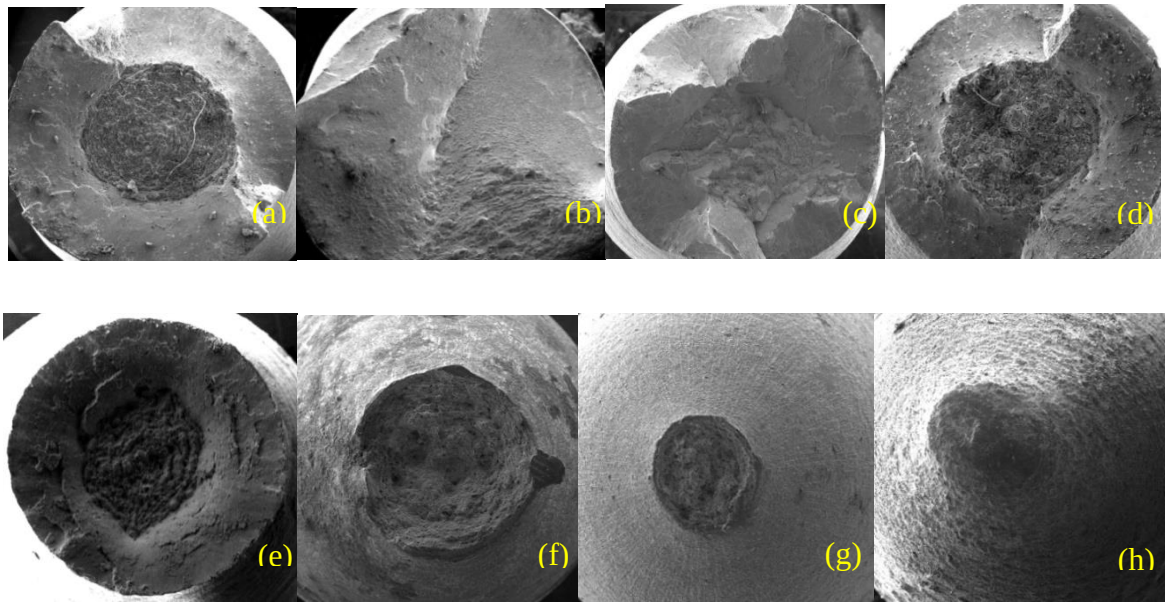

Fig. 2.25 Fractured surface with 50 x magnification at (a) 100 °C (b) 200 °C (c) 300 °C (d) 400 °C (e) 500 °C (f) 600 °C (g) 750 °C and (h) 900 °C temperatures

2.6 CALIBRATION OF ARMOX 500T STEEL

The calibration of the material parameters of the Johnson-Cook constitutive model has been carried out by using the curve fitting through least square method. The yield strength, *A*, used in the first bracket of the JC flow stress [Eqn. 5] has been obtained from the engineering stress-strain curves pertaining to the specimen oriented at 0° direction, see Fig. 2.26(a). It should be noted that the strength of the material has been found to be 1372, 1423 and 1319 MPa corresponding to specimens oriented in 0°, 45° and 90° direction, respectively. Knowing the static yield stress A, 1372 MPa, the hardening parameters *B* and *n*

employed in the first bracket of the JC flow stress were obtained by fitting the expression, $B(\bar{\varepsilon}^{pl})^n$, with the experimentally measured true stress-strain curve, see Fig. 2.26(a). The software Origin Pro version 8.5.1 was used for fitting the curve and obtaining the parameters *B* and *n*.

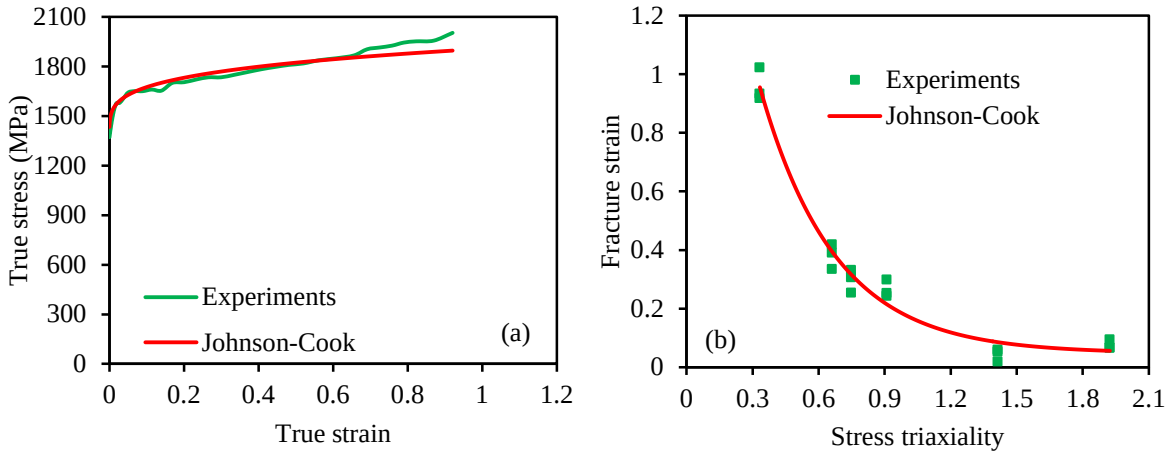

Fig. 2.26 Calibration of the Johnson-Cook model using (a) true stress-strain relation (b) fracture strain as a function of stress triaxiality

The stress-triaxiality parameters, D_1, D_2 and D_3 in the equivalent failure strain expression of the JC model [Eqn. 7] have been obtained by fitting the expression, $\left[D_1 + D_2 \exp\left(D_3 \frac{\sigma_m}{\bar{\sigma}}\right)\right]$, with the observed true failure strain under varying stress triaxiality i.e., the fracture strain corresponding to the specimens of varying notch radii, see Fig. 2.26(b). The true fracture strain of the material was obtained with the help of original diameter (d_0) and fractured diameter (d_f) of the specimens using the expression, $2\ln(\frac{d_0}{d_f})$. An exponential curve has been fitted with experimentally obtained data points using the Origin Pro.

The strain rate sensitivity parameter *C* employed in the second bracket of the JC flow stress model has been obtained by fitting the expression, $\left[1 + C\ln\left(\frac{\dot{\bar{\varepsilon}}^{pl}}{\dot{\varepsilon}_0}\right)\right]$, with the observed

yield strength under varying strain rate, see Fig. 2.27(a). A linear curve has been fitted with the experimental data points as per the requirement of the model.

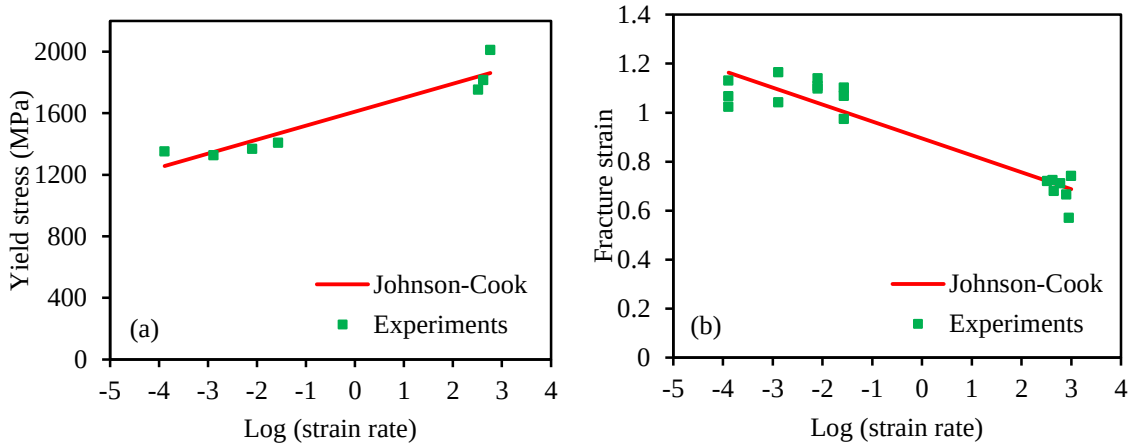

Fig. 2.27 Calibration of the Johnson-Cook model using (a) engineering stress and (b) fracture strain as a function of strain rate

The strain rate dependent damage parameter D_4 has been obtained by fitting the expression, $\left[1 + D_4 \ln\left(\frac{\dot{\bar{\varepsilon}}^{pl}}{\dot{\varepsilon}_0}\right)\right]$, with the observed true fracture strain corresponding to varying strain rate, see Fig. 2.27(b). A linear trend line has been fitted with the experimental data points.

The thermal sensitivity parameter m in the third bracket of the JC flow stress has been obtained by fitting the expression, $\left[1 - \hat{T}^m\right]$, with the observed yield strength under varying temperatures, see Fig. 2.28(a). A nonlinear curve has been fitted as per the requirement of the model. A prerequisite stress of 1456 MPa, corresponding to the 200 °C temperature, was considered in order to get the best fit.

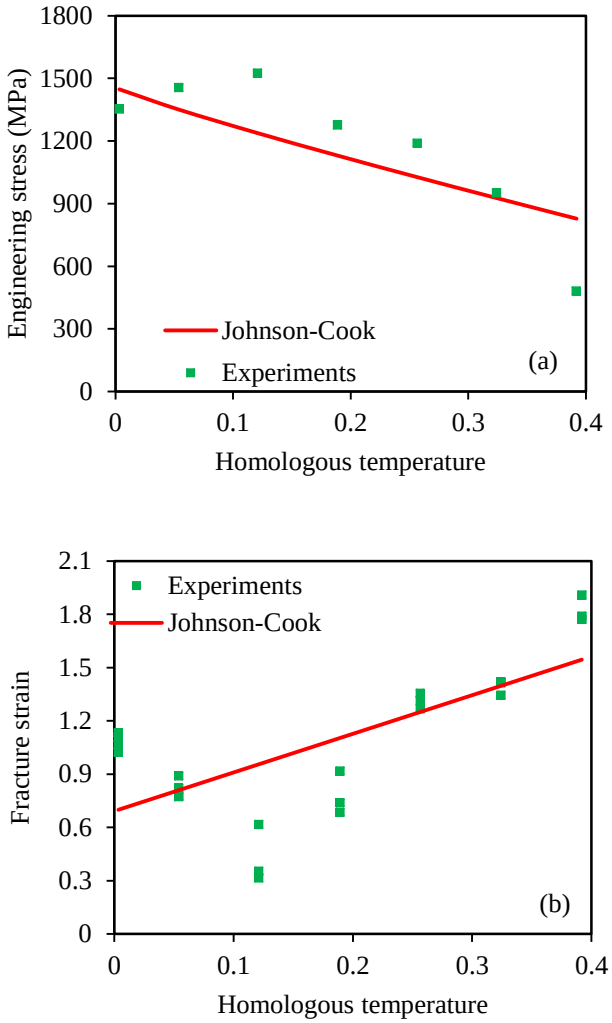

Fig. 2.28 Calibration of the Johnson-Cook model using (a) engineering stress and (b) fracture strain as a function of temperature

The temperature dependent fracture strain parameter D_5 has been obtained by fitting the corresponding expression, $\left[1 + D_5\widehat{\mathrm{T}}\right]$, with the observed failure strain at varying temperatures, see Fig. 2.28(b). In this case also a linear curve was fitted with the experimentally obtained true fracture strain at varying temperature. The calibrated material parameters of JC model for Armox 500T steel are presented in Table 2.7.

Table 2.7 Material parameters of Armox 500T steel

Description	Notation	Numerical value
Modulus of elasticity	E (N/m^2)	201 x 10^9
Poisson's ratio	ν	0.33
Density	ρ (Kg/m^3)	7850
Yield stress constant	A (N/m^2)	1372.48 x 10^6
Strain hardening constant	B (N/m^2)	835.02 x 10^6
	n	0.247
Viscous effect	C	0.061
Thermal sensitivity	m	0.84
Reference strain rate	$\dot{\varepsilon}_0$	1 s^{-1}
Melting temperature	θ_{melt} (K)	1800
Transition temperature	$\theta_{transition}$ (K)	293
Fracture strain constant	D_1	0.04289
	D_2	2.1521
	D_3	-2.7575
	D_4	-0.0066
	D_5	0.86

2.7 FLOW AND FRACTURE BEHAVIOUR OF 7075-T651 ALUMINIUM

The material characterization of 7075-T651 aluminium has been carried out by experimenting the behaviour of material under varying stress triaxiality, strain rate and temperature. The effect of stress triaxiality was studied by performing tension tests on notched cylindrical specimens. The radius of the notch has been varied as 0.4, 0.8, 2, 4 and 6 mm. The smooth cylindrical specimens were tested under tension at varying strain rate and temperature. The strain rate in the ranges 5 x 10^{-4} - 799 s^{-1}, was obtained on UTM and the Split Hopkinson Pressure Bar (SHPB) apparatus. The tests at elevated temperatures were carried out using a portable furnace which enabled the variation of temperature from 27 to 600 °C. All the parameters of Johnson-Cook flow and fracture model were calibrated through curve fitting method.

2.7.1 Preliminary Tests

The chemical composition of the 7075-T651 material has been studied by Energy-Dispersive X-ray (EDX) spectroscopy and the percentile of the constituents was compared with the data provided by the manufacturer and the ranges of allowable limit, see Table 2.8.

Table 2.8 Chemical composition of 7075-T651 aluminium

Elements	Present study by EDX (%)	As per the manufacturer (%)	Maximum limit (%)
Al	85.21	89.07	Remains
Zn	6.69	5.79	5.10 - 6.10
Mg	3.06	2.47	2.10 - 2.90
Cu	1.78	1.45	1.2 - 2.0
Fe	0.89	0.24	0.50
Si	0.43	0.29	0.40
Cr	0.37	0.22	0.18 - 0.28
Sn	0.35	0.02	-
Ti	0.32	0.09	0.20
Mn	0.30	0.16	0.30
S	0.28	0.012	-
N	0.26	0.02	-
P	0.05	0.028	-

2.7.2 Material Anisotropy

The smooth flat specimens were extracted out of 20mm thick plate in the length (X), width (Y) and thickness (Z) direction. The in plane specimens (X and Y direction) had length, width and thickness 25, 12 and 3 mm, respectively, see Fig. 2.29(a) and (c). These in-plane specimens, tested at a strain-rate of 5×10^{-4} s^{-1} corresponding to cross head speed of 1 mm/min, experienced shear dominant fracture, see Fig. 2.29(b) and (d). The engineering stress-strain relationship obtained at both in plane directions (X and Y) is shown in Fig. 2.29(e).

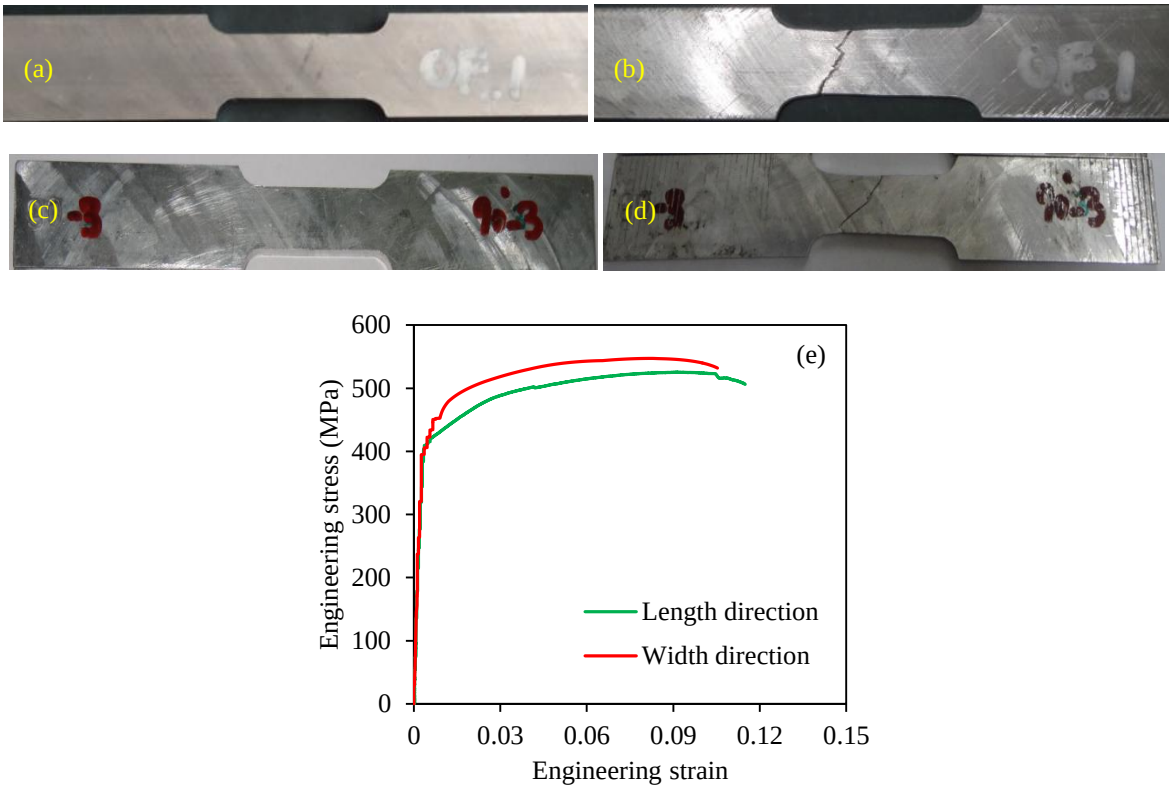

Fig. 2.29 Length-X direction specimen of (a) undeformed (b) deformed profile and Width-Y direction specimen of (c) undeformed (d) deformed profile and (e) stress-strain relationship at length and width direction

The out of plane specimens (thickness direction) were prepared as a miniature sample with 20 mm total length, 5 mm gauge length, and 2 mm thickness, see Fig. 2.30(a). A specialized dog bone arrangement designed for holding these specimens in the UTM is also shown in the figure. All the miniature specimens were tested at a strain rate of 1.33×10^{-3} s^{-1} and the corresponding cross head speed of 0.4 mm/min. The fractured specimen is shown in Fig. 2.30(b). The engineering stress-strain relationship of thickness direction (Z) specimen is shown in Fig. 2.30(c). These tension tests were performed on KIC-2-300-C universal testing machine at room temperature, 27 °C. Three repetitions were performed for each test and the average of these is reported.

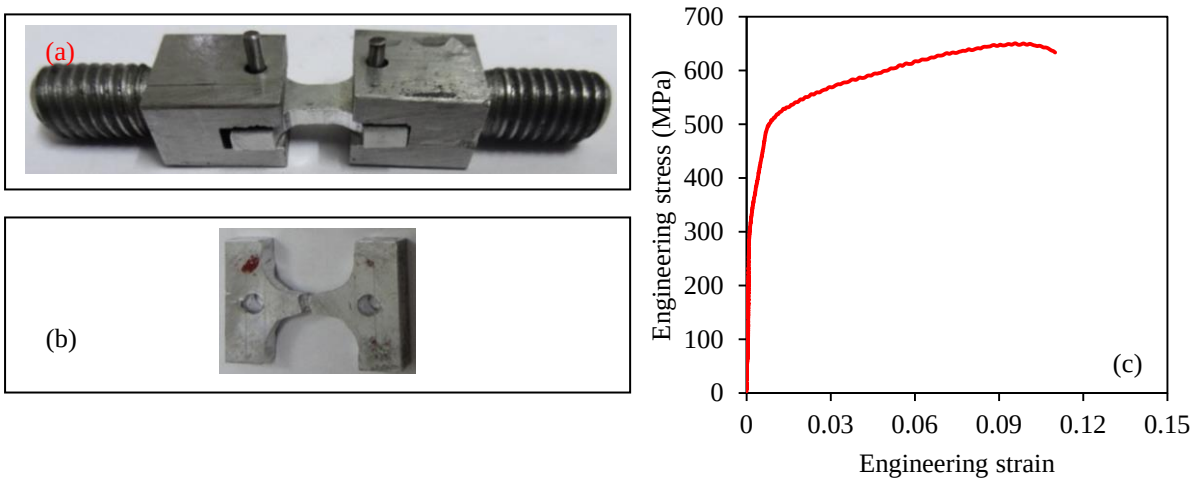

Fig. 2.30 Thickness direction specimens of (a) undeformed (b) deformed profile and (c) stress-strain relationship

Further tests were carried out on smooth cylindrical specimens extracted out from 0°, 45° and 90° orientation with respect to the rolling direction of the material for studying the influence of anisotropy on the true stress-strain relationship. The gauge diameter and length of the smooth cylindrical specimens was 6.25 and 25 mm respectively. The specimens were tested at a strain rate of 5 x 10^{-4} s^{-1} and the corresponding cross head speed of 1 mm/min. A digital vernier caliper was used to measure the reduction in the diameter of the specimen subsequent to ultimate stress until fracture.

The true stress-strain relationship of smooth cylindrical specimens thus obtained was employed to obtain the parameters A, B and n corresponding to the material orientation 0°, 45° and 90°. It has been noticed that the yield strength of the material is almost same at the 0° and 90° orientation, while at 45° orientation the strength of the material was found to be comparatively lesser. Further, the true strain of the material has been to be dependent upon the material orientation. The highest fracture strain was found to be 45% at 45° material orientation. However, at 90° orientation the specimens failed merely at 14% true strain representing highest ultimate stress due excessive brittleness, see Fig. 2.31(a).

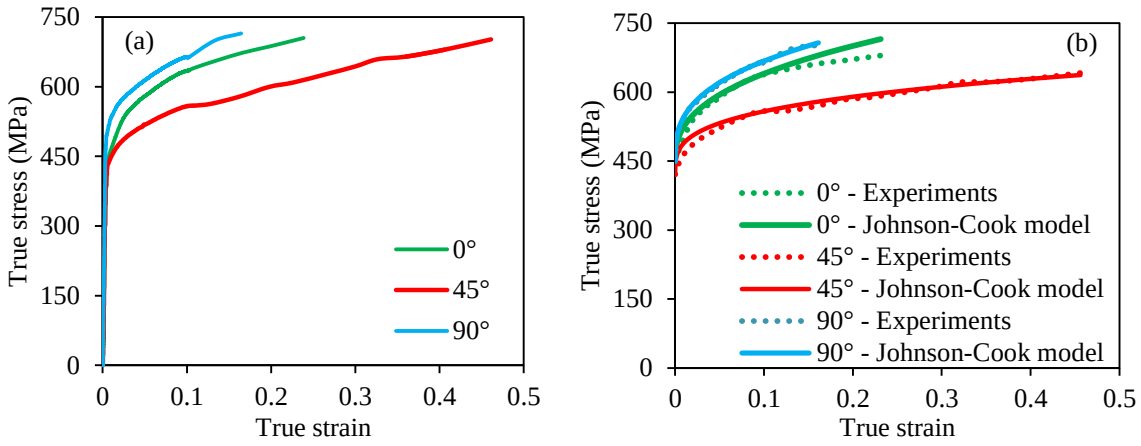

Fig. 2.31 True stress-strain relationship of (a) experiments (b) experiments with JC model

The Johnson-Cook flow stress model has been used to identify the hardening parameters of the material at 0°, 45° and 90° orientation. The parameter *A* is static yield stress of the material. The parameters *B* and *n* were obtained by fitting the expression of the first bracket of the Johnson-Cook constitutive model [Eqn. 5] with the plastic region of the true stress-strain curve, Fig. 2.31(b). It has been found that the parameters *B* and *n*, at 45° orientation, are significantly different than those of the parameters at 0° and 90° orientation, Table 2.9.

Table 2.9 Material parameters - different direction of plates

Orientation	A (MPa)	B (MPa)	n
0°	448.454	475.808	0.3948
45°	420.867	273.637	0.2994
90°	449.525	488.107	0.3498

Moreover, the cylindrical specimens corresponding to 0° orientation found to have V shaped fractured surface while the specimens corresponding to 45° orientation developed the cup-cone shaped fracture surface. Hence, the specimens at 0° and 45° orientation underwent a mixed mode of brittle and ductile fracture, see Fig. 2.32(a) and (b) respectively. However, the failure surface of the specimen corresponding to 90° orientation was exactly inclined to

45° and hence brittle in nature, Fig. 2.32(c). In general, it has been found that shear failure is the predominant fracture mode corresponding to all the three orientations. It may therefore be concluded that 7075-T651 aluminum plates possess material anisotropy and the Johnson-Cook hardening cannot be used for simulating the material hardening. An appropriate constitutive model is therefore required to enable the correct prediction of the flow behavior of the material.

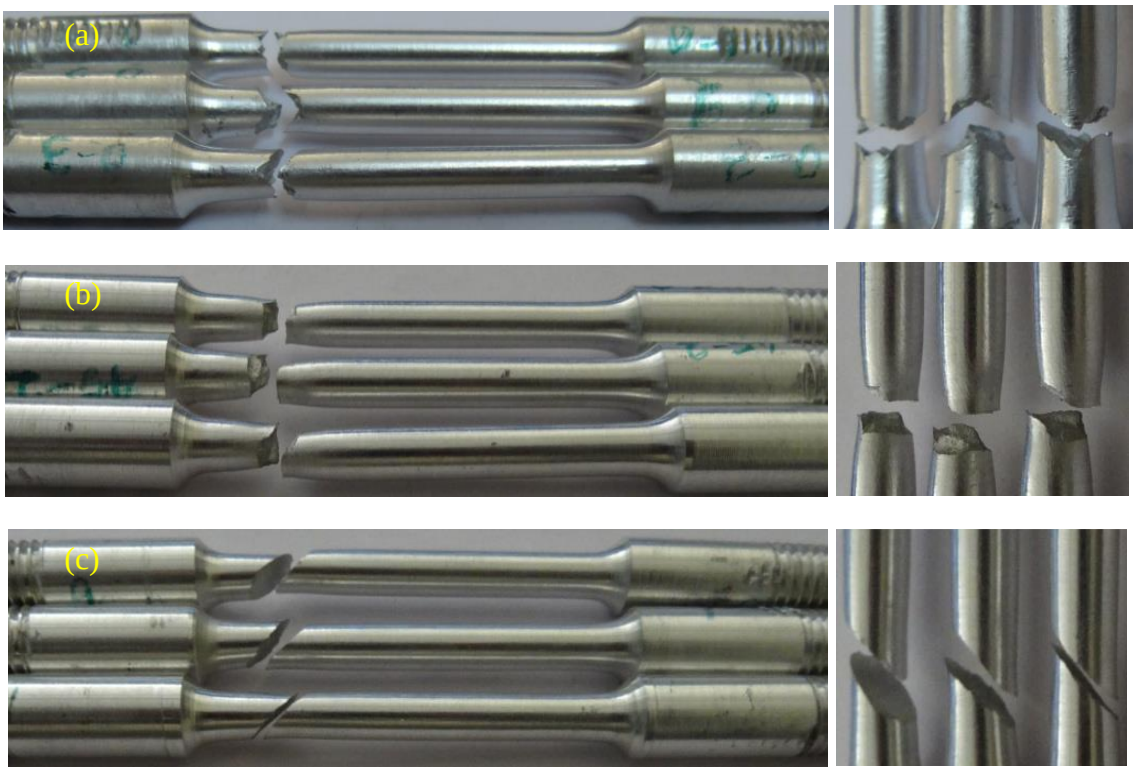

Fig. 2.32 Deformed specimens at (a) 0° (b) 45° and (c) 90° orientation

The elastic constants obtained corresponding to different orientations of the material are shown in Table 2.10.

Table 2.10 Engineering constants for different orientations

Young's modulus (MPa)	E_1	E_2	E_3
	69682	50472	61023
Poisson's ratio	v_{12}	v_{13}	v_{23}
	0.39	0.34	0.33
Shear Modulus (MPa)	G_{12}	G_{13}	G_{23}
	25022	18832	22940

The Hill's stress potentials represent the effect of anisotropy in the flow behaviour of the material and are defined as;

$$R_{11} = \frac{\sigma_{11}}{\sigma_0}, R_{22} = \frac{\sigma_{22}}{\sigma_0}, R_{33} = \frac{\sigma_{33}}{\sigma_0}, R_{12} = \frac{\sigma_{12}}{\sigma_0}, R_{13} = \frac{\sigma_{13}}{\sigma_0} \text{ and } R_{23} = \frac{\sigma_{23}}{\sigma_0}$$

where, σ_0 is reference yield stress, σ_{11} , σ_{22} and σ_{33} are tensile stress components and, σ_{12} , σ_{13} and σ_{23} are shear stress components.

The numerical values of the Hill's stress potential for 7075-T651 aluminium have been obtained as the ratio of the reference yield stress (with respect to 0° material orientation) to the yield stress of the corresponding material orientation, and these have been presented in Table 2.11.

Table 2.11 Stress potentials for anisotropic material

Stress potentials	Stress ratio
R_{11}	1.00
R_{22}	1.21
R_{33}	1.46
R_{12}	1.10
R_{13}	1.10
R_{23}	1.20

2.7.3 Effect of Stress Triaxiality

The initial stress triaxiality in the cylindrical specimens was introduced by an artificial notch produced in a smooth cylindrical specimen. The stress triaxiality is a measure of material ductility, represented in terms of maximum stress triaxiality ratio, σ^*_{max}, see Eqn. 10. The notched cylindrical specimens were prepared at 0°orientation i.e., with respect to the rolling direction of the material. The stress triaxiality in the specimen was varied by varying the curvature radius of the notch as 0.4, 0.8, 2.0, 4.0 and 6.0 mm while the gauge diameter of the notch was kept constant, 6.25 mm, see Fig. 2.33 (a)-(f). These specimens were tested on KIC-2-300-C UTM machine at a constant strain-rate of 5 x 10^{-4} s^{-1} and the corresponding cross head speed of 1 mm/min. The stress-strain curves obtained at different values of stress triaxility are shown in Fig. 2.34.

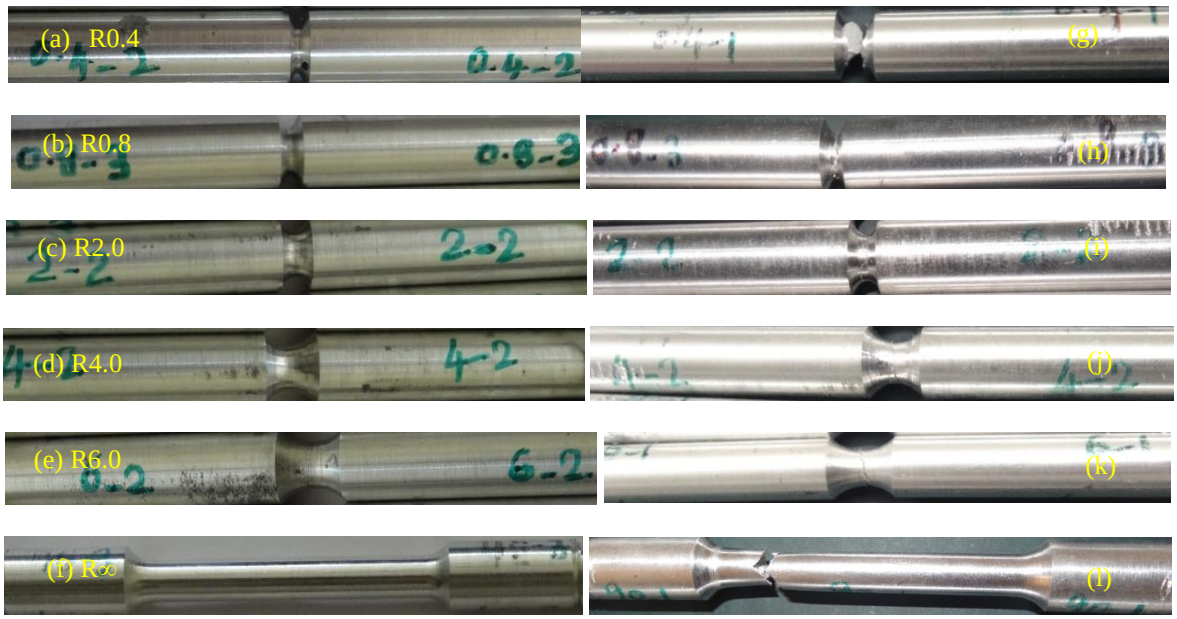

Fig. 2.33 Deformed and undeformed specimens with varying notch radii

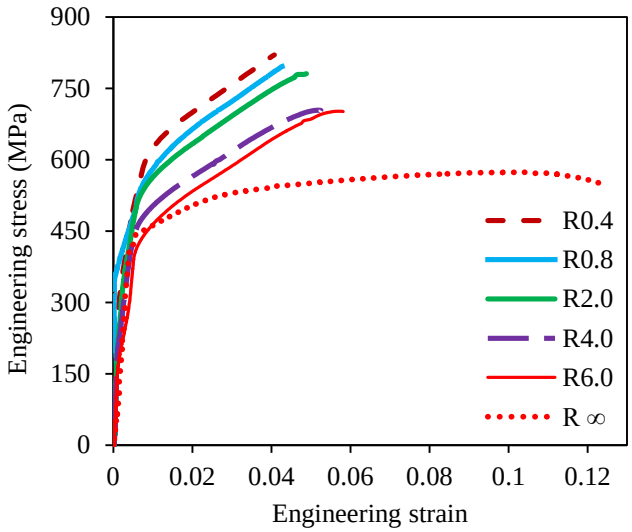

Fig. 2.34 Stress-strain relationship of material with varying notch radii

The fracture strain was found to decrease with an increase in the stress triaxiality. It may therefore be concluded here that the ductility of the material has decreased with an increase in stress triaxiality. The fractured specimens of different notch radius are shown in Fig. 2.33(g)-(l). The mode of failure of R0.4 notch radius has been found to be cup-cone shape and the specimen failed due to excessive brittleness. With further increase in notch radius the failure surface has been found to be inclined indicating shear dominant failure, however, the brittleness has been found to decrease.

2.7.4 Effect of Strain Rate

The low and intermediate strain rate tests under tension have been carried out on smooth cylindrical specimens of diameter 6.25 and gauge length 25 mm. All of these specimens were prepared at 0° orientation i.e., with respect to the rolling direction of the material. These tests were performed on KIC-2-300-C UTM machine at strain rate in the range $5 \times 10^{-4} - 5 \times 10^{-2}$ s^{-1}. The tension tests at high strain rate were performed on smooth cylindrical specimens of diameter 3 mm and gauge length 10 mm on Split Hopkinson

Pressure Bar apparatus at strain rate 500 – 1000 s^{-1}, see Fig. 2.35(a). The strain rate sensitivity of the material at low, intermediate and high strain rate has been found to be almost same. A typical fractured specimen tested at 799 s^{-1} strain rate is shown in Fig. 2.35(b).

Fig 2.35 Material specimens of (a) undeformed and (b) deformed profile at high strain rate

The engineering stress-strain relationship of the material obtained from low and intermediate strain rate has been shown in Fig. 2.36(a) and the stress-strain relations corresponding to high strain rate is shown in Fig. 2.36(b). The material did not indicate any strain rate sensitivity. The ductility of the material at low, intermediate and high strain rate has also been found to be almost same.

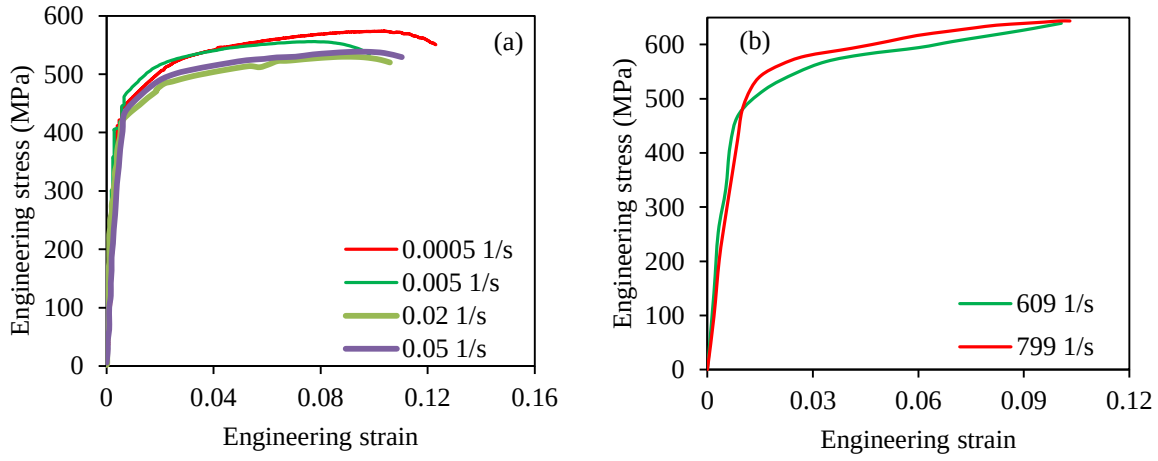

Fig. 2.36 Stress-strain relationship at (a) low and intermediate strain rate (b) high strain rate

2.7.5 Effect of Temperature

The temperature sensitivity of the material has been studied by performing the tension tests under quasi-static loading i.e., at strain rate 6 x 10^{-4} s^{-1}. The cylindrical specimens of diameter 6.25 mm and gauge length 25 mm were tested on a 500 kN universal testing machine. The tension tests were performed at 100 °C, 200 °C, 300 °C, 400 °C, 500 °C, and 600 °C. A portable furnace was employed for heating the specimen to the required temperature, see Fig. 2.11. The temperature of the furnace was controlled by a micro-temperature controller. The furnace had a hollow cylindrical shape, open from top and bottom for inserting the specimen. The specimen was held at the top and the bottom jaws of the universal testing machine while the furnace was placed on a steel platform. The opening of the furnace at the top and bottom were closed by glass wool in order to control the temperature dissipation. The specimen was heated to the desired temperature at a rate of 0.167 °C/sec. The testing temperature was maintained for half an hour in order to get the specimen heated uniformly before the application of mechanical load. The inside temperature of the furnace has been recorded using the K-Type thermocouples held near the centre of the specimen. The elongation of the specimen was measured by two LVDTs.

Fig. 2.37(a) represents the stress-strain curves of the material at varying temperature. The flow stress of the material has been found to be significantly affected with an increase in temperature. Initially the flow stress increased when the temperature was increased to 100 °C. At 400 °C however, the ultimate stress of the material started reducing while the fracture strain increased. Above 400 °C temperature the ultimate stress abruptly reduced. At 500 °C the material lost all of its strength and showed large elongation. The Young's modulus showed almost linear decrease with increase in temperature, Fig. 2.37(b).

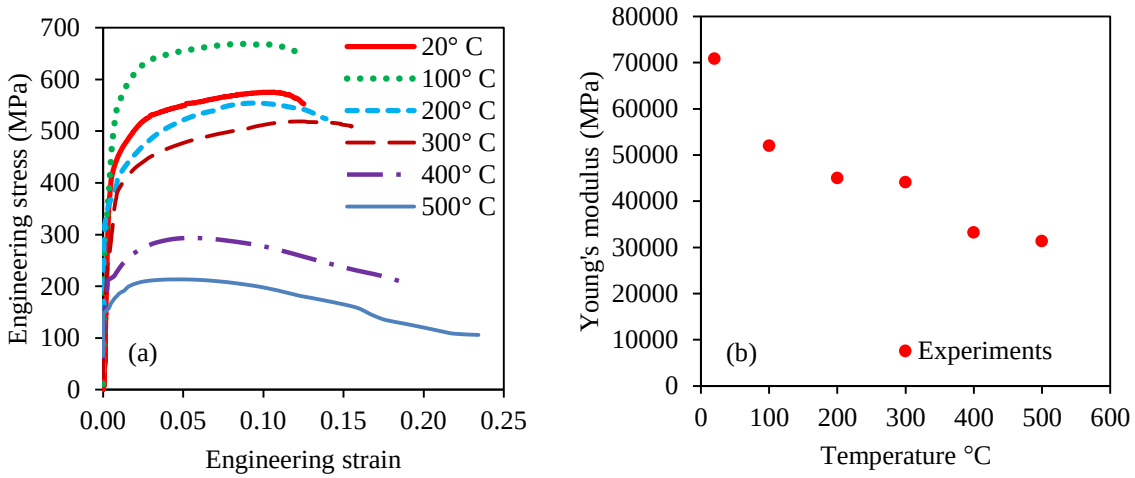

Fig. 2.37 Material (a) stress-strain relationship (b) Young's modulus with varying temperature

The fractured specimens under varying temperature are shown in Fig. 2.38. All the specimens experienced a mixed brittle and ductile failure mode up a temperature range 300 °C. A further increase in temperature resulted in a ductile fracture mechanism.

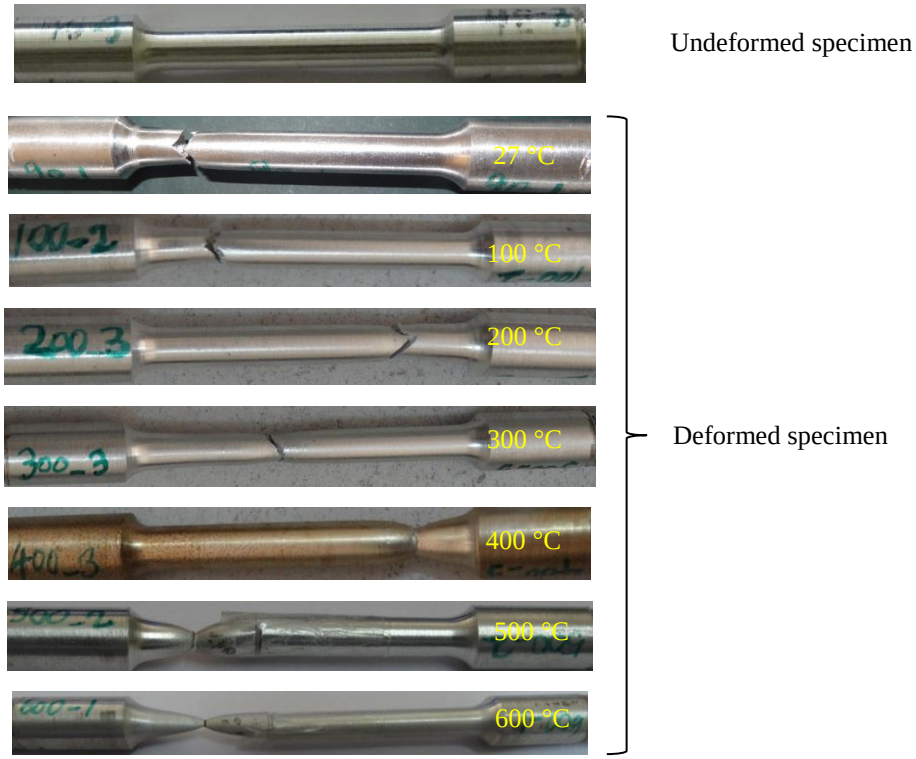

Fig. 2.38 Fractured specimens at different temperature

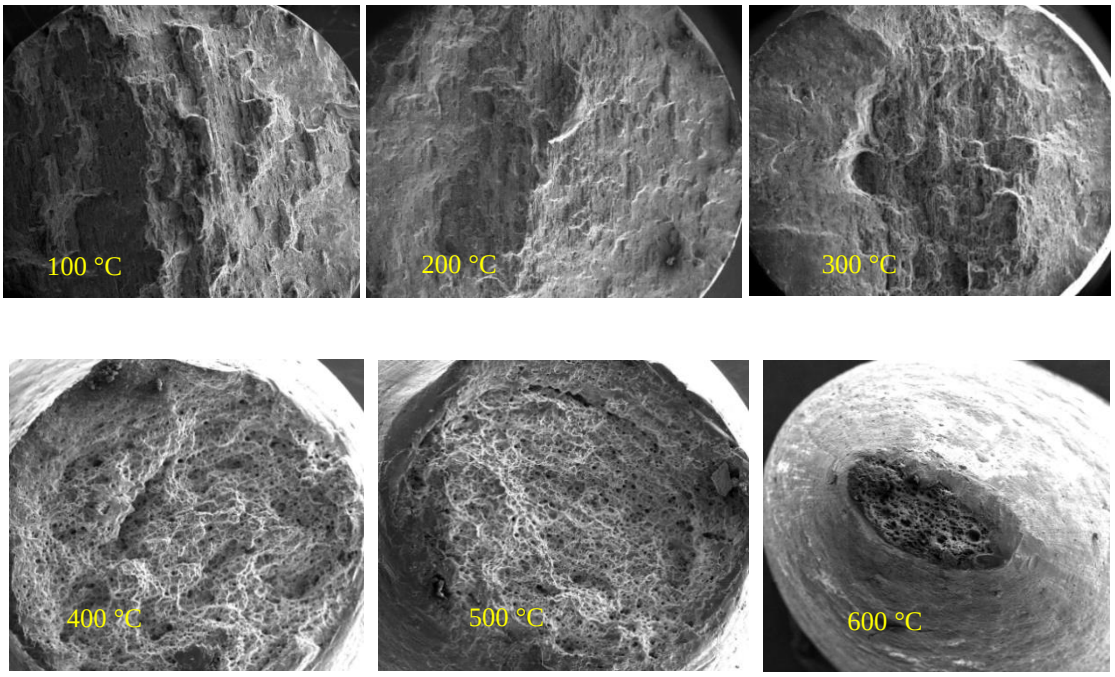

Fig. 2.39 Fractured surfaces of specimens at 50x magnification with varying temperature

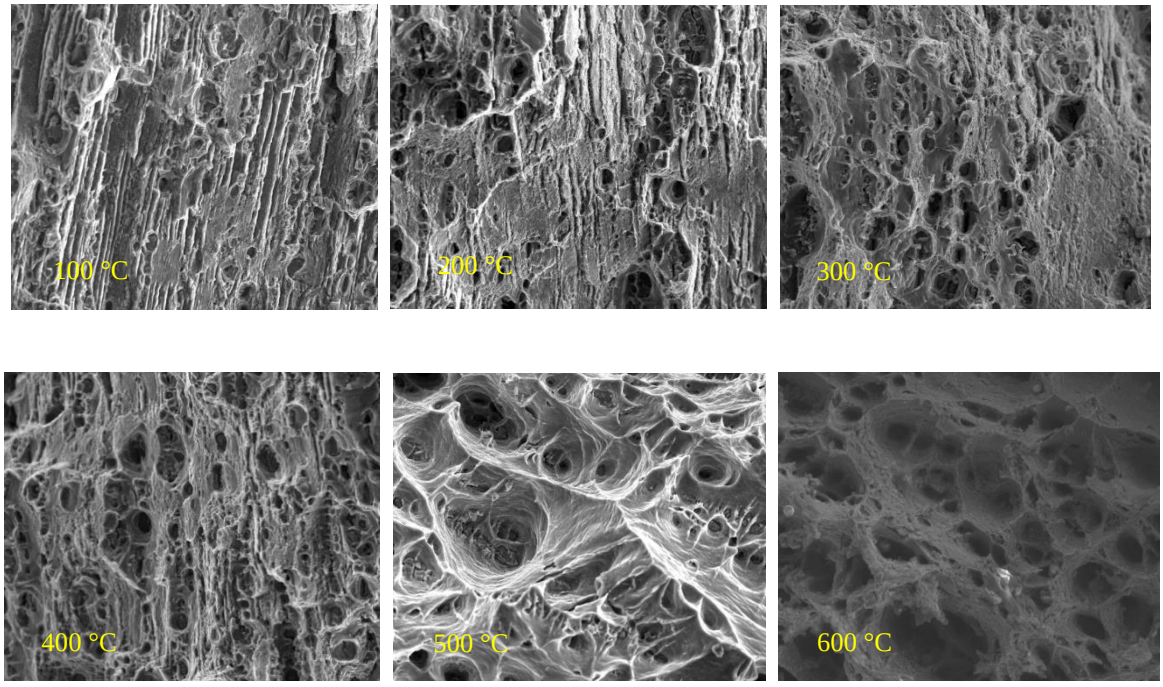

Fig. 2.40 Fractured surfaces of specimen at 500x magnification

The plastic strain and hydrostatic stresses developed at high temperature enabled the voids to grow and subsequently coalesce. The growth of voids was responsible for reduced

strength and the coalescing of voids was responsible for the increased ductility. The surface of the fractured specimens was analyzed using Scanning Electron Microscope (SEM) to identify the magnified surface and record the diameter of the fractured specimens, Fig. 2.39. The microstructure of the fractured surface was also studied by SEM to identify its texture, grain shape and particle distribution, Fig. 2.40.

2.8 CALIBRATION OF 7075-T651 ALUMINIUM

The 7075-T651 aluminum alloy has been characterized for obtaining all the Johnson-Cook material parameters. The calibration of the material parameters of the Johnson-Cook constitutive model has been carried out by using the curve fitting through least square method. The elastic constants *E* and υ at different material orientations were obtained by testing the flat specimens at low strain rate. The yield strength, *A*, used in the first bracket of the JC flow stress [Eqn. 5] has been obtained from the engineering stress-strain curves pertaining to the specimens extracted 0°, 45° and 90° orientation. Knowing the static yield stress, *A*, the hardening parameters *B* and *n* employed in the first bracket of the JC flow stress were obtained by fitting the expression, $B(\bar{\varepsilon}^{pl})^{n}$, with the experimentally measured true stress-strain curve, see Fig. 2.41(a). The stress-triaxiality parameters, D_1, D_2 and D_3 employed in the equivalent failure strain expression of the JC model [Eqn. 7] have been obtained by fitting the expression, $\left[D_1 + D_2 \exp\left(D_3 \frac{\sigma_m}{\bar{\sigma}}\right)\right]$, with the observed true failure strain under varying stress triaxiality i.e., the fracture strain corresponding to the specimens of varying notch radii, see Fig. 2.41(b). The true fracture strain of the material was obtained with the help of original and fractured diameter of the specimens. An exponential curve has been fitted with experimentally obtained data points using the software Origin Pro.

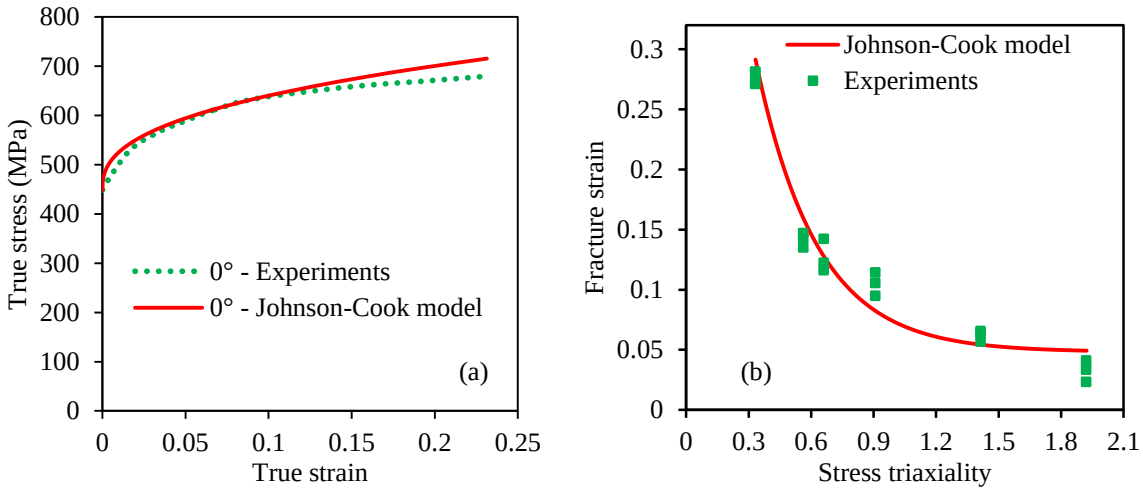

Fig. 2.41 Calibration of the Johnson-Cook model using (a) true stress-strain relation (b) fracture strain as a function of stress triaxiality

The strain rate sensitivity parameter *C* employed in the second bracket of the JC flow stress model has been obtained by fitting the expression, $\left[1 + C\ln\left(\frac{\dot{\bar{\varepsilon}}^{pl}}{\dot{\varepsilon}_0}\right)\right]$, with the observed yield strength corresponding varying strain rate, see Fig. 2.42(a). A linear curve has been fitted with the experimental data points as per the requirement of the model.

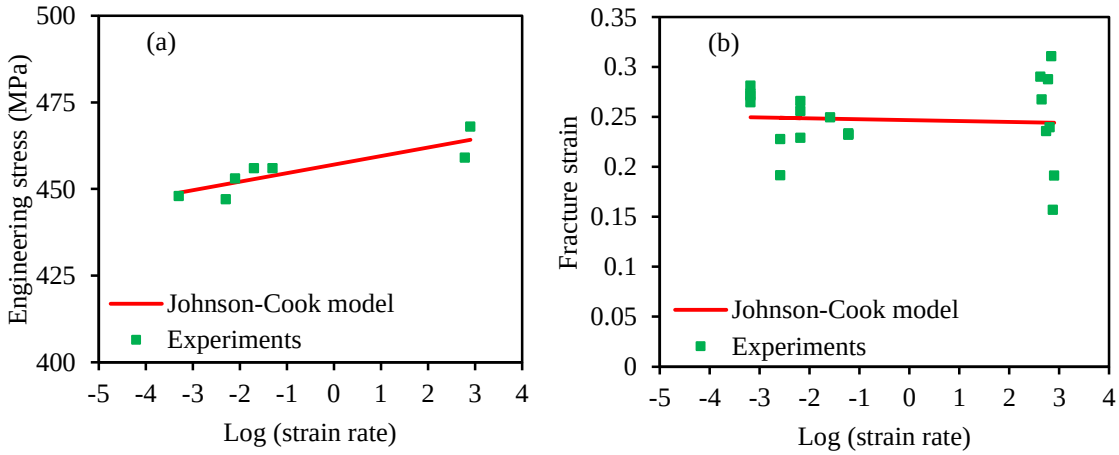

Fig. 2.42 Calibration of the Johnson-Cook model using (a) engineering stress and (b) fracture strain as a function of strain rate

The strain rate dependent damage parameter D_4 has been obtained by fitting the expression, $\left[1 + D_4 \ln\left(\frac{\dot{\bar{\varepsilon}}^{pl}}{\dot{\varepsilon}_0}\right)\right]$, with the observed true fracture strain corresponding to varying strain rate, see Fig. 2.42(b). A linear trend line has been fitted with the experimental data points.

The thermal sensitivity parameter m employed in the third bracket of the JC flow stress has been obtained by fitting the expression, $\left[1 - \hat{T}^m\right]$, with the observed yield strength under varying temperature, see Fig. 2.43(a). A nonlinear curve has been fitted as per the requirement of the model. A prerequisite stress of 534 MPa, corresponding to the 100 °C temperature was considered in order to get the best fit.

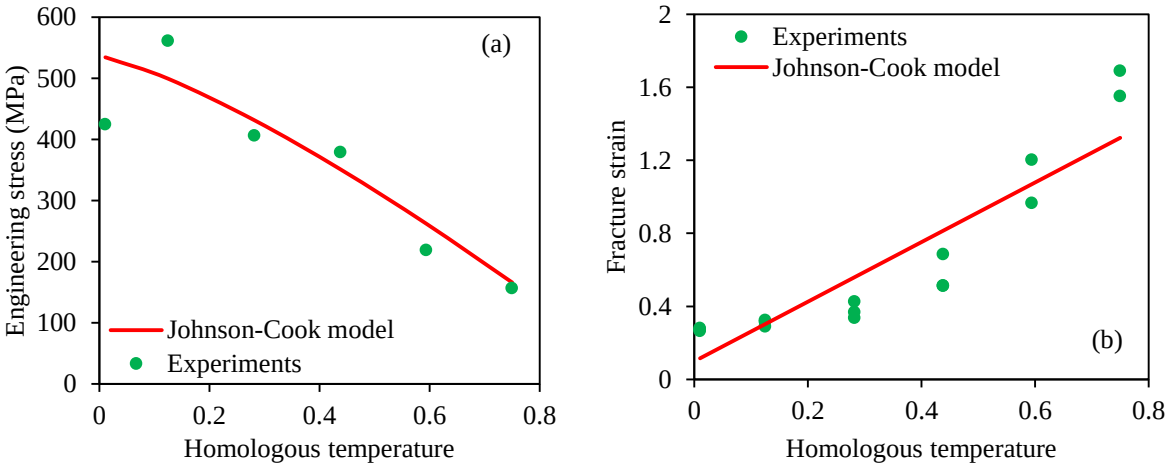

Fig. 2.43 Calibration of the Johnson-Cook model using (a) engineering stress and (b) fracture strain as a function of temperature

The temperature dependent fracture strain parameter D_5 has been obtained by fitting the corresponding expression, $\left[1 + D_5 \hat{T}\right]$, with the observed failure strain at varying temperature, Fig. 2.43(b). The calibrated material parameters of JC model for 7075-T651 aluminium alloy are presented in Table 2.12.

Table 2.12 Material parameters for the 7075-T651 aluminium

Description	Notations	Numerical values		
		0° Direction	45° Direction	90° Direction
Yield stress constant	A (N/m^2)	448.454 x 10^6	420.867 x 10^6	449.525 x 10^6
Strain hardening constant	B (N/m^2)	475.808 x 10^6	273.637 x 10^6	488.107 x 10^6
	n	0.3948	0.2994	0.3498
		X Direction	Y Direction	Z Direction
Young's Modulus	E (N/m^2)	69682 x 10^9	50472 x 10^9	61023 x 10^9
Shear Modulus	G (N/m^2)	25022 x 10^9	18832 x 10^9	22940 x 10^9
Poisson's ratio	υ	0.39	0.34	0.33
Density	ρ (Kg/m^3)		2710	
Viscous effect	C	0.0012	-	-
Thermal softening constant	m	1.29	-	-
Fracture strain constant	D_1	-0.428	-	-
	D_2	0.7566	-	-
	D_3	-3.4078	-	-
	D_4	-0.003	-	-
	D_5	24.93	-	-
Reference strain rate	$\dot{\varepsilon}_0$		0.0001 s^{-1}	
Melting temperature	θ_{melt} (K)		893	
Transition temperature	$\theta_{transition}$ (K)		293	

2.9 FLOW AND FRACTURE BEHAVIOUR OF 7.62 AND 12.7 API PROJECTILES

The characterization of Armour Piercing Incendiary (API) projectile material has also been carried out under varying stress triaxiality, strain rate and temperature. The effect of stress triaxiality was studied by performing tension tests on notched cylindrical specimens of initial notch radius 0.4, 0.8, 2 and 4 mm. The strain rate sensitivity of the material was studied by performing compression tests on tablet specimens (5 mm diameter and equivalent height) using split Hopkinson pressure bar apparatus at strain rate 2799 - 5333 s^{-1}. The temperature sensitivity of the material was studied by performing the tension tests on miniature specimens in a temperature range 27 to 950 °C. All the parameters of Johnson-Cook flow and fracture model were calibrated through curve fitting method.

2.9.1 Preliminary Tests

The 7.62 API projectile a common threat to humans is fired through standard rifles or bipod mounted machine guns, Fig. 2.44.

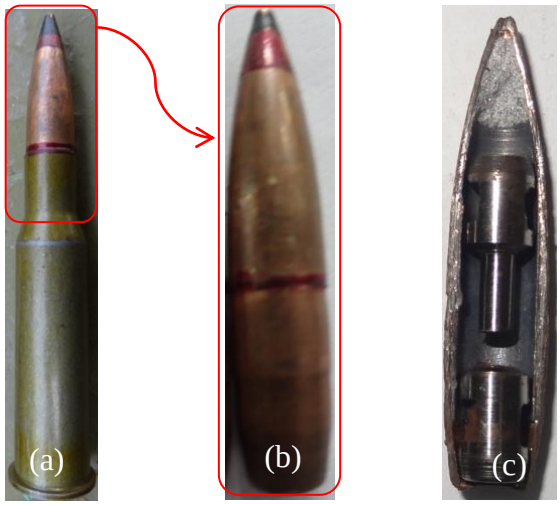

Fig. 2.44 7.62 mm API ammunition (a) projectile with shell (b) steel core with jacket and (c) cross section

The 12.7 API projectile is used against armoured vehicles, sentry bunker and aircrafts. The 12.7 mm threat is fired by carriage mounted air defense gun with quad barrels providing a fairly high rate of firing, Fig. 2.45.

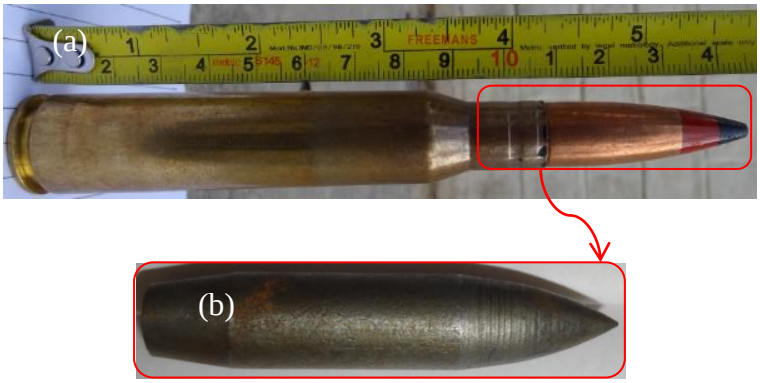

Fig. 2.45 12.7 mm API ammunition (a) projectile with shell and (b) steel core

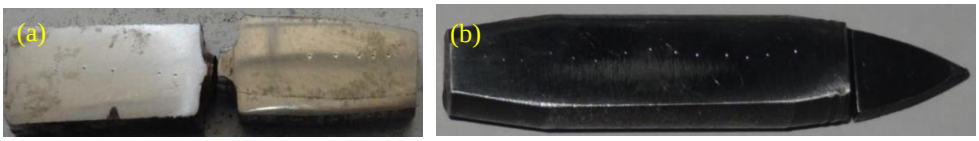

Fig. 2.46 Smoothened surface of (a) 7.62 API and (b) 12.7 API projectiles

Table 2.13 Hardness of 7.62 and 12.7 API projectiles

7.62 API Projectile	12.7 API Projectile
831	812

The hardness test of the material is considered the bench mark of the mechanical properties. Therefore, Vickers hardness (HV) of both 7.62 and 12.7 API projectile steel cores was measured at different locations from nose to tail identified in Figure 2.46. The average value of the hardness of 7.62 and 12.7 API projectiles was found to be 831 and 812 respectively, see Table 2.13. The ultimate strength can be roughly calculated to be three times the Vickers hardness number [Borvik et al. (2009b), Kilic and Ekici (2013) and Kilic et

al. (2014)]. Accordingly the ultimate strength of both of these projectiles can be estimated to be approximately 2300 MPa.

The chemical composition of 7.62 and 12.7 API projectiles has also been studied with the help of EDX spectroscopy and the constituents of both projectile materials have been compared in Table 2.14. It should be noted that the chemical composition of the steel core of both of these projectiles was studied at three different locations and the average numerical values are reported.

Table 2.14 Chemical composition of 7.62 and 12.7 API projectiles

Elements	7.62 API projectile (%)	12.7 API projectile (%)
Fe	84.06	84.49
C	12.27	11.74
Mn	0.63	0.65
Si	0.69	0.67
Cu	0.49	0.41
Cr	0.42	0.38
K	0.30	0.23
S	0.13	0.27
Ni	0.72	0.28
P	0.05	0.35
Al	0.26	0.54

The shank length of 7.62 and 12.7 API projectiles are 20.7 and 24.4 mm, respectively. The size of both of these projectiles was very small and hence it was very difficult to machine them to standard specimen. The machining of the projectiles was also restricted by the ogival curvature of the nose. These limitations led to the preparation of the miniature specimens from the shank (cylindrical region of core) of the hardened steel core of 7.62 and 12.7 API projectiles, see Fig. 2.47(a) and (b) respectively. These miniature specimens were tested under tension on Tinius Olsen H75KS machine at a cross head speed of 0.1

mm/minute with the help of a special dog-bone arrangement prepared from hardened steel, see Fig 2.48(a) and (b) respectively. Three repetitions were performed for 7.62 API projectiles and 4 repetitions for 12.7 API projectile. The average stress-strain relationship of 7.62 and 12.7 API projectiles is shown in Fig. 2.49. The specimens were found to undergo insignificant plastic deformation and experienced sudden failure at the ultimate stress. The material failed within the elastic limit and did not show strain hardening. The ultimate strength of both the projectiles was found to be approximately 2300 MPa.

Fig. 2.47 Steel core and smooth cylindrical specimens of (a) 7.62 API and (b) 12.7 API Projectile

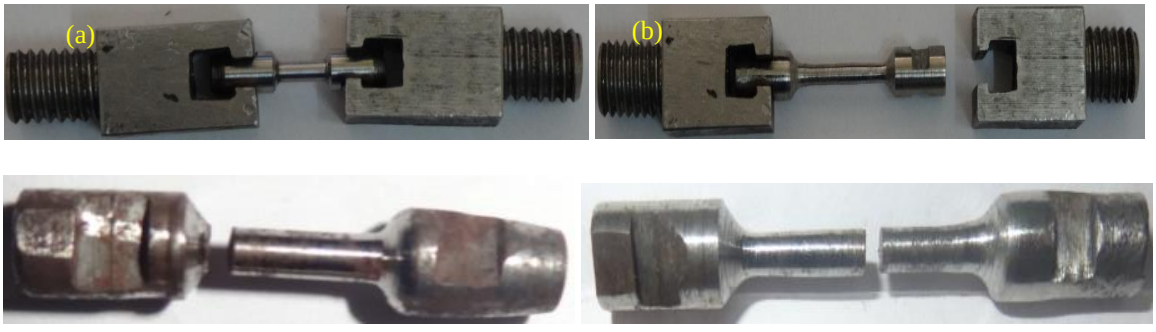

Fig. 2.48 Dog bone arrangement and the tested specimens of (a) 7.62 API and (b) 12.7 API projectiles

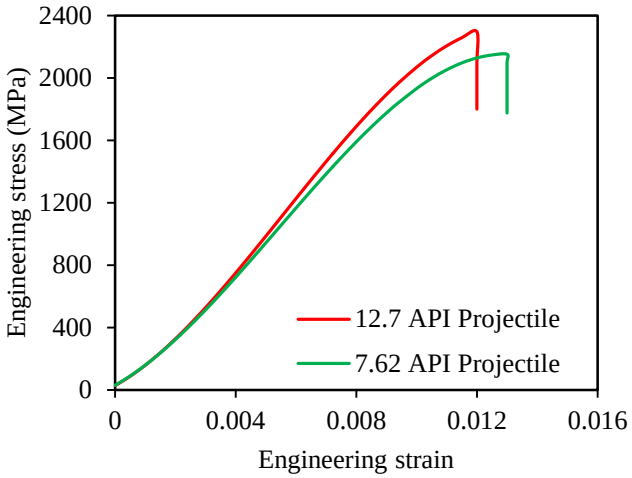

Fig. 2.49 Stress-strain response of 7.62 and 12.7 API projectiles

The results of the material characterization of 7.62 and 12.7 API projectiles with respect to hardness, chemical composition and stress-strain relations led to the conclusion that the material behaviour of both of these projectiles is almost identical. Consequently, further material tests have been performed only on the 12.7 API projectiles and the material parameters for both of these projectiles have been considered identical.

2.9.2 Effect of Stress Triaxilality

The initial stress triaxiality in the cylindrical specimens was introduced with the help of an artificial notch produced in the smooth cylindrical specimen. The stress triaxiality in the specimen was varied by varying the curvature radius of the notch as 0.4, 0.8, and 2.0 mm while the gauge diameter of the notch was kept constant, 2.5 mm, see Fig. 2.50(a)–(c). These specimens were tested on Tinius Olsen H75KS UTM machine at a constant strain-rate of 1 x 10^{-4} s^{-1} and the corresponding cross head speed of 0.1 mm/min. The stress-strain curves obtained at different values of stress triaxility are shown in Fig. 2.51. The fracture strain of the material was found to be almost constant (0.011 - 0.0125). Thus the influence of the

stress triaxiality was found to be insignificant on the material behaviour. This leads to the conclusion that the ductility of the material has not been affected by varying stress triaxiality.

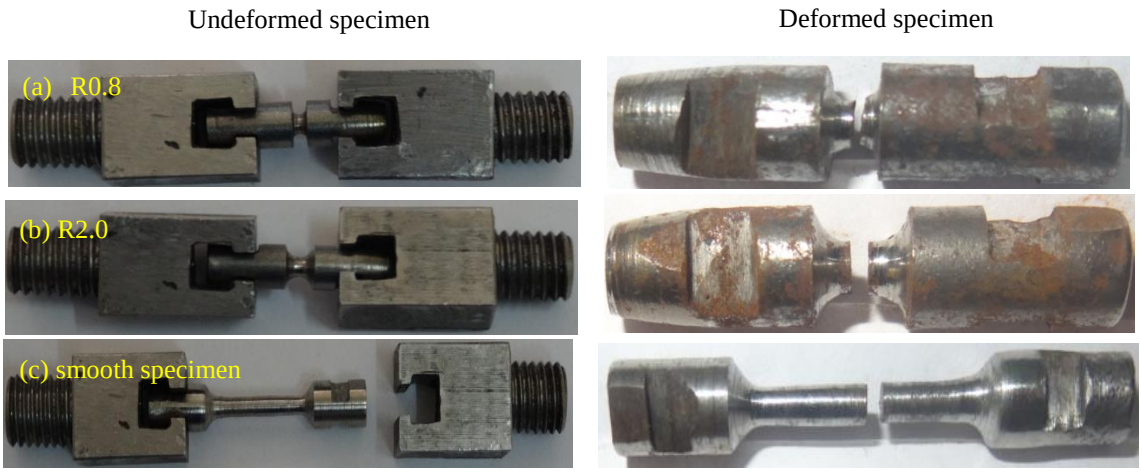

Fig. 2.50 Smooth and notched specimens of deformed and undeformed surfaces

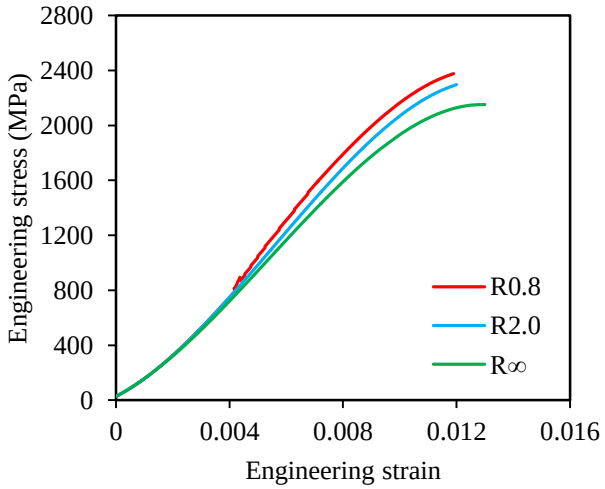

Fig. 2.51 Stress-strain response of specimens with varying notch radii

2.9.3 Effect of Strain Rate

The cylindrical tablet specimens of 5 mm diameter and equivalent height were tested under compression on Split-Hopkinson Pressure Bar at strain rate 2799 - 5333 s^{-1}. The un-deformed and deformed tablet specimens are shown in Fig. 2.52(a) and (b) respectively.

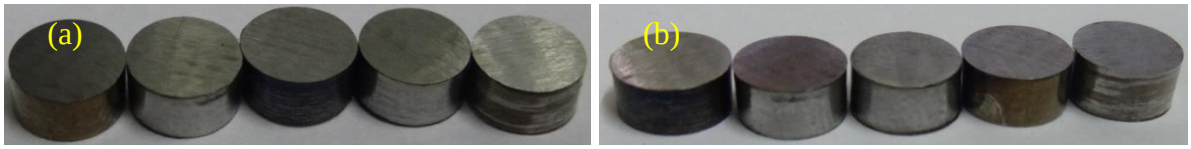

Fig. 2.52 Compression specimen of (a) undeformed and (b) deformed surfaces at high strain rate

The true stress-strain relationship obtained through the tension tests performed on cylindrical specimens at strain rate 6 x 10^{-4} s^{-1} is shown in Fig. 2.53(a). On the other hand, the true stress-strain relationship obtained through the compression tests performed on tablet specimens at 2799 - 5333 s^{-1} strain rate is shown in Fig. 2.53(b). As such no influence of strain rate has been observed on the material behaviour of the projectile. The ductility of the material at low as well as high strain rate was found to be significantly low. The stress-strain response of compression tests on cylindrical specimen exhibited serrated or jerky flow at high strain rate due to Portevin-Le Chatelier effect.

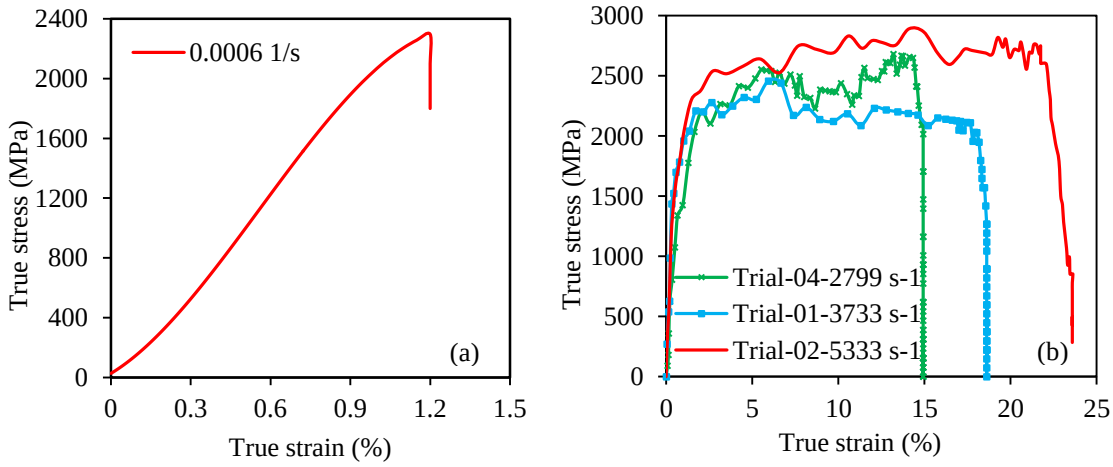

Fig. 2.53 Stress-strain response at (a) low strain rate test under tension and (b) high strain rate test under compression

2.9.4 Effect of Temperature

The specimens for temperature tests had gauge diameter 3 mm and gauge length 10 mm, see Fig. 2.54(a). The testing was performed on servo-hydraulic UTM at a strain rate of 6 x 10^{-4} s^{-1}. A portable furnace shown in Fig. 2.11 was employed for heating the specimen to the required temperature. The temperature of the furnace was controlled by a micro-temperature controller. The furnace had a hollow cylindrical shape, open from top and bottom for inserting the specimen. The specimen was held at the top and the bottom jaws of the universal testing machine while the furnace was placed on a steel platform. The opening of the furnace at the top and bottom were closed by glass wool in order to control the temperature dissipation. The specimen was heated to the desired temperature at a rate of 0.167 °C/sec. The testing temperature was maintained for half an hour in order to get the specimen heated uniformly before the application of mechanical load. The inside temperature of the furnace has been recorded using the K-Type thermocouples held near the center of specimen. The elongation of the specimen was measured by two LVDTs (Linear Variable Displacement Transducers). The tension tests were performed at 27°C, 400°C, 520°C, 600°C, 700°C, and 950°C. The fractured surface of the specimen at varying temperatures is shown in Fig. 2.54(b).

Fig. 2.54 Projectile specimens of (a) undeformed and (b) deformed surfaces at varying temperature

The flow stress of the projectile material was found to be significantly affected due to the varying temperature, Fig. 2.55. Initially the flow stress decreased slightly when the temperature was increased to 400°C. A further increase in temperature resulted in the decrease in ultimate stress and an increase in the fracture strain. At and above 600°C temperature, the ultimate stress abruptly reduced.

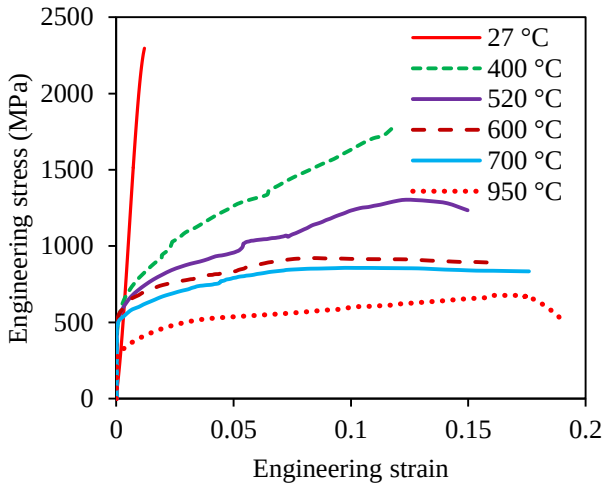

Fig. 2.55 Stress-strain relationship of projectile as a function of temperature

2.10 CALIBRATION OF API PROJECTILE

The API projectile material has been characterized for obtaining all the Johnson-Cook material parameters. The calibration of the material parameters of the Johnson-Cook constitutive model was carried out by using the curve fitting through least square method. The yield strength, *A*, in the first bracket of the JC flow stress [Eqn. 5] was obtained from the engineering stress-strain curves. Knowing the static yield stress, *A*, the hardening parameters *B* and *n* in the first bracket of the JC flow stress were obtained by fitting the expression, $B(\bar{\varepsilon}^{pl})^{n}$, with the experimentally measured true stress-strain curve, see Fig. 2.56(a). The stress triaxiality parameters, D_1, D_2 and D_3 in the equivalent failure strain expression of the

JC model [Eqn. 7] were obtained by fitting the expression, $\left[D_1 + D_2 \exp\left(D_3 \frac{\sigma_m}{\bar{\sigma}}\right)\right]$, with the observed true failure strain under varying stress triaxiality, see Fig. 2.56(b). The true fracture strain of the material was obtained with the help of original and fractured diameter of the specimens using the expression; $2\ln(\frac{d_0}{d_f})$. An exponential curve has been fitted with experimentally obtained data points using the software Origin Pro.

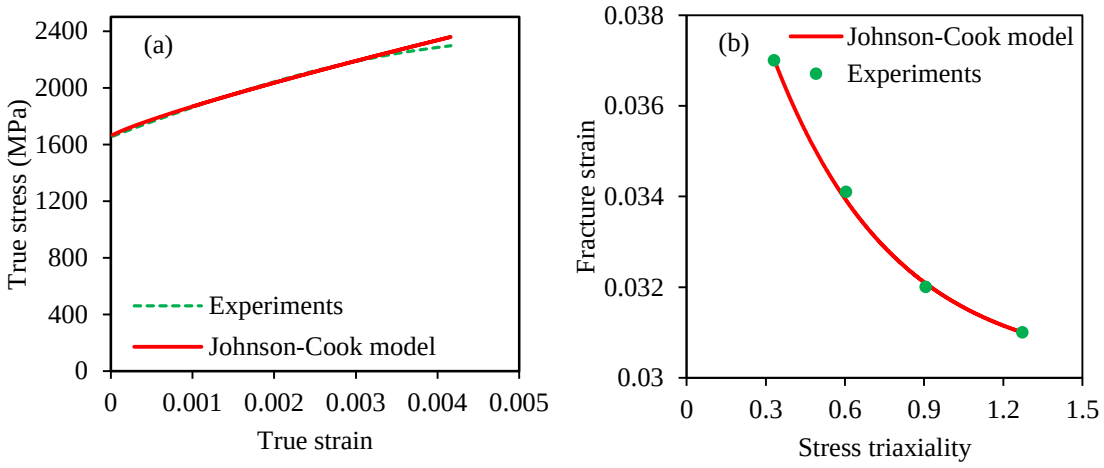

Fig. 2.56 Calibration of the Johnson-Cook model using (a) true stress-strain relation (b) fracture strain as a function of stress triaxiality

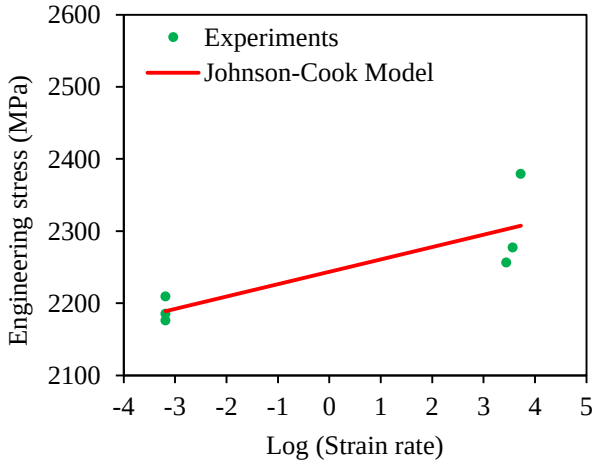

Fig. 2.57 Calibration of the Johnson-Cook model using engineering stress as a function of strain rate

The strain rate sensitivity parameter C in the second bracket of the JC flow stress was obtained by fitting the expression, $\left[1 + C\ln\left(\frac{\dot{\varepsilon}^{pl}}{\dot{\varepsilon}_0}\right)\right]$, with the observed yield strength under varying strain rate, see Fig. 2.57. A linear curve was fitted with the experimental data points as per the requirement of the model. The strain rate dependent fracture strain parameter D_4 was assumed to be zero for the projectile material due to the limitation of the experimental facility and the shortage of the material specimens. This assumption is justified due to the fact that the material is insensitive to strain rate.

The thermal sensitivity parameter m in the third bracket of the JC flow stress was obtained by fitting the expression, $\left[1 - \hat{T}^m\right]$, with the observed yield strength under varying temperature, see Fig. 2.58(a). A nonlinear curve was fitted as per the requirement of model.

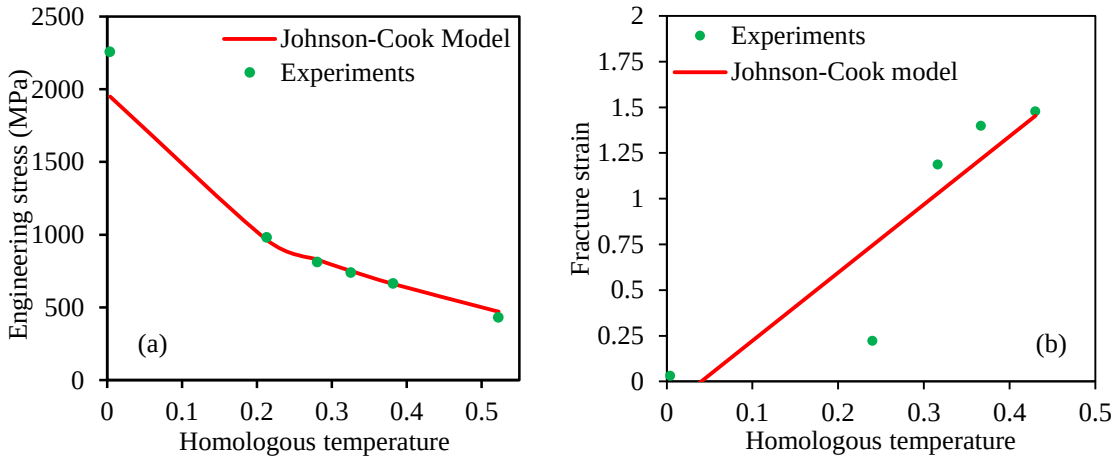

Fig. 2.58 Calibration of the Johnson-Cook model using (a) engineering stress and (b) fracture strain as a function of homologous temperature

The temperature dependent fracture strain parameter D_5 was obtained by fitting the corresponding expression, $\left[1 + D_5\hat{T}\right]$, with the observed failure strain at varying temperature, see Fig. 2.58(b). In this case also a linear curve was fitted with the experimentally obtained true fracture strain at varying temperatures. The material parameters thus obtained are

presented in the Table 2.15, and these were employed to model the material behavior of 7.62 and 12.7 API projectiles in the numerical simulations discussed in the subsequent chapters.

Table 2.15 Material parameters of 7.62 and 12.7 API projectiles

Description	Notation	Numerical value
Modulus of elasticity	E (N/m^2)	200 x 10^9
Poisson's ratio	v	0.3
Density	ρ (Kg/m^3)	7850
Yield stress constant	A (N/m^2)	1657.71 x 10^6
Strain hardening constant	B (N/m^2)	20855.6 x 10^6
	n	0.651
Viscous effect	C	0.0076
Thermal sensitivity	m	0.35
Reference strain rate	$\dot{\varepsilon}_0$	0.0005
Melting temperature	θ_{melt} (K)	1800
Transition temperature	$\theta_{transition}$ (K)	293
Fracture strain constant	D_1	0.0301
	D_2	0.0142
	D_3	-2.192
	D_4	0.0
	D_5	0.35

2.11 CONCLUSIONS

The mild steel, Armox 500T steel, 7075-T651 aluminium and API projectile materials were characterized under varying strain rate, stress triaxiality and temperature in order to calibrate the parameters of Johnson-Cook elasto-viscoplastic material model and eventually to simulate the material behaviour of the projectile and target for the numerical simulations of ballistic evaluation. The uniaxial tension tests were carried out at 0°, 45° and 90° orientations of the rolling direction of the material in order to identify the possible anisotropy in mild steel, Armox 500T and 7075-T651 aluminium plates. The stress-strain relationship of mild steel and Armox 500T showed the directional independencies while the

7075-T651 aluminium was found to possess anisotropy. The effect of varying stress triaxiality of material was studied by carrying out the uniaxial tension test on notched cylindrical specimens. The uniaxial tension tests were also conducted on conventional universal testing machine and split Hopkinson pressure bar for studying the influence of strain rate. Finally the tensions tests were conducted to identify the thermal sensitivity of the material. The hardness, chemical composition, elastic and plastic flow properties of 7.62 and 12.7 API projectiles were compared and found to be almost identical. Therefore, the material parameters for both of these projectiles were assumed to be same. The material parameters of Johnson-Cook (1983, 1985) flow stress and fracture models were finally calibrated through curve fitting method for mild steel, Armox 500T steel, 7075-T651 aluminium and API projectile materials.

CHAPTER 3

Finite Element Modelling

3.1 GENERAL

The finite element method is considered to be a powerful tool in computational mechanics and it has been applied to the field of solid mechanics, fluid mechanics, heat transfer and vibrations. The considerable attention on FEM received over the last decade mainly attributed to the efficient treatment of large-scale engineering problems. The finite element packages such as ABAQUS, Ansys-Autodyn, LS-Dyna and NASTRAN have made finite element analysis easier and very efficient into solving complex engineering problems.

The present study addresses a detailed experimental and finite element investigation of the ballistic performance of armour and aerospace materials under varying conditions of impact loading. The numerical simulation of the problem has been carried out using the commercial finite element code ABAQUS capable to simulate the complex problems of perforation mechanics [Borvik et al. (1999, 2001), Iqbal et al. (2013) and Teng et al. (2008)] as a result of its incredible material and elemental library. The present chapter discusses the finite element modelling of the problem as well as validation of the calibrated Johnson-Cook model. The geometry of the projectile and target has been modelled and their discretization has been carried out using the pre-processing module of the code, ABAQUS/CAE. The mesh convergence has been studied by varying the number of elements at the thickness of the target keeping the aspect ratio unity. The calibrated material parameters of the JC model discussed in the previous chapter were also validated by simulating the high strain rate material tests performed on Split Hopkinson Pressure Bar (SHPB) apparatus. The uniaxial tests performed under tension and compression were simulated using ABAQUS/Explicit algorithm and the results thus obtained in the form of stress-strain relations were compared with their actual correspondences.

3.2 FINITE ELEMENT MODELLING OF MILD STEEL TARGET AND 7.62 API PROJECTILE

The mild steel target of span 200 mm x 200 mm and thicknesses 4.7, 6.0, 10, 12, 16, 20 and 25 mm were modelled as three dimensional deformable continuum using ABAQUS/CAE. The geometry of the 7.62 API projectile was also created in accordance with its actual dimensions as a three dimensional deformable body using ABAQUS/CAE. The shank diameter, shank length, total length and the length of ogival-nose of the projectile core were 6.06, 20.75, 28.4, and 7.65 mm respectively. Only the steel core of the projectile has been modelled for all the finite element simulations assuming that the brass jacket has stripped off and had no influence on the perforation process. The effect of jacket and lead cap on perforation resistance during impact was studied by Borvik et al. (2009b). They removed both jacket and cap from APM8 bullet for measuring weight and dimension. By removing the jacket and cap, the mass is decreased from 10 grams to 6 grams. It was shown that the ballistic limit velocity decreased only by 3–5% when only hard core was used as projectile. This observation led to the conclusion that modeling only the projectile core will not make significant difference in the ballistic results.

The calibrated JC model of mild steel was employed to assign the flow and fracture behaviour of the target, see Table. 2.3. The material behaviour of the 7.62 API projectile was also modelled using the Johnson-Cook elsto-viscoplastic model and the parameters were considered identical to what have been obtained by Niezgoda and Morka (2009), Table 3.1. It is pertinent to mention that except for the study of mild steel the material parameters of API projectile calibrated in the present study, Table 2.15, have been employed to assign the material behaviour of projectile.

Table 3.1 Material parameters of 7.62 API projectile, Niezgoda and Morka (2009)

Description	Notations	Numerical value
Modulus of elasticity	E (N/m^2)	202 x 10^9
Poisson's ratio	v	0.32
Density	ρ (Kg/m^3)	7850
Yield stress constant	A (N/m^2)	2700 x 10^6
Strain hardening constant	B (N/m^2)	211 x 10^6
	n	0.065
Viscous effect	C	0.005
Thermal softening constant	m	1.17
Reference strain rate	$\dot{\varepsilon}_0$	0.0001 s^{-1}
Melting temperature	θ_{melt} (K)	1800
Transition temperature	$\theta_{transition}$ (K)	293
Fracture strain constant	D_1	0.4
	D_2	0
	D_3	0
	D_4	0
	D_5	0

The target was meshed with eight node linear hexahedral elements with hourglass control. The mesh sensitivity of the target was studied by varying the element size as 0.8, 0.6, 0.2 and 0.1 mm^3 in the impact region corresponding to 15, 20, 60 and 120 elements at the target thickness keeping aspect ratio close to unity, see Fig. 3.1(a). The projectile was impacted normally at incidence velocity 818 m/s on 12 mm thick target and the residual velocity was found to be 669, 663, 658 and 657 m/s respectively. Thus the residual velocity of the projectile found to have converged corresponding to element size 0.2 mm^3 and number of elements 60 at the target thickness, Fig. 3.1(b). The resultant residual velocity corresponding to element size 0.2 mm^3 was also found in agreement to that of its actual value, 661.5 m/s. Hence, the element size in the impact zone of the targets for all the simulations of mild steel was considered to be 0.2 mm^3 and the aspect ratio close to unity.

The typical finite element model of mild steel target and 7.62 API projectile is shown in Fig. 3.2 (a) and (b). Three planar zones were identified in the target based on the size of element, Fig. 3.3. The element size was kept 0.2 mm^3 and 1.0 mm^3 in the central planar zone of size 6.06 mm and (30 – 6.06 =) 23.94 mm. The remaining region of the target was assigned element size varying from 2 to 4 mm^3. The transition regions between these planar zones were meshed with tetrahedral elements in order to maintain the compatibility between the elements, Fig. 3.3. The meshing of the target was considered identical at each angle of obliquity.

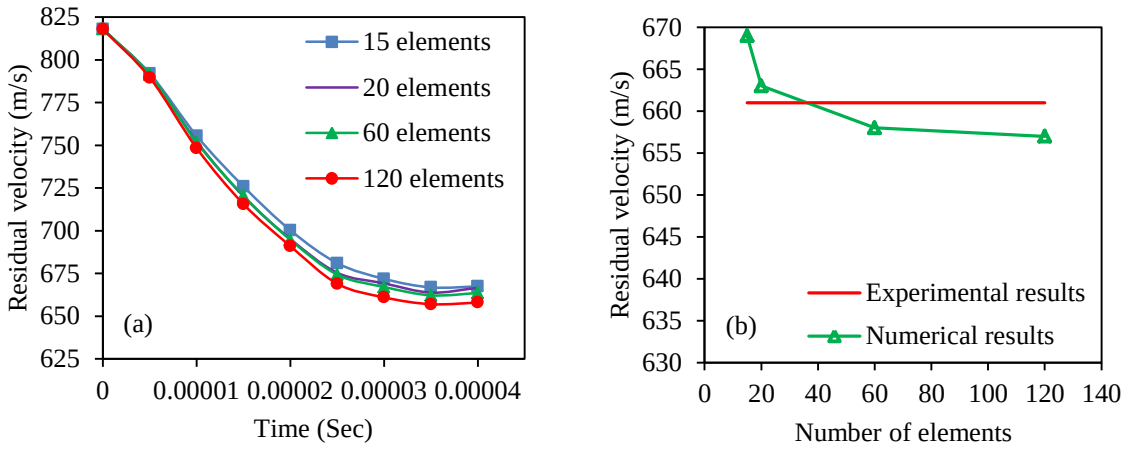

Fig. 3.1 Residual velocity of 7.62 API projectile as a function of (a) time (b) number of elements of mild steel target

The eight node reduce integration hexahedral element of 1 mm^3 was used to discretize the projectile throughout its body. The effect of mesh sensitivity of the projectile has not been addressed in this study. The contact between the projectile and target was modelled by employing the Kinematic contact algorithm, ABAQUS. The projectile was considered as master and the through thickness contact region of the target as node based slave surface. In the normal direction hard contact was defined and in the tangential direction the effect of friction has been assumed to be negligible, Iqbal et al. (2006, 2010a).

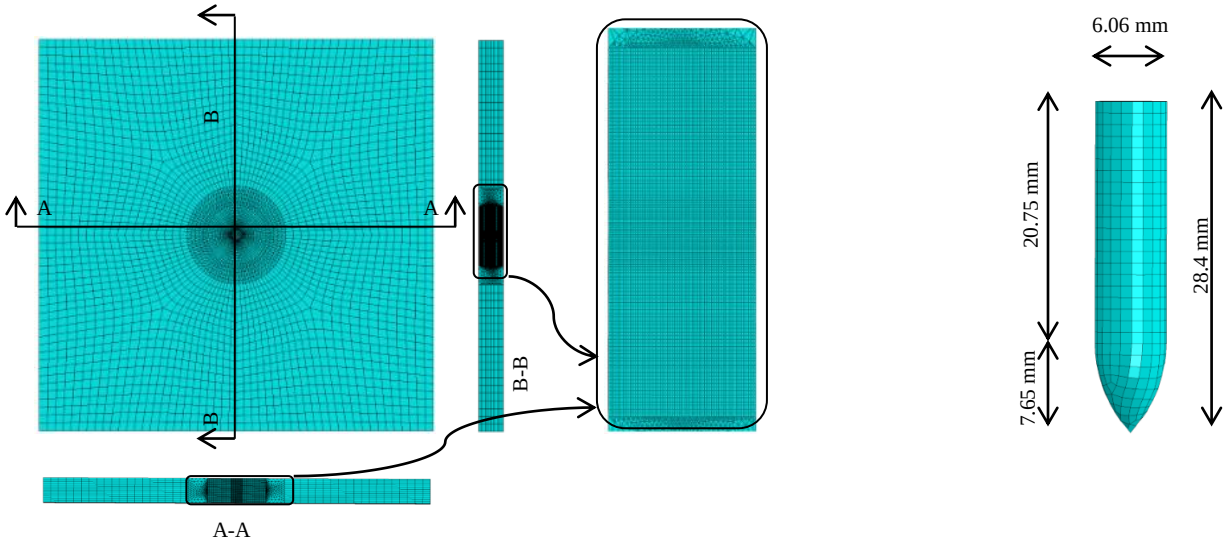

Fig. 3.2 Typical finite element model of (a) mild steel target and (b) 7.62 API projectile

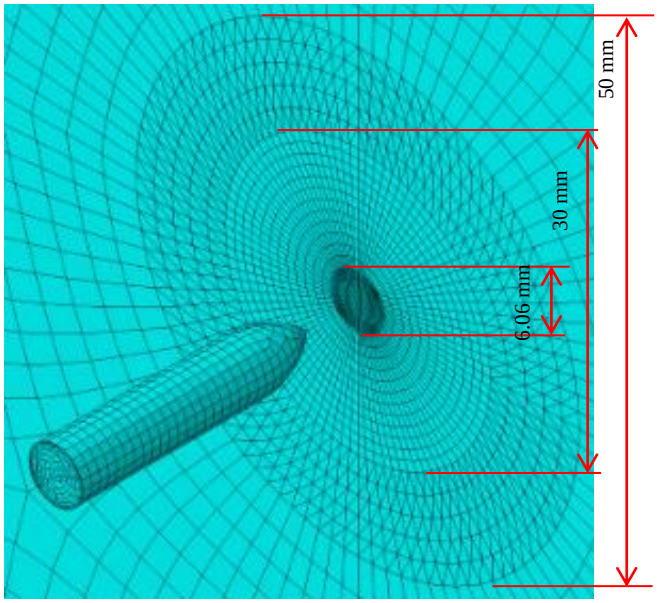

Fig. 3.3 Mesh density zones of the target

The possible effect of friction between the projectile and target was also studied by assuming the coefficient of friction 0 and 0.02 for the normal impact of 12 mm thick target at 818 m/s incidence velocity. The residual velocity of the projectile was found to be 659.4 and 653.8 m/s corresponding to the coefficient of friction 0 and 0.02 respectively. For normal

impact, the contact region of the target was considered equal to that of the diameter of projectile. For oblique impact the exact contact region of the target was not known therefore a slightly larger portion of the target than that of the diameter of the projectile was modeled as node based slave surface.

3.3 VALIDATION OF MILD STEEL PARAMETERS

The calibrated material parameters of the JC model have been validated by simulating the high strain rate material tests performed on Split Hopkinson Pressure Bar (SHPB) apparatus. It should be noted that the material tests on SHPB were carried out both under tension as well as compression. Therefore the finite element simulations for material characterization were also performed under tension as well as compression using ABAQUS/Explicit. The strain rate under compression was varied as 700, 1100, 1400 and 1500 s^{-1}, while under tension as 1450 and 1500 s^{-1}. The axisymmetric model of the compression and tension specimens was developed with respect to their actual geometry, see Fig. 3.4.

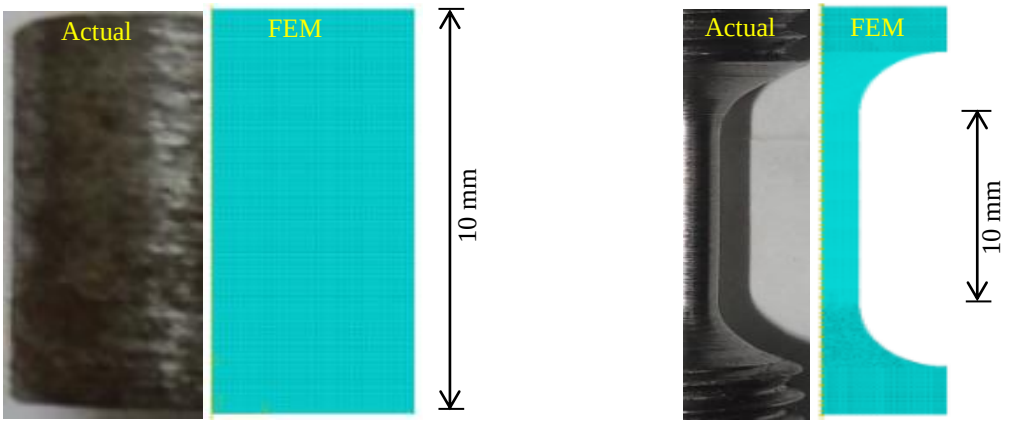

Fig. 3.4 Geometry of the specimens for axisymmetric finite element simulations for (a) compression test (b) tension test

The compression tests have been performed on the specimens prepared in the form of cylinder of diameter 10 mm and length 10 mm, Fig. 3.4(a). The tension tests were performed on the cylindrical specimens of diameter 3 mm and gauge length 10 mm, Fig. 3.4(b). The calibrated JC model was employed to assign the flow and fracture behaviour of the material, see Table. 2.3. Despite the fact that the material under compression did not experience fracture, the fracture model was assigned for the simulations performed under compression as a matter of fact that some minor deformations and material deterioration were noted under these tests. Both tension and compression specimens were considered fixed at one end while the other end was under the application of pressure in the direction opposite to the material and towards the material respectively. The pressure versus time curve was assigned with respect to the corresponding strain rate. The discretization of the geometric model was carried out using four node axisymmetric quadrilateral elements with stiffness hourglass control, and three degrees of freedom at each node.

For the compression tests, the mesh convergence was studied by varying the element size in the specimen as 0.09 mm x 0.09 mm, 0.07 mm x 0.07 mm and 0.05 mm x 0.05 mm, however, the effect of mesh sensitivity was found insignificant in this case. However, keeping in view the accuracy of the numerical simulations and low computational time required for the analysis (approximately 15 minutes) a fine mesh was generated adopting the element size 0.03 mm x 0.03 mm. The size of the element throughout the geometry of the compression test specimen was considered identical (0.03mm x 0.03 mm) giving a total number of 55611 elements.

The mesh convergence was also studied for the simulations performed under tension. The element size was varied as 0.09 mm x 0.09 mm, 0.07 mm x 0.07 mm and 0.05 mm x

0.05 mm. In this case also the mesh size effect was found insignificant due to the small size of elements already chosen. However, the size of element adopted in this case was slightly larger, 0.05 mm x 0.05 mm, than that for compression test simulations due to relatively larger number of elements as well as longer computational time, approximately 105 minutes. The element size throughout the specimen was considered identical (0.05 mm x 0.05 mm) giving a total number of 85032 elements in the whole body of the specimen.

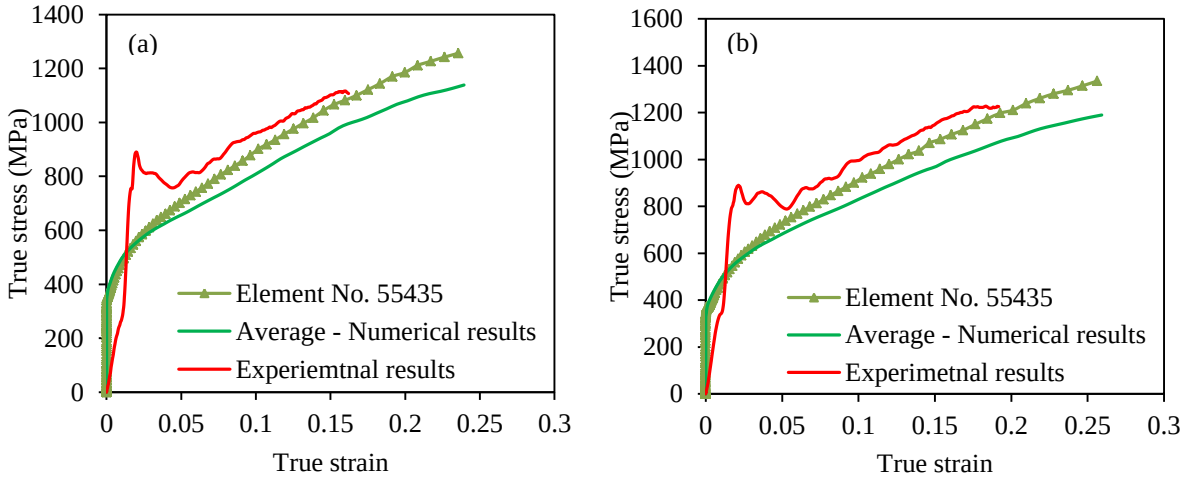

Fig. 3.5 Comparison of experimental and numerical stress-strain relationship under compression at strain rate (a) 1450 s^{-1} (b) 1500 s^{-1}

The true stress-strain relationship obtained through the numerical simulation of the compression tests have been compared with their corresponding experimental results. A close correlation between the experimental and numerical stress-strain relationship has been found at the strain rate 1450 s^{-1} and 1500 s^{-1}, see Figs. 3.5 (a) and (b) respectively. The numerical results shown in the figures have been obtained at the centroid of the specimen. The average results of the five elements selected between top to bottom of the centroidal axis (axis of symmetry) have also been plotted for comparison. The numerical results accurately predicted the pattern of stresses including the ultimate stress. The stress contours for the compression tests have also been plotted in Fig. 3.6. The flow of stress through the specimen thickness

could be seen at various time steps. The maximum compressive stress is developed in the central region of the specimen.

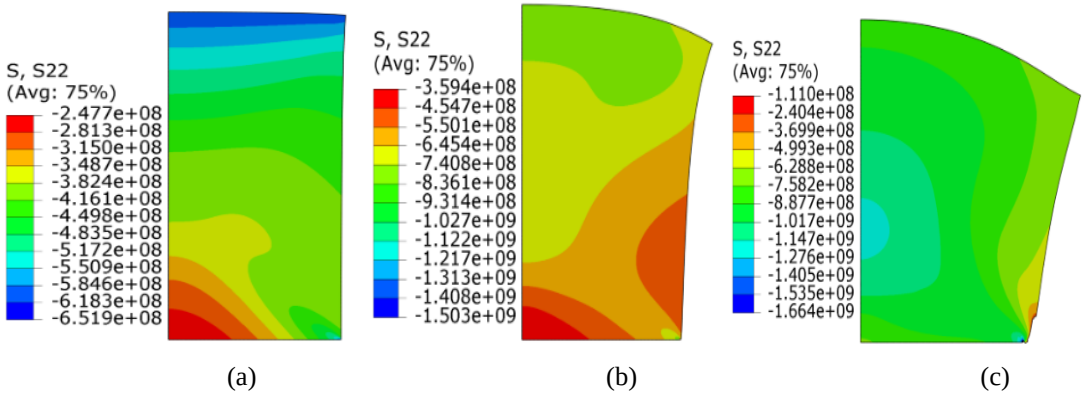

(a) (b) (c)

Fig. 3.6 Stress developed in the direction of loading in compression test simulation at 1500 s^{-1} strain rate at time interval (a) 40 μs (b) 50 μs and (c) 58 μs

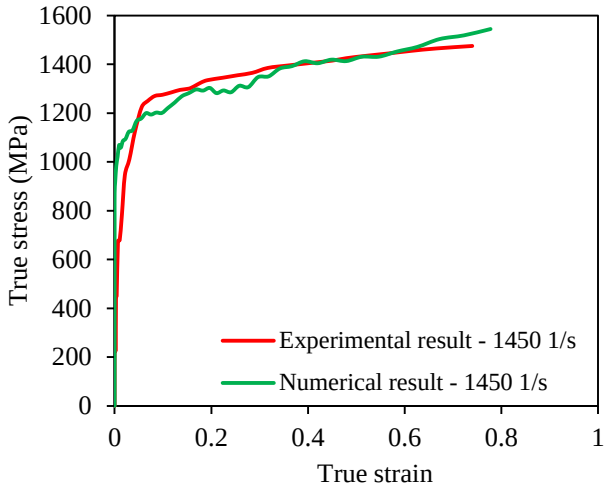

Fig. 3.7 Comparison of experimental and numerical stress-strain relationship for the test performed under tension

The true stress-strain relationship obtained from the simulations performed under tension has been compared with the corresponding actual results at 1450 s^{-1}, see Fig. 3.7. The numerical results accurately predicted the material behaviour under tension. The contours of stresses have also been plotted in the tension specimen at the same strain rate, see Fig. 3.8. The flow of stress through the specimen could be seen at various time steps before and after

necking process. The stress concentration in the necked region is clearly visible at the onset of fracture. The actual and predicted fractured diameter of the specimen was 2.07 mm and 1.938 mm respectively.

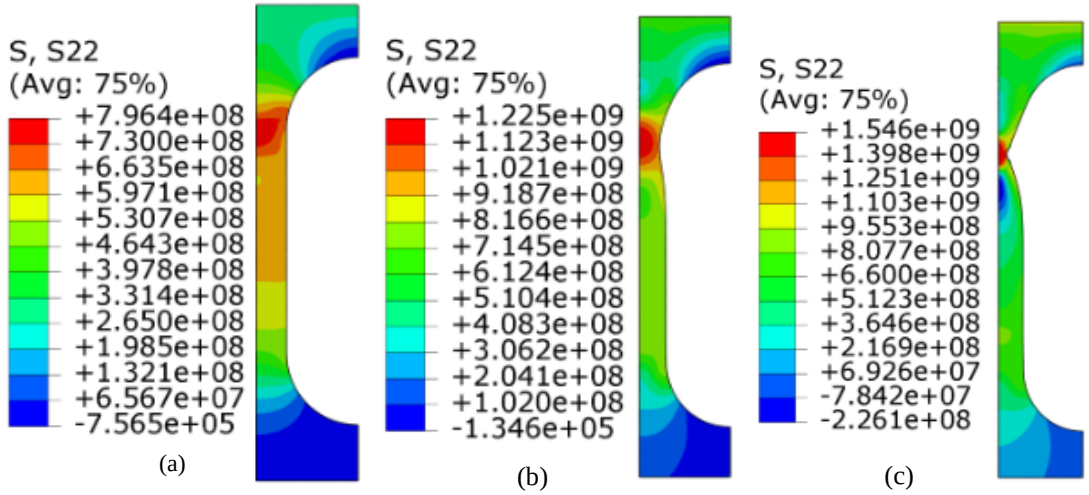

Fig. 3.8 Stresses developed in the direction of loading in tension test simulation performed at 1450 s^{-1} strain rate at time interval (a) 4.4 μs (b) 19.6 μs and (c) 24.8 μs

3.4 FINITE ELEMENT MODELLING OF ARMOX 500T STEEL TARGET, 7.62 API PROJECTILE AND 12.7 API PROJECTILE

3.4.1 Modelling of Target and 7.62 API Projectile

The Armox 500T steel targets of span 200 mm x 200 mm and thicknesses 6, 8 and 10 mm were modelled as three dimensional deformable continuum using ABAQUS/CAE. It should be noted that the actual span of the target during experiments was 500 mm x 500 mm however in order to economize the computational problem a reduced span was modelled. It was observed during ballistic experimentation that the influence of the impact zone does not spread beyond this dimension. The calibrated JC model discussed in chapter 2 was employed to assign the flow and fracture behaviour of the target material, see Table. 2.7. The geometry of 7.62 API projectile was also created in accordance with its actual dimensions as a three

dimensional deformable body using ABAQUS/CAE. The shank diameter, shank length, total length and the length of ogival nose of the projectile core was 6.06, 20.75, 28.4, and 7.65 mm respectively. As discussed above the steel core of the projectile has been modelled for all the finite element simulations assuming that the brass jacket has stripped off and had no influence the perforation process, Borvik et al. (2009b). The flow and fracture behaviour of the 7.62 API projectile was also modelled employing the JC model calibrated in the present study for the material of the projectile, see Table 2.15.

The target was meshed with eight node linear hexahedral elements with hourglass control. The mesh sensitivity was studied for 8 mm thick target by varying the element size as 0.55, 0.45, 0.35, 0.25 and 0.2 mm^3 in the impact zone corresponding to 15, 18, 23, 32 and 40 elements at the thickness keeping aspect ratio close to unity, see Fig. 3.9 (a). The 7.62 API projectile was impacted normally on the target at 835 m/s incidence velocity and the residual velocity was found to be 424, 397, 345, 329 and 328 m/s respectively. Thus, the residual velocity of the projectile was found to have converged corresponding to element size 0.25 mm^3 and number of elements 32 at the target thickness, Fig. 3.9 (b). The computational residual velocity at element size 0.25 mm^3 was also found in agreement to that of its corresponding experimental value, 334 m/s. Hence, the element size in the impact zone of the Armox 500 T steel target was considered to be 0.25 mm^3 and the aspect ratio close to unity for the simulations conducted against 7.62 API projectile. Away from the impact region, however, the size of element was slightly increased keeping the aspect ratio almost unity. The hexahedral elements of 1 mm^3 were employed to discretize the projectile throughout its body. The contact between the projectile and target was modelled by employing the Kinematic contact algorithm available in ABAQUS. A coefficient of friction of 0.02 was

assumed between the projectile and target [Borvik et al. (2002b, 2011)]. The projectile was considered as master and the through thickness contact region of the target as node based slave surface. For normal impact, the contact region of the target was considered equal to that of the diameter of projectile. For oblique impact the exact contact region of the target was not known therefore a slightly larger portion of the target than that of the diameter of the projectile was modeled as node based slave surface. The finite element model for 7.62 API projectile is shown in Fig. 3.10 and for a typical Armox 500T steel target in Fig. 3.11.

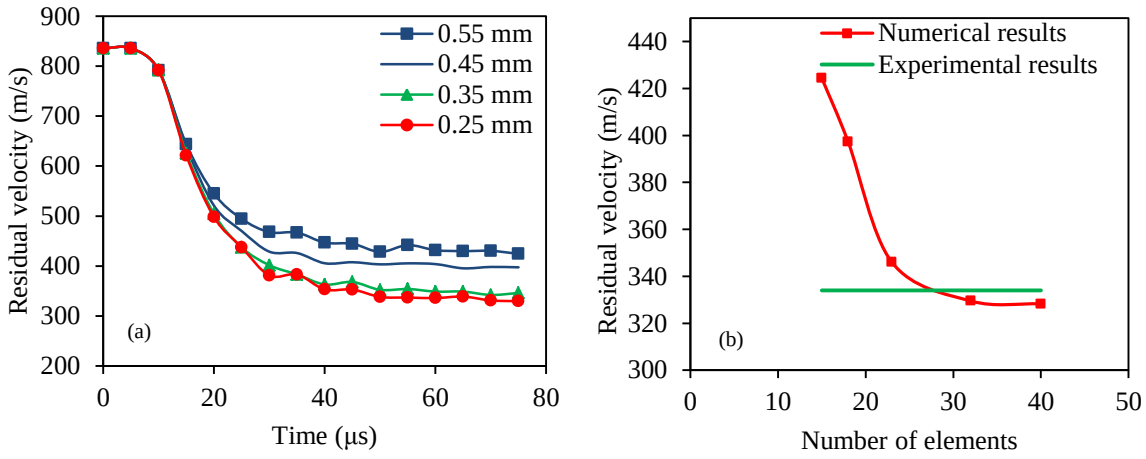

Fig. 3.9 Residual velocity of 7.62 API projectiles as a function of (a) time and (b) number of elements of Armox 500T steel target

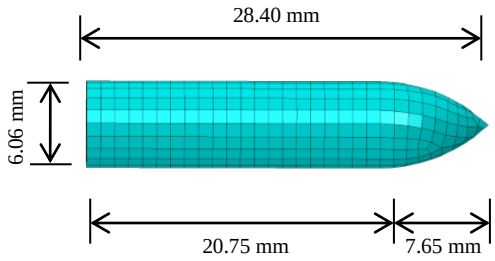

Fig. 3.10 Finite element model of 7.62 API projectile

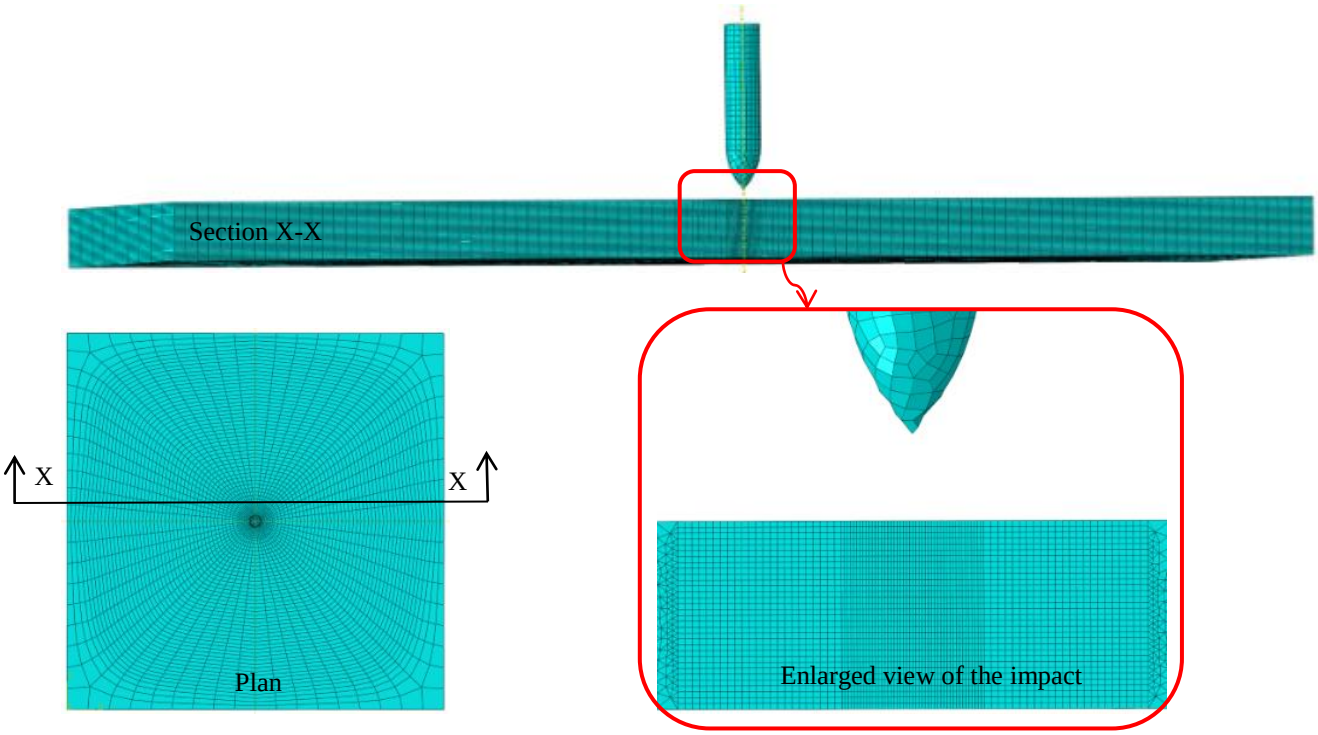

Fig. 3.11 Typical finite element model of Armox 500T steel target for the impact against 7.62 API projectile

3.4.2 Modelling of Target and 12.7 API Projectile

The Armox 500T steel target of thickness 5, 10, 15 and 20 mm was modelled in ABAQUS/CAE as three dimensional deformable continuum. The actual span of the target was 500 mm x 500 mm, however, a reduced span, 200 mm x 200 mm, was modelled in order to economize the computational problem. The size of the reduced span was chosen as twice the region influenced due to projectile impact during experimentation. The calibrated JC model discussed in chapter 2 was employed to assign the flow and fracture behaviour of the target material, see Table. 2.7. The geometry of 12.7 API projectile was also created in accordance with its actual dimensions as a three dimensional deformable body using ABAQUS/CAE. The shank diameter, shank length, total length and the length of ogival nose of the projectile core was 10.9, 24.4, 52.6 and 19.1 mm respectively. As discussed above the

steel core of the projectile has been modelled for all the finite element simulations assuming that the brass jacket has stripped off and had no influence the perforation process, Borvik et al. (2009b). The flow and fracture behaviour of 12.7 API projectile was also modelled employing the calibrated JC model for projectile material, see Table 2.15.

The target was meshed with eight node linear hexahedral elements with hourglass control. The mesh sensitivity was studied for 10 mm thick target by varying the element size as 0.55, 0.45, 0.35 and 0.25 mm^3 in the impact region corresponding to 19, 23, 29 and 40 elements at thickness of target keeping aspect ratio close to unity, see Fig. 3.12(a). The 12.7 API projectile was impacted normally on 10 mm thick target at incidence velocity 835 m/s and the residual velocity was found to be 682, 668, 650 and 644 m/s respectively. Thus, the residual velocity of the projectile was found to be converged corresponding to element size 0.35 mm^3 and number of elements 29 at the thickness, Fig. 3.12 (b). The computational residual velocity corresponding to element size 0.35 mm^3 was also found in agreement to that of the resultant experimental value, 663 m/s. Hence, the element size in the impact zone of the targets for all the simulations of Armox 500T steel was considered 0.35 mm^3 and the aspect ratio close to unity. Away from the impact region, however, the size of element was slightly increased keeping the aspect ratio unity. The hexahedral elements of 1 mm^3 were used to discretize the projectile throughout its body. The contact between the projectile and target was modelled by employing the Kinematic contact algorithm, ABAQUS. The projectile was considered as master and the through thickness contact region of the target as node based slave surface. A coefficient of friction of 0.02 was assumed between the projectile and target [Borvik et al. (2002b, 2011)]. The projectile was considered as master and the through thickness contact region of the target as node based slave surface. For normal

impact, the contact region of the target was considered equal to that of the diameter of the projectile. For oblique impact the exact contact region of the target was not known, therefore, a slightly larger portion than that of the diameter of the projectile was modeled as node based slave surface. The finite element model of 12.7 API projectile is shown in Fig. 3.13 and that of a typical Armox 500T steel target in Fig. 3.14.

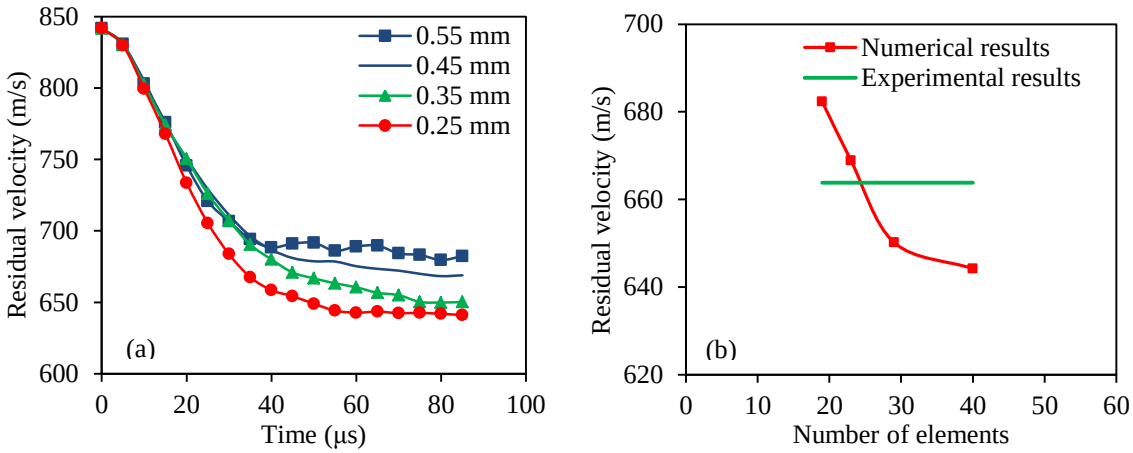

Fig. 3.12 Residual velocity of 12.7 API projectiles as a function of (a) time and (b) number of elements of Armox 500T steel target

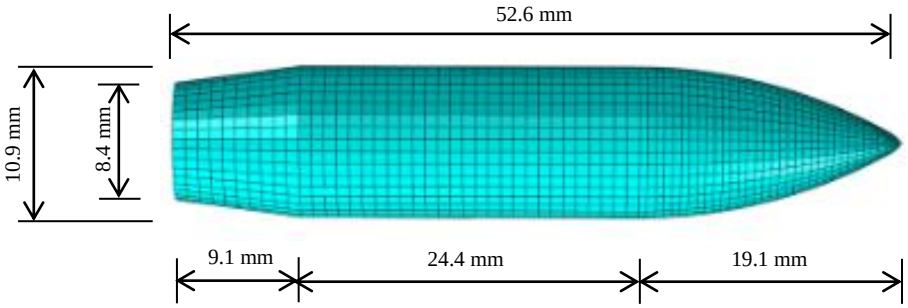

Fig. 3.13 Finite element model of 12.7 API projectile

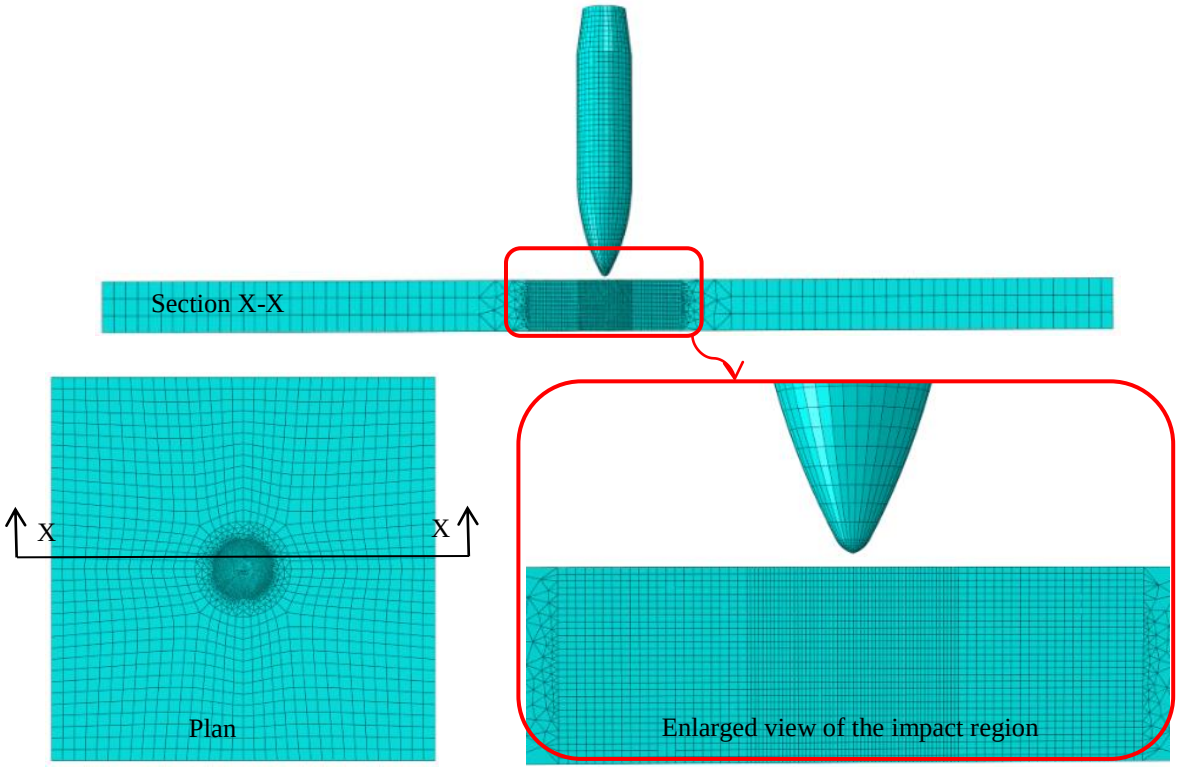

Fig. 3.14 Typical finite element model of Armox 500T steel target for the impact against 12.7 API projectile

3.5 VALIDATION OF ARMOX 500T STEEL PARAMETERS

The calibrated material parameters of the JC model have been validated by simulating the high strain rate material tests performed on Split Hopkinson Pressure Bar (SHPB) apparatus. The finite element simulations for the material tests performed under tension at strain rate 850 and 950 s^{-1} were carried out employing ABAQUS/Explicit code. The axisymmetric model of the tension specimens was developed with respect to their actual geometry, Fig. 3.15. The tests were performed on the cylindrical specimens of diameter 3 mm and gauge length 10 mm. The calibrated JC model was employed to assign the flow and fracture behaviour of the Armox 500T steel, see Table. 2.7. The specimens were considered fixed at one end while the other end was under the application of pressure in the direction

opposite to the material. The pressure versus time curve was assigned with respect to the corresponding strain rate. The discretization of the geometric model was carried out using four node axisymmetric quadrilateral elements with stiffness hourglass control, and three degrees of freedom at each node.

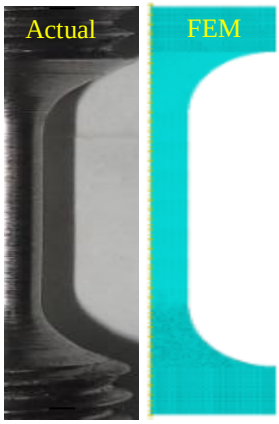

Fig. 3.15 Geometry of the tension specimen for axisymmetric finite element simulations

The mesh convergence was also studied for the simulations performed for the material characterisation. The element size in the specimen geometry was varied as 0.09 mm x 0.09 mm, 0.07 mm x 0.07 mm and 0.05 mm x 0.05 mm, however, the effect of mesh sensitivity was found insignificant on the numerical results. A sufficiently smaller size of element, 0.05 mm x 0.05 mm, was adopted throughout the geometry giving a total number of 85032 elements in the whole specimen. A typical simulation took 450 CPU minutes approximately.

The true stress-strain relationship obtained from the simulations performed under tension has been compared with the corresponding experimental results at 950 s^{-1} strain rate, see Fig. 3.16. The numerical results accurately predicted the material behaviour under tension. The contours of stresses have also been plotted in the specimen at the same strain rate, Fig. 3.17. The flow of stress throughout the specimen could be seen at various time

steps before and after necking phenomenon. The stress concentration in the necked region is clearly visible at the onset of fracture. The actual and predicted fractured diameter of the specimen was found to be 2.32 and 2.08 mm respectively.

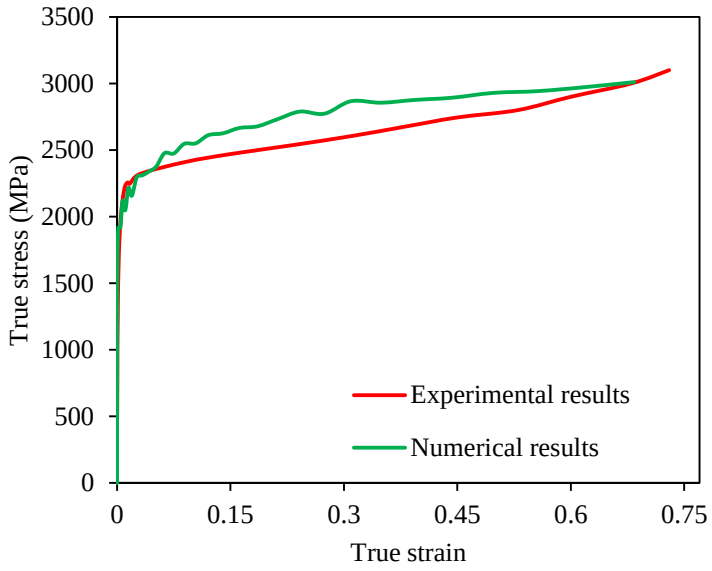

Fig. 3.16 Comparison of experimental and numerical stress-strain relationship

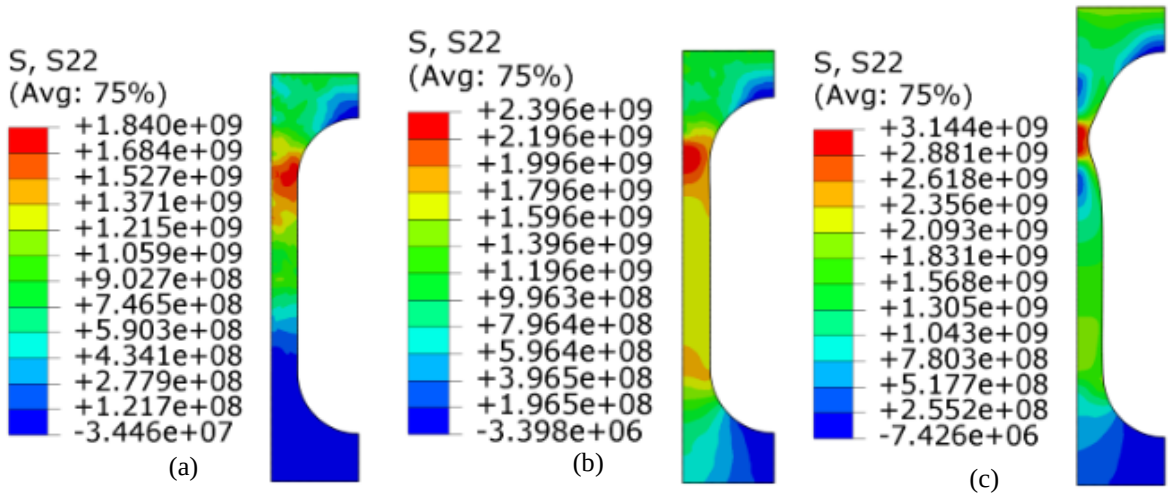

Fig. 3.17 Stresses developed in the direction of loading in tension test simulation performed at 950 s^{-1} strain rate at time interval (a) 2.8 μs (b) 5.6 μs and (c) 14.8 μs

3.6 FINITE ELEMENT MODELLING OF 7075-T651 ALUMINIUM TARGET AND 12.7 API PROJECTILE

The 7075-T651 aluminium target of thickness 20, 32, 40 and 50 mm was modelled as three dimensional deformable continuum using ABAQUS/CAE. The modelled target span, 200 mm x 200 mm, was smaller than its actual dimension, 500 mm x 500 mm, in order to reduce the computational time. It was ensured based on the experimental results that the influence of the impact would not spread beyond this region. The calibrated JC model discussed in chapter 2 was employed to assign the flow and fracture behaviour of the target material, Table. 2.12. The 12.7 API projectile was also modelled in accordance with its actual dimensions as a three dimensional deformable body in ABAQUS/CAE. The shank diameter, shank length, total length and the length of ogival portion of the projectile core was 10.9, 24.4, 52.6 and 19.1 mm respectively. The steel core of the projectile has been modelled for all the finite element simulations assuming that the brass jacket has stripped off and had no influence on the perforation process, Borvik et al. (2009b). The flow and fracture behaviour of the 12.7 API projectile was modelled employing the JC model calibrated for the projectile material, see Table 2.15.

The target was meshed with eight node linear hexahedral elements with hourglass control. The mesh sensitivity in case of 20 mm thick target was studied by varying the element size as 0.55, 0.45, 0.35 and 0.25 mm^3 in the impact region corresponding to 37, 45, 58 and 80 elements at the target thickness keeping aspect ratio close to unity, see Fig. 3.18(a). The 12.7 API projectile was normally impacted on 20 mm thick target at 820 m/s velocity and the residual velocity was found to be 713, 699, 678 and 678 m/s respectively. Thus, the residual velocity of the projectile was found to have converged corresponding to

element size 0.25 mm^3 and number of elements 58 at the thickness, Fig. 3.18 (b). The computational residual velocity at element size 0.25 mm^3 was also found in agreement to that of the resultant experimental value, 683 m/s. Hence, the element size in the impact zone of the targets for all the simulations of 7075-T651 aluminium was considered to be 0.25 mm^3 and the aspect ratio close to unity. Away from the impact region, however, the size of element was slightly increased keeping the aspect ratio almost unity.

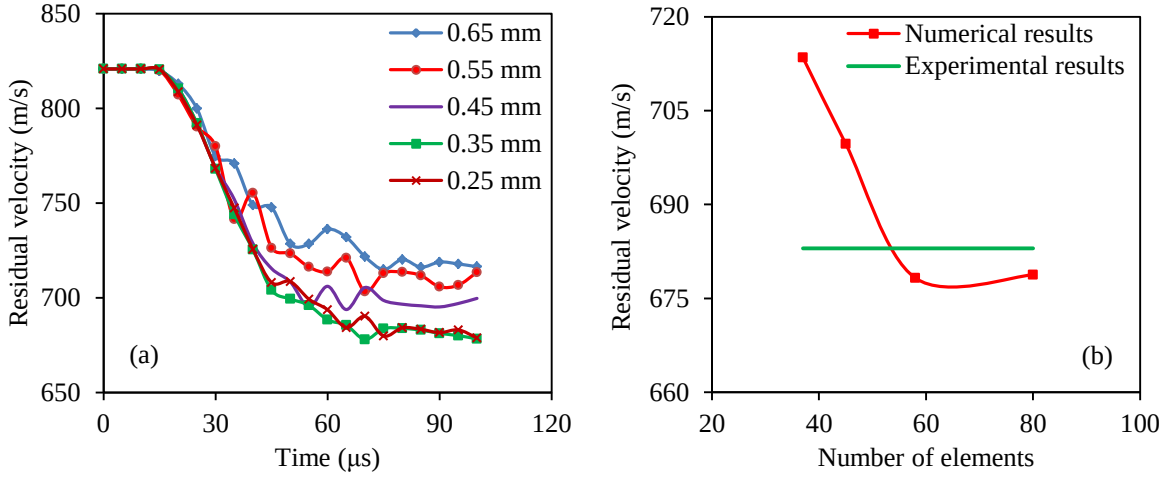

Fig. 3.18 Residual velocity of 12.7 API projectiles as a function of (a) time and (b) number of elements of 7075-T651 aluminium target

The hexahedral elements of 1 mm^3 were used to discretize the projectile throughout its body. The contact between the projectile and target was modelled by employing the Kinematic contact algorithm available in ABAQUS. A coefficient of friction of 0.02 was assumed between the projectile and target, Borvik et al. (2002b, 2011). The projectile was considered as master surface and the through thickness contact region of the target as node based slave surface. For normal impact, the contact region of the target was considered equal to that of the diameter of the projectile. For oblique impact, the exact contact region of the target was not known, therefore, a slightly larger portion of the target than that of the

diameter of the projectile was modeled as node based slave surface. The finite element model of 12.7 API projectile is shown in Fig. 3.19 and that of a typical 7075-T651 aluminium target in Fig. 3.20.

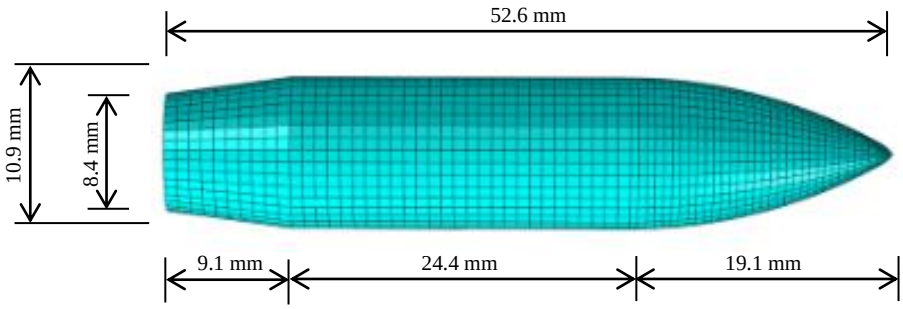

Fig. 3.19 Finite element model of 12.7 API projectile

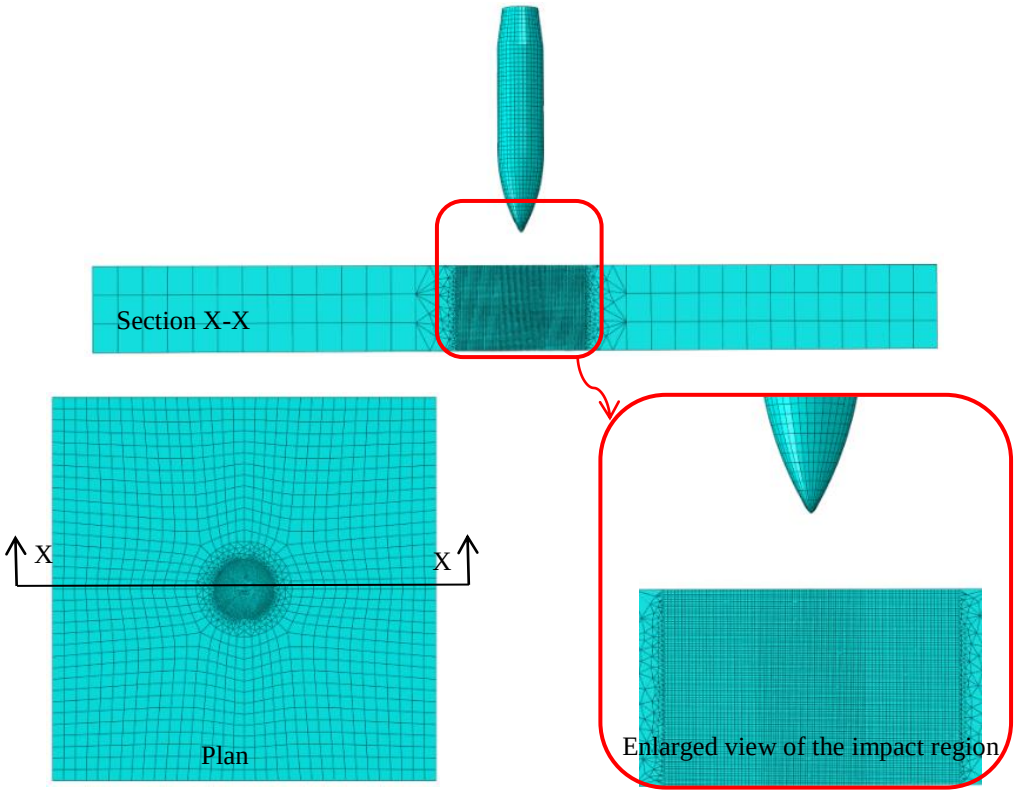

Fig. 3.20 Typical finite element model of 7075-T651 aluminium target for the impact against 12.7 API projectile

3.7 VALIDATION OF 7075-T651 ALUMINIUM PARAMETERS

The calibrated material parameters of the JC model have been validated by simulating the high strain rate material tests performed on Hopkinson pressure bar apparatus. The finite element simulations for the material tests performed under tension at strain rate 609 and 799 s^{-1} were carried out using ABAQUS/Explicit code. The axisymmetric geometric model was developed with respect to the actual geometry of the tension test specimen, diameter 3 mm and gauge length 10 mm, see Fig. 3.21. The calibrated JC model was employed to assign the flow and fracture behaviour of the material, Table. 2.12. The specimens were considered fixed at one end while the other end was under the application of pressure in the direction opposite to the material. The pressure versus time curve was assigned with respect to the corresponding strain rate. The discretization of the geometric model was carried out using four node axisymmetric quadrilateral elements with stiffness hourglass control, and three degrees of freedom at each node.

Fig. 3.21 Geometry of the tension specimen for axisymmetric finite element simulations

The mesh convergence for the material tests simulated under tension was studied by varying the size of element in the specimen geometry as 0.09 mm x 0.09 mm, 0.07 mm x 0.07 mm and 0.05 mm x 0.05 mm. However, element size was found to have insignificant

influence on the numerical results. Finally, a sufficiently smaller size of elements, 0.05 mm x 0.05 mm, was adopted giving a total number of 85032 elements in the whole specimen geometry. A typical simulation took approximately 800 CPU minutes.

The true stress-strain relationship obtained from the simulations performed under tension has been compared with those of the corresponding experimental results at 799 s^{-1}, see Fig. 3.22. The numerical results accurately predicted the material behaviour under tension with respect to yield stress and the plastic flow. The contours of stresses have also been plotted in the tension specimen at the same strain rate, see Fig. 3.23. The flow of stress through the specimen could be seen at various time steps before and after the initiation of necking. The stress concentration in the necked region is also clearly visible at the onset of fracture. The actual and predicted fractured diameter of the specimen was found to be 2.45 and 2.09 mm respectively.

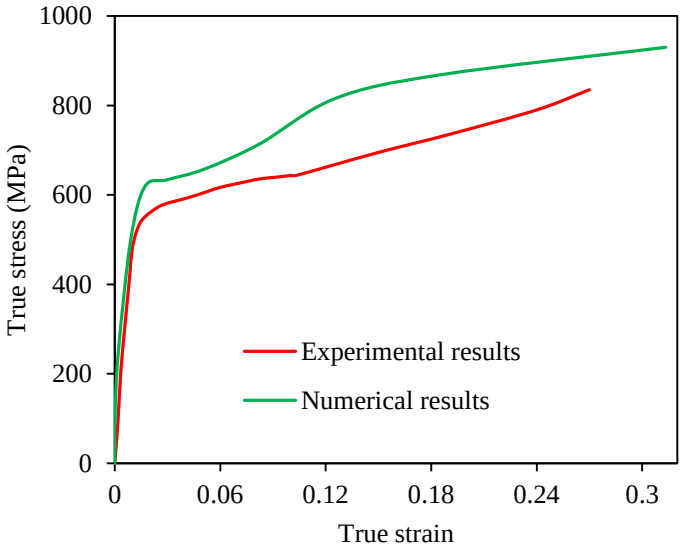

Fig. 3.22 Comparison of experimental and numerical stress-strain relationship

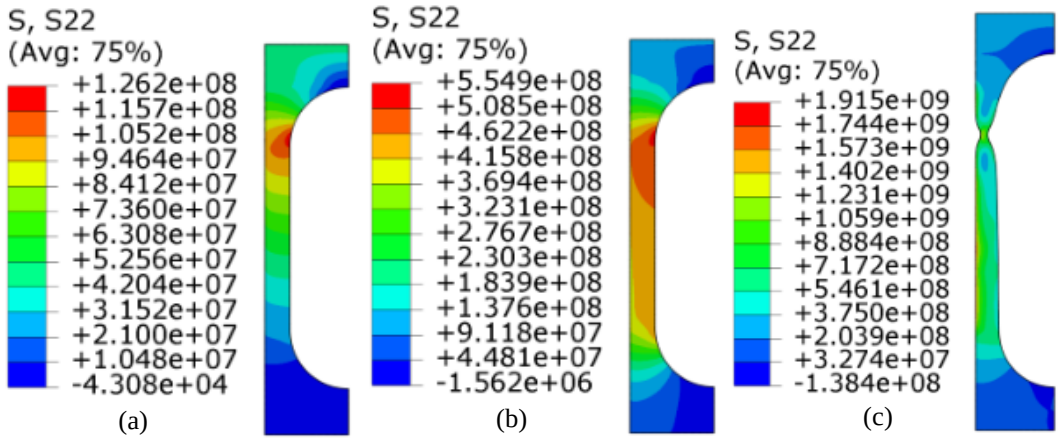

Fig. 3.23 Stresses developed in the direction of loading in tension test simulation performed at 799 s^{-1} strain rate at time interval (a) 5 μs (b) 10 μs and (c) 29 μs

3.8. CONCLUSIONS

The mild steel, Armox 500T steel and 7075-T651 aluminium targets of various thicknesses were modelled in ABAQUS/CAE as three dimensional deformable continuums. The mesh sensitivity in mild steel was studied by varying the element size in 12 mm thick target as 0.8, 0.6, 0.2 and 0.1 mm^3 and impacting it by 7.62 API projectile at normal incidence at 818 m/s velocity. The mesh convergence was obtained corresponding to element size 0.2 mm^3. The mesh convergence in Armox 500T steel target against 7.62 API projectile was studied by varying the element size in 8 mm thick target as 0.55, 0.45, 0.35, 0.25 and 0.2 mm^3 and impacting it by 7.62 API projectile at normal incidence at 835 m/s velocity. The convergence was obtained corresponding to element size 0.25 mm^3. The mesh convergence in Armox 500T steel against 12.7 API projectile was studied by varying the element size in 10 mm thick target as 0.55, 0.45, 0.35 and 0.25 mm^3 and impacting by the projectile normally at 835 m/s velocity. The residual velocity in this case converged at element size 0.35 mm^3. The mesh sensitivity in 7075-T651 aluminium was studied by varying the

element size in 20 mm thick target as 0.55, 0.45, 0.35 and 0.25 mm^3 and impacting it by 12.7 API projectile normally at 820 m/s velocity. The residual velocity was found to have converged corresponding to element size 0.25 mm^3.

The calibrated material parameters of the JC model have been validated by simulating the high strain rate material tests performed on Hopkinson pressure bar apparatus. For mild steel, the finite element simulations were carried out under tension as well as compression. The true stress-strain relationship obtained from the simulations performed under compression as well as tension was compared with the corresponding actual results and a close agreement between the two was found. The finite element simulations were also carried out for the material tests performed on Armox 500T steel and 7075-T651 aluminium specimens under tension. The predicted true stress-strain relationship thus obtained was found to have close correlation with the corresponding experimental results.

CHAPTER 4

Experimental and Finite Element Studies on Armox 500T Steel Targets

4.1 GENERAL

The ballistic experiments were performed on Armox 500T steel targets against 7.62 and 12.7 API projectiles by varying the angle of incidence untilled the occurrence of critical projectile ricochet. The targets impacted by 7.62 API projectile had thickness 6, 8 and 10 mm and corresponding areal density 47, 63 and 78 kg/m^2. On the other hand, those impacted by 12.7 API projectiles had thickness 5, 10, 15 and 20 mm and corresponding areal density 40, 79, 118 and 157 kg/m^2. Both the projectiles were fired at incidence velocities close to 820 m/s. The initial and residual velocity of the projectile was measured by optical measurement device. The high speed videography was also carried out for recording the residual projectile velocity and perforation phenomenon. The ballistic resistance, failure mechanism and deformation of the target and critical angle of ricochet was studied. The experimental findings with respect to residual projectile velocity, damage mechanism and critical angle of ricochet were simulated by carrying out the finite element analysis on ABAQUS/Explicit finite element code. The experimental and numerical results thus obtained were compared and discussed. The finite element simulations were subsequently performed for obtaining the ballistic limit of each target at the normal incidence.

4.2 EXPERIMENTAL INVESTIGATION

The ballistic experiments were carried out at Terminal Ballistic Research Laboratory, Chandigarh (TBRL). The small arms projectiles identified for studying the response of Armox 500 T steel targets were 7.62 and 12.7 API. The thicknesses to be studied against 7.62 API projectile were 6, 8 and 10 mm and those against 12.7 API projectile were 5, 10, 15 and 20 mm. The 7.62 API projectiles were fired by Sniper rifle, Fig. 4.1(a), and 12.7 API projectiles by Air Defence gun, Fig. 4.1 (b), at a constant incidence velocity close to 820 m/s.

The experiments were conducted at the ballistic test range in the open field. The detailed experimental arrangement is shown in Fig. 4.2(a). The target was placed at a distance of 10 m from the Sniper rifle and 15 m from the Air Defence gun as per the standard practice. The fixtures for holding the target as well as the gun were made of structural steel, see Fig. 4.2 (b) and (c). The square target plates of span 500 mm x 500 mm were held at their bottom onto the fixture with the help of heavy nut and bolts. These were tightened effectively to enable the fixed boundary. The clear distance between the shots fired at the target surface was considered 75 mm in order to avoid the overlapping of the damage zones of the subsequent shots. In view of maintaining the sufficient vicinity between the impact positions the total number of shots at a given target was limited to 10. The target holding fixture could be suitably adjusted in horizontal and vertical plane in order to enable the adjustment of the impact location on the target surface. The target-holding fixture was also designed to position the target at the desired angle of obliquity between 0° to 90°.

Fig. 4.1 Projectiles fired from (a) Sniper rifle and (b) Air Defence gun mounted on mounting fixture

Fig. 4.2 Experimental arrangements of (a) complete test set up (b) Sniper rifle mounted on mounting platform (c) target mounting platform (d) infrared emitter device (e) projectile catcher

The impact and residual velocities of the projectile were measured with the help of infrared optical sensors, see Fig. 4.2(d). These infrared optical sensors used to measure the velocity of the impacting projectile, being non-contact and non-destructive in nature, could be used repeatedly. The signals generated from the projectile obstruction are used to start and

stop the high speed counter for time measurement. The measured time interval was used to calculate the speed of the projectile. To measure the initial velocity, two such infrared emitters were placed at 6 and 8 m distance from the muzzle of the Sniper rifle and 11 and 13 m distance from the muzzle of the Air Defence gun, see Fig. 4.2 (d). Two emitters, each at 2 and 4 m behind the target, were placed to measure the residual velocity. These were particularly used for the normal impact. For most of the cases of oblique impact, the residual velocities were measured with the help of high speed framing camera. The projectiles were recovered after perforation of the target with the help of the recovery platform of the cushion pad bundles, see Fig. 4.2(e). The alignment of the gun, optical devices, target and the projectile catcher was carefully maintained with respect to the projectile trajectory. Moreover, for performing repetitions, the position of the target was carefully changed subsequent to each shot so that the bullet shall hit at the designated position on the surface of the target and should not influence the zone of the previous shot.

The Photron Fastcam-APX RS High-Speed Video Camera System was employed to measure the residual projectile velocity and to record the perforation phenomenon, Fig. 4.3 (a). The capability of APX RS of extremely high-speed recording (up to 2,50,000 frames per second) with high resolution enabled the vivid capturing of the event even under extremely low visibility. The high speed photography was found to be very useful to capture the perforation, fragmentation and the projectile exit velocity. In general, the rate of framing during the experimentation was considered 9000 fps. In order to avoid the damage of the camera due to splinters and fragments a robust camera shelter was employed which ensured the safety of the camera as well as the personnel, see Fig. 4.3 (b). The shelter had an opening

covered by the bullet proof glass, Fig. 4.3 (c), which enabled to view the event from the shelter.

Fig. 4.3 High speed videography setup of (a) high speed camera – PHOTRON Fastcam APX-RS (b) camera shelter and target mounting platform (c) bullet proof glass

4.3 RESULTS AND DISCUSSION

The behaviour of Armox 500T steel target against 7.62 and 12.7 API projectile has been studied at varying angle of incidence and the experimental and numerical results thus obtained with respect to residual projectile velocities, deformation and failure mechanism of the target and critical projectile ricochet have been discussed and compared. The finite element simulations also enabled the determination of the ballistic limit of the target at normal incidence.

4.3.1 Ballistic Resistance of Armox 500T Steel Targets against 7.62 API Projectiles

The ballistic resistance of Armox 500T steel target of thicknesses 6, 8 and 10 mm was studied against 7.62 API projectiles by varying the angle of incidence until the occurrence of projectile ricochet. The experimental results have been reproduced through finite element simulations employing ABAQUS/Explicit finite element code in conjunction with Johnson-Cook elasto-viscoplastic material model. The calibrated material parameters for the JC model were used to predict the material behaviour of the target as well as the projectile. The details of the material characterization and finite element modelling have been discussed in Chapter 2 and 3 respectively.

The experimental and numerical results for 6 mm thick target are presented in Table 4.1 corresponding to varying angles of obliquity. These have been found to have close correlation with respect to residual projectile velocities. The target was initially impacted at angles of incidence 0°, 15°, 30° and 45° at incidence velocity 814-837 m/s. However, it experienced perforation up to 40° obliquity. At 45° obliquity, the experimental results suggested that the projectile ricocheted after impacting the target. The simulations on the

other hand predicted the embedment of projectile in the target at 45° obliquity. The ricochet of the projectile has been predicted through numerical simulations at 48° obliquity. In general, the resistance of target has been found to increase significantly with increase in the angle of incidence. It is important to mention here that during the experimentation when the projectile came in contact with the target, huge flash (lightening) was generated due to friction. In some of the tests when the flash was very high, the view of the projectile was obstructed and hence the residual velocity could not be obtained through the high speed camera.

Table 4.1 Resistance of 6 mm thick target by 7.62 API projectile

Incidence angle (°)	Impact velocity (m/s)	Residual velocity (m/s)	
		Experimental results	Numerical results
00	835.91	672.31	641.3
00	820.08	653.21	619.6
15	837.84	498.46	489.48
30	833.37	Perforated	318.55
35	820.68	Perforated	212.35
40	814.03	113.69	146.34
45	823.25	Ricochet	Rebound
48	823.25	-	Ricochet

The 7.62 API projectile failed the targets through the formation of a clear hole. However, the size and shape of the hole varied with increase in angle of obliquity. The size of the perforated hole has been found to increase initially with an increase in the angle of incidence up to 30° and thereafter it decreased with further increase in obliquity, see Figs. 4.4 and 4.5. The shape of the hole was circular at 0° and 15° obliquity, while at 30° obliquity it became elliptical. However, at subsequent angles of obliquity, the hole took the circular shape. The numerical simulations accurately predicted the failure mode of 6 mm thick target. The spalling of the material at 30°, 35° and 40° obliquity was also reproduced through

numerical simulations. The scabbing of the material from rear face occurred only at the normal impact, Fig. 4.5. However, spalling was noticed at all the incidence angles and became more significant with increase in target obliquity, Fig. 4.4.

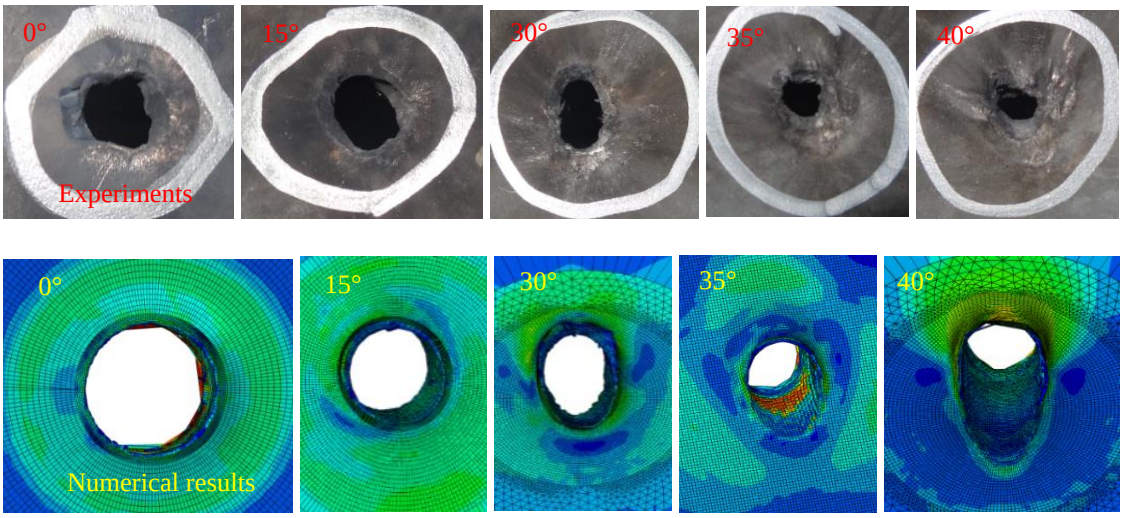

Fig. 4.4 Front side failure modes of 6 mm thick target against 7.62API projectile

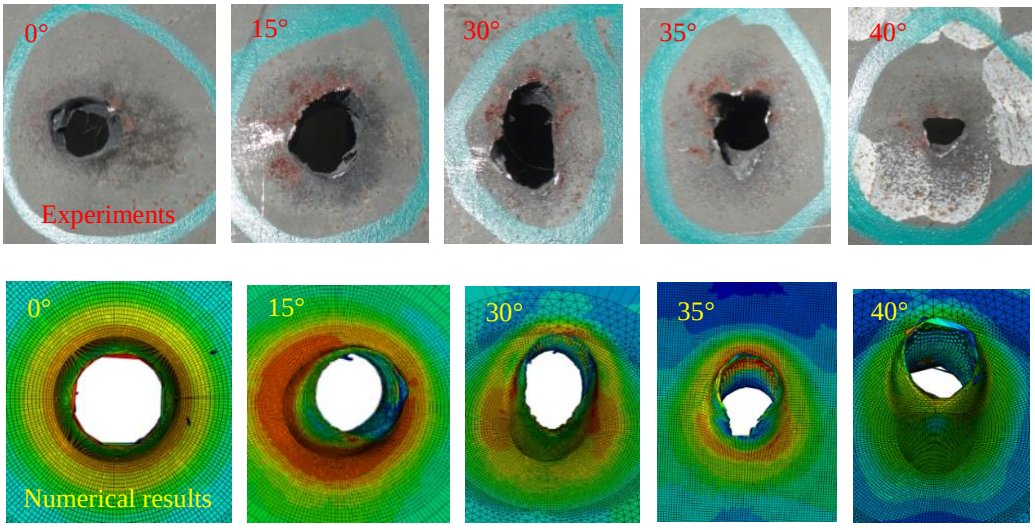

Fig. 4.5 Rear side failure modes of 6 mm thick target against 7.62API projectile

The experimental and numerical results for 8 mm thick target are presented in Table 4.2 corresponding to the varying angles of obliquity. The actual and predicted residual velocities have been found to have close correlations up to 20° obliquity. At 25° obliquity, the experimental residual velocity was 97 m/s while the simulations predicted residual velocity 138.4 m/s. At 30° obliquity, the experimental and the numerical results showed rebounding of the projectile after hitting the target, while the simulations predicted embedment of the projectile in the target. At 45° obliquity the experiments suggested the ricochet of the projectile, however, the finite element simulations predicted the embedment of the projectile in the target, in the same manner as noticed in case of 6 mm thick target. The simulations predicted the projectile ricochet at 47°.

Table 4.2 Resistance of 8 mm thick target by 7.62 API projectile

Incidence angle (°)	Impact velocity (m/s)	Residual velocity (m/s)	
		Experimental results	Numerical results
00	823.62	334.28	328.33
00	828.02	343.74	340.13
15	811.13	Perforated	317.55
20	825.05	275.95	288.15
25	816.63	97.05	138.48
30	813.17	Rebound	Rebound
45	813.17	Ricochet	Embedment
46	813.17	-	Embedment
47	813.17	-	Ricochet

For 8 mm thick target no significant variation was noticed in the size of hole with varying angle of incidence. The shape of the hole was found to be almost circular for all the angles of incidence. At the front surface some spalling of material was observed which increased with increase in obliquity, Fig. 4.6. The spalling of the material from the front surface was also predicted through simulations. At the rear surface however, no sign of

scabbing was observed, Fig. 4.7, either through experiments or finite element simulations. The failure mode at the rear surface also indicated the signs of hole enlargement and this behaviour was also confirmed through numerical simulations.

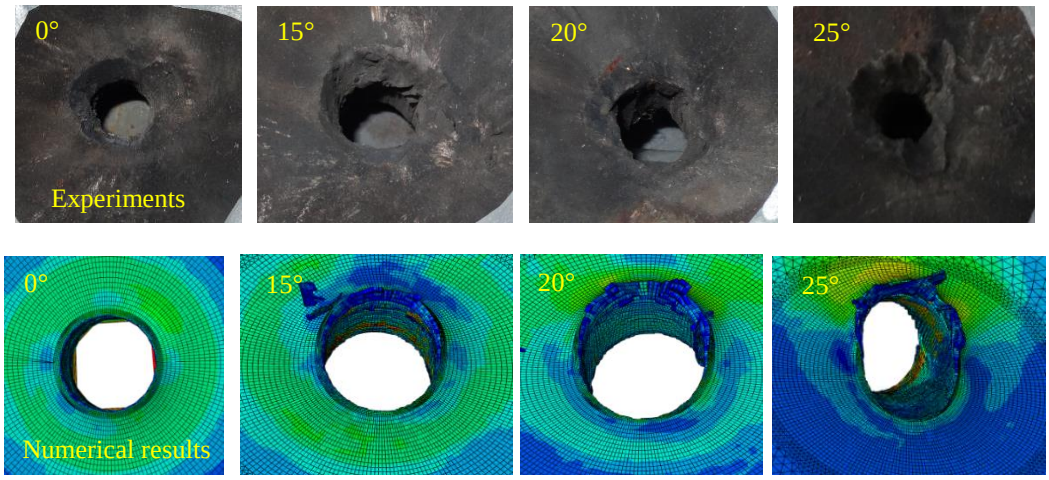

Fig. 4.6 Front side failure modes of 8 mm thick target against 7.62 API projectile

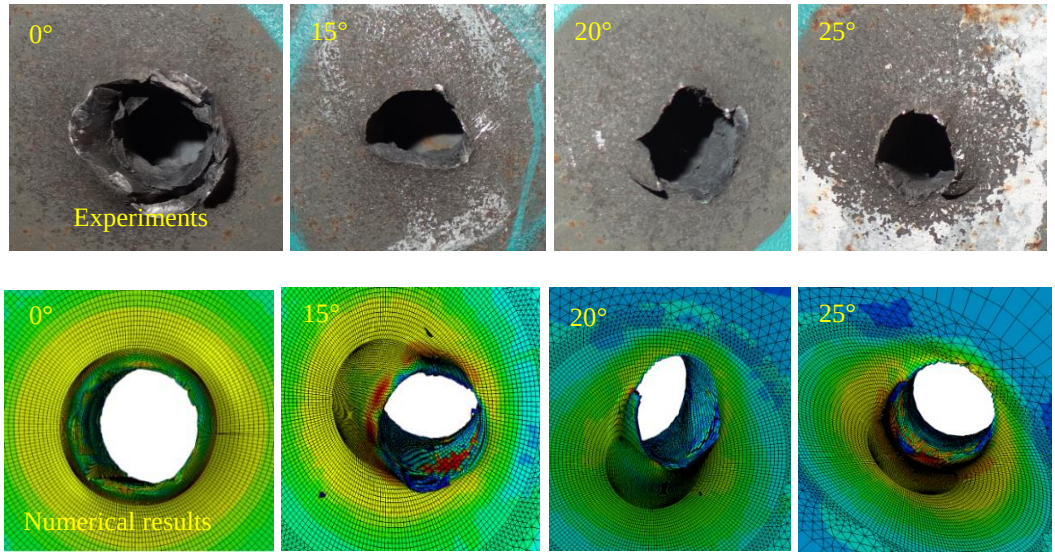

Fig. 4.7 Rear side failure modes of 8 mm thick target against 7.62 API projectile

The experimental and numerical results for 10 mm thick target are presented in Table 4.3 corresponding to the varying angles of obliquity. The target was impacted at 0°, 15°, 30° and 45° obliquity at incidence velocity 814-838 m/s. However, it experienced perforation only at the normal impact. The actual and predicted residual velocities at the normal impact have been found in close agreement. At 15° and 30° obliquity the projectile rebounded after hitting the target and this behaviour was also confirmed through numerical simulations. The critical angle of ricochet was found to be 45° and the same was predicted to be 47°. The failure modes of 10 mm thick target have been accurately predicted through the numerical simulations are shown in Fig. 4.8. A significant spalling of the material was noticed from front surface and at the rear surface it was found to be nominal. As such the numerical simulations did not predict significant spalling from the influenced zone and only minor fragmentation was noticed at the front surface, Fig. 4.8. However, the predicted contours showed that the stress in the influenced zone reduced to zero which indicate that the material did not develop any stress and hence may be assumed to have been removed. The rear surface of the target also witnessed scabbing of the material and fragmentation. The fragmentation was also confirmed through finite element simulations.

Table 4.3 Resistance of 10 mm thick target by 7.62 API projectile

Incidence angle (°)	Impact velocity (m/s)	Residual velocity (m/s)	
		Experimental results	Numerical results
00	831.98	238.50	256.34
00	814.90	222.91	241.36
00	838.89	256.78	265.94
15	820.48	Rebound	Rebound
30	826.45	Rebound	Rebound
45	834.45	Ricochet	Embedment
46	834.45	-	Embedment
47	834.45	-	Ricochet

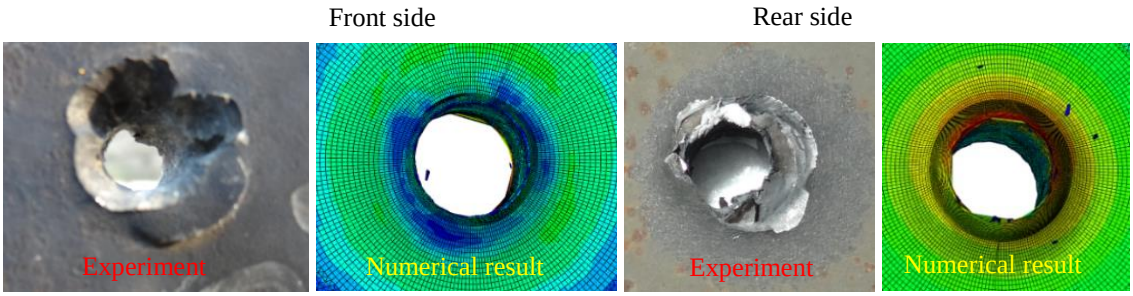

Fig. 4.8 Failure mode of 10 mm thick target impacted normally by 7.62 API projectile

It should be noted that the ricochet of the projectile through experiments was found to occur at 45° for 6, 8 and 10 mm thicknesses. However, it was predicted to have occurred at 48°, 47° and 47° for 6, 8 and 10 mm thickness respectively, see Table 4.4. Thus it may be concluded that the target thickness in the studied regime does not have influence on the critical angle of ricochet. The maximum angle of perforation for 6, 8 and 10 mm thickness was found to be 40°, 25° and 0° respectively, which has been exactly reproduced through finite element simulations, Table 4.4.

Table 4.4 Resistance of target against 7.62 API projectile at varying obliquity

Thickness of target (mm)	Experimental results	Numerical results
Critical angle of ricochet		
6	45°	48°
8	45°	47°
10	45°	47°
Maximum angle for perforation		
6	40°	40°
8	25°	25°
10	0°	0°

4.3.2 Evaluation of Ballistic Limit against 7.62 API Projectiles

The ballistic limit of the 6, 8 and 10 mm thick targets has also been obtained numerically against 7.62 API projectiles at normal impact. The numerical simulations were carried out at assumed incidence velocities to obtain the ballistic limit, see Table 4.5-4.7. The

ballistic limit velocity was calculated as the average of the highest projectile velocity not giving perforation and the lowest projectile velocity giving complete perforation of the target. After obtaining the ballistic limit velocity, the calculation of the residual projectile velocity corresponding to a given incidence velocity was also carried out using the Recht-Ipson model, see Table 4.5. The residual velocities were calculated based on the following model originally proposed by Recht and Ipson (1963),

$$v_r = a(v_i^p - v_{bl}^p)^{\frac{1}{p}} \quad (11)$$

where v_i, v_r and v_{bl} is initial, residual and ballistic limit velocity, a and p are the model constants. The least square method was used to obtain a best fit to the numerical data using suitable values of a and p calibrated through numerical results. For 6 mm thick target, the value of a and p was found to be 1 and 2.2 respectively. The ballistic limit velocity, V_{50}, for 6 mm thick target has been found to be 625 m/s. For 8 mm thick target, the corresponding model constants a and p were found to be 1 and 1.74 respectively and the ballistic limit velocity, V_{50}, 713 m/s. For 10 mm thick target the model constants a and p were found to be 1 and 1.35 respectively and the ballistic limit velocity, V_{50}, 796.5 m/s.

Table 4.5 Ballistic limit velocity of 7.62 API projectile impacted on 6 mm thick target

Impact velocity (m/s)	Residual velocity (m/s)		Model constants		Ballistic limit (m/s)
	Numerical results	Recht-Ipson model results	a	p	
820.08	619.6	570.3	1.0	2.2	625
720	327.5	395.3			
660	177.2	244.9			
640	104.9	165.2			
630	50.4	99.8			
620	0	0			

Table 4.6 Ballistic limit velocity of 7.62 API projectile impacted on 8 mm thick target

Impact velocity (m/s)	Residual velocity (m/s)		Model constants		Ballistic limit (m/s)
	Numerical results	Recht-Ipson model results	a	p	
823.62	340.1	346.7	1.0	1.74	713
760	229.3	208.2			
730	140.9	115.1			
720	74.51	68.9			
716	39.67	42.2			
710	0	0			

Table 4.7 Ballistic limit velocity of 7.62 API projectile impacted on 10 mm thick target

Impact velocity (m/s)	Residual velocity (m/s)		Model constants		Ballistic limit (m/s)
	Numerical results	Recht-Ipson model results	a	p	
831.98	251.36	208.7	1.0	1.35	796.5
805	105.3	95.6			
799	63.21	49.2			
794	0	0			

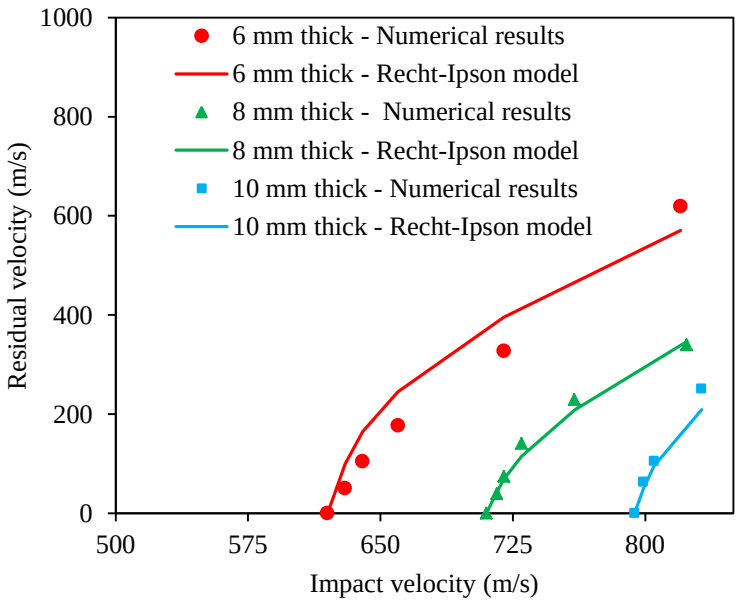

Fig. 4.9 Ballistic resistance of targets against 7.62 API projectile

Fig. 4.9 shows the impact and residual velocity data points and the corresponding Recht-Ipson fit through solid lines for 6, 8 and 10 mm thick targets. The ballistic limit velocity, V_{50}, for 6, 8 and 10 mm thick targets has been found to be 625, 713 and 796.5 m/s respectively.

The ballistic limit of various target thicknesses has been compared for 7.62 API projectiles at normal impact, Table 4.8. The ballistic limit of 10 mm thick target was found to be 14% and 27% higher than that of 8 and 6 mm thick target respectively. The ballistic limit of the target has been found to increase almost linearly with increase in target thickness, Fig. 4.10.

Table 4.8 Ballistic limit of targets against 7.62 API projectile

Thickness of target (mm)	Areal density (kg/m^2)	Ballistic limit (m/s)
6	47	625
8	63	713
10	78	796.5

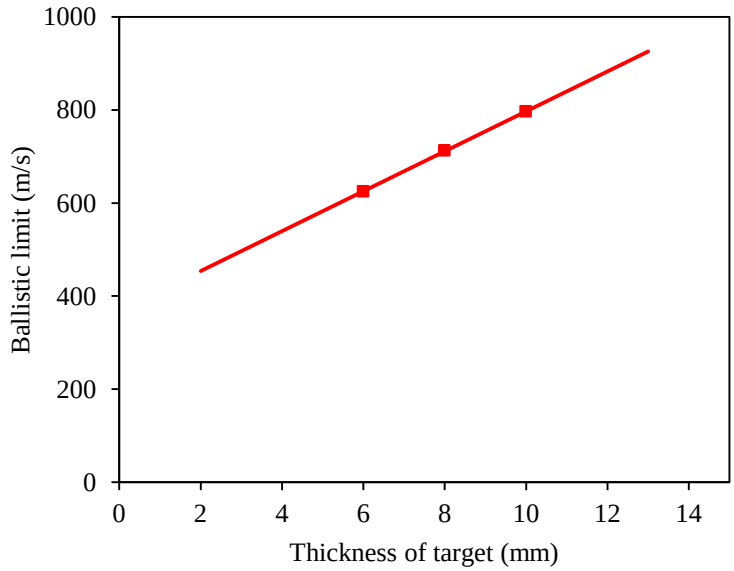

Fig. 4.10 Ballistic limit of targets against 7.62 API projectile

4.3.3 Ballistic Resistance of Armox 500T Steel Targets against 12.7 API Projectiles

The ballistic performance of Armox 500T steel targets of thicknesses 5, 10, 15 and 20 mm was studied against 12.7 API projectiles by carrying out experiments at varying angles of obliquity and the results thus obtained were reproduced through finite element simulations. The angle of incidence was varied until the occurrence of projectile ricochet. ABAQUS/Explicit finite element code in conjunction with Johnson-Cook elasto-viscoplastic material model was employed for carrying out the numerical simulations. The calibrated material parameters for the JC model were used to predict the material behaviour of the target as well as the projectile. The details of the material characterization and finite element modelling have been discussed in Chapter 2 and 3 respectively.

The experimental and numerical results for 5 mm thick target are presented in Table 4.9 corresponding to 0°, 35°, 45° and 56°obliquity. These have been found to have close correlation with respect to residual projectile velocities. The residual projectile velocity in some of the experiments could not be obtained (Table 4.9) due to heavy flashing (lightening) during contact of projectile and target. The flashing has been found to be more pronounced corresponding to thick targets and high obliquity. However, corresponding to all the incidence velocities, the numerical value of the residual velocity has been obtained. It has been observed that there is no influence on the residual projectile velocity up to an angle of obliquity of 45°. Subsequent to 45° however, a minor reduction in the residual velocity has been noticed. It should be noted that both experiments and finite element simulations showed perforation of projectile up to 56° obliquity. At, 57° obliquity also the numerical results predicted perforation with residual velocity 604.8 m/s while at 58° obliquity the simulations predicted ricochet of the projectile.

Table 4.9 Resistance of 5 mm thick target by 12.7 API projectile

Incidence angle (°)	Impact velocity (m/s)	Residual velocity (m/s)	
		Experimental results	Numerical results
00	837.14	Perforated	764.32
00	837.35	776.34	763.84
00	834.10	768.09	757.43
35	846.42	Perforated	741.52
35	845.67	Perforated	739.21
35	837.63	Perforated	731.23
45	821.70	Perforated	720.22
45	846.20	Perforated	739.76
45	843.28	760.9	736.15
55	837.89	-	675.99
56	851.35	622.04	651.66
56	841.08	Perforated	642.13
57	837.89	-	604.86
58	837.89	-	Ricochet

Fig. 4.11 shows the actual and predicted failure modes of 5 mm thick target impacted by 12.7 API projectile corresponding to 0°, 35°, 45° and 56°obliquity. The target has experienced insignificant global deformation. At normal impact, the projectile made a circular hole in the target which took elliptical shape at oblique impact. The size of the holes at oblique impact has also been found to be higher than at normal impact. The target experienced petalling at the rear surface along with the formation of hole. However, the petals were indistinct and unequal in size. The size and shape of the hole has been closely predicted through finite element simulations. The numerical simulations also witnessed the formation of petals in the target. At the front surface of the target a clear hole was formed of the shape and size equivalent to that of the rear surface. It should be noted that the formation of distinct petals was observed only for 5 mm thick target.

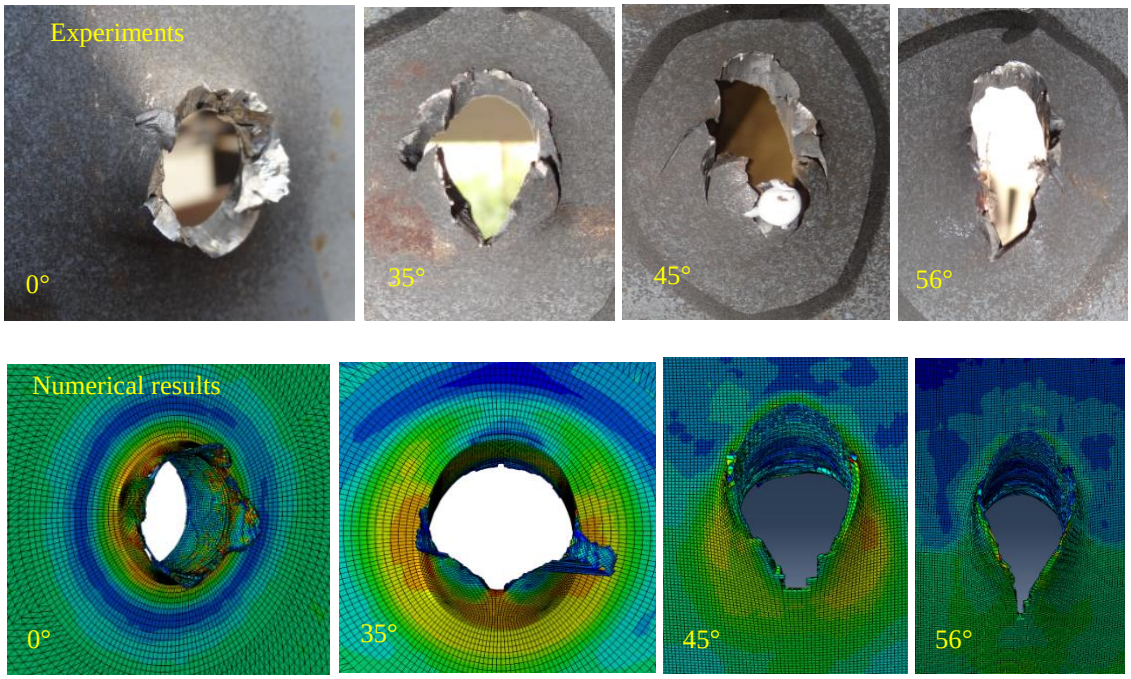

Fig. 4.11 Rear side failure surface of 5 mm thick target impacted against 12.7 API projectile

Table 4.10 Resistance of 10 mm thick target by 12.7 API projectile

Incidence angle (°)	Impact velocity (m/s)	Residual velocity (m/s)	
		Experimental results	Numerical results
00	841.89	686.37	708.99
00	835.21	Perforated	699.34
00	831.67	663.82	702.43
35	846.68	Perforated	676.85
35	850.30	Perforated	682.30
46	859.18	Perforated	559.16
51	845.0	-	373.6
55	837.89	-	Ricochet

For 10 mm thick target the experiments were carried out at 0°, 35° and 46° obliquity keeping in view that the influence of obliquity would not be significant at low incidence angles. The experimental results suggested perforation of projectile up to 46° obliquity while the numerical results predicted perforation up to 51° obliquity. The residual projectile velocities remained unaffected up to 35° obliquity. At 46° and 51° obliquity, the numerical

simulations predicted an increment in the ballistic resistance of 22% and 82% respectively. The ricochet of the projectile was predicted at 55° obliquity, see Table 4.10.

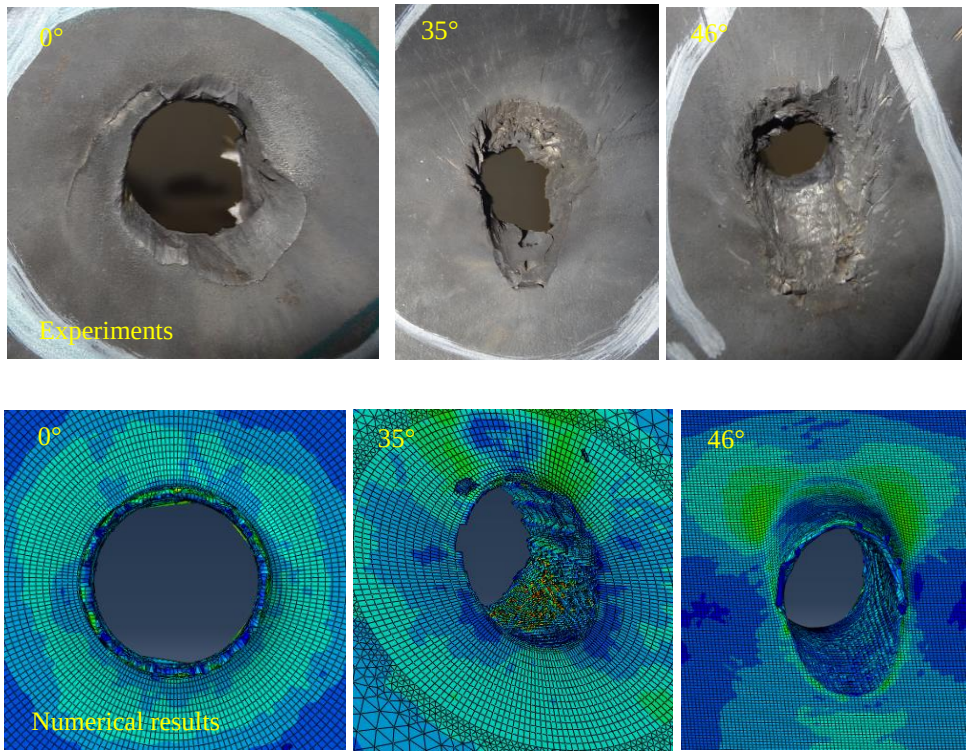

Fig. 4.12 Front side failure surface of 10 mm thick target impacted against 12.7 API projectile

Fig. 4.12 shows the actual and predicted failure modes of the front surface of 10 mm thick target impacted at different angles of incidence. The size of the perforated hole has been found to have decreased significantly with an increase in the angle of incidence. At normal impact, the projectile made a circular hole in the target. At 35° obliquity, the hole has been found to be elliptical in shape while at 46° obliquity again the shape of the hole has been found to be circular. However, the damage induced in the target around the hole has been found to be elliptical in shape at 35° as well as 46° obliquity. Particularly, at 46° obliquity a significant amount of material has been eroded from the impact zone of the target while the size of hole was very small indicating the very high resistance offered by the target.

There is also a possibility that at 46° obliquity, only the nose of the projectile would have perforated and the remaining projectile would have rebounded. However, the numerical simulations did not confirm this possibility and indicated the perforation of the complete projectile. At the rear surface of the target no significant deformation was noticed except the formation of almost circular shape hole corresponding to each angle of obliquity.

The angle of incidence of 15 mm thick target was varied as 0°, 15°, 25°, 35° and 45° due to the fact that the thickness of the target was comparatively high and almost 50% velocity drop was observed at normal impact itself, see Table 4.11. Corresponding to three shots, each fired at 0°, 15° and 25°, the residual velocity could not be obtained. Moreover, the experimental results showed perforation up to 25° obliquity. At 35° obliquity, the experimental results showed rebounding of the projectile while the simulations predicted perforation with a very low residual velocity about 100 m/s. At 45° obliquity, the experimental results showed ricochet of the projectile while the simulations predicted rebounding. It should be noted that the high speed camera could not capture the ricochet phenomenon. It was only the deformation pattern of the target through which it was concluded that the projectile has actually ricocheted, see Fig. 4.13 (a). The numerical simulations on the other hand predicted ricochet of the projectile at 53° obliquity, see Fig. 4.13 (b).

Fig. 4.14 shows the failure modes of 15 mm thick target impacted by 12.7 API projectiles at 0°, 15° and 25° obliquity. The size of the perforated hole has been found to be almost same corresponding to different angles of incidence. The size and shape of the hole has been closely reproduced through finite element simulations. At 0° and 15° obliquity, the spalling of the target material has been found to be almost same in magnitude. At 25°

obliquity however, the spalling was lesser in magnitude. At the rear surface of the target, no sign of material erosion was observed and a clear hole was formed at each angle of obliquity.

Table 4.11 Resistance of 15 mm thick target by 12.7 API projectile

Incidence angle (°)	Impact velocity (m/s)	Residual velocity (m/s)	
		Experimental results	Numerical results
00	850.45	568.38	575.40
00	839.03	554.16	561.48
00	829.46	Perforated	550.03
00	836.33	539.36	559.75
15	838.82	280.40	345.50
15	842.18	Perforated	351.76
25	841.26	234.02	279.21
25	828.29	Perforated	268.24
35	829.39	Rebound	112.32
35	846.88	Rebound	126.35
45	839.67	Ricochet	Rebound
53	839.67	-	Ricochet

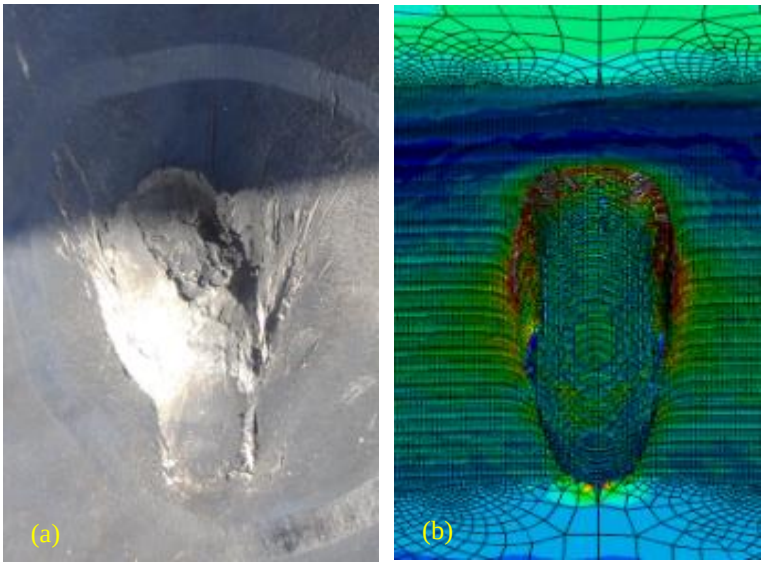

Fig. 4.13 Critical angle of ricochet at (a) 45° experimentally (b) 53° obliquity numerically impacted on 15 mm thick target by 12.7 API projectile

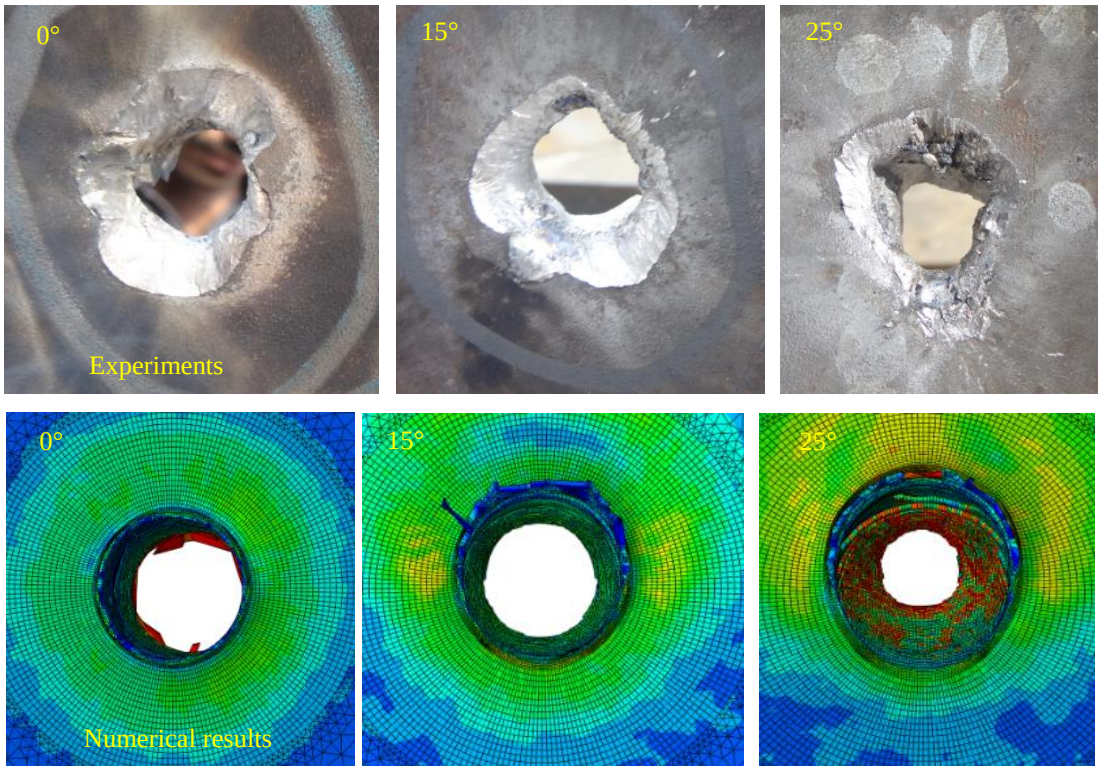

Fig. 4.14 Front side failure surface of 15 mm thick target impacted against 12.7 API projectile

Table 4.12 Resistance of 20 mm thick target by 12.7 API projectile

Incidence angle (°)	Impact velocity (m/s)	Residual velocity (m/s)	
		Experimental results	Numerical results
00	815.39	449.38	406.25
00	812.91	423.96	401.68
00	826.10	Perforated	419.35
15	822.57	Rebound	Rebound
30	821.32	Rebound	Rebound
45	816.73	Ricochet	Embedment
49	816.73	-	Ricochet

The experimental and numerical results for 20 mm thick target are presented in Table 4.12 corresponding to 0°, 15°, 30° and 45°obliquity. The perforation of the targets has been found to occur only at normal impact through experiments as well as finite element

simulations. At 15° and 30° obliquity, both actual and predicted results showed rebounding of the projectile. However, the experiments suggested the critical projectile ricochet at 45° while the numerical simulations at 49° obliquity.

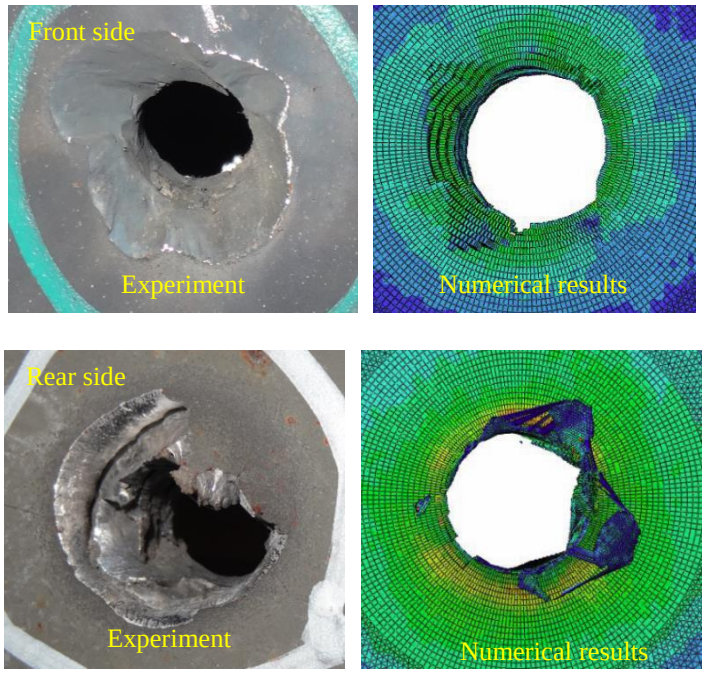

Fig. 4.15 Failure surface of 20 mm thick target impacted against 12.7 API projectile

Fig. 4.15 shows the front and rear side deformation modes of 20 mm thick target impacted normally by 12.7 API projectile. Both front as well as rear surface experienced material erosion around the perforated hole and the same has been witnessed through finite element simulation results. At the front surface the span of the spall was found to be almost double the size of the hole formed in the target. The shape of the hole was found to be circular at the front surface. At the rear surface the shape of the hole was not distinct. The mode of failure on the distal side of the target was found to be a combination of scabbing and distorted petalling. The formation of distorted petals has also been witnessed through numerical results.

It may be concluded here that the maximum angle of perforation in case of 5, 10, 15 and 20 mm thicknesses was 56°, 46°, 25° and 0° respectively and the same was reproduced 57°, 51°, 35° and 0°, see Table 4.13. The actual critical angle of ricochet for 15 and 20 mm thick targets has been found to be identical, 45°, and it has been predicted to be 53° and 49° respectively. Corresponding to 5 and 10 mm thick target the critical angle of ricochet could not be obtained. These targets however, have been found to experience perforation up to 56° and 46° obliquity respectively. However, due to some technical problems, the trials could not be performed on these targets by further increasing the angle of obliquity. Nevertheless, the finite element simulations predicted the critical angle of ricochet for 5 and 10 mm thick targets to be 58° and 55° respectively.

Table 4.13 Resistance of target against 12.7 API projectile at varying obliquity

Target thickness (mm)	Experimental results	Numerical results
Critical angle of ricochet		
5	-	58°
10	-	55°
15	45°	53°
20	45°	49°
Maximum angle for perforation		
5	56°	57°
10	46°	51°
15	25°	35°
20	0°	0°

4.3.4 Evaluation of Ballistic Limit against 12.7 API Projectiles

The ballistic limit of 5, 10, 15 and 20 mm thick targets has also been obtained numerically against 12.7 API projectiles at normal impact. The numerical simulations were carried out at assumed incidence velocities to obtain the ballistic limit, see Tables 4.14-4.17. The ballistic limit velocity was calculated as the average of the highest projectile velocity not

giving perforation and the lowest projectile velocity giving complete perforation of the target. After obtaining the ballistic limit velocity, the residual projectile velocity corresponding to a given incidence velocity was also calculated using the Recht-Ipson model. These calculated residual projectile velocities have also been provided in Tables 4.14 to 4.17 respectively for 5, 10, 15 and 20 mm thicknesses. The residual velocities were calculated based on the model [Eqn. 11] originally proposed by Recht and Ipson (1963). The least square method was used to obtain a best fit to the numerical data and thus calibrate the value of *a* and *p*. For 5 mm thick target, the ballistic limit velocity, V_{50}, has been found to be 387.5 m/s and the parameters *a* and *p* were calibrated to be 1 and 2.1 respectively. For 10 mm thick target, the ballistic limit velocity was found to be 507.5 m/s and model constants, *a* and *p*, 1 and 1.99 respectively. For 15 mm thick target the ballistic limit velocity was found to be 612.5 m/s and the model constants, *a* and *p*, calibrated to be 1 and 1.93 respectively. For 20 mm thick target ballistic limit velocity was found to be 685 m/s and constants, *a* and *p*, 1 and 1.75 respectively. Fig. 4.16 shows the impact and residual velocity data points and the corresponding Recht-Ipson fit through solid lines for 5, 10, 15 and 20 mm thick targets.

Table 4.14 Ballistic limit velocity of 12.7 API projectile impacted on 5 mm thick target

Impact velocity (m/s)	Residual velocity (m/s)		Model constants		Ballistic limit (m/s)
	Numerical results	Recht-Ipson model results	a	p	
837.35	761.8	763.8	1.0	2.1	387.5
700	584.9	595.1			
600	472.2	470.7			
480	301.3	295.9			
440	236.8	220.4			
400	127.3	108.4			
395	89.2	84.73			
390	45.6	50.1			
385	0	0			

Table 4.15 Ballistic limit velocity of 12.7 API projectile impacted on 10 mm thick target

Impact velocity (m/s)	Residual velocity (m/s)		Model constants		Ballistic limit (m/s)
	Numerical results	Recht-Ipson model results	a	p	
831.67	702.4	658.8	1.0	1.99	507.5
700	469.9	480.3			
600	300.7	318.3			
550	182.1	210.5			
520	80.6	112.1			
510	43.1	49.7			
505	0	0			

Table 4.16 Ballistic limit velocity of 12.7 API projectile impacted on 15 mm thick target

Impact velocity (m/s)	Residual velocity (m/s)		Model constants		Ballistic limit (m/s)
	Numerical results	Recht-Ipson model results	a	p	
839.03	561.4	557.7	1.0	1.93	612.5
740	399.8	400.5			
690	298.2	303.8			
670	261.9	258.4			
650	225.3	205.5			
630	140.9	137.4			
615	49.3	49.84			
610	0	0			

Table 4.17 Ballistic limit velocity of 12.7 API projectile impacted on 20 mm thick target

Impact velocity (m/s)	Residual velocity (m/s)		Model constants		Ballistic limit (m/s)
	Numerical results	Recht-Ipson model results	a	p	
815.3	406.2	379.9	1.0	1.75	685
750	251.2	250.4			
720	134.2	174.2			
700	123.1	106.7			
690	43.2	56.7			
680	0	0			

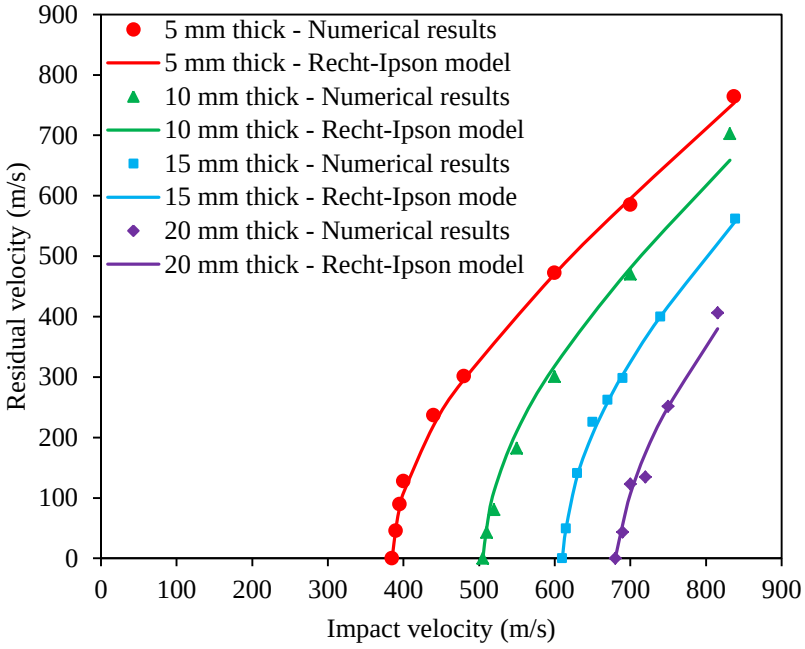

Fig. 4.16 Ballistic resistance of targets against 12.7 API projectile

The predicted ballistic limit of different target thicknesses has been compared in Table 4.18. The ballistic limit of 20 mm thick target was found to be 12%, 35% and 76% higher than 15, 10 and 5 mm thick target respectively. Moreover, the ballistic limit has been found to increase almost linearly with increase in target thickness, see Fig. 4.17.

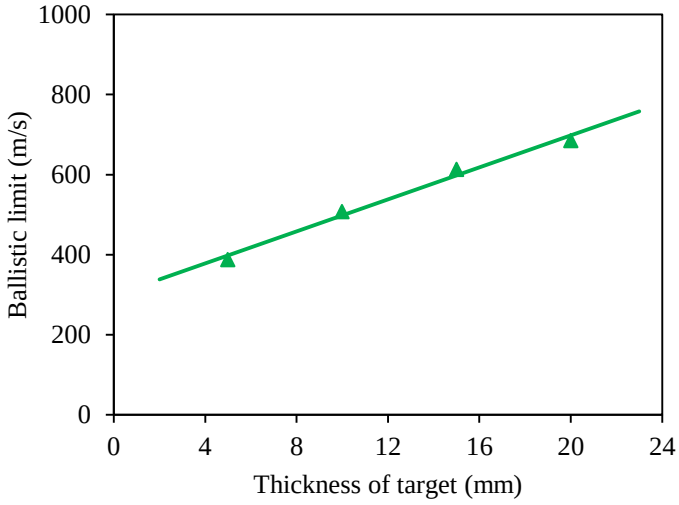

Fig. 4.17 Ballistic limit of targets against 12.7 API projectile

Table 4.18 Ballistic limit of targets against 12.7 API projectile

Target thickness (mm)	Areal density (kg/m^2)	Ballistic limit (m/s)
5	40	387.5
10	79	507.5
15	118	612.5
20	157	685

4.4 CONCLUSIONS

The experimental and finite element investigation was carried out for studying the ballistic performance of Armox 500T steel targets against 7.62 API and 12.7 API projectiles. The target thickness as well as angle of obliquity was varied corresponding to each projectile. The experimental and numerical results with respect to failure mechanism, residual projectile velocity, maximum angle of perforation and critical angle of ricochet have been compared. In general, the resistance of the target has been found to increase with increase in target obliquity. The critical angle of ricochet for 7.62 API projectile has been found to 45° for 6, 8 and 10 mm thicknesses. However, it has been predicted to be 48°, 47° and 47° for 6, 8 and 10 mm thickness respectively. The critical angle of ricochet for 12.7 API projectiles has been found to be 45° for 15 and 20 mm thick targets. The value of the critical angle of ricochet for 12.7 API projectile has been predicted to be 58°, 55º, 53º and 49º for 5, 10, 15 and 20 mm thick targets respectively. The ballistic limit of various thicknesses of Armox 500T steel targets against 7.62 and 12.7 API projectiles has also been obtained numerically. The ballistic limit of 6, 8 and 10 mm thick target against 7.62 API projectiles has been found to be 625, 713 and 796.5 m/s respectively. Similarly, the ballistic limit of 5, 10, 15 and 20 mm thick targets against 12.7 API projectiles has been predicted to be 387.5, 507.5, 612.5 and 685 m/s respectively.

CHAPTER 5

Experimental and Finite Element Studies on 7075-T651 Aluminium Targets

5.1 GENERAL

The ballistic experiments were performed on 7075-T651 aluminium targets of thicknesses 20, 32, 40 and 50 mm (corresponding areal densities 54, 87, 108 and 135 kg/m^2) respectively against 12.7 API projectiles by varying the angle of incidence until the occurrence of critical ricochet. The projectiles were fired using air defence gun at incidence velocities close to 820 m/s. The initial and residual velocity of the projectile was measured by employing the optical measurement arrangement. The high speed videography was also carried out in order to record the residual projectile velocity and perforation phenomenon. The ballistic resistance, failure mechanism and deformation of the target corresponding to a given incidence angle was studied. The critical angle of projectile ricochet for a given target thickness was also obtained experimentally. The experimental findings with respect to residual projectile velocity, damage mechanism and critical angle of ricochet were reproduced by carrying out the finite element simulations on ABAQUS/Explicit finite element code. The experimental and numerical results thus obtained were compared and discussed. The finite element simulations were subsequently performed for obtaining the ballistic limit of each target thickness at the normal incidence.

5.2 EXPERIMENTAL INVESTIGATION

The ballistic experiments were carried out at Terminal Ballistic Research Laboratory, Chandigarh (TBRL). The small arms projectiles identified for studying the response of 7075-T651 aluminium targets were 12.7 API. A detailed description of the projectile is provided in Chapter 3. The thicknesses to be studied against 12.7 API projectile were 20, 32, 40 and 50 mm. The 12.7 API projectiles were fired through the Air Defence gun, Fig. 5.1, at a constant incidence velocity close to 820 m/s. The Air Defence Gun is a typical Heavy Machine Gun.

The experiments were conducted at the ballistic test range in the open field. A detailed description of the experimental arrangement is shown in Fig. 5.2. The target was placed at a distance of 15 m from the Air Defence gun as per the standard practice. The fixtures for holding the target as well as the gun were fabricated through structural steel. The square target plates of span 500 mm x 500 mm were held at their bottom onto the fixture with the help of heavy nuts and bolts. These were tightened effectively to enable the fixed boundary. The target holding fixture could be suitably adjusted in horizontal and vertical plane in order to enable the adjustment of the impact location on the target surface. The target-holding fixture was also designed to position the target at the desired angle of obliquity between 0° to 90°. A clear distance of 75 mm was considered between the subsequent shots in order to avoid the overlapping of the damage zones. Moreover, the total number of shots at a given target was also limited to 8 in order to maintain the sufficient distance between the consecutive shots.

Fig. 5.1 Air Defence gun mounted on mounting fixture

The impact velocities of the projectile were measured with the help of infrared optical sensors. These sensors being non-contact and non-destructive in nature could be used repeatedly. To measure the incidence projectile velocity, two such infrared optical sensors were placed at distance of 11 and 13 m each from the muzzle of the Air Defence gun. A high speed counter was attached to these devices for recording the time interval. The signals generated from the projectile obstruction were used to start and stop the high speed counter. The time interval between the two consecutive obstructions was used to calculate the speed of the projectile for the given distance between the two optical sensors. The residual velocity of the projectile was measured with the help of two aluminium foil screens, particularly at the normal impact. This is due to the fact that the projectile generally followed its central axis during perforation at normal incidence. Two aluminium foil screens, each at a distance of 2 and 2.2 m, were placed behind the target. A close view of the target fixture, aluminium foil screens, reflecting screen for high speed videography and the projectile catcher is shown in Fig. 5.3. In most of the cases of oblique impact, the residual projectile velocities were measured with the help of high speed video camera. The Photron Fastcam-APX RS High-Speed Video Camera System was employed to record the perforation phenomenon and measure the residual projectile velocity. A large reflecting screen, Fig. 5.3, was used in order to trace the projectile out of fragmentation and flash. The rate of framing was in general considered to be 9000 fps. In order to avoid the damage of the camera due to splinters and fragments a robust camera shelter was employed which ensured the safety of the camera as well as the handling personnel. The projectiles were recovered after perforation of the target with the help of the recovery platform provided with the bundles of cushion pads, see Fig. 5.3. The alignment of the gun, optical devices, target and the projectile catcher was carefully

maintained with respect to the projectile trajectory, Fig. 5.2. Moreover, for performing repetitions, the position of the target was carefully changed subsequent to each shot such that the bullet hit at the designated position at the surface of the target and should not influence the zone of the previous shot.

Fig. 5.2 Experimental arrangements of (a) complete test set up (b) Air Defence gun mounted on mounting platform (c) target mounted on mounting platform (d) infrared emitter device (e) aluminium foil screen

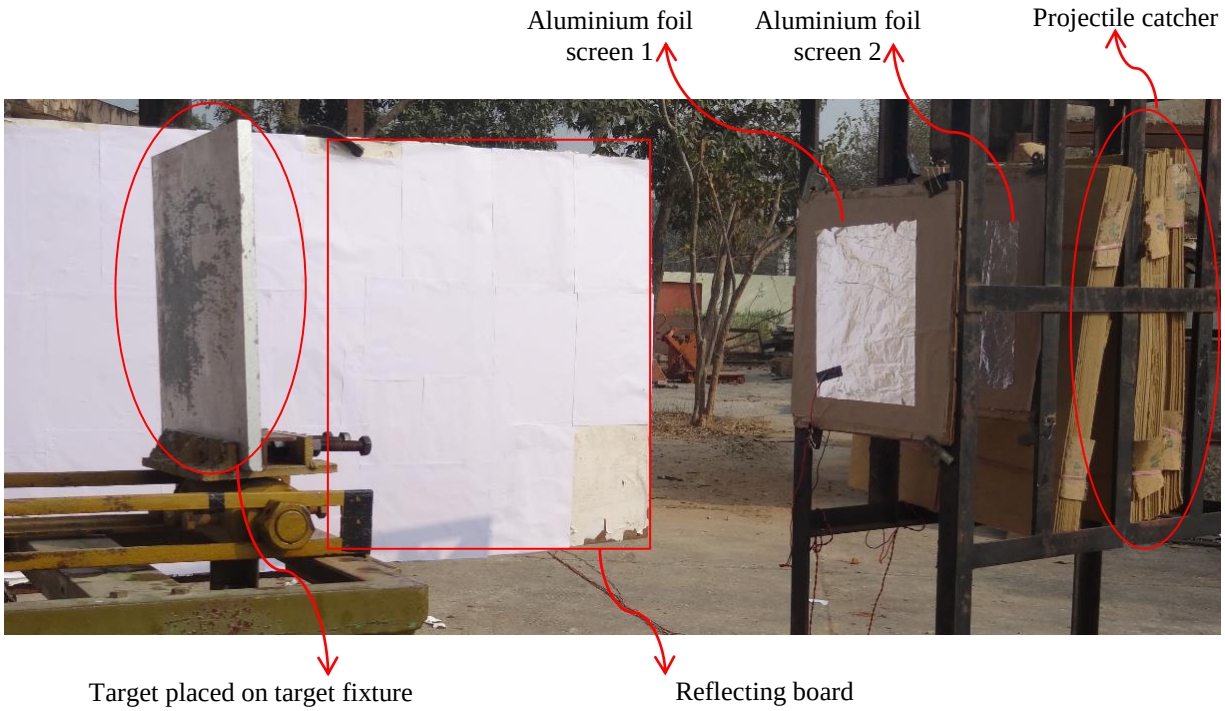

Fig. 5.3 Arrangement of target and aluminium foil screen

5.3 RESULTS AND DISCUSSION

The behaviour of 7075-T651 aluminium target against 12.7 API projectile has been studied at varying angle of incidence and the experimental and numerical results thus obtained with respect to residual projectile velocities, deformation and failure mechanism of target and critical projectile ricochet have been discussed and compared. The finite element simulations also enabled the determination of the ballistic limit at normal incidence.

5.3.1 Ballistic Resistance of 7075-T651 Aluminium Targets against 12.7 API Projectiles

The ballistic evaluation of 7075-T651 aluminium target of thicknesses 20, 32, 40 and 50 mm was carried out against 12.7 API projectiles by varying the angle of incidence until

the occurrence of projectile ricochet. The experimental results have been reproduced through finite element simulations employing ABAQUS/Explicit finite element code in conjunction with Johnson-Cook elasto-viscoplastic material model. The calibrated material parameters for the JC model were employed to predict the material behaviour of the target as well as the impacting projectile. The details of the material characterization and finite element modelling have been discussed in Chapter 2 and 3 respectively.

The experimental and numerical results for 20 mm thick target are presented in Table 5.1 corresponding to the varying angles of obliquity. The target was experimentally impacted at angles of incidence 0°, 30°, 45°, 54° and 60° at incidence velocity 818-840 m/s, however, it experienced perforation up to 54° obliquity. The residual projectile velocities remained unaffected up to 30° obliquity. At 45° obliquity, however, about 50% increase was observed in the ballistic resistance. The residual projectile velocity in some of the experiments could not be obtained, Table 5.1, due to heavy flashing (lightening) during contact of projectile and target particularly at higher obliquities. However, the numerical simulation results corresponding to all the incidence velocities have been obtained and these have been found to have close correlation with the actual results, Table 5.1. The maximum angle of perforation through experimentation as well as numerical simulations has been found to be 54°. At 60° obliquity, the experimental results showed ricochet of the projectile while the simulations predicted rebounding. The numerical simulations on the other hand predicted ricochet of the projectile at 64° obliquity. The damage pattern registered by the projectile on the target during ricochet has been accurately predicted through finite element simulations, see Fig. 5.4 (b).

Table 5.1 Resistance of 20 mm thick target by 12.7 API projectile

Incidence angle (°)	Impact velocity (m/s)	Residual velocity (m/s)	
		Experimental results	Numerical results
0	820.82	683	679
0	818.33	664	674
30	821.29	667	661
30	832.02	Perforated	679
45	838.79	439	489
45	827.71	Perforated	479
54	834.90	Perforated	236
60	840.41	Ricochet	Rebound
60	824.67	Ricochet	Rebound
62	824.67	-	Rebound
64	824.67	-	Ricochet

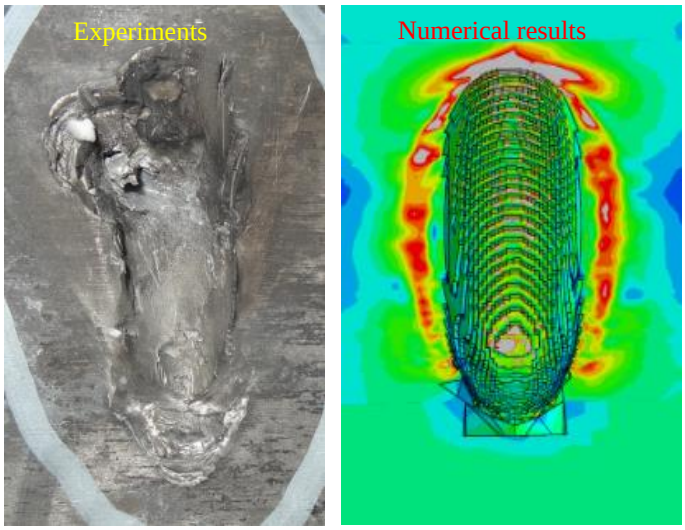

Fig. 5.4 Critical angle of ricochet at (a) 60° experimentally (b) 64° obliquity numerically impacted on 20 mm thick target

Fig. 5.5 and 5.6 show the actual and predicted failure modes of 20 mm thick target impacted by 12.7 API projectile corresponding to 0°, 35°, 45° and 54°obliquity. At normal impact, the projectile made a clean cut circular hole at the front as well back side of the target. However, the shape of the hole has been found to be elliptical at 30°, 45° and 54° obliquity. At 0° and 30° obliquity, the spallation of material at the front as well as back side

of the target has been found to be almost same in magnitude. At 45° and 54° obliquity, spallation form at the front surface of the target has been found to be deep however confined to a smaller area. Moreover, the shape of the spallation confirms the elliptical shape of the hole. At the rear surface of the target, the erosion of the material was found to be very shallow, however, it was spread over a significantly larger area. Moreover, the chipping of the material had a typical butterfly shape was also confirmed through finite element simulations. The metallurgy of the brittle material of the plate seemed responsible for this typical behavior. The outer diameter of the chipping was measured to be 75, 81, 110 and 140 mm at 0°, 30°, 45° and 54° obliquity, respectively.

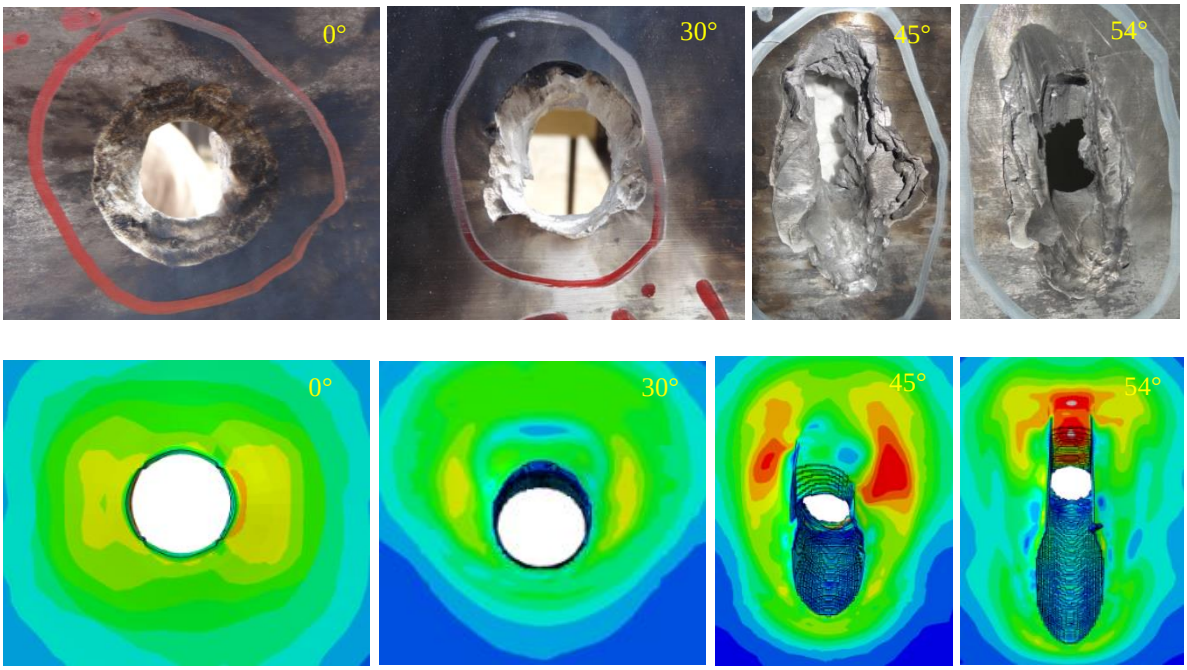

Fig. 5.5 Front side failure surface of 20 mm thick target

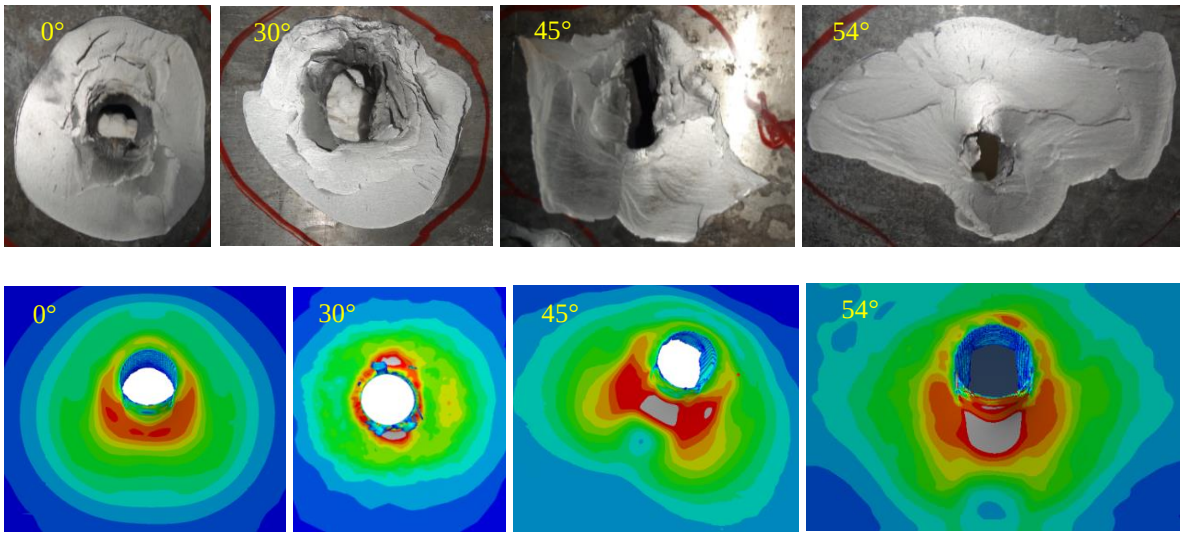

Fig. 5.6 Rear side failure surface of 20 mm thick target

Table 5.2 Resistance of 32 mm thick target by 12.7 API projectile

Incidence angle (°)	Impact velocity (m/s)	Residual velocity (m/s)	
		Experimental results	Numerical results
0	811.06	558	558
0	818.36	567	566
0	815.36	556	561
30	834.65	505	455
30	830.98	474	449
30	823.32	447	447
34	814.83	137	376
34	825.56	159	384
38	821.96	Rebound	298
38	819.57	Rebound	294
45	821.05	Ricochet	Rebound
49	821.05	-	Rebound
54	821.05	-	Ricochet

The experimental and numerical results for 32 mm thick target are presented in Table 5.2 corresponding to 0°, 30°, 34°, 38°, 45°, 49° and 54°obliquity. At normal incidence the velocity drop of the projectile has been found to be 31%. However, at 30° obliquity it has been found to be almost 42% and at 34° obliquity, it increased to 80%. At 38° obliquity, the

projectile lost all the kinetic energy and rebounded back after hitting the target. The numerical simulations accurately predicted the performance of the target at low angles of obliquity, however, these under predicted the target resistance at higher incidence angles. At 45° obliquity, the experimental results showed critical ricochet of the projectile while the same has been predicted to be at 54° obliquity.

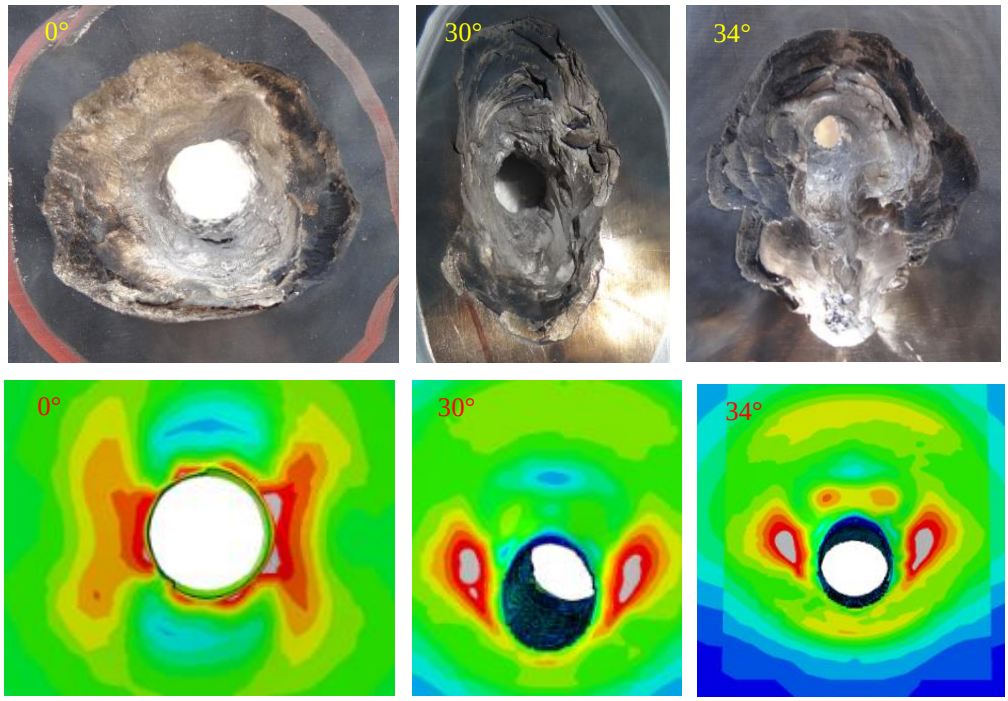

Fig. 5.7 Front side failure surface of 32 mm thick target

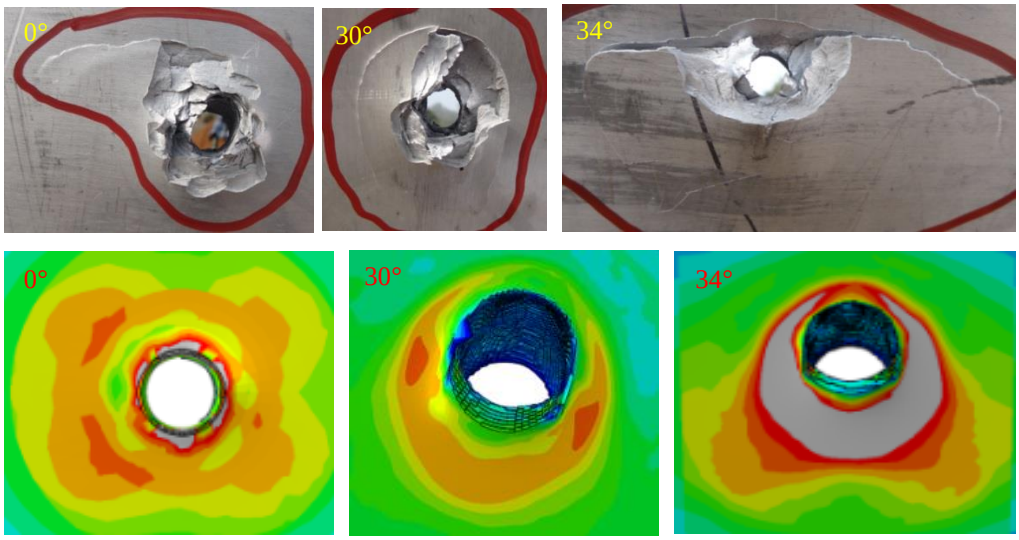

Fig. 5.8 Rear side failure surface of 32 mm thick target

Fig. 5.7 and 5.8 show the actual and predicted failure modes of 32 mm thick target impacted at varying angle of incidence. The size of the perforated hole at the front as well as rear side of the target has been found to be equivalent to that of the projectile diameter. However, the spalling of the material has been found to be more prominent at the front surface. At normal incidence the spall of the material at the front surface has been found to be circular and deep. At 30° obliquity, it took an elliptical shape. However, at 34° obliquity it was a combination of circular and elliptical shape and has been found to spread to a larger extent compared to 0° and 30° obliquity. The simulations predicted the size of hole accurately however, the chipping of the material could not be predicted. At the rear surface the scabbing of the material has been found to be smaller than what has been observed at the front surface. The sign of delamination of the material have also been observed at the rear surface. The predicted stress contours also suggested very high stresses in the impact zone adjoining the hole.

In case of 40 mm thick target the angle of incidence during experimentation was varied as 0°, 25°, 35°, 36°, 38° and 40°, see Table 5.3. As the thickness of the target was comparatively high in this case, therefore, almost 41% velocity drop was observed at normal impact itself. At 25° obliquity, the velocity drop has been found to be 56% while at 35° obliquity, it was 73%. It should be noted however that among the four shots fired at 35° obliquity, the projectile embedded in the target for two shots, while it perforated for the other two shots with residual velocity 224 and 244 m/s. The numerical simulations indicated that the perforation against all the four shots with a residual velocity in the range 168 – 174 m/s. At 36° obliquity, the experimental results showed rebounding of the projectile while the

simulations predicted embedment. The experimental results showed ricochet of the projectile at 40° obliquity while the numerical simulations at 51° obliquity.

Table 5.3 Resistance of 40 mm thick target by 12.7 API projectile

Incidence angle (°)	Impact velocity (m/s)	Residual velocity (m/s)	
		Experimental results	Numerical results
0	834.27	503	490
0	809.29	454	474
0	819.87	487	484
25	829.36	352	324
25	831.70	361	329
25	822.06	322	323
35	834.93	224	168
35	847.85	244	188
35	838.08	Embedment	172
35	839.24	Embedment	174
36	840.90	Rebound	Embedment
38	847.35	Rebound	Embedment
38	841.79	Rebound	Embedment
40	807.40	Ricochet	Rebound
40	818.16	Ricochet	Rebound
45	818.16	-	Rebound
51	818.16	-	Ricochet

Fig. 5.9 and 5.10 describe the actual and predicted failure modes of 40 mm thick target impacted at varying angle of incidence. The size of the circular hole formed in the target has been found to be equivalent to that of the projectile diameter at the front as well as rear surface. Moreover, the size of the perforated hole has been found to be same at all the angles of incidence. The spalling of the material was noticed to be very deep at the front surface and it was circular in shape at the normal impact while elliptical at oblique impact. The minor axis of the ellipse reduced as the obliquity increased from 25° to 35°. At the rear surface, the spalling was shallow and spread to a comparatively smaller area. The shape of the spalling was in agreement with that of the front surface for 0° and 25° obliquity however,

the ellipse formed at the 35° was oriented differently than the ellipse formed at the front surface. The predicted hole has been found in close agreement with that of the actual size and shape of the hole. Also, the spalling was indicated through the high intensity stress contours which agreed in shape and size with that of the actual spalling.

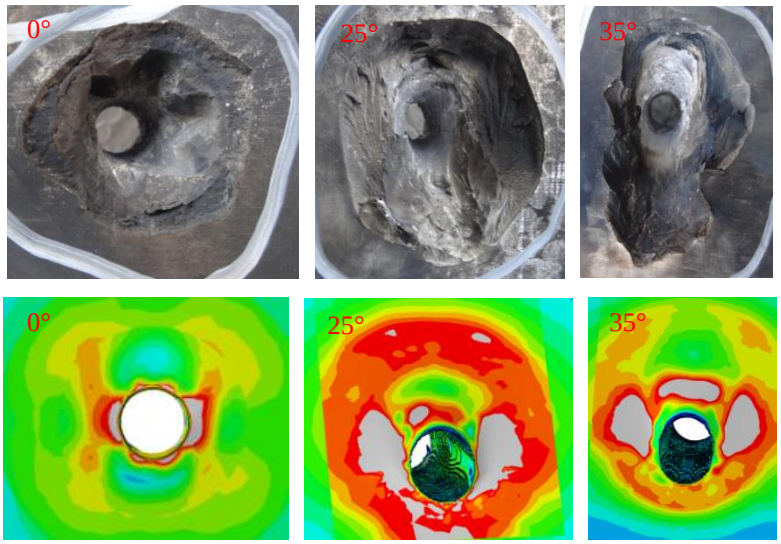

Fig. 5.9 Front side failure surface of 40 mm thick target

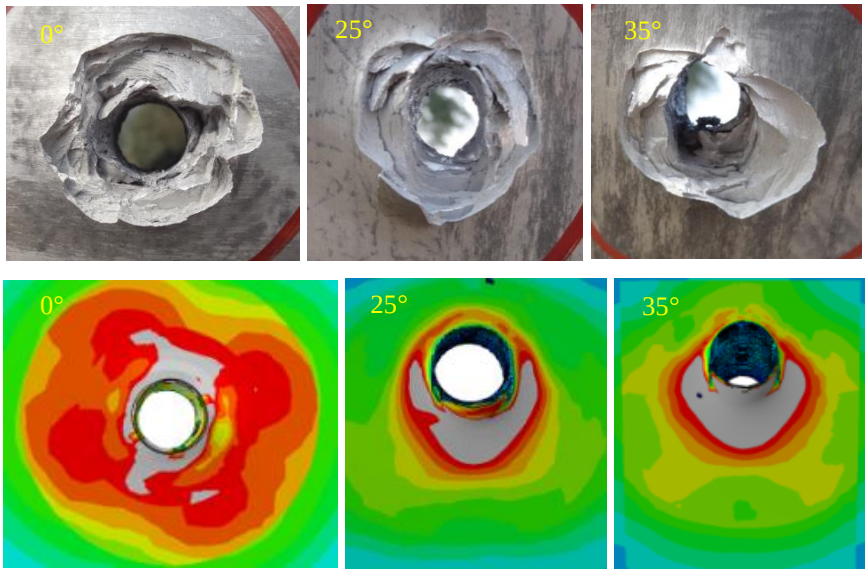

Fig. 5.10 Rear side failure surface of 40 mm thick target

The angle of incidence of 50 mm thick target was varied as 0°, 20°, 25°, 30°, 35°, and 40° due to the fact that the thickness of the target was comparatively high and almost 60%

velocity drop was observed at normal impact, Table 5.4. At 20° obliquity, the velocity drop increased to 70% and at 25° obliquity, 85%. The residual projectile velocities were closely reproduced through finite element simulations. A maximum difference between the actual and predicted residual velocity was found to be 15%. However, it has been found through experimentation that at 0°, 20° and 25° obliquity, the nose of the projectile perforated however, the broken shank remained stuck to the target. The failure mode of the front and back face of the target is shown in Fig. 5.11 and 5.12 respectively. However, the breakage of the projectile and embedment is not predicted through finite element simulations. At 30° and 35° obliquity, the experimental results showed a combination of embedment and rebounding. It was noticed that half of the projectile was embedded in the target while the remaining rebounded. The simulations however, predicted rebounding of the complete projectile. The experimental results showed the critical ricochet of the projectile at 40° obliquity while the numerical simulations predicted the same at 50° obliquity.

Table 5.4 Resistance of 50 mm thick target by 12.7 API projectile

Incidence angle (°)	Impact velocity (m/s)	Residual velocity (m/s)	
		Experimental results	Numerical results
0	813.17	312	335
0	816.63	336	338
0	828.71	346	348
20	846.17	254	246
25	850.48	122	144
25	826.04	118	131
30	833.40	Embedment	Rebound
30	832.54	Embedment	Rebound
35	847.35	Rebound	Rebound
35	829.88	Rebound	Rebound
40	824.81	Ricochet	Rebound
40	821.69	Ricochet	Rebound
49	821.69	-	Embedment
50	821.69	-	Ricochet

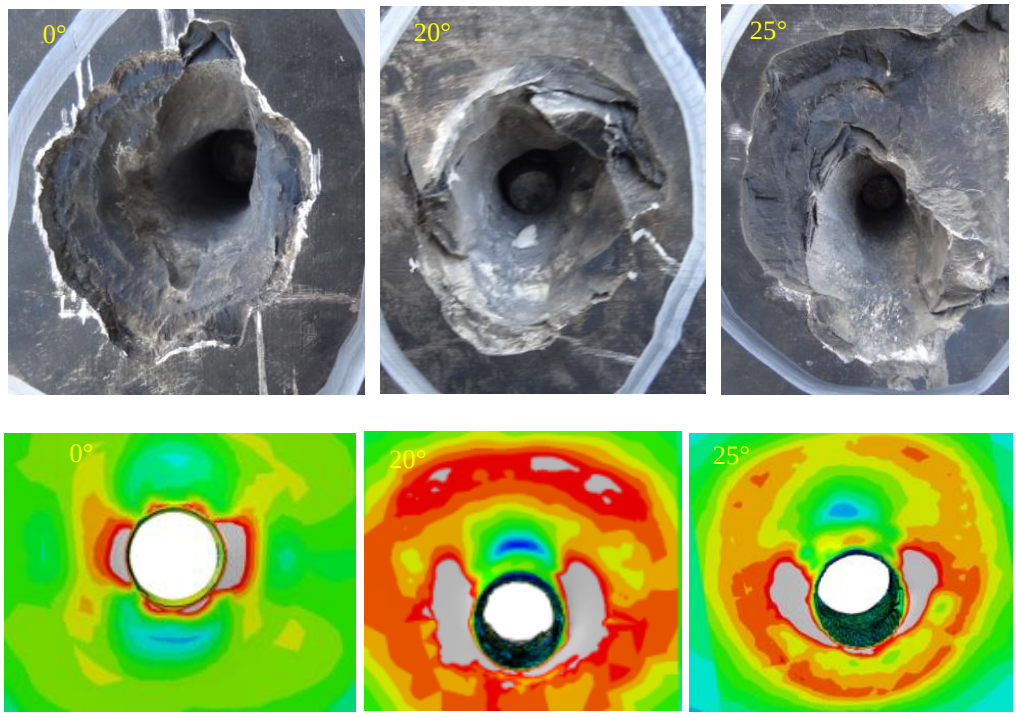

Fig. 5.11 Front side failure surface of 50 mm thick target

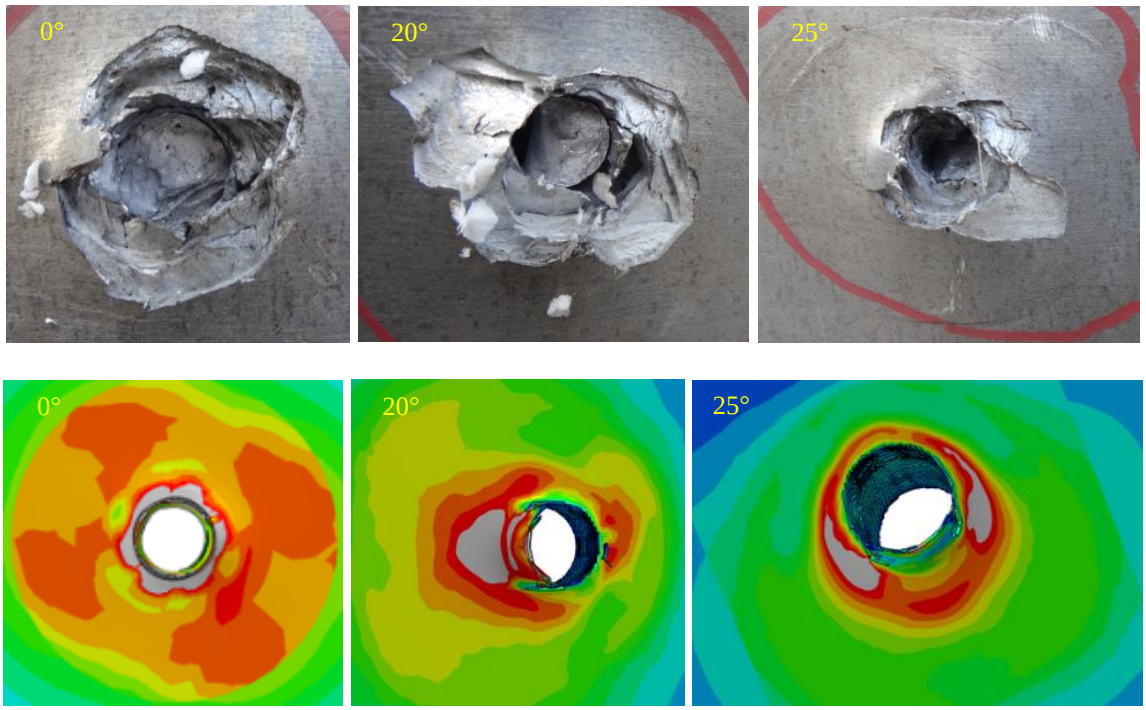

Fig. 5.12 Rear side failure surface of 50 mm thick target

The failure of the target has been found to occur in the same manner as in case of 40 mm thick target except the fact that hole formation did not occur in this case, Fig. 5.11 and 5.12. A circular crater has been formed at the front face of the target along with a tunnel indicating the penetration of projectile at normal impact. At 20° obliquity the crater was deep due to significant spalling. However, the spalling area was found equivalent to that observed in the normal impact. At 25° obliquity, the spall was spread to a larger area and a deeper tunnel was observed. The simulations indicated the formation of a clear hole at 0°, 20° and 25° obliquity while the damage induced in the adjoining area was predicted through contour plots. At the front face of the target the hole formation did not occur as the part of projectile remained stuck in the target. The scabbing was also not significant at the rear surface and the influenced area of scabbing reduced with increase in angle of obliquity. The predicted damage at the rear face of the target was in the formation of hole due to piercing of projectile, while the scabbing of material was exactly reproduced through the stress contours.

A large number of fragments ejected from 20mm thick target from the back surface of the target during projectile perforation at normal impact, see Fig 5.13. The fragmentation phenomenon was also predicted through finite element results. The flash produced during experimentation due to the contact of projectile and target is also visible in the frame and captured through the high speed video camera. The 50 mm thick target also witnessed fragmentation from the back face of the target. However, in this case the fragmentation as well as flash was not as severe as in case of 20 mm thick target, see Fig 5.14. It may be concluded that due to the low ductility, the perforation process changed when the thickness of material was varied from 20 to 50 mm.

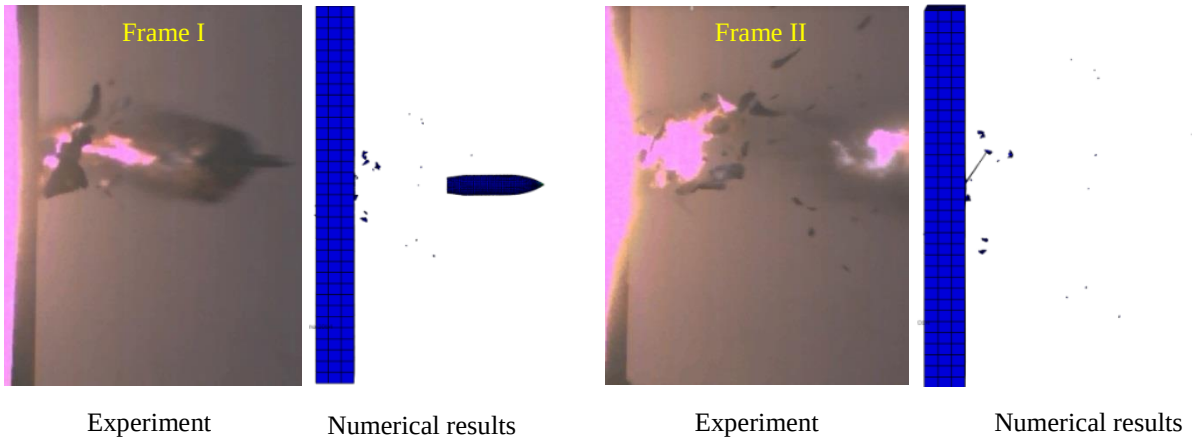

Fig. 5.13 Perforation of 12.7 API projectile on 20 mm thick target

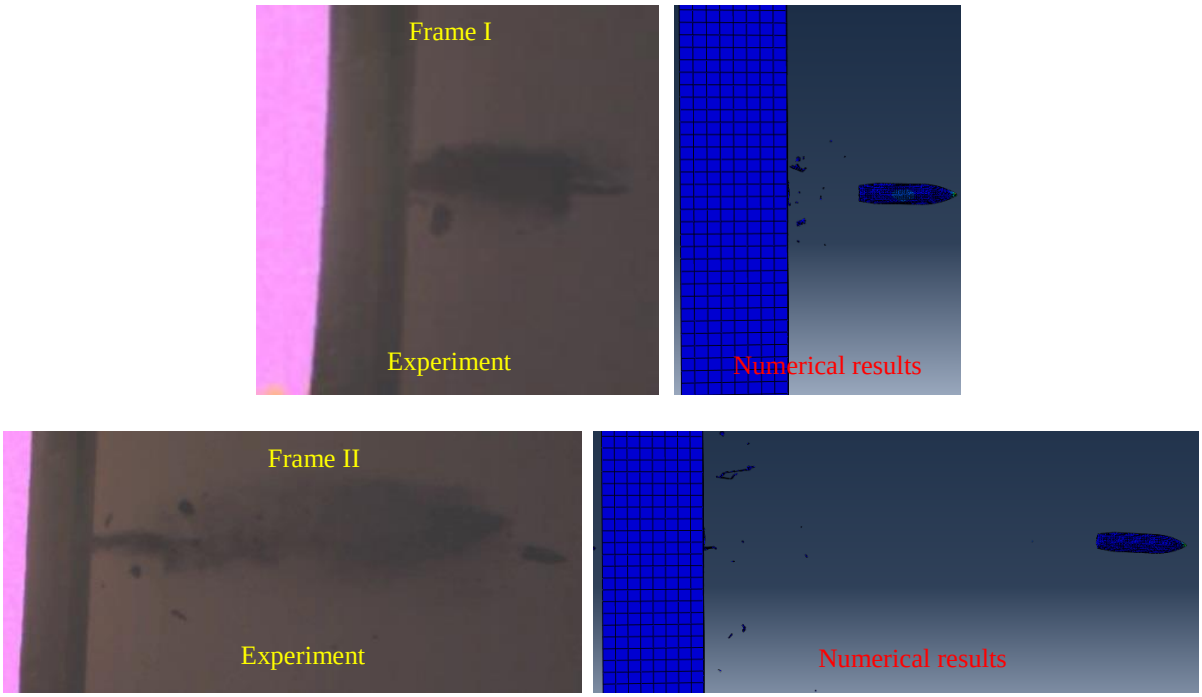

Fig. 5.14 Perforation of 12.7 API projectile on 50 mm thick target

It may be concluded here that the actual critical angle of ricochet of 20, 32, 40 and 50 mm thick target has been found to be 60°, 45°, 40°and 40° respectively and the same has been reproduced to be 64°, 54°, 51° and 50° respectively. It may also be concluded that the maximum angle of perforation in case of 20, 32, 40 and 50 mm thick target was 54°, 35°, 25°

and 25° respectively and the same was reproduced to be 54°, 38°, 35° and 25° respectively, see Table 5.5.

Table 5.5 Resistance of target against 12.7 API projectile at varying obliquity

Thickness of target (mm)	Experimental results	Numerical results
Critical angle of ricochet		
20	60°	64°
32	45°	54°
40	40°	51°
50	40°	50°
Maximum angle for perforation		
20	54°	54°
32	35°	38°
40	35°	35°
50	25°	25°

5.3.2 Evaluation of Ballistic Limit

The ballistic limit of 20, 32, 40 and 50 mm thick targets has also been obtained numerically against 12.7 API projectiles at normal impact. The numerical simulations were carried out at assumed incidence velocities to obtain the ballistic limit, see Tables 5.6-5.9. The ballistic limit velocity was calculated as the average of the highest projectile velocity not giving perforation and the lowest projectile velocity giving complete perforation of the target. After obtaining the ballistic limit velocity, the residual projectile velocity corresponding to a given incidence velocity was also calculated using the Recht-Ipson model. These calculated residual projectile velocities have also been provided in Tables 5.6-5.9 respectively for 20, 32, 40 and 50 mm thicknesses. The residual velocities were calculated based on the empirical model proposed by Recht and Ipson (1963), see Eqn. 11. The least square method was used to obtain a best fit to the numerical data and thus calibrate the parameter a and p of the model. For 20 mm thick target, the ballistic limit velocity, V_{50}, has been found to be 437.5 m/s and the parameters a and p were calibrated to be 1 and 1.91

respectively. For 32 mm thick target, the ballistic limit velocity was found to be 576.5 m/s and parameters a and p, 1 and 1.9 respectively. For 40 mm thick target the ballistic limit velocity was found to be 647.5 m/s and the model constants 1 and 1.9 respectively. For 50 mm thick target ballistic limit velocity was found to be 751.5 m/s and the parameters a and p, 1 and 1.96 respectively. Fig. 5.15 shows the impact and residual velocity data points and the corresponding Recht-Ipson fit through solid lines for 20, 32, 40 and 50 mm thick targets.

Table 5.6 Ballistic limit velocity of 12.7 API projectile impacted on 20 mm thick target

Impact velocity (m/s)	Residual velocity (m/s)		Model constants		Ballistic limit (m/s)
	Numerical results	Recht-Ipson model results	a	p	
820.82	679.2	680.6	1.0	1.91	437.5
700	524.5	532.2			
600	409.6	396.3			
500	229.2	229.1			
475	156.6	173.1			
450	57.1	96.1			
445	49.4	73.3			
440	33.8	41.1			
435	0	0			

Table 5.7 Ballistic limit velocity of 12.7 API projectile impacted on 32 mm thick target

Impact velocity (m/s)	Residual velocity (m/s)		Model constants		Ballistic limit (m/s)
	Numerical results	Recht-Ipson model results	a	p	
818.3	566.0	559.8	1.0	1.9	576.5
720	413.7	410.8			
660	305.5	302.1			
600	169.3	151.4			
580	75.0	55.1			
573	0	0			

Table 5.8 Ballistic limit velocity of 12.7 API projectile impacted on 40 mm thick target

Impact velocity (m/s)	Residual velocity (m/s)		Model constants		Ballistic limit (m/s)
	Numerical results	Recht-Ipson model results	a	p	
819.87	484.6	479.8	1.0	1.9	647.5
740	318.6	336.7			
690	191.6	219.8			
650	28.3	48.7			
645	0	0			

Table 5.9 Ballistic limit velocity of 12.7 API projectile impacted on 50 mm thick target

Impact velocity (m/s)	Residual velocity (m/s)		Model constants		Ballistic limit (m/s)
	Numerical results	Recht-Ipson model results	a	p	
816.63	338.3	321.0	1.0	1.96	751.5
790	224.2	235.5			
770	156.1	161.0			
760	112.2	107.9			
756	64.7	77.9			
753	52.2	44.4			
750	0	0			

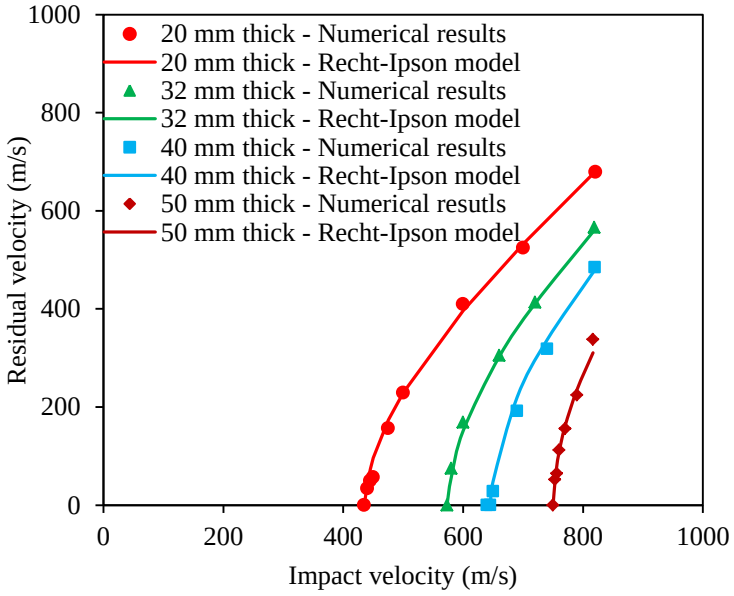

Fig. 5.15 Ballistic resistance of 7075-T651 targets against 12.7 API projectile

The predicted ballistic limit of various target thicknesses has been compared in Table 5.10. The ballistic limit of 50 mm thick target was found to be 16%, 30% and 71% higher than 40, 32 and 20 mm thick target respectively. Moreover, the ballistic limit has been found to increase almost linearly with increase in target thickness, see Fig. 5.16.

Table 5.10 Ballistic limit of 7075-T651 aluminium targets with different thickness

Thickness of target (mm)	Areal density (kg/m^2)	Ballistic limit (m/s)
20	54	437.5
32	87	576.5
40	108	647.5
50	135	751.5

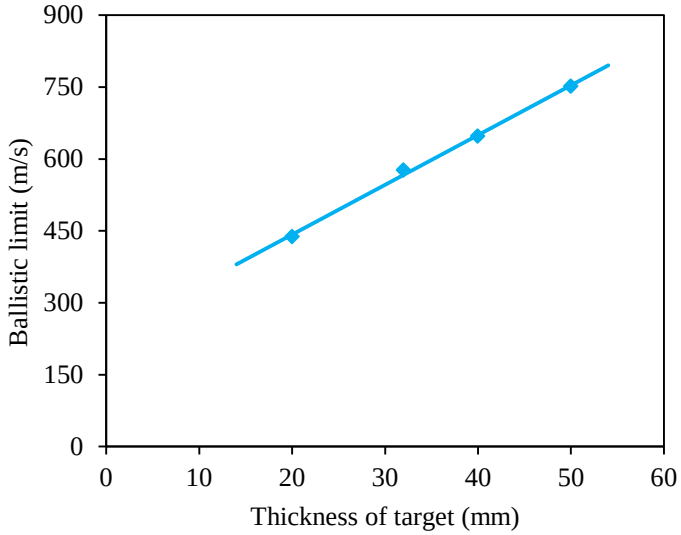

Fig. 5.16 Ballistic limit of 7075-T651 targets against 12.7 API projectile

5.4. CONCLUSIONS

The experimental and finite element investigation was carried out for studying the ballistic performance of 7075-T651 aluminium targets against 12.7 API projectiles. The target thickness as well as angle of obliquity was varied in order to study the influence on the

ballistic resistance. The experimental and numerical results with respect to failure mechanism, residual projectile velocity, maximum angle of perforation and critical angle of ricochet have been compared. In general, the resistance of the target has been found to increase with increase in angle of obliquity. For 20 and 32 mm thick targets however, the resistance of the target remained almost same up to 30° obliquity and thereafter increased with further increase in the angle of obliquity. In other target thicknesses, significant increase in the ballistic resistance was noticed even at low obliquity. The critical angle of ricochet has been found to occur at 60°, 45°, 40° and 40° for 20, 32, 40 and 50 mm thickness respectively. However, it has been predicted to be 64°, 54°, 51° and 50° for 20, 32, 40 and 50 mm thickness respectively. The ballistic limit of various thicknesses of 7075-T651 aluminium target against 12.7 API projectile has also been obtained numerically. The ballistic limit of 20, 32, 40 and 50 mm thick target against 12.7 API projectiles has been found to be 437.5, 576.5, 647.5 and 751.5 m/s respectively.

CHAPTER 6

Finite Element Studies on Mild Steel Targets

6.1 GENERAL

The finite element simulations were carried out wherein mild steel targets were subjected to impact by 7.62 API projectiles at varying angle of incidence until the occurrence of critical projectile ricochet. The thickness of the target was varied as 4.7, 6.0, 10, 12, 16, 20 and 25 mm and the corresponding areal density of the target as 37, 47, 79, 94, 126, 157 and 196 kg/m^2 respectively. The results of the finite element simulations with respect to failure mechanism of target and residual projectile velocities were compared with the experiments carried out by Gupta and Madhu (1992, 1997). The objective in framing the present study was threefold (i) the comparison of the ballistic performance of mild steel targets with Armox 500T steel targets, see the next chapter (ii) the validation of the constitutive model calibrated for mild steel (iii) the evaluation of ballistic limit for mild steel targets that has not been obtained by Gupta and Madhu (1992, 1997). The ballistic resistance, failure mechanism and deformation of the target corresponding to a given incidence angle was carefully studied. The critical angle of projectile ricochet for a given target thickness was also obtained numerically. The incidence velocity of the projectile was considered identical to what has been reported by Gupta and Madhu (1992, 1997).

6.2 EXPERIMENTAL METHODOLOGY [Gupta and Madhu (1992, 1997)]

The 7.62 API projectiles during the experimentation were fired through the standard rifle at a constant incidence velocity close to 820 m/s. The thicknesses to be studied against 7.62 API projectile were 4.7, 6.0, 10, 12, 16, 20 and 25 mm. The target was placed at a distance of 10 m from the gun and could be rotated to hold a plate at any desired angle for oblique impact. All the targets were square, 200 mm x 200 mm, in shape and were held by

their four corners onto the steel fixture with C-clamps. The impact and residual velocities of the projectile were measured with the help of four aluminium foil screens. The incidence velocity of the projectile was measured with the help of two such screens placed at a distance of 6 and 8 m each from the muzzle of the rifle. The residual velocity measurement screens were placed at 0.2 and 0.4 m each behind the target, see Fig. 6.1.

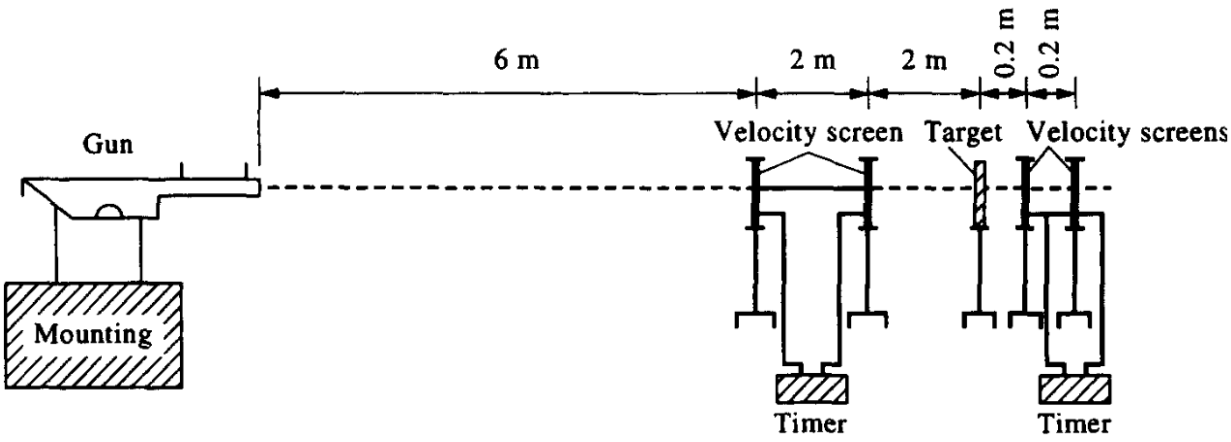

Fig. 6.1 Ballistic experimental set up, Gupta and Madhu (1997)

6.3 RESULTS AND DISCUSSION

The ballistic response of mild steel target has been studied against 7.62 API projectile by carrying out the finite element simulations on ABAQUS/Explicit finite element code. The calibrated material parameters for the JC model were employed to predict the material behaviour of the target, while the material behaviour of the projectile was incorporated from Niezgoda and Morka (2009). The material characterization and finite element modelling has been discussed in Chapter 2 and 3 respectively. All the experimental results with respect to incident and residual projectile velocities are the average of the three tests, Gupta and Madhu (1992, 1997).

6.3.1 Ballistic Resistance of Mild Steel Targets against 7.62 API Projectiles

The experimental and numerical results for 4.7 and 6 mm thick targets are presented in Table 6.1. It should be noted that for 4.7 and 6 mm thick targets, the experiments were performed only at the normal impact, Gupta and Madhu (1992), hence the finite element simulations have also been carried out at the normal incidence for these targets. The velocity drop was found to be almost 8% against both the targets. The residual projectile velocity for 4.7 and 6.0 mm thick target has been predicted with 2% and 1% deviation respectively.

Table 6.1 Resistance of 4.7 and 6 mm thick target by 7.62 API projectile

Thickness of target (mm)	Impact velocity (m/s)	Residual velocity (m/s)	
		Experimental results Gupta and Madhu (1992)	Numerical results (Present study)
4.7	821.0	758.6	772.36
6.0	866.3	792.2	799.79

Table 6.2 Resistance of 10 mm thick target by 7.62 API projectile

Incidence angle (°)	Impact velocity (m/s)	Residual velocity (m/s)	
		Experimental results Gupta and Madhu (1992)	Numerical results (Present study)
00	827.5	702.2	701.40
15	815.0	690.4	679.48
30	825.7	654.0	674.24
45	790.0	500.0	556.18
52	819.9	-	517.31
54	819.9	-	452.09
56	819.9	-	366.62
58	819.9	-	Embedment
60	819.9	493.7	Ricochet
61.5	827.9	293.6	-
62	821.4	0	-

The experimental and numerical results for 10 mm thick target are presented in Table 6.2 corresponding to varying obliquity. The target was impacted experimentally at 0°, 30°, 45°, 60°, 61.5° and 62° at incidence velocities 790 to 827 m/s, however, it experienced

perforation up to 61.5° obliquity. The simulations however predicted the perforation up to 56° obliquity. At 58° obliquity, the simulations predicted embedment while at 60° obliquity, critical projectile ricochet. The velocity drop at 0°, 15° and 30° obliquity was found to be almost identical, 15%, and this finding was also witnessed through finite element simulations. At 45° obliquity, a maximum deviation of 10% has been found between the actual and predicted residual velocities.

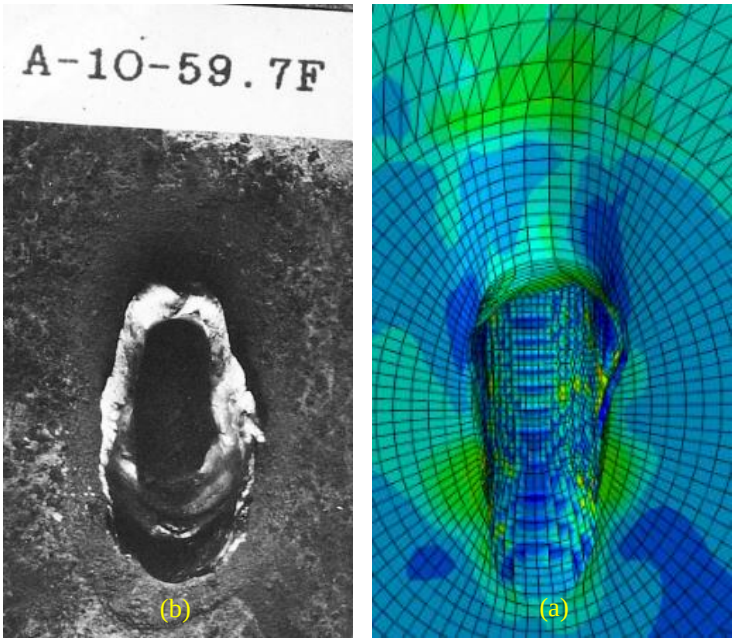

Fig. 6.2 (a) Perforation of 10 mm thick target at 59.7° and (b) embedment of the projectile at 58° obliquity

The actual and predicted failure mechanisms of 10 mm thick target at 59.7° obliquity and 58° obliquity respectively are compared in Fig. 6.2 and a close correlation between the two has been found. However, it should be noted that experimentally the projectile perforated the target, however, the simulations predicted the embedment of the projectile. The residual projectile velocity could not be obtained through experimental results for this test. However, the actual residual velocity at 45° obliquity was 500 m/s which has been reproduced, 556 m/s, within 10% deviation. However, at 60° obliquity the actual residual velocity was 493.7

m/s, while at 61.5° obliquity, 293.6 m/s. It should be noted here that with increase in target obliquity from 45° to 60° the residual velocity remained almost same while with further increase in 1.5° obliquity, it suddenly dropped almost 200 m/s. Thus, the actual residual velocities at 60° and 61.5° obliquity seem to have been overestimated.

Table 6.3 Resistance of 12 mm thick target by 7.62 API projectile

Incidence angle (°)	Impact velocity (m/s)	Residual velocity (m/s)	
		Experimental results Gupta and Madhu (1992)	Numerical results (Present study)
00	818.0	661.5	658.42
15	842.7	671.6	677.73
30	801.8	598.0	603.97
45	808.0	555.3	515.82
50	808.0	-	409.59
53	815.3	-	318.76
57	809.0	368.9	Embedment
59	815.3	Ricochet	Ricochet

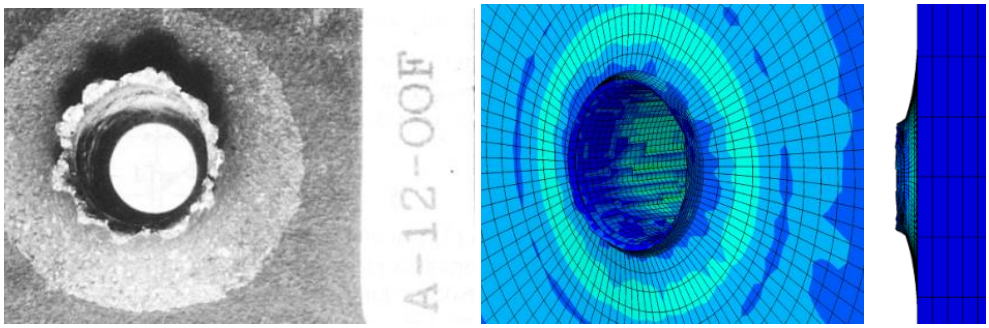

Experimental result Numerical results

Fig. 6.3 Front side failure surface of 12 mm thick target

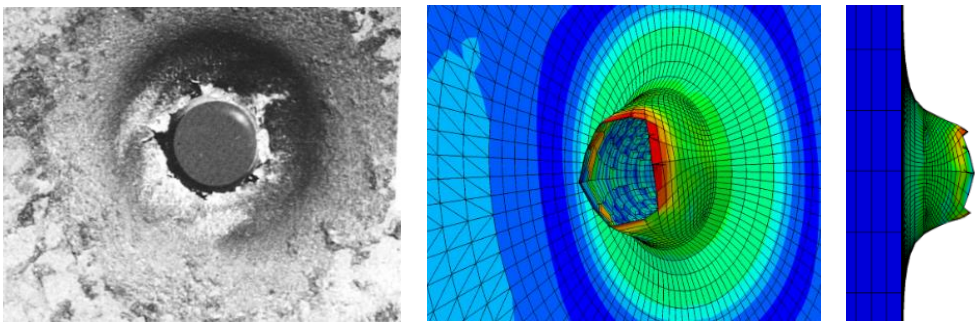

Experimental result Numerical results

Fig. 6.4 Rear side failure surface of 12 mm thick target

In case of 12 mm thick target the angle of incidence during experimentation was varied as 0°, 15°, 30°, 45°, 57° and 59° obliquity, see Table 6.3. At 0°, 15° and 30° obliquity, the predicted residual velocities are in close agreement to their actual values, [66]. The maximum difference between the actual and predicted residual velocity was found to be 7.6%, at angle of incidence 45°. At 57° obliquity, the experimental results suggested perforation of target with a residual velocity 368.9 m/s. At the same angle of obliquity however, the numerical results predicted that the projectile embedded in the target. The residual velocity, 368.9 m/s, measured during experiments through the optical measurement system could be the velocity of the fragments ejected out of the projectile or target material. At 59° obliquity, both actual and predicted results showed ricochet of the projectile.

Figs. 6.3 and 6.4 show the actual and predicted failure modes of 12 mm thick target impacted by 7.62 API projectile corresponding to 0° obliquity. The 7.62 API projectile failed the target through hole enlargement. The formation of petals at the front surface and bulge at the rear surface has also been witnessed through experiments. The numerical simulations accurately predicted the failure mode including the size of hole, petalling at the front and the bulge at the rear surface. The hole actually formed in the target was slightly bigger in size at the front than at the rear surface. The diameter of the hole in target was 9.6 and 9.0 mm at the front and rear surface respectively. A similar variation in the size of hole was predicted through the numerical simulations. The predicted diameter of the hole was 9.32 and 7.66 mm at the front and rear surface respectively.

The actual and predicted deformation of the 12 mm thick target as a result of projectile ricocheted at 59° obliquity is shown in Fig. 6.5. The projectile has registered an elliptical deformation pattern and erosion of material while sliding over the target surface. An

exact pattern of deformation and material erosion has been predicted through the numerical simulations.

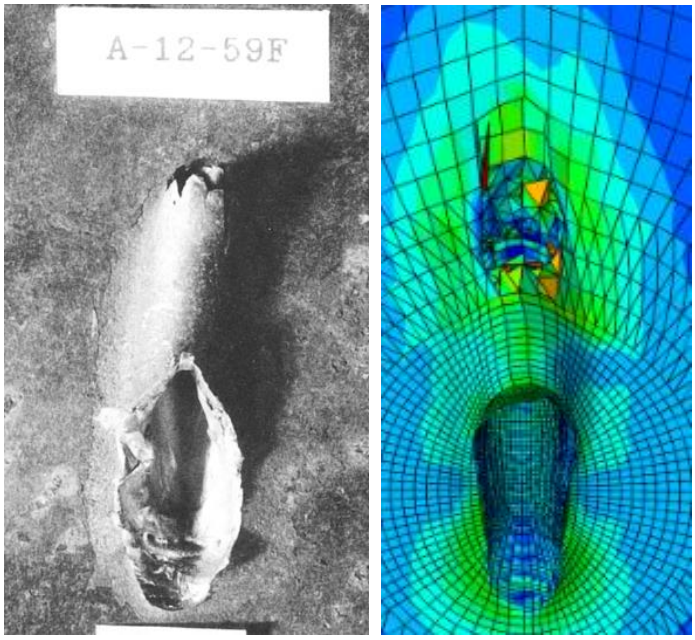

Experimental results Numerical results

Fig. 6.5 Deformation of 12 mm thick target as a result of critical ricochet at 59° obliquity

The experimental and numerical results for 16 mm thick target are presented in Table 6.4 corresponding to 0°, 15°, 30°, 45°, 47°, 49°, 51° and 58° obliquity. At normal incidence the velocity drop of the projectile has been found to be 31%. A maximum deviation of 6% has been found between the actual and predicted residual velocities. However, at 45° obliquity, the experiments revealed the embedment of the projectile, while the numerical simulations predicted perforation. The embedment of the projectile on the other hand was predicted at 51° obliquity. The critical ricochet of the projectile has been found to occur at 51° obliquity through experiments and at 58° obliquity through finite element simulations.

Table 6.4 Resistance of 16 mm thick target by 7.62 API projectile

Incidence angle (°)	Impact velocity (m/s)	Residual velocity (m/s)	
		Experimental results Gupta and Madhu (1992)	Numerical results (Present study)
00	819.7	562.3	594.09
15	817.3	544.4	577.83
30	817.7	496.3	526.09
45	806.1	0.0	314.88
47	819.2	-	266.01
49	819.2	-	133.18
51	819.2	Ricochet	0.0
54.6	819.2	Ricochet	Embedment
58	819.2	-	Ricochet

The actual and predicted deformation of the target as a result of projectile ricochet has been compared in Fig. 6.6. The projectile has registered an elliptical deformation pattern and caused erosion of material while sliding over the target surface. An exact pattern of deformation and material erosion has been predicted through the finite element simulations.

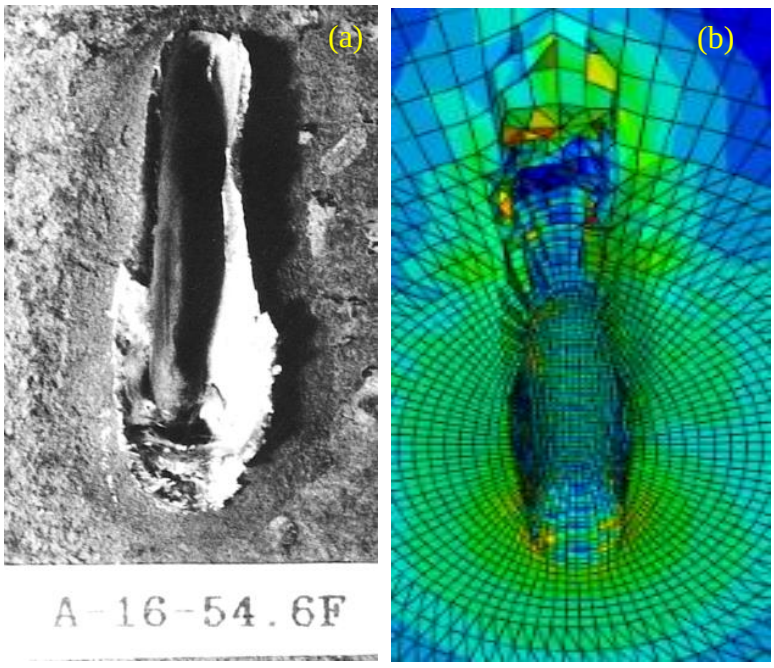

Fig. 6.6 Deformation of 16 mm thick target as a result of projectile ricochet (a) observed at 54.6° obliquity and (b) predicted at 58° obliquity

Table 6.5 Resistance of 20 mm thick target by 7.62 API projectile

Incidence angle (°)	Impact velocity (m/s)	Residual velocity (m/s)	
		Experimental results Gupta and Madhu (1992)	Numerical results (Present study)
00	820.6	404.8	429.15
15	825.6	295.6	408.72
30	817.5	151.9	312.77
35	817.5	-	232.35
38	817.5	-	106.62
45	797.3	0.0	Embedment
51	812.8	Ricochet	Rebound
57	817.5	-	Ricochet

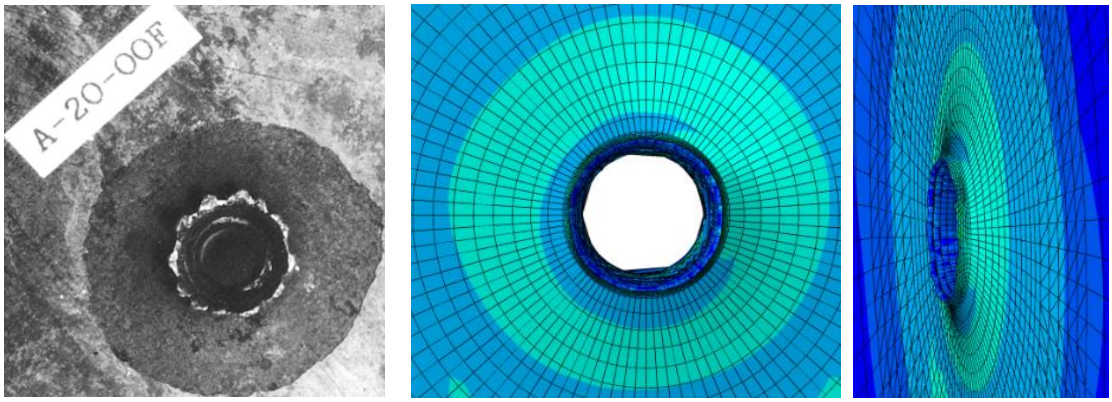

Experimental result Numerical results – Front view

Fig. 6.7 Front side failure surface of 20 mm thick target

The experimental and numerical results for 20 mm thick target are presented in Table 6.5 corresponding to varying angles of obliquity. The target was impacted at 0°, 15°, 30° and 45° obliquity at incidence velocity 812-825 m/s. At normal incidence, the velocity drop of the projectile has been found to be 50%. However, at 15° obliquity it was almost 64%, and at 30° obliquity, 81%. The actual and predicted residual projectile velocities at the normal impact have been found in close agreement. At 15° and 30°obliquity a larger difference between the experimental and numerical residual velocities was found. It may be due to the fact that the experimental residual velocity might not be measured accurately. It is also evident from the experimental result at normal impact, wherein the residual velocity was

measured to be 404.8 m/s. However, at 15° obliquity there is a sudden drop in the measured residual velocity which seems to be unrealistic. At 45° obliquity, the projectile embedded after hitting the target. The numerical simulations also witnessed embedment of projectile at 45° obliquity. The actual critical angle of ricochet was found to be 51° and it was predicted to be 57° obliquity. The actual and predicted failure modes of 20 mm thick target have been compared in Fig. 6.7 at normal impact and these have been found to be in close agreement. The failure of the target occurred through ductile hole enlargement making a clear circular hole in the target and a bulge at front surface. The size of the hole was larger at the front and smaller at the rear surface of the target.

The size of the hole formed in 12 mm thick target was also large at the front and small at the rear surface of the target, see Figs. 6.3 and 6.4. The variation of hole diameter along the target thickness may be an effect of the projectile jacket, which itself has momentum. For thin plates of low hardness material the jacket may perforate. For moderately thick targets, the jacket may be jammed and its debris may come out from the rear face along with the projectile causing increase in the rear surface hole diameter. For thicker and harder targets, the jacket may be stripped close to the entry point resulting in larger hole diameter at the front surface. The diameter of the projectile is also a driving force behind the failure mechanism particularly in thin ductile targets, Senthil and Iqbal (2013a). The size of the circular hole formed in these targets is found to be exactly equivalent to that of the projectile diameter. A larger diameter projectile requires more energy to open a hole through the target and bending of the petals. Thus, the ballistic resistance offered by the target has been found to be higher against a larger diameter projectile. The calibre radius of the projectile is also responsible for the shape and sharpness of the petals formed in thin

ductile targets. The larger projectile diameter with small nose radius and large contact area resulted in the formation of sharp and clear petals. The global target deformation is also a predominant mode of energy absorption in targets with smaller thickness and low hardness. With increase in thickness and hardens of the material the global dishing is seen to have diminished.

The experimental and numerical results for 25 mm thick target are presented in Table 6.6 for different angles of obliquity. The target was impacted at 0°, 15° and 50° obliquity at incidence velocity 799-842 m/s. However, it experienced perforation only at the normal impact. At normal incidence the velocity drop of the projectile has been found to be 87%. At 15° obliquity, the projectile lost all the kinetic energy while the finite element simulations predicted the perforation with a very low residual velocity, 14 m/s. At 50° obliquity, the experiments showed critical ricochet of the projectile while the same has been predicted to be at 57° obliquity.

Table 6.6 Resistance of 25 mm thick target by 7.62 API projectile

Incidence angle (°)	Impact velocity (m/s)	Residual velocity (m/s)	
		Experimental results Gupta and Madhu (1992)	Numerical results (Present study)
00	842.3	107.6	272.62
15	799.5	0.0	14.0
50	819.0	Ricochet	Rebound
57	819.0	-	Ricochet

Fig 6.8 (a)-(e) shows the incidence and residual velocity curves for 10, 12, 16, 20 and 25 mm thick targets as a function of angle of obliquity. It has been noticed that in case of 10, 12 and 16 mm thicknesses the resistance of target remained unaffected up to 30° obliquity. However, for 20 mm thick target there was a linear decrement of the residual velocity with

increase in angle of obliquity. On the other hand, for 25 mm thick target the perforation occurred only at the normal incidence.

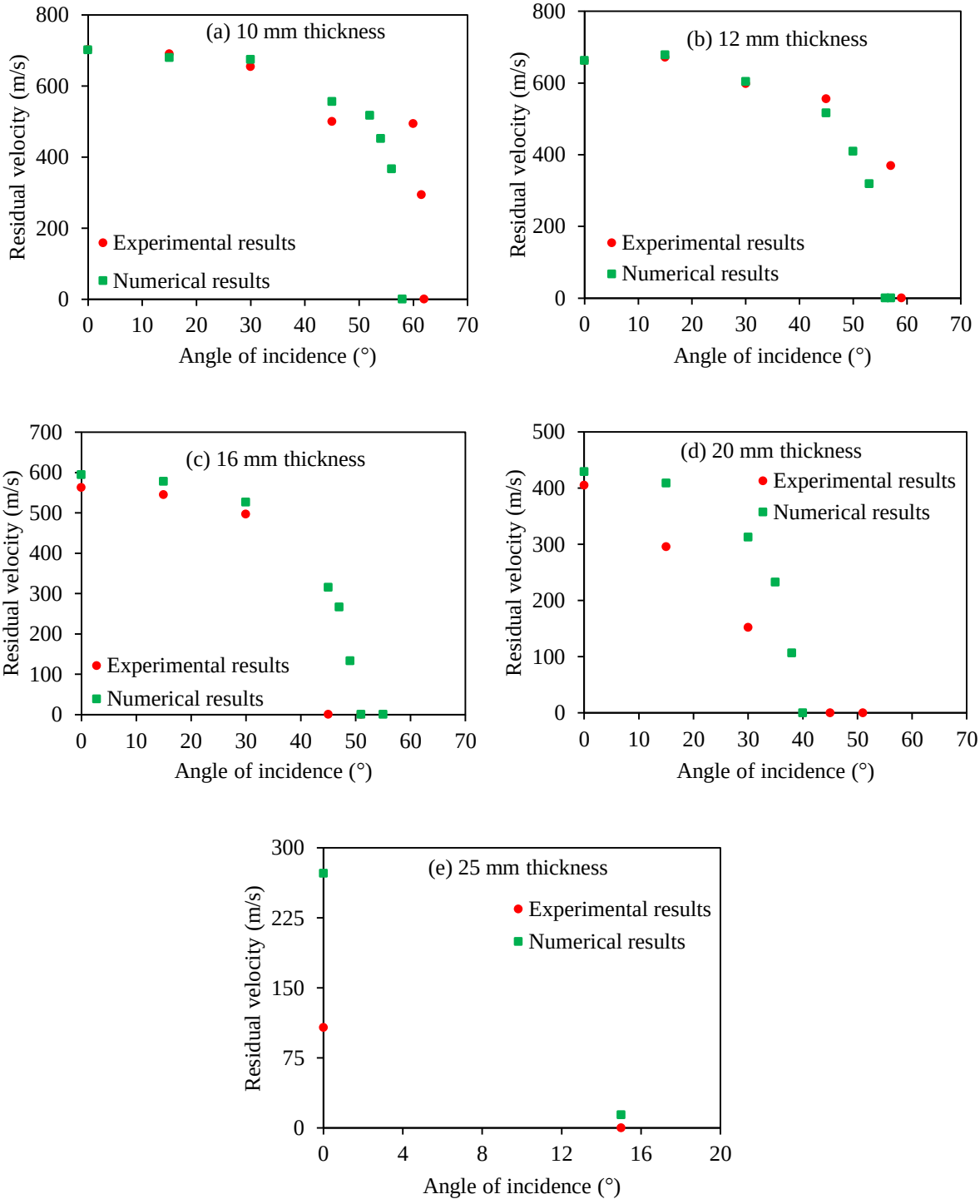

Fig. 6.8 Residual velocity of projectile as a function of varying angle of incidence

It may be concluded that the actual critical angle of ricochet decreased with increase in target thickness, Table 6.7. The actual angle of critical ricochet for 10, 12, 16, 20 and 25 mm thick target has been found to be 62°, 59°, 51°, 51° and 50° respectively, and the same has been reproduced to be 60°, 59°, 58°, 57° and 57° respectively. It may also be concluded that the maximum angle of perforation also decreased with increase in target thickness. The maximum angle of perforation for 10, 12, 16, 20 and 25 mm thick target was 61°, 59°, 45°, 45° and 0° respectively and the same was reproduced to be 58°, 56°, 51°, 40° and 17°, respectively, Table 6.7.

Table 6.7 Critical angle for ricochet and maximum angle for perforation on different thickness of target

Thickness of target (mm)	Experimental results	Numerical results
Critical angle of ricochet		
10	62°	60°
12	59°	59°
16	51°	58°
20	51°	57°
25	50°	57°
Maximum angle for perforation		
10	61°	58°
12	59°	56°
16	45°	51°
20	45°	40°
25	0°	17°

6.3.2 Ballistic Evaluation of Mild Steel Targets

The ballistic limit of 4.7, 6.0, 10, 12, 16, 20 and 25 mm thick target has also been obtained numerically against 7.62 API projectile at normal impact. The numerical simulations were carried out at assumed incidence velocities to obtain the ballistic limit, see Tables 6.8-6.14. The ballistic limit velocity was calculated as the average of the highest

projectile velocity not giving perforation and the lowest projectile velocity giving complete perforation of the target. After obtaining the ballistic limit velocity, the residual projectile velocity corresponding to a given incidence velocity was also calculated using the Recht-Ipson model. These calculated residual projectile velocities have also been provided in Tables 6.8 to 6.14 respectively for 4.7, 6.0, 10, 12, 16, 20 and 25 mm target thickness. The residual velocities were calculated based on the empirical model proposed by Recht and Ipson (1963), see Eqn. 11. The least square method was used to obtain a best fit to the numerical data and thus calibrate the parameter *a* and *p* of the model. For 4.7, 6, 10, 12, 16, 20 and 25 mm thick target, the ballistic limit velocity, V_{50}, has been found to be 274, 304.5, 400.5, 447.5, 533, 682.5 and 791 m/s and the corresponding model parameters *a* and *p* were calibrated to be 1 and 1.9 respectively. Fig. 6.9 shows the impact and residual velocity data points and the corresponding Recht-Ipson fit through solid lines for 4.7, 6, 10, 12, 16, 20 and 25 mm thick targets.

Table 6.8 Ballistic limit velocity of 7.62 API projectile impacted on 4.7 mm thick target

Impact velocity (m/s)	Residual velocity (m/s)		Ballistic limit (m/s)
	Numerical results	Recht-Ipson model results	
821.0	772.36	765.60	274
720	650.25	657.07	
620	547.46	546.95	
520	437.29	432.28	
430	333.89	321.42	
330	186.69	174.39	
280	59.88	51.66	
275	21.94	20.03	
273	0.0	0	

Table 6.9 Ballistic limit velocity of 7.62 API projectile impacted on 6 mm thick target

Impact velocity (m/s)	Residual velocity (m/s)		Ballistic limit (m/s)
	Numerical results	Recht-Ipson model results	
866.3	799.79	801.57	304.5
720.0	642.33	642.34	
620.0	528.35	529.51	
520.0	413.19	410.55	
380.0	222.52	216.54	
310.0	42.74	51.83	
306.0	22.0	26.08	
303.0	0.0	0	

Table 6.10 Ballistic limit velocity of 7.62 API projectile impacted on 10 mm thick target

Impact velocity (m/s)	Residual velocity (m/s)		Ballistic limit (m/s)
	Numerical results	Recht-Ipson model results	
827.5	701.40	710.29	400.5
750.0	609.12	619.94	
650.0	497.32	497.43	
550.0	367.86	362.40	
450.0	194.80	192.20	
440.0	170.19	169.72	
430.0	144.27	144.73	
410.0	68.29	78.80	
404.0	15.25	46.43	
397.0	0.0	0.00	

Table 6.11 Ballistic limit velocity of 7.62 API projectile impacted on 12 mm thick target

Impact velocity (m/s)	Residual velocity (m/s)		Ballistic limit (m/s)
	Numerical results	Recht-Ipson model results	
818.0	662.42	668.81	447.5
750.0	585.76	585.69	
650.0	451.91	455.09	
550.0	304.07	304.01	
520.0	251.97	249.73	
490.0	481.85	185.75	
460.0	94.27	96.05	
455.0	66.25	73.21	
450.0	20.71	40.96	
445.0	0.0	0	

Table 6.12 Ballistic limit velocity of 7.62 API projectile impacted on 16 mm thick target

Impact velocity (m/s)	Residual velocity (m/s)		Ballistic limit (m/s)
	Numerical results	Recht-Ipson model results	
819.7	594.09	603.32	533
750.0	497.21	508.22	
650.0	354.63	353.37	
620.0	293.34	298.70	
580.0	222.28	212.44	
540.0	74.44	76.64	
535.0	29.11	39.55	
531.0	0.0	0.00	

Table 6.13 Ballistic limit velocity of 7.62 API projectile impacted on 20 mm thick target

Impact velocity (m/s)	Residual velocity (m/s)		Ballistic limit (m/s)
	Numerical results	Recht-Ipson model results	
820.6	429.15	431.91	682.5
750.0	276.59	289.66	
710.0	157.78	178.17	
685.0	15.48	50.00	
680.0	0.0	0.00	

Table 6.14 Ballistic limit velocity of 7.62 API projectile impacted on 25 mm thick target

Impact velocity (m/s)	Residual velocity (m/s)		Ballistic limit (m/s)
	Numerical results	Recht-Ipson model results	
842.3	272.62	266.78	791
820.0	238.44	196.31	
810.0	196.55	156.68	
795.0	71.71	68.70	
787.0	0	0.00	

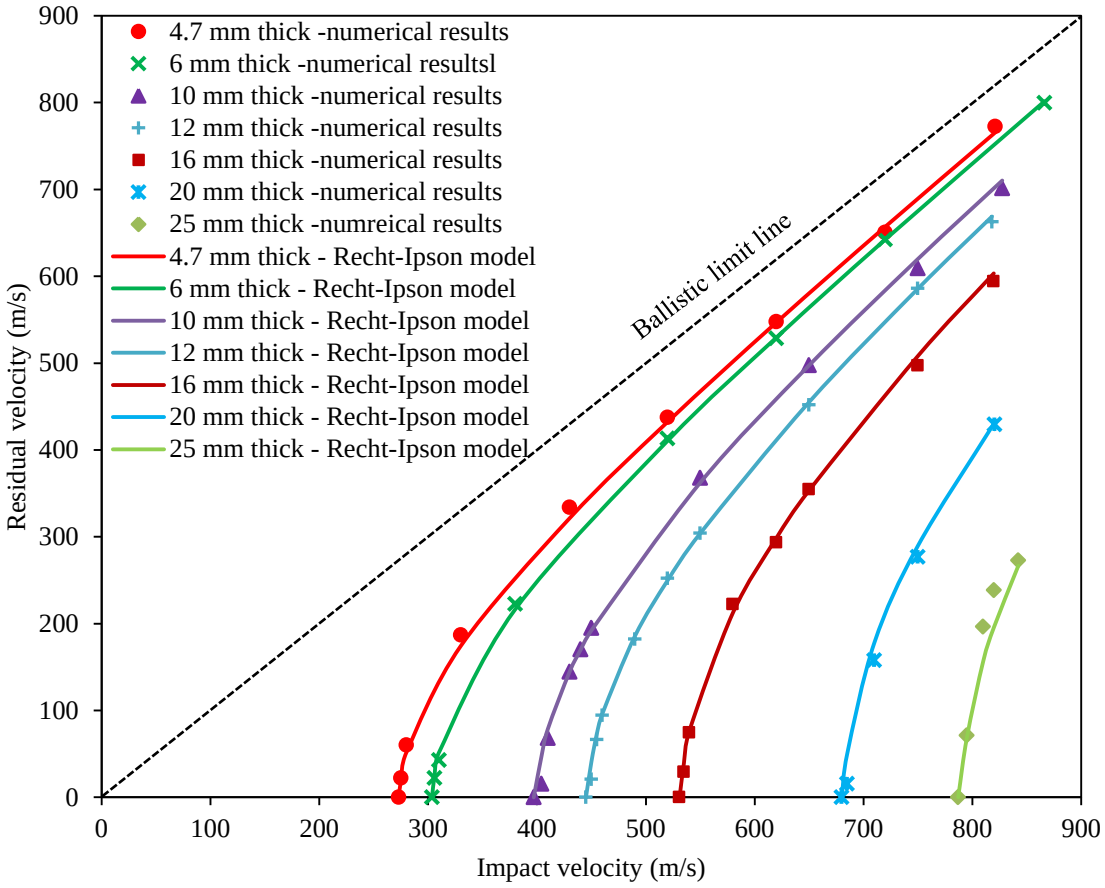

Fig. 6.9 Predicted incidence and residual velocities and the Recht-Ipson fit

Table 6.15 Ballistic limit of mild steel targets with different thickness

Thickness of target (mm)	Areal density (kg/m^2)	Ballistic limit (m/s)
4.7	37	274.0
6	47	304.5
10	78.5	400.5
12	94	447.5
16	126	533.0
20	157	682.5
25	196	791.0

The predicted ballistic limit of various target thicknesses has been compared in Table 6.15. The ballistic limit of 25 mm thick target was found to be 13%, 32%, 43%, 49%, 61% and 65% higher than 20, 16, 12, 10, 6 and 4.7 mm thick target respectively. Moreover, the ballistic limit has been found to increase almost linearly with increase in target thickness, see Fig. 6.10.

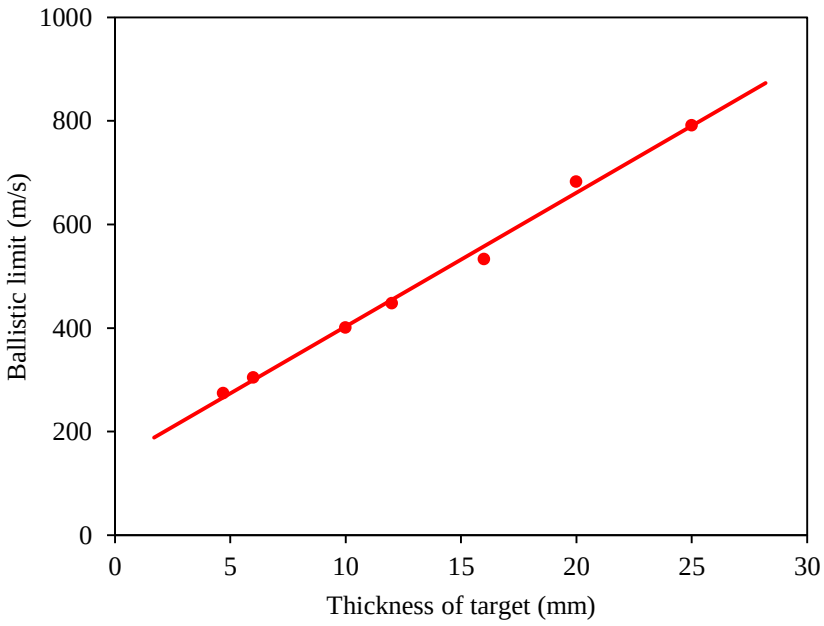

Fig. 6.10 Ballistic limit of mild steel targets against 7.62 API projectile

6.4 CONCLUSIONS

The finite element studies were carried out for studying the ballistic performance of mild steel targets against 7.62 API projectiles. The target thickness as well as angle of obliquity was varied. The experimental and numerical results with respect to failure mechanism, residual projectile velocity, maximum angle of perforation and critical angle of ricochet have been compared. A close correlation between the experimental findings and the predicted results has been found. In general, the resistance of the target has been found to increase with increase in target obliquity. For 10, 12 and 16 mm thick targets however, the resistance of the target remained almost same up to 30° obliquity and thereafter increased with further increase in angle of obliquity. For 20 mm thick target the residual velocity of the projectile decreased linearly with increase in target obliquity. For 25 mm thick target the perforation occurred only at the normal incidence. The critical angle of projectile ricochet has been found to decrease with increase in target thickness. The ballistic limit for all the mild steel targets has also been obtained numerically. The ballistic limit of 4.7, 6, 10, 12, 16, 20 and 25 mm thick target against 7.62 API projectiles has been found to be 274, 304.5, 400.5, 447.5, 533, 682.5 and 791 m/s respectively. The ballistic limit thus obtained has been employed to calibrate the Recht-Ipson empirical model for calculating the residual projectile velocity corresponding to a given incidence velocity.

CHAPTER 7

Comparison of Ballistic Performance of Armox 500T Steel, 7075-T651 Aluminium and Mild steel Targets

7.1 GENERAL

A comparative study has been carried out wherein the ballistic performance of different target materials has been compared. A brief comparison of the constitutive properties of each target material has been provided in the beginning of the chapter. Thereafter, the behaviour of mild steel, Armox 500T steel and 7075-T651 aluminum targets has been compared against 7.62 and 12.7 API projectiles with respect to failure mechanism, ballistic limit, maximum angle of perforation and critical angle of ricochet. The efficiency of 7.62 and 12.7 API projectiles has also been compared for Armox 500T steel targets.

7.2 MATERIAL HARDNESS, STRENGTH AND DUCTILITY

The stress strain relationship of mild steel, Armox 500T steel and 7075-T651 aluminum alloy has been compared in Fig. 7.1. The hardness of the material was found to be 145, 500 and 215 BHN respectively and the yield strength 304 MPa , 1372 MPa and 448 MPa respectively. The mild steel did not depict significant strain hardening. Though there was a sharp increase in the strength immediately after yielding, 300 to 400 MPa, however, thereafter the stress remained almost constant until the fracture, Fig. 7.1 (a). A nominal drop in the strength was however, noticed at the onset of fracture. The ultimate strength of mild steel was found to be 450 MPa and the total elongation of the material almost 30%. The Armox 500T steel on the other hand, described a sharp and significant material hardening subsequent to yield point, Fig. 7.1 (b). The ultimate strength of the material was 1600 MPa. The softening of the material subsequent to peak load was also found to be highly steep due to significant necking; a measure of material ductility. However, the total elongation of the material was found to be (10%), substantially lesser than mild steel. The aluminium 7075-

T651 showed a nominal strain hardening and sudden fracture with insignificant necking. The total elongation of the material was found to be (12%) close to that of the Armox 500T steel, 7.1 (c). It may be concluded here that the mild steel had better ductility than the other two materials and it also described a purely isotropic behaviour. On the other hand, the degree of anisotropy was found to be highest in the aluminium. A detailed discussion and investigation about the anisotropic behaviour of aluminium is presented in Chapter 2.

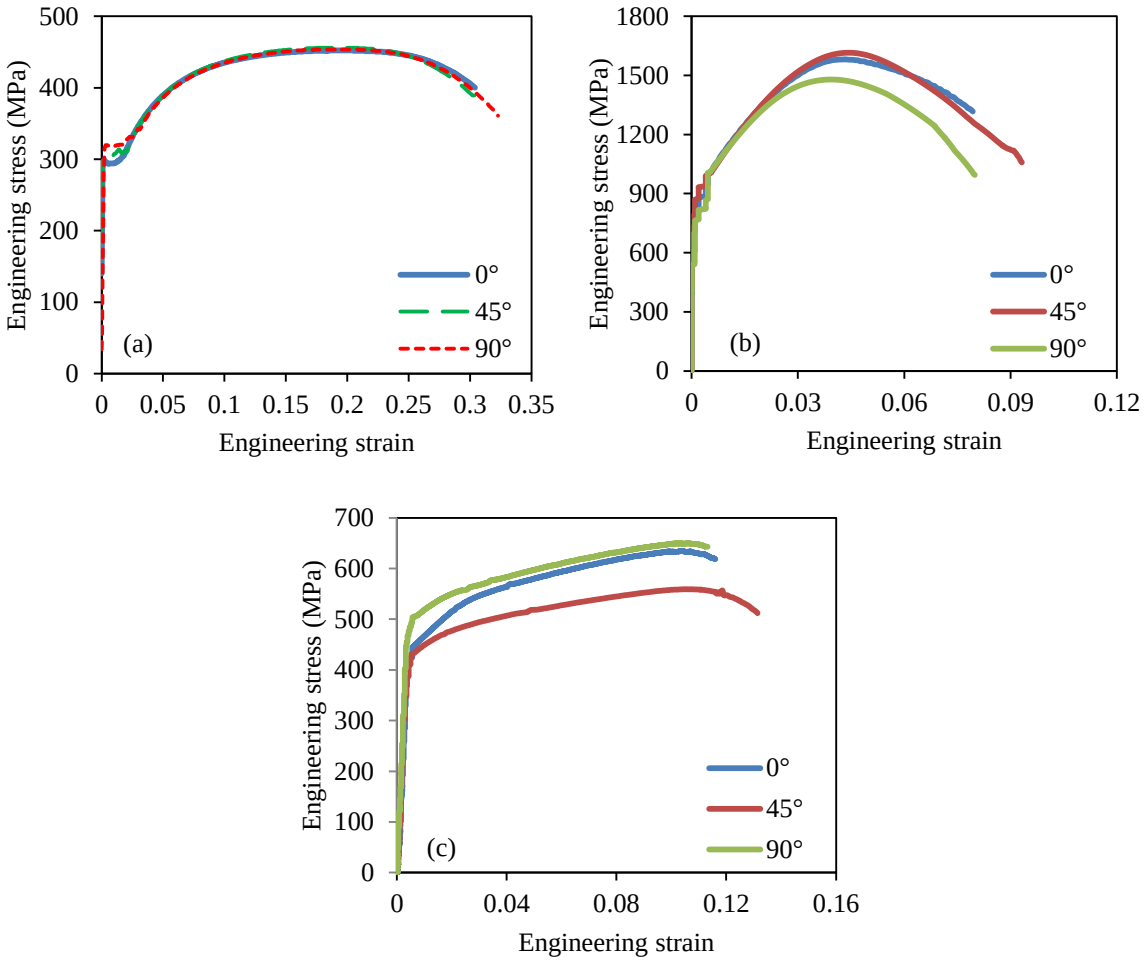

Fig. 7.1 Stress-strain relationship under quasi-static loading for (a) mild steel (b) Armox 500T steel (c) 7075-T651 aluminium target

7.3 DEFORMATION AND FAILURE MECHANISM

The mild steel target experienced hole enlargement and bulging when impacted by the 7.62 API projectile, Fig. 7.2 (a). The circular hole formed in the target was equivalent to that of the diameter of the projectile and there was no scabbing or spalling of the material during perforation process. At the front face the sign of petal formation was also observed which indicated the expansion of the hole created by the tip of the projectile. The Armox 500T steel target however, experienced significant spalling from the front as well as rear face of the target and the hole developed in the target was also not distinctly circular, Fig.7.2 (b). The material aslo experineced fragmentation during perforation process. The high strength, high hardness is responsible behined such fracture behaviour.

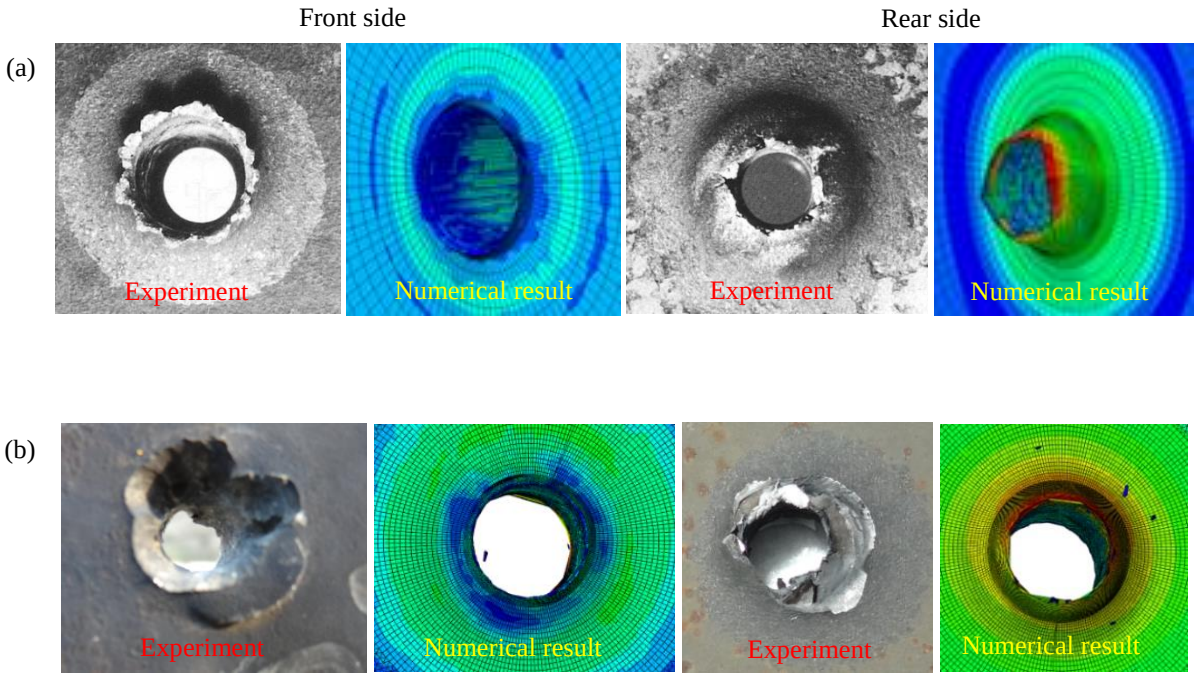

Fig. 7.2 Failure mechanism of (a) 12mm thick mild steel and (b) 10 mm thick Armox 500T steel targets against 7.62 API projectile

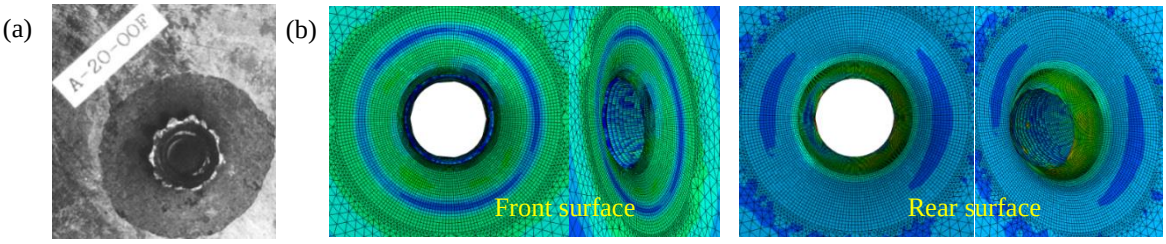

Fig. 7.3 Failure mechanism of 20 mm thick mild steel target against (a) 7.62 API and (b) 12.7 API projectiles

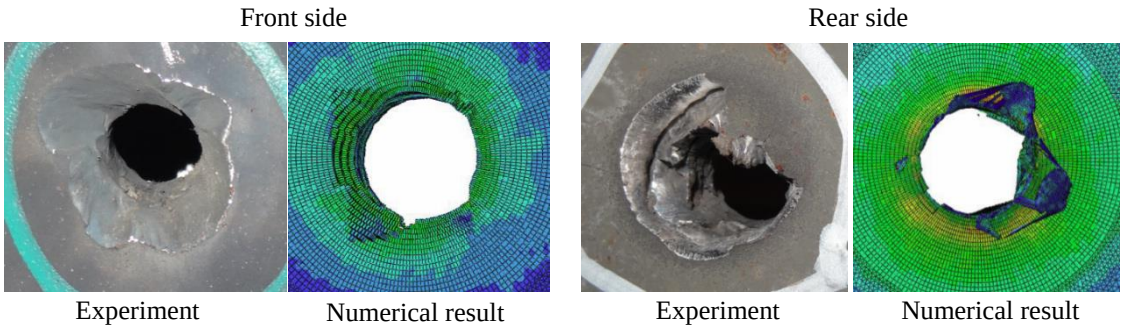

Fig. 7.4 Failure mechanism of 20 mm thick Armox 500T steel target against 12.7 API projectile

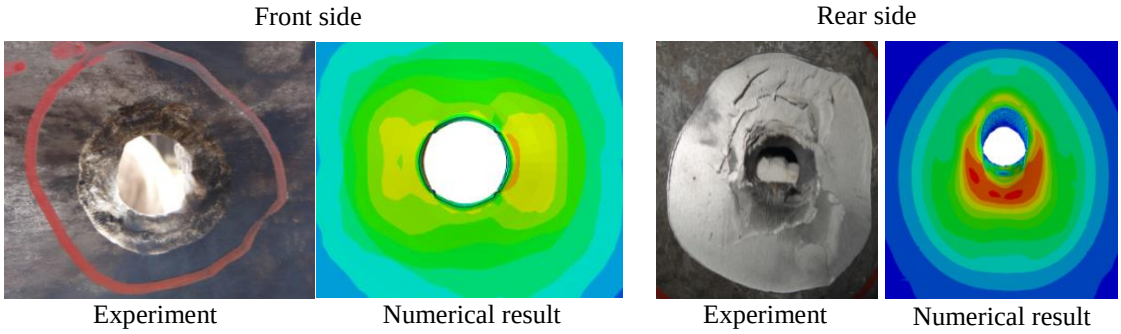

Fig. 7.5 Failure mechanism of 20 mm thick 7075-T651 aluminium target against 12.7 API projectile

The failure mechanism of 20 mm thick mild steel, Armox 500T steel and aluminium 7075-T651 target against 12.7 API projectile is shown in Figs. 7.3 to 7.5 respectively. The experimental result of mild steel target impacted by 7.62 API projectile is also presented in Fig. 7.3 (a) Gupta and Madhu (1992). Fig. 7.3 (b) presents the numerical simulation results of the failure mechanism of the target against 12.7 API projectile. The target has experienced

bulging at the front as well as rear side and developed a clean cut circular hole. No sign of fragmentation was observed either through the experimental results reported by Gupta and Madhu (1992) against 7.62 API projectile or through the finite element simulations conducted in the present study against 12.7 API projectile. The 20 mm thick Armox 500T steel target however, experienced significant scabbing at the front as well as rear side and distorted petal formation, Fig. 7.4. The size of the hole was equivalent to that of the projectile diameter in mild steel as well as Armox steel targets. The failure mechanism of 20 mm thick 7075-T651 aluminium target was almost similar to that of the Armox steel target, Fig. 7.5. However, in this case the material erosion from the front side was smaller but deep however, from the rear side it was spread over a larger area. The rear side scabbing indicated a sort of delamination of the material from the impact zone.

The damage induced in the mild steel, Armox 500T steel and 7075-T651 aluminium alloy targets as a result of projectile ricochet is indicated in Figs. 7.6 (a) – (f) respectively. The damage in case of mild steel target has been shown as a result of 7.62 API projectile impact while in case of Armox steel and aluminium targets as a result of 12.7API projectile. In case of mild steel target the material has been pushed aside by the impacting projectile however, there is no removal of the material from the surface due to high ductility and low strength. On the other hand, in case of Armox steel and aluminum targets the erosion of the material has been noticed. The formation of damaged pattern on the mild steel is also very clear [Fig. 7.6(a)] indicating the flight path of the projectile while in case of Armox steel and aluminium target the signature of the projectile is not clearly defined experimentally, see Fig. 7.6 (c) and (e). However, the simulations predicting the projectile ricochet against Armox

steel and aluminum target revealed a clearer pattern of the projectile sliding over the target surface, see Fig. 7.6 (d) and (f).

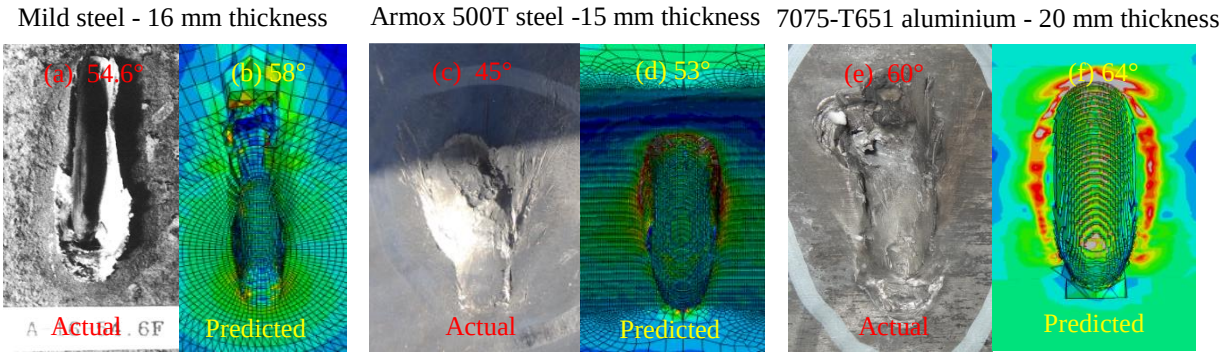

Fig. 7.6 Damage induced in mild steel target due to critical ricochet of 7.62 API projectile while Armox 500T steel and 7075-T651 aluminium target due to critical ricochet of 12.7 API projectile

7.4 BALLISTIC PERFORMANCE OF MILD STEEL AND ARMOX 500T STEEL TARGET AGAINST 7.62 API PROJECTILES

The ballistic limit of 6 and 10 mm thick mild steel and Armox 500T steel targets has been compared against 7.62 API projectiles at the normal incidence, see Table 7.1. For both of these thicknesses, the ballistic limit of Armox 500T steel has been found to be 100% higher than the mild steel despite the fact that the hardness as well as strength of Armox 500T steel is about four to five times higher than mild steel.

Table 7.1 Ballistic resistance of 6 and 10 mm thick targets against 7.62 API projectile

Target Material	Hardness (BHN)	Yield strength (MPa)	Ultimate strength (MPa)	Ballistic limit (m/s)	
				6 mm	10 mm
Armox 500T	510	1352	1475	625	796.5
Mild steel	140	304	449	305	401

The incidence and residual velocities of 7.62 API projectile simulated numerically and calibrated through the Recht-Ipson model (1963) for mild steel and Armox 500 T steel targets have been compared in Fig. 7.7 (a) and (b) respectively for 6 and 10 mm thickness. As such the ballistic resistance of Armox 500T steel has been found to be significantly higher than the equivalent mild steel target. However, the difference between the ballistic resistance of two materials has been found to decrease with increase in the incidence projectile velocity.

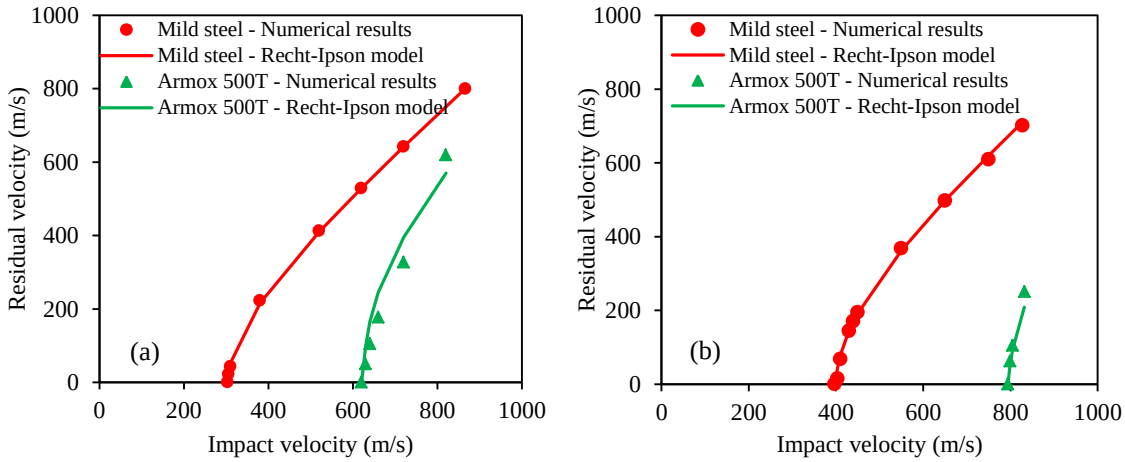

Fig. 7.7 Impact and residual velocity of 7.62 API projectile impacted on (a) 6 mm and (b) 10 mm thick targets

7.5 BALLISTIC PERFORMANCE OF ARMOX 500T STEEL AND 7075-T651 ALUMINIUM TARGET AGAINST 12.7 API PROJECTILES

The ballistic limit of 20 mm thick Armox 500T steel and 7075-T651 aluminium target has been compared in Table 7.2 at the normal incidence against 12.7 API projectile. The ballistic limit of Armox 500T steel target has been found to be 55% higher than the equivalent 7075-T651 aluminum target. The weight of Armox 500T steel target was 39 kg while that of the 7075-T651 aluminium target was 14 kg. Therefore, it may be concluded that the weight of Armox 500T steel target is 280% higher than the equivalent aluminium target

while the increment in the ballistic limit is merely 55%. The incidence and residual velocities of 12.7 API projectile have also been shown for comparison of the ballistic resistance between the two materials and these lead to the similar conclusion Fig. 7.8.

Table 7.2 Ballistic resistance of 20 mm thick targets against 12.7 API projectile

Target Material	Hardness (BHN)	Yield strength (MPa)	Ultimate strength (MPa)	Ballistic limit (m/s)
Armox 500T	510	1352	1475	685
AA 7075-T651	215	448	575	437.5

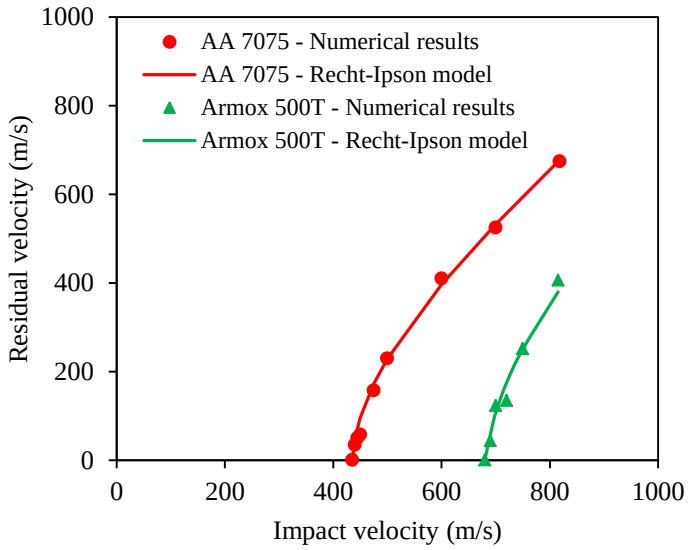

Fig. 7.8 Impact and residual velocities of 12.7 API projectile impacted on 20 mm thick target

7.6 COMPARISON OF THE PERFORMANCE OF 7.62 AND 12.7 API PROJECTILES AGAINST ARMOX 500T STEEL TARGET

The performance of 7.62 and 12.7 API projectiles has also been compared against 10 mm thick Armox 500T steel target, see Table 7.3. The mass of the 12.7 API projectile was about five times higher than that of the 7.62 API projectile thus the kinetic energy offered by 12.7 API projectile was also five times higher than that offered by 7.62 API projectile.

However, the energy absorbed by the 10 mm thick target against 7.62 API projectile was three times higher than the energy absorbed by the same target against 12.7 API projectiles.

Table 7.3 Performance of API projectiles impact on 10 mm thick Armox 500T plate

Projectile	Mass of projectile (g)	Impact velocity (m/s)	Residual velocity (m/s)		Energy offered by projectile (J)	Energy absorbed by target (J)
			Experimental results	Numerical results		
7.62 API	5.5	831	238	251	1903	927
12.7 API	30.06	831	686	702	10395	251

7.7 BALLISTIC LIMIT OF MILD STEEL, ARMOX 500T STEEL AND 7075-T651 ALUMINIUM TARGETS

The ballistic limit of mild steel and Armox 500T steel targets has been compared against 7.62 API projectiles, see Fig. 7.9. It has been concluded that the 10 mm thick Armox 500T steel target offered the ballistic limit equivalent to that of the 25 mm thick mild steel target. The ballistic resistance of Armox 500T steel and 7075-T651 aluminium has also been compared against 12.7 API projectiles, see Fig. 7.10. It has been concluded that the 20 mm thick Armox 500T steel target offered the ballistic limit equivalent to that of 40 mm thick 7075-T651 aluminium target.

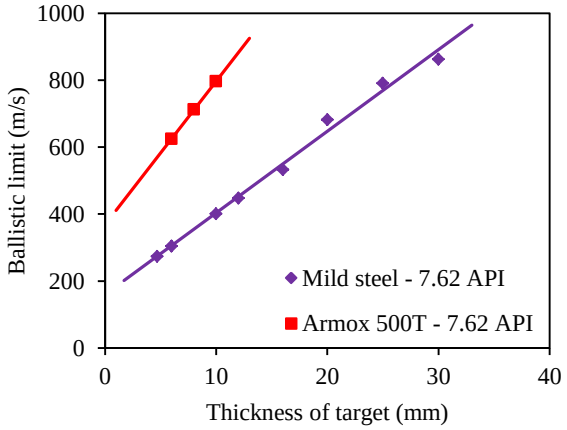

Fig. 7.9 Ballistic resistance of targets against 7.62 API projectile as a function of thickness of targets

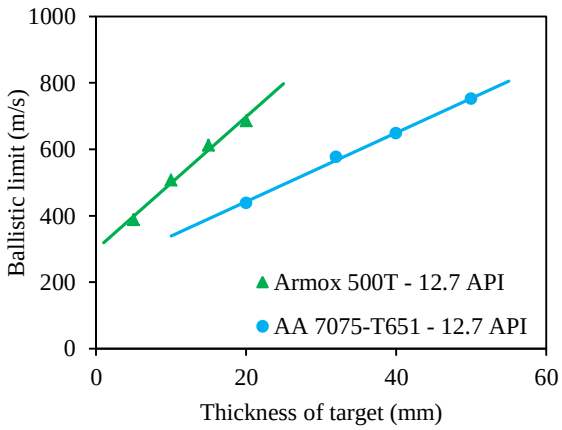

Fig. 7.10 Ballistic resistance of targets against 12.7 API projectile as a function of thickness of targets

The ballistic performance of mild steel and Armox 500T steel as a function of target areal density has been compared against 7.62 API projectile, Fig. 7.11. It has been found that 78 kg/m^2 Armox 500T steel offered the ballistic limit equivalent to that of the 196 kg/m^2 mild steel. Therefore, with respect to thickness as well as areal density the capacity of Armox steel is 2.5 time higher than mild steel against 7.62 API threat. Similarly, the ballistic performance of Armox 500 T and aluminium materials has also been compared against 12.7 API projectiles as a function of their areal densities, Fig. 7.12. It has been observed that 108 kg/m^2 of 7075-T651 aluminium offered the ballistic limit equivalent to that of the 157 kg/m^2 of Armox 500T steel. Therefore, if the performance of Armox steel and aluminium is compared with respect to thickness, the aluminium target should be two times thicker than Armox steel target to stop the 12.7 API projectile. However, if the areal density of the two materials is compared, Armox would be two times heavier than the equivalent aluminium target to stop the 12.7 API projectile. Thus, with respect to weight aluminium is twice as capable as Armox steel.

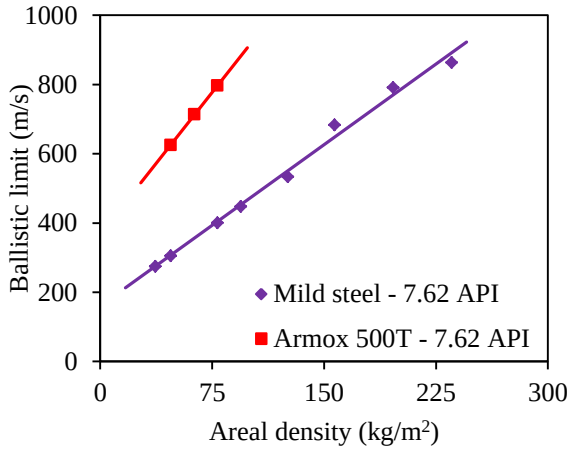

Fig. 7.11 Ballistic resistance of targets against 7.62 API projectile as a function of areal density of targets

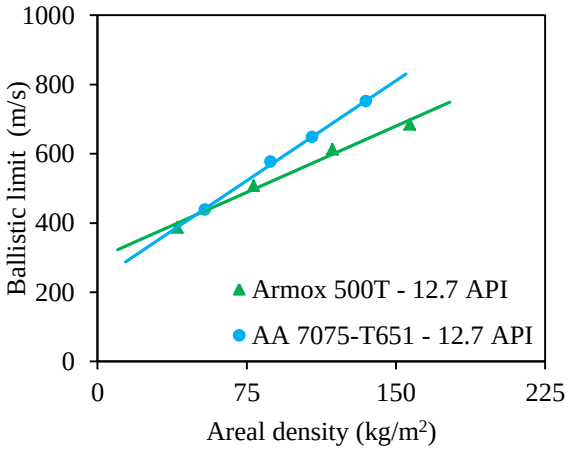

Fig. 7.12 Ballistic resistance of targets against 12.7 API projectile as a function of areal density of targets

7.8 EFFECT OF OBLIQUE IMPACT ON MILD STEEL, ARMOX 500T AND 7075-T651 ALUMINIUM TARGETS

The critical angle of ricochet and maximum angle for perforation has been found to decrease with an increase in the thickness of the target. Therefore, in general, the ballistic resistance of the target increased with increase in the angle of obliquity.

For 7.62 API projectile and 10 mm thick Armox 500T target the critical angle of ricochet was found to be 45° and for an equivalent thick mild steel target it was found to be 62°, see Fig. 7.13(a). For 12.7 API projectile and 20 mm thick Armox 500T steel target the critical angle of ricochet was found to be 45° while for an equivalent thick aluminum target it was found to be 60°, see Fig. 7.13(b).

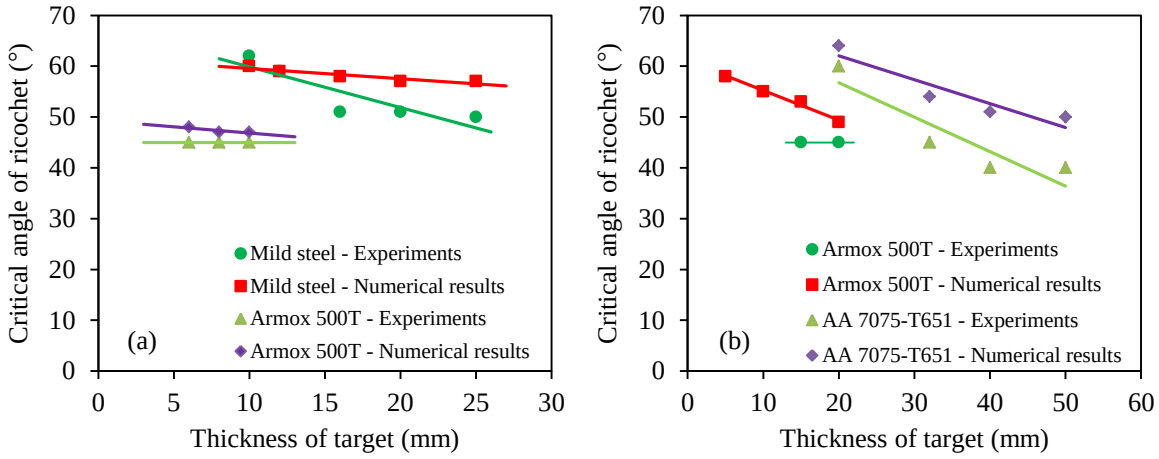

Fig. 7.13 Critical angle of ricochet of (a) 7.62 API (b) 12.7 API projectiles

7.9 CONCLUSIONS

The material behaviour and ballistic performance of different target materials studied in the present thesis has been compared. The ballistic limit of Armox 500T steel target has been found to be merely 100% higher than the equivalent mild steel target against 7.62 API projectile despite the fact that the hardness as well as the strength of Armox 500T steel was

four to five times higher than mild steel. Further, the weight of Armox 500T steel target was 280% higher than the equivalent aluminium target however, the ballistic limit of Armox steel target was 55% higher than the equivalent aluminium target against 12.7 API projectile. The mass of 12.7 API projectile was about five times higher than that of the 7.62 API projectile thus the kinetic energy offered by 12.7 API projectile was also five times higher than that offered by 7.62 API projectile. However, the energy absorbed by the 10 mm thick target against 7.62 API projectile was three times higher than the energy absorbed by the same target against 12.7 API projectiles. The 10 mm thick Armox 500T steel target offered the ballistic limit equivalent to that of the 25 mm thick mild steel target against 7.62 API projectile. Similarly, the 20 mm thick Armox 500T steel target offered the ballistic limit equivalent to that of 40 mm thick 7075-T651 aluminium target against 12.7 API projectiles.

CHAPTER 8

Conclusions and Scope for Future Work

8.1 CONCLUSIONS

The present study addresses the experimental and finite element investigation of the behaviour of metallic plats subjected to small arms projectile impact. The mild steel, Armox 500T steel and 7075-T651 aluminium targets of various thicknesses were impacted by Armor Piercing Incendiary (API) projectiles by changing the angle of incidence. The maximum angle of projectile perforation and critical ricochet was obtained. The target as well as projectile material was also characterized under varying state of stress, strain rate and temperature. The material parameters of the Johnson-Cook elasto-viscoplastic model were calibrated. The calibrated parameters were validated by carrying out the finite element simulation of the high strain rate tension tests performed on Hopkinson Pressure apparatus. The material parameters were subsequently employed for simulating the behaviour of projectile and target in order to numerically reproduce the ballistic tests. The numerical simulations enabled the determination of ballistic limit at normal impact. Salient findings of the study are given below;

- The mild steel and Armox 500T steel plates were found to be isotropic. Particularly, the stress-strain relations of mild steel obtained at different orientations overlapped each other. For Armox 500T steel, the maximum deviation between the elastic properties obtained from different orientations was 7%, however, the total strain in different orientations was found to be almost identical. On the other hand, for 7075-T651 aluminum the yield strength was almost same even for 0° and 90° orientation, however, it was significantly lesser at 45° orientation. Further, the highest fracture strain was found to be 45% at 45° orientation. However, at 90° orientation the

specimens failed merely at 14% strain. Thus it was concluded that 7075-T651 aluminum possesses high degree of anisotropy.

- The notched cylindrical specimens of mild steel, Armox 500T steel and 7075-T651 aluminium of varying initial notch radius, 0.2 – 10, were tested under tension for studying the influence of stress triaxiality on the material behaviour. The results thus obtained revealed a decrease in ductility and an increase in strength of the material with increase in stress triaxiality.
- The strain rate sensitivity of the material was studied by carrying out the material tests at low, intermediate and high strain rate. A nominal increase in the strength of mild steel from 325 to 400 MPa was found when the strain rate increased from 6×10^{-4} s^{-1} to 6×10^{-2} s^{-1}. However, at high strain rate, 1450 s^{-1}, the strength of the material increased abruptly to 850 MPa, and the ductility decreased. In order to verify this behaviour, the high strain rate tests for mild steel were also performed under compression, and these tests confirmed the findings of the tension tests. The strain rate sensitivity of Armox 500T steel was found similar to that of the mild steel. However, the 7075-T651 aluminium alloy did not reveal any strain rate sensitivity either with respect to strength or strain.
- The thermal sensitivity of the material was studied by carrying out tension tests at varying temperature, 27 °C - 900 °C. The flow stress of mild steel, Armox 500T steel and 7075-T651 aluminum increased initially with increase in temperature between 100 °C to 300 °C due to blue brittle effect. The elongation of mild steel remained unaffected up to 600 °C. However, at 750 °C temperature the material lost all of its strength and the corresponding elongation registered was 50%. Armox 500 T steel

lost all the strength at 900°C temperature and underwent 50% elongation before rupture. The 7075-T651 aluminum lost its strength at 500 °C and experienced 25% elongation at failure.

- The hardness, chemical composition, elastic and plastic flow properties of 7.62 and 12.7 API projectiles were found to be almost identical. The material of the projectile was also characterized at varying stress triaxility, strain rate and temperature. There was no influence of stress triaxiality and strain rate on the material behavior of projectile. However, the thermal sensitivity of the material was found to be highly significant. At 400 °C temperature, the strength of the material reduced from 2257 MPa to 1706 MPa. At 600 °C temperature, the material lost all of its strength and underwent 20% elongation at fracture.
- The material parameters of Johnson-Cook flow stress and fracture models were calibrated through curve fitting method for mild steel, Armox 500T steel, 7075-T651 aluminium and API projectile materials. The calibrated material parameters were validated by simulating the high strain rate tests performed on Split Hopkinson Pressure Bar (SHPB) apparatus. A good correlation between the actual and predicted stress-strain relationship was found.
- The mild steel target experienced hole enlargement and bulging when impacted by the projectile. The circular hole formed in the target was equivalent to that of the diameter of the projectile and no scabbing or spalling of the material was noticed during perforation. Armox 500T steel target however, experienced significant spalling from the front as well as rear face and the hole developed in the target was also not distinctly circular. The material aslo experineced fragmentation during

perforation process. The failure mechanism of aluminium targets was almost similar to that of the Armox steel. However, in this case the spalling from the front surface was deep but confined to smaller area and at the rear surface it was shallow but spread to a larger area.

- In general, the ballistic resistance has been found to increase with increase in angle of obliquity. Moreover, the critical angle of projectile ricochet and maximum angle of perforation was found to decrease with increase in target thickness.
- The ballistic limit of 10 mm thick Armox 500T steel target has been found to be 100% higher than the equivalent mild steel target against 7.62 API projectile. The 10 mm thick Armox 500T steel target on the other hand, offered the ballistic limit equivalent to that of the 25 mm thick mild steel target against 7.62 API projectile.
- The ballistic limit of 20 mm thick Armox 500T steel target has been found to be 55% higher than the equivalent 7075-T651 aluminum target against 12.7 API projectile. The 20 mm thick Armox 500T steel target, however, offered the ballistic limit equivalent to that of the 40 mm thick 7075-T651 aluminium target against 12.7 API projectile.
- The ballistic performance of mild steel and Armox 500T steel as a function of target areal density has been compared against 7.62 API projectile. It has been found that 78 kg/m^2 Armox 500T steel offered the ballistic limit equivalent to that of the 196 kg/m^2 mild steel. Therefore, with respect to thickness as well as areal density the capacity of Armox steel is 2.5 time higher than mild steel against 7.62 API threat.
- The ballistic performance of Armox 500T and aluminium materials has also been compared against 12.7 API projectiles as a function of their areal densities. It has

been observed that 108 kg/m^2 of 7075-T651 aluminium offered the ballistic limit equivalent to that of the 157 kg/m^2 of Armox 500T steel. Therefore, if the performance of Armox steel and aluminium is compared with respect to thickness, the aluminium target should be two times thicker than Armox steel target to stop the 12.7 API projectile. However, if the areal density of the two materials is compared, Armox would be two times heavier than the equivalent aluminium target to stop the 12.7 API projectile.

- For 7.62 API projectile and 10 mm thick Armox 500T target the critical angle of ricochet was found to be 45° and for an equivalent thick mild steel target it was found to be 62°. For 12.7 API projectile and 20 mm thick Armox 500T steel target the critical angle of ricochet was found to be 45° while for an equivalent thick aluminum target it was found to be 60°.

8.2 SCOPE FOR FUTURE WORK

The following may be considered as the scope of work for the extension of present study in future;

- A constitutive model with lesser number of material parameters may be characterized and employed for carrying out the finite element simulations.
- The modification in the flow stress and fracture strain expression of the Johnson-Cook model may be proposed in view of the strain rate and temperature sensitivity of the material.
- The ballistic performance of layered target configuration may be studied and the results may be compared with that of the monolithic target of equivalent thickness.

REFERENCES

1. ABAQUS/Explicit User's Manual, Version 6.8.
2. AGARD (Advisory Group for Aerospace Research and Development), Design manual for impact damage tolerant aircraft structure, 7 Rue, Ancelle 92200, France, 2001, 1–244.
3. Agarwal**.** S., Chakraborty. A., Gopalakrishnan. S. (2006) Large deformation analysis for anisotropic and inhomogeneous beams using exact linear static solutions, Composite Structures, (72) 91–104.
4. Aretz. H., Hopperstad. O.S., Lademo. O.G. (2007) Yield function calibration for orthotropic sheet metals based on uniaxial and plane strain tensile tests, Journal of Materials Processing Technology, (186) 221–235.
5. Arminjon. M., Bacroix. B. (1991) On plastic potentials for anisotropic metals and their derivation from the texture function, Acta Mechanica, (88) 219–243.
6. Arminjon. M., Bacroix. B., Imbault. D., Raphanel. J.L. (1994) A fourth-order plastic potential for anisotropic metals and its analytical calculation from the texture function, Acta Mechanica, (107) 33–51.
7. Balos. S., Grabulov. V., Sidjanin. L., Pantic. M., Radisavljevic. I. (2010) Geometry, mechanical properties and mounting of perforated plates for ballistic application, Materials and Design, (31) 2916–2924.
8. Banerjee. B. (2005) An evaluation of plastic flow stress models for the simulation of high temperature and high strain rate deformation of metals, arXiv:cond-mat/0512466v1. 1–43.

9. Barlat. F., Chung. K. (1993) Anisotropic potentials for plastically deformation metals, Modelling and Simulation in Materials Science and Engineering, (1) 403–416.

10. Barlat. F., Brem. J.C., Yoon. J.W., Chung. K., Dick. R.E., Lege. D.J., Pourboghrat. F., Choi. S.H., Chu. E. (2003) Plane stress yield function for aluminum alloy sheets - Part 1: theory, International Journal of Plasticity, (19) 1297–1319.

11. Bhat. T.B. (1985) Science of armour materials, Defence Science Journal, (35) 219–223.

12. Borvik. T., Langseth. M., Hopperstad O.S., Malo .K. A. (1999) Ballistic penetration of steel plates, International Journal of Impact Engineering, (22) 855–886.

13. Borvik. T., Hopperstad. O.S., Berstad. T., Langseth. M. A. (2001) Computational model of viscoplasticity and ductile damage for impact and penetration, European Journal of Mechanics and Solids, (20) 685–712.

14. Borvik. T., Langseth. M., Hopperstad. O.S., Malo. K.A. (2002a) Perforation of 12mm thick steel plates by 20mm diameter projectiles with flat, hemispherical and conical noses part I: Experimental study, International Journal of Impact Engineering, (27) 19–35.

15. Borvik. T., Langseth. M., Hopperstad. O.S., Malo. K.A. (2002b) Perforation of 12mm thick steel plates by 20mm diameter projectiles with flat, hemispherical and conical noses part II: Numerical simulations, International Journal of Impact Engineering, (27) 37–64.

16. Borvik. T., Hopperstad. O.S., Langseth. M., Malo. K. A. (2003) Effect of target thickness in blunt projectile penetration of Weldox 460 E steel plates, International Journal of Impact Engineering, (28) 413–464.

17. Borvik. T., Clausen. A.H., Hopperstad. O.S., Langseth. M. (2004) Perforation of AA5083-H116 aluminium plates with conical-nose steel projectiles – experimental study, International Journal of Impact Engineering, (30) 367–384.

18. Borvik. T., Forrestal. M.J., Hopperstad. O.S., Warren. T., Langseth. M., (2009a) Perforation of AA5083-H116 aluminium plates with conical-nose steel projectiles – Calculations, International Journal of Impact Engineering, (36) 426–437.

19. Borvik. T, Dey. S., Clausen. A.H. (2009b) Perforation resistance of five different high-strength steel plates subjected to small-arms projectiles, International Journal of Impact Engineering, (36) 948–964.

20. Borvik. T., Hopperstad. O.S., Pedersen. K.O. (2010) Quasi-brittle fracture during structural impact of AA7075-T651 aluminium plates, International Journal of Impact Engineering, (37) 537–551.

21. Borvik. T., Olovsson. L., Dey. S. Langseth. M. (2011) Normal and oblique impact of small arms bullets on AA6082-T4 aluminum protective plates, International Journal of Impact Engineering, (38) 577–589.

22. Borvik. T., Dey. S., Olovsson. L. (2015) Penetration of granular materials by small-arms bullets, International Journal of Impact Engineering, (75) 123–139.

23. Brian Leavy R. (1996) Improved rolled homogeneous armor. Army Research Laboratory. March 1996, ARL-CR-285: 1–28.

24. Bridgman P.W. Studies in large plastic flow and fracture, New York, McGraw-Hill, (1952).

25. Bron. F., Besson. J. (2004) A yield function for anisotropic materials - Application to aluminum alloys, International Journal of Plasticity, (20) 937–963.

26. Buchar. J., Voldrich. J., Rolc. S., Lisy. J. Ballistic performance of dual hardness armour," 20th international symposium of ballistics. Orlando, 23–27 September 2002.

27. Chakraborty. A., Gopalakrishnan. S. (2005) Wave propagation in inhomogeneous beam: A spectral element formulation, Computational Mechanics, (36) 1–12.

28. Choi. Y., Han. C.S., Lee. J.K., Wagoner. R.H. (2006) Modelling multiaxial deformation of planar anisotropic elasto-plastic materials, Part I: Theory, International Journal of Plasticity, (22)1745–1764.

29. Clausen. A.H., Borvik. T., Hopperstad. O.S., Benallal. A. (2004) Flow and fracture characteristic of aluminum alloy AA 5083-H116 as function of strain rate, temperature and triaxiality, Material Science Engineering, (A364) 260–272.

30. Chocron. S. J., Anderson. C., Grosch. J.D., Popelar. H.C. (2001) Impact of the 7.62 mm APM2 projectile against the edge of a metallic target, International Journal of Impact Engineering (25) 423–437.

31. Corran. R.S.J., Shadbolt. P.J., Ruiz. C. (1983) Impact loading of plates – An experimental investigation, International Journal of Impact Engineering, (1) 3-22.

32. Corbett. G.G., Reid. S.R., Johnson. W. (1996) Impact loading of plates and shells by free-flying projectiles: A Review, International Journal of Impact Engineering, (18) 141–230.

33. Demir. T., Ubeyli. M., Yıldırım. R.O. (2008) Investigation on the ballistic impact behavior of various alloys against 7.62 mm armor piercing projectile. Materials and Design, (29) 2009–2016.

34. Dey. S., Børvik. T., Hopperstad. O.S., Leinum. J.R., Langseth. M. (2004) The effect of target strength on the perforation of steel plates using three different projectile nose shapes, International Journal of Impact Engineering (30) 1005–1038.

35. Dey. S., Borvik. T., Hopperstad. O.S., Langseth. M. (2006) On the influence of fracture criterion in projectile impact of steel plates. Computational Material Science, (38) 176–191.

36. Dey. S., Børvik. T., Teng. X., Wierzbicki. T., Hopperstad. O.S. (2007) On the ballistic resistance of double-layered steel plates: An experimental and numerical investigation, International Journal of Solids and Structures, (44) 6701–6723.

37. Dikshit. S.N., Kutumbarao. V.V., Sundararajan. G. (1995) The influence of plate hardness on the ballistic penetration of thick steel plates. International Journal of Impact Engineering, (16) 293–320.

38. Dikshit. S.N. (1998) Ballistic Behaviour of thick steel armor plate under oblique impact: Experimental investigation-I, Defence Science Journal, (48) 271–276.

39. El. Magd E., Abouridouane M. (2006) Characterization, modelling and simulation of deformation and fracture behaviour of the light-weight wrought alloys under high strain rate loading, International Journal of Impact Engineering, (32) 741–758.

40. Emrah. K. H., Murat Ç. M., Kayran. A. (2011) Computational and experimental study of high-speed impact of metallic Taylor cylinders, Acta Mechanica, (220) 61–85.

41. Forrestal. M.J., Luk. V.K., Rosenberg. Z., Brar. N. S. (1992) Penetration of 7075-T651 aluminum targets with ogival nose projectiles, International Journal of Solids and Structures, (29) 1729–36.

42. Forrestal. M.J., Borvik. T., Warren. T.L. (2010) Perforation of 7075-T651 aluminium armor plates with 7.62 mm APM2 bullets, Experimental Mechanics, (50) 1245–1251.

43. Forrestal. M.J., Børvik. T., Warren. T.L., Chen. W. (2014) Perforation of 6082-T651 aluminum plates with 7.62 mm APM2 bullets at normal and oblique impacts, Experimental mechanics, (54) 471–481.

44. Fourmeau. M., Børvik. T., Benallal. A., Lademo. O.G., Hopperstad. O.S. (2011) On the plastic anisotropy of an aluminium alloy and its influence on constrained multiaxial flow, International Journal of Plasticity, (27) 2005–2025.

45. Goldsmith. W., Finnegan. S.A. (1986) Normal and oblique impact of cylindro-conical and cylindrical projectiles on metallic plates, International Journal of Impact Engineering, (4) 83–105.

46. Gooch. W.A., Showalter. D.D., Burkins. M.S., Thorn. V., Cimpoeru. S. J., Barnett. R. (2007) Ballistic testing of Australian bisalloy steel for armor application, 23rd International Symposium on ballistics Tarragona, 1181–1188.

47. Gupta. N.K., Madhu. V. (1992) Normal and oblique impact of a kinetic energy projectile on mild steel plates, International Journal of Impact Engineering, (12) 333–343.

48. Gupta. N.K., Madhu. V. (1997) An experimental study of normal and oblique impact of hard-core projectile on single and layered plates, International Journal of Impact Engineering, (19) 395–414.

49. Gupta. N.K., Iqbal. M.A., Sekhon. G.S. (2007) Effect of projectile nose shape, impact velocity and target thickness on deformation behavior of aluminum plates, International Journal of Solids and Structures, (44) 3411–3439.

50. Gupta. N.K., Iqbal. M.A., Sekhon. G.S. (2008) Effect of projectile nose shape, impact velocity and target thickness on the deformation behavior of layered plates, International Journal of Impact Engineering, (35) 37–60.

51. Hancock. J.W., Mackenzie. A.C. (1976) On the mechanisms of ductile failure in high-strength steels subjected to multi-axial stress-states, Journal of the Mechanics and Physics of solids, (24) 147–169.

52. Hill. R. (1948) A theory of the yielding and plastic flow of anisotropic metals. Proceedings of the Royal Society of London, Series A, Mathematical and Physical Sciences, (193) 281–297.

53. Hill. R. (1950) The Mathematical Theory of Plasticity, Oxford University Press.

54. Hill. R. (1987) Constitutive dual potentials in classical plasticity, Journal of the Mechanics and Physics of Solids, (35) 22–33.

55. Hill. R. (1990) Constitutive modelling of orthotropic plasticity in sheet metals, Journal of the Mechanics and Physics of Solids, (38) 405–417.

56. Hillerborg. A., Modeer. M., Petersson. P.E. (1976) Analysis of crack formation and crack growth in concrete by means of fracture mechanics and finite elements, Cement and Concrete Research, (6) 773–782.

57. Hong. H., Andrew. D. J., Wu. C. (2008) Numerical simulations of the performance of steel guardrails under vehicle impact, Transaction of Tianjin University and Springer-Verlag, (14) 318–323.

58. Hopperstad. O.S., Børvik. T., Langseth. M., Labibes. K., Albertini. C. (2003a) On the influence of stress triaxiality and strain rate on the behaviour of a structural steel. Part I Experiments, European Journal of Mechanics A/Solids, (22) 1–13.

59. Hopperstad. O.S., Borvik. T., Berstad. T. (2003b) On the influence of stress triaxiality and strain rate on the behaviour of a structural steel, Part II Numerical study, European Journal of Mechanics A/Solids, (22) 15–32.

60. Hosseini. M., Abbas. H. (2006) Growth of hole in thin plates under hypervelocity impact of spherical projectiles, Thin-Walled Structures, (44) 1006–1016.

61. Iqbal. M.A., Gupta. N.K., Sekhon G.S. (2006) Behavior of thin aluminum plates subjected to impact by ogive-nosed projectiles, Defence Science Journal, (56) 841–852.

62. Iqbal. M.A., Gupta. G., Gupta. N.K. (2010a) 3D numerical simulations of ductile targets subjected to oblique impact by sharp nosed projectiles, International Journal of Solids and Structures, (47) 224–237.

63. Iqbal. M.A., Gupta. G., Diwakar. A., Gupta. N.K. (2010b) Effect of projectile nose shape on the ballistic resistance of ductile targets, European Journal of Mechanics – AA/Solids, (29) 683–694.

64. Iqbal. M.A., Gupta. P.K., Deore. V.S., Tak. S.K., Tiwari. G., Gupta. N.K. (2012) Effect of target span and configuration on the ballistic limit, International Journal of Impact Engineering, (42) 11–24.

65. Iqbal. M.A., Khan. S.H., Ansari. R., Gupta. N.K. (2013) Experimental and numerical studies of double-nosed projectile impact on aluminum plates, International Journal of Impact Engineering, (54) 232–245.

66. Iqbal. M.A., Senthil. K., Bhargava. P., Gupta. N.K. (2015) The characterization and ballistic evaluation of mild steel, International Journal of Impact Engineering (78), 98-113.

67. Jena. P.K., Mishra. B., Siva Kumar. K., Bhat. T.B. (2010a) An experimental study on the ballistic impact behavior of some metallic armour materials against 7.62 mm deformable projectile, Materials and Design, (31) 3308–3316.

68. Jena. P.K., Mishra. B., Ramesh Babu. M., Arvindha. B., Siva Kumar. K., Bhat. T.B. (2010b) Effect of heat treatment on mechanical and ballistic properties of high strength armour steel, International Journal of Impact Engineering, (37) 242–249.

69. Johnson G.R., Cook W.H. A constitutive model and data for metals subjected to large strains, high strain rates and high temperatures, In: Proceedings of the 7th International Symposium on Ballistics, 1983. The Hague, Netherlands: 541–547.

70. Johnson G.R., Cook W.H. (1985) Fracture characteristics of three metals subjected to various strains, strain rates, temperatures, and pressures, Engineering Fracture Mechanics, (21) 31–48.

71. Johnson. E.A.F., Salesh. M., Edwards. L. (2011) Ballistic performance of multi-layered metallic plates impacted by a 7.62 mm APM2 projectile, International Journal of Impact Engineering, (38) 1022–1032.

72. Kant. T. (1982) Numerical analysis of thick plates, Computer Methods in Applied Mechanics and Engineering, (31) 1–18.

73. Karafillis. A.P., Boyce. M.C. (1993) A general anisotropic yield criterion using bounds and a transformation weighting tensor, Journal of Mechanics and Physics of Solids, (41) 1859–1886.

74. Kilic. N., Ekici. B. (2013) Ballistic resistance of high hardness armor steels against 7.62 mm armor piercing ammunition, Materials and Design, (44) 35–48.

75. Kilic. N., Bedir. S., Drik. A., Ekici. B., Tasdemirci. A., Guden. M. (2014) Ballistic behavior of high hardness perforated armor plates against 7.62 mm armor piercing projectile, (63) 427–438.

76. Kim. D., Barlat. F., Bouvier. S., Rabahallah. M., Balan. T., Chung. K. (2007) Non-quadratic anisotropic potential based on linear transformation of plastic strain rate, International Journal of Plasticity, (23) 1380–1399.

77. Kolla. H.H., Mishra. B., Jena. P.K., Siva Kumar. K., Bhat. T.B. (2011) Development of new ultra high strength low alloy steel for armour applications, Material Science Technology, (27) 551–555.

78. Krishnamurthy. K.S., Mahajan. P., Mittal. R.K. (2001) A parametric study of the impact response and damage of laminated cylindrical composite shells, Composites Science and Technology, (61) 1655–1669.

79. Krishnamurthy. K.S., Mahajan. P., Mittal. R.K. (2003) Impact response and damage in laminated composite cylindrical shells, Composite Structures, (59) 15–36.

80. Leacock. A.G. (2006) A mathematical description of orthotropy in sheet metals, Journal of the Mechanics and Physics of Solids, (54) 425–444.

81. Le Roy. G., Embury. J.D., Edwards. G., Ashby. M.F. (1981) A model of ductile fracture based on the nucleation and growth of voids, Acta Metallurgica**,** (29) 1509–1522.

82. Lee. W.S., Sue. W.C., Lin. C.F., Wu. C.J. (2000) The strain rate and temperature dependence of the dynamic impact properties of 7075 alloy, Journal of Material Processing Technology, (100) 116–22.

83. Madhu. V., Ramanjaneyulu. K., Bhata. T.B., Gupta N.K. (2005) An experimental study of penetration resistance of ceramic armour subjected to projectile impact, International Journal of Impact Engineering, (32) 337–350.

84. Madhu. V., Bhat. T.B. (2011) Armour protection and affordable protection for futuristic combat vehicles, Defence Science Journal, 61(4) 394–402.

85. Mallikarjuna, Kant. T. (1992) Effect of cross sectional warping of anisotropic sandwich laminates to dynamic load using a refined theory and C^0 finite elements, International Journal for numerical methods in engineering, (35) 2031–2047.

86. Mannan. M.N., Ansari. R., Abbas. H., (2008) Failure of aluminium beams under low velocity impact, International Journal of Impact Engineering, (35) 1201–1212.

87. Mishra B., Jena. P.K., Rama krishna. B., Mahdu. V., Bhat. T.B., Gupta. N.K. (2012) Effect of tempering temperature, plate thickness and presence of holes on ballistic impact behavior and ASB formation of a high strength steel, International Journal of Impact Engineering, (44) 17–28.

88. Mishra B., Rama krishna. B., Jena. P.K., Kumar. S.V., Mahdu. V., Gupta. N.K. (2013) Experimental studies on the effect of size and shape of holes on damage and microstructure of high hardness armour steel plastes under ballistic impact, Materials and Design, (43) 17–24.

89. Monchiet. V., Cazacu. O., Charkaluk. E., Kondo. D. (2008) Macroscopic yield criteria for plastic anisotropic materials containing spheroidal voids, International Journal of Plasticity, (24) 1158–1189.

90. Nadeem. A.S, Khateeb. B.M.A., Almusallam. T.H., Al-Salloum. Y.A., Iqbal. R.A., Abbas. H., (2014) Reliability of RC shielded steel plates against the Impact of sharp nose projectiles, International Journal of Impact Engineering, (69) 122–135.

91. Niezgoda. T., Morka. A. (2009) On the numerical methods and physics of perforation in the high-velocity impact mechanics, World Journal Engineering, 414–416.

92. Nilsson M. Constitutive model for Armox 500T and Armox 600T at low and medium strain rates. FOI, Swedish Defence Research Agency, TR FOI-R-1068-SE, 2003.

93. Piekutowski. A.J., Forrestal. M.J., Poormon. K.L., Warren. T.L., (1996) Perforation of aluminum plates with ogive-nose steel rods at normal and oblique impacts, International Journal of Impact Engineering, (18) 877–887.

94. Prince Sharma, Pradeep Chandel, Vikas Mangla, Puneet Mahajan, Manjit Singh (2013) Effect of strain rate on constitutive behavior of AA-5052 H34, Key Engineering Materials, (535-536) 60–63.

95. Prifti J., Castro M., Squillacioti R., Cellitti R. (1997) Improved rolled homogeneous armour (IRHA) steel through higher hardness, April 1997, ARL-TR-1347, 1–49.

96. Rahul, S.S., Velmurugan. R., Madhu. V. (2012) Experimental and analytical study of high velocity impact on Kevlar/Epoxy composite plates, Central European Journal of Engineering, (2) 838–850.

97. Recht. R.F., Ipson. T.W. (1963) Ballistic perforation dynamics, Journal of Applied Mechanics, (30) 384–90.

98. Sandeep S.P., Kant. T., Desai. Y.M. (2008) Application of polymer composites in civil construction: A general review, Composite Structures, (84) 114-124.

99. Senthil. K., Iqbal. M.A. (2013a) Effect of projectile size on the ballistic resistance and fracture behavior of thin aluminum plates, Theoretical and Applied Fracture Mechanics (67-68) 53–64.

100. Senthil. K., Tiwari. G., Iqbal. M.A., Gupta. N.K. (2013b) Impact response of single and layered thin plates, Proceedings of Indian National Science Academy, (79) 705–716.

101. Singh. N.K., Cadoni. E., Singha. M.K., Gupta. N.K., (2013) Dynamic tensile and compressive behaviors of mild steel at wide range of strain rates, Journal of Engineering Mechanics, ASCE, (139) 1197–1206.

102. Sjoberg. T., Sundin. K.G., Oldenburg. M. (2013) Calibration and validation of plastic high strain rate models for alloy 718. XII International Conference on Computational Plasticity, Fundamentals and Applications, September 3–5 Barcelona, Spain.

103. Showalter D.D., Gooch W.A., Burkins M.S., Koch. R.S. Ballistic testing of SSAB Ultra-high-hardness steel for armour applications, June 2008, ARL-RP-181, 1–52.

104. Soare, S., Barlat, F. (2010) Convex polynomial yield functions, Journal of the Mechanics and Physics of Solids, (58) 1804–1818.

105. Sridhar. R., Chakraborty. A., Gopalakrishnan. S. (2006) Wave propagation in a isotropic and inhomogeneous uncracked and cracked structures using pseudo-spectral finite element method, International Journal for Solids and Structures, (43) 4997–5031.

106. Starke Jr. E.R., Staley J.T. (1996) Application of modern aluminium alloys to aircraft. Progress in Aerospace Science, (32) 131–172.

107. Su. Y., Wu. C., Griffith. M. (2008) Mitigation of blast effects on aluminum foam protected masonry walls, Transaction of Tianjin University and Springer-Verlag, (14) 558–562.

108. Tajally. M., Emadoddin. E. (2011) Mechanical and anisotropic behaviors of 7075 aluminum alloy sheets, Materials and Design, (32) 1594–1599.

109. Teng. X., Wierzbicki. T. (2006) Evaluation of six fracture models in high velocity perforation Engineering Fracture Mechanics, (73) 1653–1678.

110. Teng. X., Wierzbicki. T., Huang. M., (2008) Ballistic resistance of double-layered armor plates, International Journal of Impact Engineering, (35) 870–884.

111. Ubeyli. M., Yıldırım. R.O., Ogel. B. (2007) On the comparison of the ballistic performance of steel and laminated composite armors, Materials and Design, (27) 1257–1262.

112. Van Houtte. P., Van Bael. A. (2004) Convex plastic potentials of fourth and sixth rank for anisotropic materials, International Journal of Plasticity, (20) 1505–1524.

113. Velmurugan. R., Gupta. N.K. (2003) Energy Absorption Characteristics of Metallic and Composite Shells, Defence Science Journal, (53) 127–138.

114. Velmurugan R., Sikarwar. R.S., Gupta. N.K. (2010) Analytical modeling for ballistic perforation of angle- ply and hybrid composite laminates, Proceedings of the IMPLAST 2010 Conference, October 12-14, 2010 Providence, Rhode Island USA.

115. Pedersen. K.O., Børvik. T., Hopperstad. O.S. (2011) Fracture mechanisms of aluminium alloy AA7075-T651 under various loading conditions, Materials and Design, (32) 97–107.

116. Woodward. R.L. (1978) The penetration of metal targets which fail by adiabatic shear plugging, International Journal of Mechanical Science, (20) 599–607.

117. Wu. C., Huang. L., Oehlers. D.J. (2011) Blast testing of aluminum foam protected reinforced concrete slabs. Journal of Performance for Constructed Facilities, ASCE, (25) 464–474.

118. Yang. Y., Zeng. Y., Gao. Z.W. (2008a) Numerical and experimental studies of self-organization of shear bands in 7075 aluminum alloy, Material Science Engineering, (A496) 291–302.

119. Yang. Y., Zeng. Y., Li DH., Li. M. (2008b) Damage and fracture mechanism of aluminum alloy thick-walled cylinder under external explosive loading, Material Science Engineering, (A490) 378–384.

120. Zinkham. R.E. (1968) Anisotropy and thickness effects in fracture of 7075-T6 and -T651 aluminum alloy, Engineering Fracture Mechanics, (1) 275–89.

PUBLICATIONS

(a) Publications in Refereed Journals

1. **Senthil. K.,** Iqbal. M.A. (2013) Effect of projectile size on the ballistic resistance and fracture behavior of thin aluminum plates, Theoretical and Applied Fracture Mechanics, (67-68) 53–64.
2. Iqbal. M.A., **Senthil. K.,** Bhargava. P., Gupta N.K. (2015) The characterization and ballistic evaluation of mild steel, International Journal of Impact Engineering (78), 98–113.
3. **Senthil. K.,** Tiwari. G., Iqbal. M.A., Gupta. N.K. (2013) Impact response of single and layered thin plates, Proceedings of Indian National Science Academy, (79) 705–716.

(b) Publications in Refereed Conferences

1. **Senthil. K.,** Iqbal. M.A., Bhattacharjee. D., Bhargava. P., Gupta. N.K. Ballistic Resistance of Armox 500T Steel Plates against 7.62 API Projectiles, 3rd International Conference on Protective Structures, 03-06 February, 2015, Australia, Newcastle. (Accepted for publication)
2. Iqbal. M.A., **Senthil. K.,** Madhu. V., Gupta. N.K. (2013) Material characterization and ballistic evaluation of mild steel, Indo-Russian Workshop at IIT Madras, 11–15, November.
3. **Senthil. K.,** Iqbal. M.A., Gupta. N.K. (2014) Thin metallic plates subjected to projectile impact, 4th International Conference on Impact Loading of light Weight Structures, Cape Town, South Africa, 12–16 January 2014.
4. Khan. S.H., Iqbal. M.A, **Senthil. K.,** Ansari. R., Gupta. N.K. (2014) Ballistic response of 1100-H14 thin aluminum plates against blunt and conical nose projectiles, 4th International Conference on Impact Loading of light Weight Structures, Cape Town, South Africa, 12–16 January 2014.
5. **Senthil. K.,** Iqbal. M.A., Gupta. N.K. (2012) Finite element studies on behavior of thin aluminum plates subjected to hollow and solid projectile impact, Symposium on Large Deformation under Dynamic Loading, 1st September 2012, INSA Building, New Delhi.